



저작자표시-비영리-변경금지 2.0 대한민국

이용자는 아래의 조건을 따르는 경우에 한하여 자유롭게

- 이 저작물을 복제, 배포, 전송, 전시, 공연 및 방송할 수 있습니다.

다음과 같은 조건을 따라야 합니다:



저작자표시. 귀하는 원저작자를 표시하여야 합니다.



비영리. 귀하는 이 저작물을 영리 목적으로 이용할 수 없습니다.



변경금지. 귀하는 이 저작물을 개작, 변형 또는 가공할 수 없습니다.

- 귀하는, 이 저작물의 재이용이나 배포의 경우, 이 저작물에 적용된 이용허락조건을 명확하게 나타내어야 합니다.
- 저작권자로부터 별도의 허가를 받으면 이러한 조건들은 적용되지 않습니다.

저작권법에 따른 이용자의 권리는 위의 내용에 의하여 영향을 받지 않습니다.

이것은 [이용허락규약\(Legal Code\)](#)을 이해하기 쉽게 요약한 것입니다.

[Disclaimer](#)

Doctor of Philosophy

**Designing Heteroatom Doped Carbon Dots
for Sensing Applications**

The Graduate School of the University of Ulsan

School of Chemical Engineering

Linlin Wang

**Designing Heteroatom Doped Carbon Dots
for Sensing Applications**

Supervisor: Professor Seung Hyun Hur

A Dissertation

Submitted to

The Graduate School of the University of Ulsan

In partial Fulfillment of the Requirements

for the Degree of

Doctor of Philosophy

by

Linlin Wang

School of Chemical Engineering

University of Ulsan, Korea

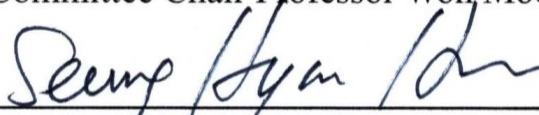
August 2021

Designing Heteroatom Doped Carbon Dots for Sensing Applications

This certifies that the dissertation of Linlin Wang is approved.



Committee Chair Professor Won Mook Choi



Committee Member Professor Seung Hyun Hur



Committee Member Professor Jin Suk Chung



Committee Member Professor Ik-Keun Yoo



Committee Member Professor Mun Ho Kim

School of Chemical Engineering

University of Ulsan, Korea

August 2021

ABSTRACT

In CHAPTER 1, introduced the production, development, and molecular recognition mechanisms of small molecule fluorescent probes, reviewed by the research frontier, present the basic design ideas and research methods of this paper.

In CHAPTER 2, nitrogen and boron-incorporated carbon dots (NBCDs) were fabricated using a hydrothermal process with ascorbic acid (AA) and 4-aminobenzeneboronic acid hydrochloride as novel precursors. The size and morphology were examined using the appropriate spectrochemical characterization. The NBCDs emission was examined in the presence of different metal ions. The fluorescence was quenched selectively in the presence of the Fe^{3+} ions and with increasing Fe^{3+} concentration in the reaction medium. From this fluorescence “Turn Off” phenomenon, Fe^{3+} could be detected in aqueous solution with a limit of detection (LOD) of 7.50 μM . This quenched fluorescence was recovered in the presence of AA selectively. This “Turn On” phenomenon was AA concentration dependent and AA could be detected in aqueous solution with a LOD value of 7.72 μM . Analysis of a real sample was conducted for the detection of Fe^{3+} ions in solution, which was collected from iron sheet reacted over the pH range of 2–7 for set times.

In CHAPTER 3, the water-soluble N-doped carbon dots (NCDs) are designed by simple hydrothermal treatment of aqueous mixture of citric acid and urea. The initially prepared NCDs are further been passivated by L-glutathione (GSH) through carbodiimide-activated coupling reaction to enhance the emissive properties of the NCDs. The as-obtained passivated carbon dots (GSH-NCDs) show intense blue emission at 440 nm when excited at 355 nm. However, this emission is observed to be quenched selectively in the presence of

dopamine (DA) leading to design a platform for DA detection. The quenching of fluorescence of GSH-NCDs is dependent on DA concentration. The limit of detection is 1.01 nM, with a linear detection ranges from 20 nM to 10 μ M ($R^2 = 0.992$). The average lifetime values and the spectral profile of GSH-NCDs in absence and presence of DA indicate the possibility of photoinduced electron transfer assisted inner filter effect mechanism for the DA induced quenching of GSH-NCDs' fluorescence. Further experiments show that the as-designed DA detection technique works successfully for biological fluids.

In CHAPTER 4, we report the green, blue, and orange color emitting N-doped carbon dots (CDs), which are being synthesized from ascorbic acid (AA) and o-/m-/p-phenylenediamine (o-PDA, m-PDA, and p-PDA, respectively). The effects of the solvent polarity and solution pH on the PL emission properties of the as-synthesized CDs have been systematically investigated. It has been observed that the PL emission of the as-synthesized CDs decreases with the increase in solvent polarity due to the greater agglomeration. The surface charge of CDs also shows prominent effects on the pH-dependent PL emission properties.

In CHAPTER 5, high quantum yield 3-aminophenylboronic acid-functionalized nitrogen-doped carbon dots (GAAP-CDs) were fabricated using a simple hydrothermal route and used as a sensing probe for toxic hypochlorite (ClO^-). The as-synthesized GAAP-CDs showed absorption peaks at 252, 297, and 370 nm and an emission peak at 375 nm with an excitation wavelength of 310 nm. The quantum yield of GAAP-CDs reached 58.28%, with no noticeable fluorescence change observed under high ionic strength conditions and a three-month long-term test. GAAP-CDs-based ClO^- sensing was carried out by UV-vis absorbance and fluorescence spectroscopy; the detection limit was as low as 0.77 μ M (linear range of 0–100 μ M), and 0.50 μ M (linear range of 0.1–100 μ M), respectively. In addition,

the as-synthesized GAAP-CDs showed excellent selectivity towards ClO^- ions in the presence of various interfering chemicals. The satisfactory results from the proposed method of ClO^- detection in tap water and drinking water samples, suggesting promising application of GAAP-CDs for ClO^- detection.

In CHAPTER 6, the low-cost and abundant nitrogen and boron-doped high quantum yield carbon dots (CPAP-CDs) were successfully synthesized through the facile hydrothermal process. The obtained CPAP-CDs showed wide absorption and strong fluorescence, the quantum yield can be achieved to 64.07%. The obtained carbon dots showed pH-dependent behavior and fluorescent response for hazardous anions nitrite in solutions. The fluorescence of CPAP-CDs was quenched in the presence of nitrite anion. The detection limit was 6.6 nM with a linear detection range of $2 \mu\text{M} \sim 1 \text{ mM}$. It is speculated that a diazotization between nitrites and CPAP-CDs, which induces photoinduced electron transfer process from the excited state of CPAP-CDs to the diazo compounds on the surface, quenches the inherent fluorescence of the as-synthesized carbon dots. The sensitivity was analyzed with different water samples, such as tap, drinking and sea water.

In CHAPTER 7, summary.

ACKNOWLEDGEMENT

Upon the completion of my dissertation, when I look back on my five years as a graduate student, I have experienced a lot of happy and unhappy things, and gained a lot. I have been pleased of working and making friends with many interesting individuals at the University of Ulsan. I would like to express my gratitude to all those who have offered me assistance, both in the science and life.

First and foremost, I would like to express my heartiest thanks to my advisor, Professor Seung Hyun Hur, for his generous guidance, expert advice through all stages of this research as well as the preparation of all the manuscripts for publication. Besides my advisor, I would like to thank all of my committee members, Professor Jin Suk Chung, Professor Won Mook Choi, Professor Ik-Keun Yoo and Professor Mun Ho Kim, for spending their valuable time to review this dissertation and contribute their insightful comments and suggestions to this work.

Thanks to all my former and present labmates, Lijun Sui, Jayasmita Jana, Hye-Jin Lee, Yen-Linh Thi Ngo, Tran Van Phuc, and Huynh Ngoc Diem for their professional supports in researching and their friendships. Also, I would like to thank my beloved friends, Di Liu, Yuanyuan Li, Yiming Meng, Hanshuang Cao, Hao Xu, always beside me whether hard or cheerful, thank you for coming into my life and make it so interesting. Special thanks should be given to Ms. Kyong Cho Lim for her assistance in the analysis instruments.

Finally, I would like to extend my deep gratefulness to my family, for their endless love and whole-hearted support gave throughout my graduate study. Thank you for your love and companionship, which have become an essential source of strength to me during the Ph.D. course. My heart swells with gratitude to all the people who helped me.

With their wonderful helps, I can achieve my Ph.D. degree. Thank you.

TABLE OF CONTENTS

CHAPTER 1. Introduction	1
1.1. Overview	1
1.2. Classification of CDs	2
1.3. Synthesis of CDs	4
1.4. Characterizations	6
1.5. Quenching mechanisms of CDs	8
1.5.1. Static quenching mechanism of CDs	8
1.5.2. Dynamic quenching mechanism of CDs	9
1.5.3. PET quenching mechanism of CDs	11
1.5.4. IFE mechanism of CDs	12
Reference	12
CHAPTER 2. Nitrogen and boron-incorporated carbon dots for the sequential sensing of ferric ions and ascorbic acid sensitively and selectively	15
2.1. Introduction	15
2.2. Experimental details	17
2.2.1. Materials	17
2.2.2. Characterization	17
2.2.3. Synthesis of NBCDs	18
2.2.4. Detection of metal ions and biochemical molecules	18
2.3. Results and discussion	20
2.3.1. Instrumental analysis of NBCDs	20
2.3.2. Optical properties	23

2.3.3. Selectivity and Sensitivity towards Fe ³⁺	25
2.3.4. One pot selective sensing of AA with Fe ³⁺ saturated NBCDs.....	29
2.3.5. The mechanism of NBCDs for sensing the Fe ³⁺ ion and AA	33
2.3.6. Acid rain monitoring.....	34
2.4. Conclusion.....	40
Reference	40
CHAPTER 3. Glutathione Modified N-doped Carbon Dots for Sensitive and Selective Dopamine Detection	44
3.1. Introduction	44
3.2. Experimental Section.....	48
3.2.1. Materials	48
3.2.2. Characterization.....	48
3.2.3. Synthesis of the NCDs.....	48
3.2.4. Synthesis of the GSH-NCDs and Quantum Yield (QY) Measurement.....	49
3.3. Results and discussion.....	49
3.3.1. Physical characterization of the GSH-NCDs.....	49
3.3.2. Optical Characterization of the GSH-NCDs	53
3.3.3. Effect of biomolecules on the fluorescence of the GSH-NCDs	57
3.3.4. The study on interference for DA sensing.....	61
3.3.5. Fluorescence quenching mechanism of the GSH-NCDs.....	62
3.3.6. Analysis of DA in real samples	66
3.4. Conclusion.....	67
References	67
CHAPTER 4. Multicolor emitting N-doped carbon dots derived from ascorbic acid and phenylenediamine precursors.....	71

4.1. Introduction	71
4.2. Experimental section	72
4.2.1. Materials	72
4.2.2. Characterizations	72
4.2.3. Synthesis of Am-, Ao-, and Ap-CDs	72
4.2.4. Quantum yield measurement	76
4.3. Results and discussions	76
4.3.1. Characterization of the as-synthesized CDs	76
4.3.2. Optical properties of the Ax-CDs	83
4.3.3. Solvent effects and QY on the PL emission properties	85
4.3.4. pH effects on the fluorescence emission of Ax-CDs	88
4.4. Conclusion	91
Reference	91
CHAPTER 5. High quantum yield aminophenylboronic acid-functionalized N-doped carbon dots for highly selective hypochlorite ion detection.....	94
5.1. Introduction	94
5.2. Experimental Section.....	96
5.2.1. Materials	96
5.2.2. Instruments	96
5.2.3. Synthesis of GAAP-CDs	97
5.2.4. ClO ⁻ sensing	97
5.3. Results and discussion	99
5.3.1. Characterization of GAAP-CDs	99
5.3.2. Optical properties of GAAP-CDs.....	102
5.3.3. ClO ⁻ sensing with as-synthesized GAAP-CDs	109

5.3.4. Fluorescence quenching mechanism	115
5.3.5. Analysis of ClO ⁻ in real samples	119
5.4. Conclusion	120
Reference	120
CHAPTER 6. A selective and sensitive sensor for fluorescent determination of nitrite based on high quantum yield nitrogen and boron doped carbon nanodots	124
6.1. Introduction	124
6.2. Experimental details	125
6.2.1. Materials	125
6.2.2. Characterization	126
6.2.3. Synthesis of CPAP-CDs	126
6.2.4. NO ₂ ⁻ sensing	127
6.3. Results and discussion	128
6.3.1. Characterization of CPAP-CDs	128
6.3.2. Optical properties of CPAP-CDs	131
6.3.3. Nitrites sensing of CPAP-CDs	135
6.3.4. Fluorescence quenching mechanism	143
6.3.5. Analysis of NO ₂ ⁻ in real samples	150
6.4. Conclusion	151
References	151
CHAPTER 7. Summary	154
LIST OF PUBLICATIONS	156

LIST OF FIGURES

Figure 1.1. Several Major Milestones in CDs Development [2].	2
Figure 1.2. Three types of CDs and their structures graphene quantum dots (GQDs), carbon nanodots (CNDs), and polymer dots (PDs) [10].	3
Figure 1.3. Different synthetic methodologies for CDs [17].	4
Figure 1.4. The main approaches to fabricating CDs: “Top-down” cutting from different carbon sources and “bottom-up” synthesis from organic molecules or polymers [19].	5
Figure 1.5. Quenching mechanisms of fluorescent CDs which is used in the process of detecting analytes [36].	10
Figure 2.1. Scheme of NBCDs for Fe ³⁺ and AA detection.	16
Figure 2.2. The optimization of reaction conditions for the fabrication of NBCDs.	19
Figure 2.3. (A) TEM image of NBCDs. (B) Particle size distribution histogram of NBCDs. (C) High-resolution TEM image of an individual NBCDs.	21
Figure 2.4. (A) FTIR and (B) XPS survey spectra of the NBCDs.	22
Figure 2.5. High-resolution XPS spectra of (A) C1s, (B) O1s, (C) N1s and (D) B1s of NBCDs.	22
Figure 2.6. (A) Normalized UV–vis absorption PL excitation ($\lambda_{ex}=455$ nm), and PL emission spectra of the NBCDs solution ($\lambda_{ex}=350$ nm). The inset in (A): photograph image of the NBCDs solution under the ambient (left) and 365 nm UV lamp (right). (B) PL emission spectra of the NBCDs under the various excitation wavelengths.	24
Figure 2.7. Quantum yield of NBCDs compared with quinine sulfate dye as a reference.	24
Figure 2.8. (A) PL emissions of the NBCDs at various pH values. (B) PL intensity of the NBCDs at various pH under an excitation wavelength of 350 nm.	25
Figure 2.9. The selectivity of the NBCDs in pH 7 (A) and pH 11 (B), and fluorescence response to various metal ions.	26
Figure 2.10. (A) Fluorescence response to various metal ions at pH 3. (B) Selectivity of NBCDs towards various metal ions. The concentration of metal ions was 500 μ M. (C) PL emission spectra of the NBCDs with various concentrations of Fe ³⁺ ions at pH 3. (D) Linear	

log (I/I_0) plot of NBCDs quenching by Fe^{3+} ions in aqueous solution.....	27
Figure 2.11. The selectivity of the NBCDs in pH 3 solution, and fluorescence response to various biomolecules.	28
Figure 2.12. (A) Detection limit of NBCDs as the fluorescent probe for Fe^{3+} , $3\sigma/k = 7.50 \mu M$; (B) Detection limit of NBCDs-Fe for AA, $3\sigma/k = 7.72 \mu M$	28
Figure 2.13. (A) PL intensity change and (B) PL recovery ratio of Fe^{3+} saturated NBCDs by various biochemical molecules. The concentration of NBCDs and biomolecules were $0.06 \mu g mL^{-1}$ and $500 \mu M$, respectively.	30
Figure 2.14. (A) Time course of the transition of the Fe^{3+} saturated NBCDs for the addition of $3.5 mM$ AA. (B) PL intensity changes at $454 nm$ with time in the presence of $3.5 mM$ AA. (C) PL emission spectra of Fe^{3+} saturated NBCDs at various AA concentrations. (D) The log (I/I_0) plot of Fe^{3+} saturated NBCDs changing by various concentrations of AA in an aqueous solution.	31
Figure 2.15. Reaction kinetic curve of the Fe^{3+} saturated NBCDs solution with AA.	32
Figure 2.16. The schematic illustration of the Fe^{3+} ion and AA sensing mechanism. (The photograph images (left) under daylight and (right) UV light at each condition.).....	33
Figure 2.17. The pictures of iron sheets reacted under various pH (2-7) conditions with reaction times increasing from 0 to 48 hours.	35
Figure 2.18. The PL emission spectra of the NBCDs under various pH (2-7) solutions with reaction times increasing from 0 to 48 hours, including (A) pH = 7, (B) pH = 6, (C) pH = 5, (D) pH = 4, (E) pH = 3, (F) pH = 2.	36
Figure 2.19. PL quenching (I/I_0) of NBCDs at various pH and reaction times.	37
Figure 2.20. PL emission spectra of the NBCDs under various pH (2-7) solutions with different Fe^{3+} ion concentration, including (A) pH = 7, (B) pH = 6, (C) pH = 5, (D) pH = 4, (E) pH = 3, and (F) pH = 2.	38
Figure 2.21. Linear regression of PL intensity of the NBCDs under various pH (2-7) solutions with different Fe^{3+} ion concentration, including (A) pH = 7, (B) pH = 6, (C) pH = 5, (D) pH = 4, (E) pH = 3, and (F) pH = 2.	39
Figure 3.1. Schematics of the GSH-NCDs fabrication process and DA detection by the as-synthesized GSH-NCDs.	46
Figure 3.2. (A) TEM image of the GSH-NCDs. (B) The particle size distribution histogram	

of the GSH-NCDs. (C) HRTEM image of the GSH-NCDs with lattice fringe. (D) XRD pattern of the GSH-NCDs, and (E) FTIR spectra of the GSH, NCDs, and GSH-NCDs. ... 51

Figure 3.3. (A) XPS survey spectra of the GSH-NCDs. The high-resolution XPS spectra of (B) C 1s, (C) N 1s, (D) O 1s, and (E) S 2p of the GSH-NCDs. 52

Figure 3.4. (A) The UV-vis absorption (UV), emission (PL), and excitation (PLE) spectra of the GSH-NCDs in the aqueous solution (Inset: the photographs of the GSH-NCDs under daylight lamp (left) and UV light ($\lambda=365$ nm) (right) illumination.). (B) Emission spectra of the GSH-NCDs at different excitation wavelength. 54

Figure 3.5. QY of GSH-NCDs use the QS as the reference. 55

Figure 3.6. Stability of GSH-NCDs with the relative PL intensity..... 55

Figure 3.7. Effect of different concentrations of NaCl solutions on the emission of GSH-NCDs. 56

Figure 3.8. (A) PL emission and (B) absorption spectra of GSH-NCDs at different pH solutions..... 56

Figure 3.9. (A) The relative PL emission intensities, and (B) absorbance spectra of the GSH-NCDs in different biomolecules. (Inset: the PL emission intensities spectra of the GSH-NCDs in different biomolecules.) $\lambda_{\text{ex}} = 355$ nm, [GSH-NCDs] = 0.1 mg/mL, [biomolecules] = 1×10^{-3} M, where I_0 and I show the PL emission intensity of the GSH-NCDs in the absence and presence of biomolecules, respectively..... 59

Figure 3.10. (A) The variation of the PL emission intensities of the GSH-NCDs with the gradually addition of DA. (B) The relative PL emission intensities (I_0/I) of the GSH-NCDs vs [DA]. Inset (B): the linear relationship of the relative PL emission intensity on [DA]. I_0 is the PL emission intensity of the GSH-NCDs, and I denote the PL emission intensities of the GSH-NCDs in the presence of DA with different concentrations. 59

Figure 3.11. PL spectra of GSH-NCDs in the presence of biomolecules at different pH solutions. (A) pH = 2, (B) pH = 4, (C) pH = 6, (D) pH = 7, (E) pH = 7.4 and (F) pH = 10. 60

Figure 3.12. The relative PL emission intensities of the GSH-NCDs-DA system with addition of other molecules. [GSH-NCDs] = 0.1 mg/mL, [DA and other molecules] = 1.0×10^{-3} M. 61

Figure 3.13. The zeta potential values for (A) GSH-CDs and (B) GSH-CDs -DA (in the

presence of DA).....	63
Figure 3.14. The FTIR spectra of DA, GSH-NCDs and GSH-NCDs-DA.	64
Figure 3.15. Time-resolved fluorescence decay curves of GSH-NCDs (A) and GSH-NCDs-DA (B) excited at 375 nm with the emission peak at 440 nm. [GSH-NCDs] = 0.1 mg/mL, [DA] = 1×10^{-3} M.	64
Figure 3.16. (A) Normalized UV–vis spectrum of DA overlap with normalized emission and excitation spectra of GSH-NCDs in the aqueous solution. (B) UV–visible spectra of GSH-NCDs in the absence and presence of 1 mM DA.....	65
Figure 3.17. Schematic of the interaction between DA and the GSH-NCDs.	65
Figure 4.1. (A, B) Fluorescence spectra of Am-CDs at different ratio, and different reaction temperature and time from AA and m-PDA. (C) Fluorescence spectra of Ao-CDs at different ratio from AA and o-PDA. (D) Fluorescence spectra of Ap-CDs at different ratio from AA and p-PDA.	74
Figure 4.2. (A) Fluorescence spectra, and (B) normalized fluorescence spectra of Ax-CDs and various precursor materials. Inset: Photographs of Am-CDs, Ao-CDs, and Ap-CDs dispersed in water under natural light (left), and under UV irradiation ($\lambda_{\text{ex}} = 365$ nm) (right).	75
Figure 4.3. (A) TEM images of Am-CDs, (B) the particle size distribution histograms, and (C) HR-TEM images.	78
Figure 4.4. (A) TEM images of Ao-CDs, (B) the particle size distribution histograms, and (C) HR-TEM images.	78
Figure 4.5. (A) TEM images of Ap-CDs, (B) the particle size distribution histograms, and (C) HR-TEM images.	79
Figure 4.6. (A) XRD patterns, and (B) FTIR spectra of Ax-CDs.....	79
Figure 4.7. (A) XPS survey spectrum of Am-CDs. The high resolution (B) C1s, (C) O1s, and (D) N1s XPS spectra of Am-CDs.	80
Figure 4.8. (A) XPS survey spectrum of Ao-CDs. The high resolution (B) C1s, (C) O1s, and (D) N1s XPS spectra of Ao-CDs.	81
Figure 4.9. (A) XPS survey spectrum of Ap-CDs. The high resolution (B) C1s, (C) O1s, and (D) N1s XPS spectra of Ap-CDs.	82
Figure 4.10. The normalized UV–vis absorption spectra, PL excitation, and PL emission	

spectra of the (A) Am-CDs, (C) Ao-CDs, and (E) Ap-CDs. The normalized PL emission spectra of the (B) Am-CDs, (D) Ao-CDs, and (F) Ap-CDs at different excitation wavelengths.	84
Figure 4.11. The effect of different solvents on PL emission properties of (A, B) Am-CDs, (C, D) Ao-CDs and (E, F) Ap-CDs.....	86
Figure 4.12. (1) Plots of integrated PL intensity of Am-CDs and rhodamine 101 as a function of optical absorbance at 450 nm in (A) water and (B) ethanol, respectively. (2) Plots of integrated PL intensity of Ao-CDs and quinine sulfate as a function of optical absorbance at 360 nm in (C) water and (D) ethanol, respectively. (3) Plots of integrated PL intensity of Ap-CDs and rhodamine B as a function of optical absorbance at 514 nm in (E) water and (F) ethanol, respectively.	87
Figure 4.13. PL emission and intensity change of (A, B) Am-CDs, (C, D) Ao-CDs, and (E, F) Ap-CDs under various pH conditions.	89
Figure 4.14. Zeta potential of (A) Am-CDs, (B) Ao-CDs, and (C) Ap-CDs under various pH values, respectively.	90
Figure 5.1. Schematic diagram of GAAP-CDs fabrication and ClO^- detection. (GA: Glutaric acid, and 3-APBA: 3-Aminophenylboronic acid.)	96
Figure 5.2. The reaction temperature (A) and the precursor ratio (B) were optimized to obtain the highest fluorescence for the GAAP-CDs.....	98
Figure 5.3. The optimize concentration of GAAP-CDs. PL emission spectra of GAAP-CDs with different concentration under excitation wavelength at 310 nm, buffer pH = 7.	98
Figure 5.4. (A) TEM image (Inset: particle size distribution), (B) SAED image, (C) XRD pattern, and (D) FTIR spectrum of GAAP-CDs.....	100
Figure 5.5. (A) XPS survey spectra of GAAP-CDs. The high-resolution XPS spectra of (B) C 1s, (C) N 1s, (D) O 1s, and (E) B 1s for GAAP-CDs.	101
Figure 5.6. (A) The UV–vis absorption (UV), PL emission (PL), and PL excitation (PLE) spectra of GAAP-CDs in the aqueous solution. The inset shows the photographs of GAAP-CDs under visible light (left) and UV light (right). (B) PL emission spectra of GAAP-CDs at various excitation wavelengths.....	103
Figure 5.7. Plots integrated PL intensity of quinine sulfate (QS, the reference) and GAAP-CDs as a function of optical absorbance at 360 nm and relevant data.	104

Figure 5.8. Long-term stability of as-synthesized GAAP-CDs.....	104
Figure 5.9. Effect of different concentrations of NaCl solutions on the emission of GAAP-CDs	105
Figure 5.10. The influence of pH on (A) UV–vis absorbance at 370 nm, and (B) PL emission intensity at 375 nm of GAAP-CDs in the absence and presence of 1 mM ClO ⁻ in various pH solutions, respectively. Measurement conditions: [GAAP-CDs] = 0.19 mg/mL, [ClO ⁻ & interfering analytes] = 200 μM, pH = 7, and λ _{ex} = 310 nm.	107
Figure 5.11. The bar diagram showing ClO ⁻ mediated quenching of the fluorescence of GAAP-CDs with respect to time, [ClO ⁻] = 1.0 mM, [GAAP-CDs] = 0.19 mg/mL, λ _{ex} = 310 nm.	108
Figure 5.12. (A) The UV–vis absorbance of GAAP-CDs in the presence of various concentration of ClO ⁻ . (B) The relative absorbance $[(A-A_0)/A_0]$ of GAAP-CDs at 370 nm vs [ClO ⁻]. (C) The photographs of GAAP-CDs in various concentration of ClO ⁻ under visible light. Measurement conditions: [GAAP-CDs] = 0.19 mg/mL, pH = 7, and λ _{ex} = 310 nm.	111
Figure 5.13. (A) Variation of the PL emission intensities of GAAP-CDs with the gradual addition of ClO ⁻ . Inset: photographs of GAAP-CDs in the absence and presence of 1 mM ClO ⁻ under 365 nm UV light (right). (B) Relative PL emission intensities $[(I_0-I)/I_0]$ of GAAP-CDs vs [ClO ⁻]. The linear relationships of the relative PL emission intensity vs. [ClO ⁻] over (C) 0.1–100 μM, (D) 100–600 μM, and (E) 600–1000 μM, respectively. Measurement conditions: [GAAP-CDs] = 0.19 mg/mL, pH = 7, and λ _{ex} = 310 nm.	112
Figure 5.14. (A) Relative UV–vis absorbance and (B) relative PL emission intensity spectra of GAAP-CDs in the presence of various analytes, respectively. [Inset: (A) The absorbance and (B) PL emission intensity spectra of GAAP-CDs in the presence of various analytes, respectively.] Measurement conditions: [GAAP-CDs] = 0.19 mg/mL, [ClO ⁻ & interfering analytes] = 200 μM, pH = 7, and λ _{ex} = 310 nm.	113
Figure 5.15. (A) The relative UV–vis absorbance and (B) relative PL emission spectra of the GAAP-CDs-ClO ⁻ system in the presence of various analytes, respectively. [GAAP-CDs] = 0.19 mg/mL, [ClO ⁻ & interfering analytes] = 200 μM, pH = 7, and λ _{ex} = 310 nm.	114
Figure 5.16. (A) Proposed reaction mechanism within GAAP-CDs-ClO ⁻ system. (B) FTIR spectra of GAAP-CDs in the absence and presence of ClO ⁻ , respectively. (C) Time-resolved	

fluorescence decay curves of GAAP-CDs and GAAP-CDs-ClO ⁻ , respectively, and [GAAP-CDs] = 0.19 mg/mL, [ClO ⁻] = 1 mM, pH = 7, and λ_{ex} = 375 nm.	116
Figure 5.17. The zeta potential values for (A) GAAP-CDs and (B) GAAP-CDs-ClO ⁻ (in the presence of ClO ⁻), respectively. [GAAP-CDs] = 0.19 mg/mL, [ClO ⁻] = 1 mM, pH = 7.	117
Figure 5.18. Normalized UV-vis spectrum of ClO ⁻ overlap with normalized emission and excitation spectra of GAAP-CDs in the aqueous solution.	118
Figure 6.1. (A) The precursor ratio and (B) reaction temperature were optimized to obtain the highest fluorescence for CPAP-CDs.	127
Figure 6.2. (A) TEM image (Inset: SAED image), (B) particle size distribution, (C) XRD pattern, and (D) FTIR spectrum of CPAP-CDs.	129
Figure 6.3. (A) XPS survey spectra of CPAP-CDs. The high-resolution XPS spectra of (B) C1s, (C) O1s, (D) B1s, and (E) N1s for CPAP-CDs. XPS analysis was done using the vacuum dried solid under 60 °C.	130
Figure 6.4. (A) Spectra of CPAP-CDs, blank line: UV-vis absorbance, peaks at 283 and 373 nm; red line: PL emission spectra at excitation wavelength of 370 nm; blue dot line: PL excitation spectra at the emission wavelength of 421 nm. The inset shows the photographs of CPAP-CDs under visible light (left) and UV light (right). (B) PL emission spectra of CPAP-CDs with different excitation wavelengths.	132
Figure 6.5. Plots integrated PL intensity of quinine sulfate (QS, the reference) and CPAP-CDs as a function of optical absorbance at 360 nm and relevant data.	132
Figure 6.6. Time-resolved fluorescence decay curves of CPAP-CDs and CPAP-CDs-NO ₂ ⁻ , respectively, and [CPAP-CDs] = 0.22 mg/mL, [NO ₂ ⁻] = 1 mM, pH = 3, and λ_{ex} = 375 nm.	133
Figure 6.7. Stability of CPAP-CDs with the relative PL intensity.	133
Figure 6.8. Effect of different concentrations of NaCl solutions on the emission of CPAP-CDs.	134
Figure 6.9. PL emission spectral of CPAP-CDs in various pH solutions. [CPAP-CDs] = 0.22 mg/mL and λ_{ex} = 370 nm.	134
Figure 6.10. (A) The PL emission, (B) relative PL emission (at 421 nm), (C) absorbance, and (D) relative UV-vis absorbance spectra (at 444 nm) of CPAP-CDs in the presence of	

various analytes, respectively. The inset: the photographs of CPAP-CDs in the presence of NO_2^- under UV light (B) and visible light (D). [CPAP-CDs] = 0.22 mg/mL, pH = 3, and λ_{ex} = 370 nm..... 137

Figure 6.11. The bar diagram showing NO_2^- mediated quenching of the fluorescence of CPAP-CDs with respect to time, [NO_2^-] = 1.0 mM, [CPAP-CDs] = 0.22 mg/mL, λ_{ex} = 370 nm. 138

Figure 6.12. The influence of pH on PL emission intensity at 421 nm of CPAP-CDs in the absence and presence of 1 mM NO_2^- in various pH solutions, respectively. [CPAP-CDs] = 0.22 mg/mL and λ_{ex} = 370 nm. 139

Figure 6.13. (A) Variation of the PL emission intensities of CPAP-CDs with different concentrations of NO_2^- . (B) Relative PL emission intensities of CPAP-CDs vs [NO_2^-]. (C) The linear dynamic range of the relative PL emission intensity vs. [NO_2^-] from 2–1000 μM . (D) The linear relationships at the low concentration range from 0–0.5 μM . [CPAP-CDs] = 0.22 mg/mL, pH = 3, and λ_{ex} = 370 nm..... 140

Figure 6.14. The relative PL emission spectra of the CPAP-CDs- NO_2^- system in the presence of various anions. [CPAP-CDs] = 0.22 mg/mL, [NO_2^- /other anions] = 500 μM , pH = 3, and λ_{ex} = 370 nm. 141

Figure 6.15. The zeta potential values for (A) CPAP-CDs and (B) CPAP-CDs- NO_2^- system, respectively. [CPAP-CDs] = 0.22 mg/mL, [NO_2^-] = 1 mM, and pH = 3. 144

Figure 6.16. FTIR spectra of CPAP-CDs in the absence and presence of NO_2^- 145

Figure 6.17. (A) XPS survey spectra of CPAP-CDs- NO_2^- . The high-resolution XPS spectra of (B) C1s, (C) O1s, (D) B1s, and (E) N1s for CPAP-CDs. XPS analysis was done using the vacuum dried solid under 60 °C. 146

Figure 6.18. The hydrodynamic diameter values for (A) CPAP-CDs and (B) PAP-CDs- NO_2^- system, respectively. [CPAP-CDs] = 0.22 mg/mL, [NO_2^-] = 1 mM, and pH = 3... 147

Figure 6.19. (A) The spectra showing the effect of various cations on the relative PL emission of CPAP-CDs- NO_2^- system. 148

Figure 6.20. Schematic illustration of a suggested fluorescence quenching mechanism of CPAP-CDs in the presence of NO_2^- in solutions (pH=3) (not to scale). 149

LIST OF TABLES

Table 3.1. The comparison of different fluorometric sensors for DA determination.	47
Table 3.2. Detection of DA in real urine samples.	66
Table 4.1. The excitation wavelength, emission peak wavelength and fluorescence color of different CDs.	75
Table 4.2. The elemental compositions of Ax-CDs.	77
Table 5.1. The comparison of different sensors for ClO ⁻ detection.	106
Table 5.2. Detection of ClO ⁻ in tap water and drink water samples (n=3).	119
Table 6.1. The comparison of different sensors for NO ₂ ⁻ detection.	142
Table 6.2. Detection of the concentration of NO ₂ ⁻ in water obtained from different sources using the proposed method (n=3).	150

NOMENCLATURES

Abbreviations

CDs	Carbon Dots
AA	Ascorbic Acid
CA	Citric Acid
APBA	Amino Phenylboronic Acid
DA	Dopamine
GSH	L-Glutathione
PDA	Phenylenediamine
QS	Quinine sulfate
LOD	Limit of Detection
PBS	Phosphate Buffer Solution
PL	Photoluminescence Spectra
UV-vis	Ultraviolet – visible
HR-TEM	High Resolution Transmission Electron Microscopy
FT-IR	Fourier Transform Infrared spectroscopy
XRD	X-ray Diffraction
XPS	X-ray Photoelectron Spectroscopy

Roman and Greek letters

QY	Quantum yield (%)
λ	Wavelength (nm)

CHAPTER 1. Introduction

1.1. Overview

Carbon dots (CDs) are a subclass of nanoparticles, defined by a quasi-spherical morphology and the characteristic size of less than 10 nm. CDs were first isolated from arc-discharge soot in 2004 [1], and immediately attracted significant attention due to their photoluminescent properties (Figure 1.1A). Figure 1.1 highlights several major milestones from the course of CDs development [2]. In 2006, surface passivation was employed to enhance the photoluminescence of CDs by altering surface chemistry [3] (Figure 1.1B). In 2010, crystalline CDs were successfully isolated, exhibiting size-dependent photoluminescence [4] (Figure 1.1C). In 2013, amorphous CDs (polymer dots) were first prepared, expanding the CD material portfolio from graphite to include crosslinked-polymeric materials [5] (Figure 1.1D). In recent years, CDs with well-defined chemical structure and morphology are being pursued. Recent examples include: (i) chiral CDs from chiral precursors [6] (Figure 1.1E); (ii) 2D crystalline C₃N of varying size [7] (Figure 1.1F); and (iii) triangularly shaped CD-like nanoparticles with fewer defects that show unprecedented narrow-bandwidth photoluminescence [8] (Figure 1.1G). Historically, CDs have exhibited highly desirable and tunable properties (e.g., upconversion photoluminescence and biocompatibility), rendering them promising candidates for wide applications in bioimaging, disease therapy, and optoelectronics.

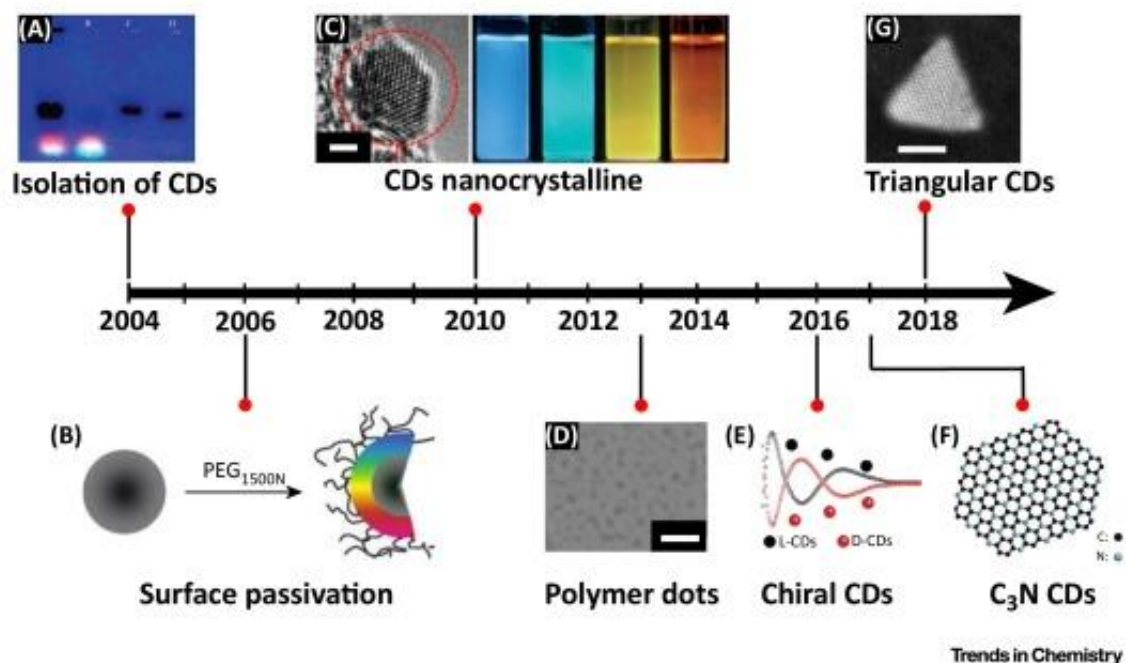


Figure 1.1. Several Major Milestones in CDs Development [2].

1.2. Classification of CDs

CDs are a term used for various nanosized carbon materials with fluorescence. The structure of CDs is usually a nanocrystalline core mostly made of carbons with sp^2 hybridization and an amorphous shell containing functional groups on the edges of the particle [9]. CDs are divided into three different categories: graphene quantum dots (GQDs), carbon nanodots (CNDs), and polymer dots (PDs) (Figure 1.2) [10]. All have at least one dimension <10 nm in size, and each one has a different structure. GQDs have one or very few layers of graphene that are connected to functional groups on the edges. They usually have a larger horizontal dimension than in height and have an average crystal lattice size of 0.24 nm [11]. CNDs are spherical, with multiple carbon nanoparticles and no crystal lattice, whereas carbon quantum dots (CQDs) have a crystal lattice with an interlayer difference of 0.34 nm. This is the same spacing as is observed in graphite. Therefore, the photoluminescent

center varies in CNDs and CQDs. In the third category, PDs contain a carbon core with aggregated or cross-linked polymers attached, which were synthesized from linear polymers or monomers [12]. They are dispersible in aqueous solutions, and their luminescence and electrical conductivity can be enhanced by functionalizing the CDs with heteroatoms such as oxygen, nitrogen, or sulfur or tuning the electronic structures [13-16]. As a result, both the CDs hybridization of the carbon core and its functional groups all affect its photoluminescence.

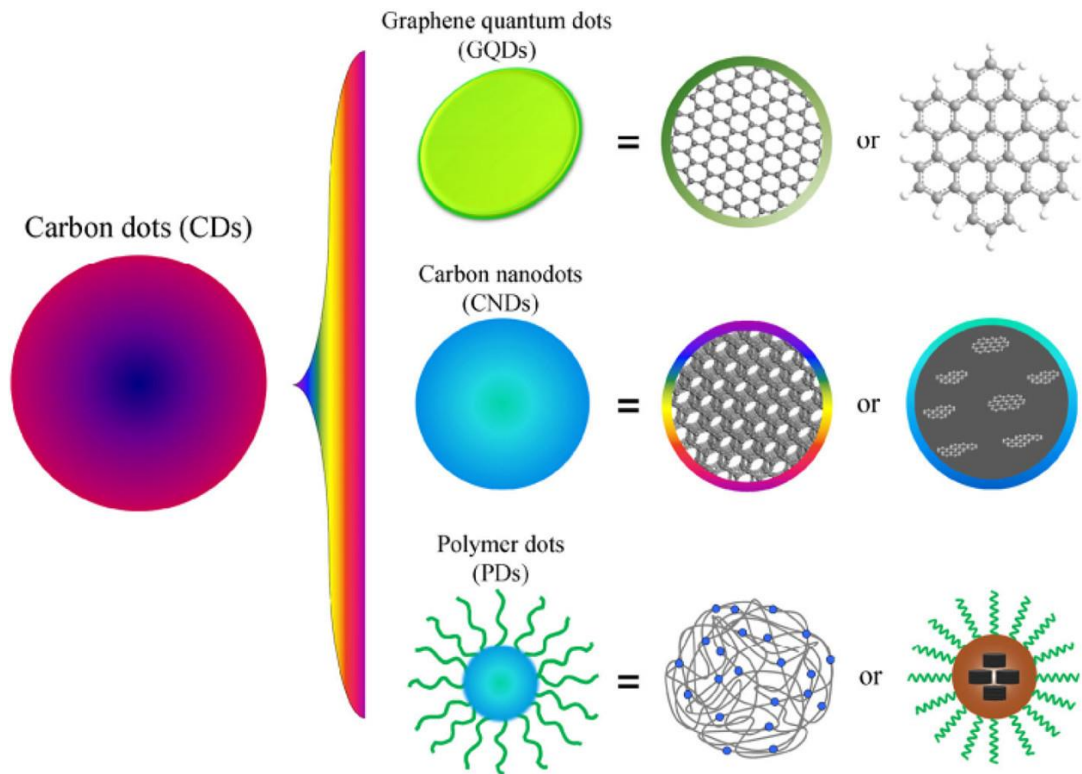


Figure 1.2. Three types of CDs and their structures graphene quantum dots (GQDs), carbon nanodots (CNDs), and polymer dots (PDs) [10].

1.3. Synthesis of CDs

Owing to the diversity of CDs, numbers of facile synthetic methodologies have been developed for making CDs with varied functionalities and photophysical properties. Synthetic pathways for CDs are mainly classified into two categories: (a) “bottom-up” and (b) “top-down” approaches (Figure 1.3) [17, 18].

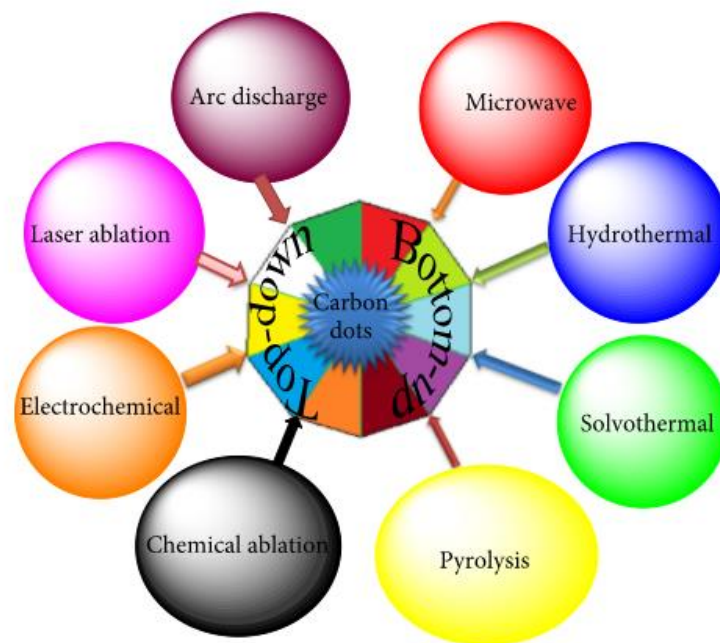


Figure 1.3. Different synthetic methodologies for CDs [17].

Top-down methods refer to cutting large carbon materials, such as carbon rods, carbon fibers, carbon nanotubes, graphite powder, graphene oxide, activated carbon, carbon black, coal, or soot, into carbon nanoparticles (Figure 1.4) [10, 19]. This method usually requires multiple steps in decomposition and exfoliation of cheap and readily available carbon materials in harsh conditions, involving strong oxidants, concentrated acids, and high temperatures. Examples of the top-down process include acidic exfoliation, electrochemical oxidation, metal-graphite intercalation, and strong physical routes, such as arc discharge, electron beam lithography, laser ablation, chemical ablation, and nanolithography by reactive ion etching [20]. However, the size distribution and morphology of the produced

particles cannot be precisely controlled with the top-down method.

The “bottom-up” methods are efficient routes to produce fluorescent CDs on a large scale. For example, small molecules and polymers may undergo dehydration and further carbonization to form CNDs and PDs [21]. The applied molecules always possess $-OH$, $-COOH$, $-C=O$, and $-NH_2$ groups, which can dehydrate at elevated temperatures. There are many approaches for carrying out the dehydration and carbonization processes, such as hydrothermal, solvothermal, microwave, and combustion methods, pyrolysis in concentrated acid, carbonization in a microreactor, and so on (Figure 1.4) [19]. It is difficult to control these formation processes, resulting in CDs with polydispersity. However, using designed precursors may allow us to accurately obtain GQDs with the desired molecular weight and size, such as intramolecular oxidative polycyclic aromatic hydrocarbons. Although organic-synthesized GQDs are the perfect model for understanding the PL mechanism of fluorescent carbon materials, the complicated synthesis method and variations in fluorescence as compared with common fluorescent CDs reduce their usefulness [22].

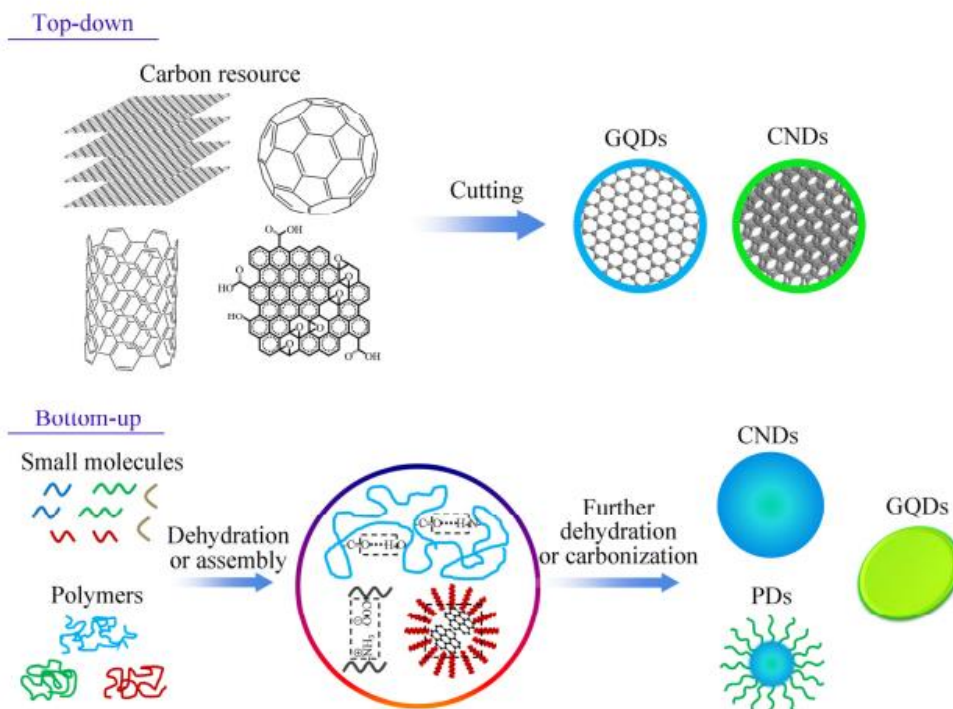


Figure 1.4. The main approaches to fabricating CDs: “Top-down” cutting from different carbon sources and “bottom-up” synthesis from organic molecules or polymers [19].

1.4. Characterizations

Due to various synthesis methods, the chemical structure of each CDs will be different. However, all have connected or modified oxygen, amino, or polymer-based groups on the surface. Many characterization methods are used to determine the CDs' structure. For example, high-resolution transmission electron microscopy (HRTEM), X-ray diffraction (XRD), and Raman spectroscopy are used to determine the carbon core. X-ray photoelectron spectroscopy (XPS), Fourier transform infrared (FTIR), are used to determine the functional groups and general structure.

Morphology and microstructure of CDs are analyzed by transmission electron microscopy (TEM) and scanning electron microscopy (SEM). These methods are used to measure the size and dimension of CDs. Crystal structures can be observed using TEM image, when electron diffraction patterns are present [23]. The crystal structure of CDs is also studied by XRD. A broad peak observed at 23° specifies highly amorphous carbon. However, the presence of two broad peaks at 25° and 44° , indicates low-graphitic carbon structure corresponding to (002) and (100) diffraction [24]. The extent of disordered graphite is measured by Raman spectra. Peaks found near 1360 and 1560 cm^{-1} using visible excitation represent the D and G bands. The intensity ratio of the two bands (I_D/I_G) is an indication of the atomic ratio of sp^3 vs sp^2 carbon hybridization [25].

The elemental composition and carbon bonding configurations of the organic CDs are quantified by XPS and qualitatively verified by FTIR and NMR analyses. In the high-resolution C 1s spectra (obtained from XPS), the peaks at binding energies of 284.8, 286.5, and 288.2 eV are attributed to sp^2 carbon atoms, alcoholic (C–OH) carbon atoms, and carbonyl (C=O) carbon atoms, respectively. In FTIR spectra, the stretching vibrations of C–OH, C–H, C=O, and C=C appear as peaks at around 3436 cm^{-1} , 2960 and 2870 cm^{-1} , 1710 cm^{-1} , and 1660 cm^{-1} , respectively [24]. FTIR has also been used to study the interactions between CDs and metal oxides in complexes of those. Wei et al. observed two new peaks in the FTIR of CDs/NiCo₂O₄ composites, proving formation of complexes between the two components, which creates structural stability and facilitates charge transfer [26].

Electronic transition of CDs can be observed in the UV–vis absorption spectra. A

peak at 310 nm indicates the n- π^* electronic transition on the surface [24]. Other research shows a narrow peak at 235 nm was assigned to the π - π^* transition of CDs, and the band at 355 nm was assigned to the n- π^* transition of the functional groups on the CDs. The prominence of the latter peak was attributed to the increased number of carboxylic acid groups on the surface of CDs due to the type of raw material used [25]. Controversially, others state that a strong optical absorption will typically be observed between 230 and 320 nm, with a shoulder extending into the visible absorption region. A broad peak seen at roughly 230 nm is attributed to the aromatic C=C transition of π to π^* , and the tail end is due to the C=O transition of n to π^* . Surface passivation, hybridization, functional groups, size, and structure all affect the optical absorption characteristics [27, 28].

One of the methods to determine the optical properties of CDs PL is done by measurement of fluorescence emission spectra at different excitation wavelengths [24]. When the aqueous solution of CDs is excited at 355 nm, a homologous PL emission peak appears at 450 nm [25]. The QY of CDs is estimated using the following equation (1) [29]:

$$\Phi_s = \Phi_r \cdot (I_s / I_r) \cdot (A_r / A_s) \cdot (\eta_s / \eta_r)^2$$

$$\Phi_s = \Phi_r \cdot (I_s / A_s) / (I_r / A_r) \cdot (\eta_s / \eta_r)^2$$

$$\text{If } K = I/A ,$$

$$\Phi_s = \Phi_r \cdot (K_s / K_r) \cdot (\eta_s / \eta_r)^2 \quad (1-1)$$

Where Φ is the relative quantum yield, I is the measured integrated emission intensity, η is the refractive index of the solvent, and A is the absorption of testing solutions. The subscript "r" refers to the reference, quinine sulfate dye dissolved in 0.1M H₂SO₄ with quantum yield (54%), and "s" for the sample. For the aqueous solutions, the refractive index $\eta_s = \eta_r = 1.33$.

The time-resolved fluorescence decay spectra were investigated by time-correlated single photon counting technique (TCSPC). The fluorescence emission decay curve was recorded for CDs at 375 nm emission. The time-resolved fluorescence decay curves were fitted using exponential model as following equation (2) [30]:

$$I(t) = A + \sum_{i \rightarrow n}^n B_i \exp(-\frac{t}{\tau_i}) \quad (1-2)$$

where I(t) is the intensity assumed to decay as the sum of individual single exponential

decays, A and Bi are constant and pre-exponential factors after fitting decay curve, τ_i is the decay time. The fluorescence decay curve of CDs is fitted to double exponential functions. So, this equation generates a fast (τ_1) and a slow (τ_2) decay component, respectively [31]. Then, the average lifetime (τ_{av}) is calculated by following equation (3) [30, 31]:

$$\tau_{av} = \frac{\sum_{i=1}^n B_i \tau_i^2}{\sum_{i=1}^n B_i \tau_i} = \frac{B_1 \tau_1^2 + B_2 \tau_2^2}{B_1 \tau_1 + B_2 \tau_2} \quad (1-3)$$

1.5. Quenching mechanisms of CDs

The fluorescence of CDs can be quenched by analytes which included inorganics and organics. Based on this phenomenon, the CDs can be used as a sensor to detect these analytes. In the process of detecting these analytes, the quenching mechanisms of CDs included the static quenching, dynamic quenching, PET, and IFE.

1.5.1. Static quenching mechanism of CDs

Static quenching occurs when a nonfluorescent ground-state complex is formed through the interaction between CDs and quencher. The complex immediately returns to the ground state without emission of a photon when the complex absorbs light [32]. For static quenching (a) $\tau_0/\tau = 1$; (b) The formation of the ground-state complex can result in the change of the absorption spectrum of the CDs; (c) A rise of temperature can cause the decline of the stability of the ground-state complex, so reduces the effect of static quenching [33], as showed in Figure 1.5(b).

There are the CDs which can be quenched by hemoglobin (HGB) [34], this process can verify the theory of static quenching mechanism well. The CDs can react with HGB to form the ground state complex, which led to the fluorescence quenching of CDs. In order to prove that the quenching mechanism of CDs was static quenching, the average fluorescence lifetime of CDs was measured to be 6.46 ns. When HGB was added into the solution of CDs, the average fluorescence lifetime of CDs was measured to be 6.51 ns. The average fluorescence lifetime of CDs was almost unchanged in the absence or presence of HGB, this phenomenon met (a) UV-vis absorption spectra of CDs, HGB, and CDs-HGB system were measured. The absorbance peak of HGB was at 403 nm, The CDs-HGB system also showed

the absorbance peak at 403 nm, it implied the formation of CDs-HGB complex, it met (b) The quenching mechanism of CDs was static quenching.

1.5.2. Dynamic quenching mechanism of CDs

Dynamic quenching can be explained that the excited state of CDs return to the ground state by the collision between the quencher and CDs with the mechanism of energy transfer or the mechanism of charge transfer [32], this process can be represented by a simple equation:



where A is CDs, Q is a quencher and * designates an excited state.

The kinetics of this process follows the Stern–Volmer relationship [35]:

$$F_0/F = 1 + K_q\tau_0[Q] \quad (1-5)$$

where F_0 and F are the fluorescence intensities in the absence and presence of quencher, K_q is the quencher rate coefficient, τ_0 is the lifetime of the emissive excited state of CDs, without a quencher present, $[Q]$ is the concentration of the quencher.

There are some different characteristics compared to static quenching. (a) The lifetime of CDs would change in the absence and presence of quencher. (b) Dynamic quenching only affected the excited states of the CDs, so no changes in the absorption spectra CDs were observed. (c) A rise of temperature can lead to the increase of the effect of dynamic quenching, as showed in Figure 1.5(a).

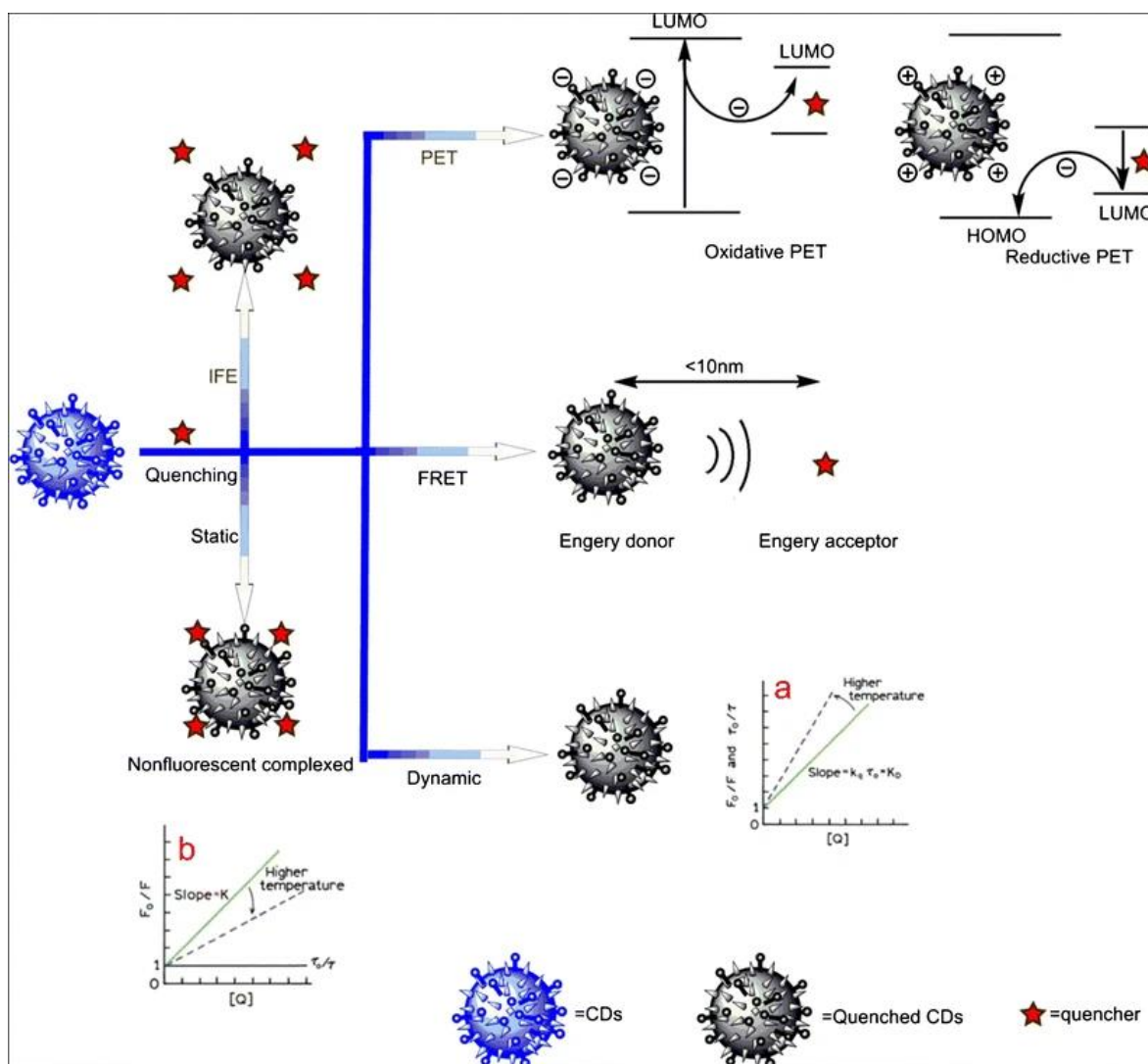


Figure 1.5. Quenching mechanisms of fluorescent CDs which is used in the process of detecting analytes [36].

1.5.3. PET quenching mechanism of CDs

PET can be explained that between the CDs (electron donor or electron receptor) and the quencher (electron receptor or electron donor) occurred the electron transfer, formed the cation radical and the anion radical respectively. In this process, a complex that can return to the ground state without emission of a photon was formed between the electron donor and the electron receptor. PET contained reductive PET and oxidative PET. Reductive PET was that CDs as an electron receptor got electron from the electron donor. Oxidative PET was contrary to reductive PET. The driving force for reductive electron transfer was the energy gap between the lowest unoccupied molecular orbitals (LUMO) of quencher and the highest occupied molecular orbitals (HOMO) CDs. The driving force for oxidative electron transfer was the energy gap between the LUMO of the CDs and the LUMO of the quencher [32, 37]. So, (a) the lifetimes of CDs decreased, (b) the energy gap of the LUMO and HOMO or the LUMO and LUMO between the CDs and the quencher existed, it would demonstrate that the quenching mechanisms was PET. There were the CDs which can be quenched by picric acid (PA) [37], the process can prove the theory of PET quenching mechanism of CDs well. In order to investigate the quenching mechanism of CDs, the cyclic voltammetry was used. The E_{red} which was the onset of reduction potential for CDs was measured to be -0.56 V, the E_g which was the energy band gap resulting from the absorption edge in the absorption spectrum of CDs was estimated to be 3.29 eV. The values of the HOMO and LUMO of CDs were calculated to be -7.13 and -3.84 eV according to the empirical formula equations (6) and (7).

$$E_{HOMO} = -e(E_{ox} + 4.4) \quad (1-6)$$

$$E_{LUMO} = -e(E_{red} + 4.4) \quad (1-7)$$

The E_{HOMO} and E_{LUMO} of PA can be calculated to be -8.70 and -5.82 eV, by the B3LYP method in Dmol3 mode. Due to the LUMO of CDs was larger than the LUMO of PA, so the electron can transfer from CDs to PA, it met (b), this process met the oxidative PET.

1.5.4. IFE mechanism of CDs

IFE occurs when the absorption spectrum of quencher in the detection system overlapped with the excitation or emission spectra of CDs. IFE sometimes can be called apparent quenching, it is not a quenching process at all but is rather due to an attenuation of the excitation beam or absorption of emitted radiation by an excess concentration of CDs or by the quencher in solution [38]. This effect also leads to a reduction of intensity (but not decay time), but this effect should not be termed “quenching”. Rather, a second absorber is simply filtering off the emission of a particle. This also occurs if distances between emitted and re-absorber exceed 10 nm. Because the process of IFE does not belong to the static or dynamic quenching process, so the absorption peaks of the CDs would not change, it also indicates that there is not new substance to form. So, the fluorescence lifetime of CDs will not be changed.

Reference

- [1] X. Xu, R. Ray, Y. Gu, H. J. Ploehn, L. Gearheart, K. Raker, W. A. Scrivens. *Journal of the American Chemical Society*, 2004, 126, 12736-12737.
- [2] B. Yao, H. Huang, Y. Liu, Z. Kang. *Trends in Chemistry*, 2019, 1, 235-246.
- [3] Y. Sun, B. Zhou, Y. Lin, W. Wang, K. A. S. Fernando, P. Pathak, M. J. Mezirani, B. A. Harruff, X. Wang, H. Wang, P. G. Luo, H. Yang, M. E. Kose, B. Chen, L. M. Veca, S. Xie. *Journal of the American Chemical Society*, 2006, 128, 7756-7757.
- [4] H. Li, X. He, Z. Kang, H. Huang, Y. Liu, J. Liu, S. Lian, C. H. A. Tsang, X. Yang, S. Lee. *Angewandte Chemie*, 2010, 122, 4532-4536.
- [5] S. Zhu, Q. Meng, L. Wang, J. Zhang, Y. Song, H. Jin, K. Zhang, H. Sun, H. Wang, B. Yang. *Angewandte Chemie*, 2013, 125, 4045-4049.
- [6] L. Hu, H. Li, C. a. Liu, Y. Song, M. Zhang, H. Huang, Y. Liu, Z. Kang. *Nanoscale*, 2018, 10, 2333-2340.
- [7] S. Yang, W. Li, C. Ye, G. Wang, H. Tian, C. Zhu, P. He, G. Ding, X. Xie, Y. Liu, Y. Lifshitz, S. T. Lee, Z. Kang, M. Jiang. *Advanced Materials*, 2017, 29, 1605625.

- [8] F. Yuan, T. Yuan, L. Sui, Z. Wang, Z. Xi, Y. Li, X. Li, L. Fan, Z. a. Tan, A. Chen, M. Jin, S. Yang. *Nature communications*, 2018, 9, 1-11.
- [9] L. Wang, X. Chen, Y. Lu, C. Liu, W. Yang. *Carbon*, 2015, 94, 472-478.
- [10] M. Semeniuk, Z. Yi, V. Poursorkhabi, J. Tjong, S. Jaffer, Z. Lu, M. Sain. *ACS nano*, 2019, 13, 6224-6255.
- [11] L. Lin, S. Zhang. *Chemical communications*, 2012, 48, 10177-10179.
- [12] X. Yan, X. Cui, L. Li. *Journal of the American Chemical Society*, 2010, 132, 5944-5945.
- [13] S. Qu, X. Wang, Q. Lu, X. Liu, L. Wang. *Angewandte Chemie*, 2012, 124, 12381-12384.
- [14] D. Qu, M. Zheng, P. Du, Y. Zhou, L. Zhang, D. Li, H. Tan, Z. Zhao, Z. Xie, Z. Sun. *Nanoscale*, 2013, 5, 12272-12277.
- [15] W. Wei, C. Xu, L. Wu, J. Wang, J. Ren, X. Qu. *Scientific reports*, 2014, 4, 1-7.
- [16] Y. Dong, H. Pang, H. B. Yang, C. Guo, J. Shao, Y. Chi, C. M. Li, T. Yu. *Angewandte Chemie International Edition*, 2013, 52, 7800-7804.
- [17] B. Gayen, S. Palchoudhury, J. Chowdhury. *Journal of Nanomaterials*, 2019, 2019.
- [18] Z. Qiao, Y. Wang, Y. Gao, H. Li, T. Dai, Y. Liua, Q. Huo. *Chemical communications*, 2010, 46, 8812-8814.
- [19] S. Zhu, Y. Song, X. Zhao, J. Shao, J. Zhang, B. Yang. *Nano research*, 2015, 8, 355-381.
- [20] A. Sharma, J. Das. *Journal of nanobiotechnology*, 2019, 17, 1-24.
- [21] X. Wang, Y. Feng, P. Dong, J. Huang. *Frontiers in chemistry*, 2019, 7, 671.
- [22] C. Zhang, Y. Liu, X. Xiong, L. Peng, L. Gan, C. Chen, H. Xu. *Organic letters*, 2012, 14, 5912-5915.
- [23] Y. Zheng, D. Yang, X. Wu, H. Yan, Y. Zhao, B. Feng, K. Duan, J. Weng, J. Wang. *RSC advances*, 2015, 5, 90245-90254.
- [24] H. Hou, C. E. Banks, M. Jing, Y. Zhang, X. Ji. *Advanced Materials*, 2015, 27, 7861-7866.
- [25] X. Zhang, J. Wang, J. Liu, J. Wu, H. Chen, H. Bi. *Carbon*, 2017, 115, 134-146.

- [26] J. Wei, H. Ding, P. Zhang, Y. Song, J. Chen, Y. Wang, H. Xiong. *Small*, 2016, 12, 5927-5934.
- [27] J. Peng, W. Gao, B. K. Gupta, Z. Liu, R. Romero-Aburto, L. Ge, L. Song, L. B. Alemany, X. Zhan, G. Gao, S. A. Vithayathil, B. A. Kaiparettu, A. A. Marti, T. Hayashi, J.-J. Zhu, P. M. Ajayan. *Nano letters*, 2012, 12, 844-849.
- [28] S. M. Sharker, S. M. Kim, S. H. Kim, I. In, H. Lee, S. Y. Park. *Journal of Materials Chemistry B*, 2015, 3, 5833-5841.
- [29] J. Wu, Y. Qu, L. Wang, L. Huang, Y. Rui, J. Cao, J. Xu. *Dyes and Pigments*, 2017, 136, 175-181.
- [30] S. Barman, M. Sadhukhan. *Journal of Materials Chemistry*, 2012, 22, 21832-21837.
- [31] J. Ran, T. Y. Ma, G. Gao, X. Du, S. Z. Qiao. *Energy & Environmental Science*, 2015, 8, 3708-3717.
- [32] J. R. Lakowicz. Maryland, USA, 2006.
- [33] A. Iqbal, Y. Tian, X. Wang, D. Gong, Y. Guo, K. Iqbal, Z. Wang, W. Liu, W. Qin. *Sensors and Actuators B: Chemical*, 2016, 237, 408-415.
- [34] S. Huang, L. Wang, C. Huang, J. Xie, W. Su, J. Sheng, Q. Xiao. *Sensors and Actuators B: Chemical*, 2015, 221, 1215-1222.
- [35] W. Liu, H. Diao, H. Chang, H. Wang, T. Li, W. Wei. *Sensors and Actuators B: Chemical*, 2017, 241, 190-198.
- [36] F. Zu, F. Yan, Z. Bai, J. Xu, Y. Wang, Y. Huang, X. Zhou. *Microchimica Acta*, 2017, 184, 1899-1914.
- [37] Y. Z. Fan, Y. Zhang, N. Li, S. G. Liu, T. Liu, N. B. Li, H. Q. Luo. *Sensors and Actuators B: Chemical*, 2017, 210, 949-955.
- [38] T. D. Gauthier, E. C. Shane, W. F. Guerin, W. R. Seitz, C. L. Grant. *Environmental Science & Technology*, 1986, 20, 1162-1166.

CHAPTER 2. Nitrogen and boron-incorporated carbon dots for the sequential sensing of ferric ions and ascorbic acid sensitively and selectively

2.1. Introduction

Carbon dots (CDs) have attracted considerable attention because of their unique optical properties [1, 2]. CDs were first discovered during the process of purifying single-walled carbon nanotube fragments fabricated by arc-discharge soot [3]. Generally, small CDs with sizes less than 10 nm exhibit excellent photoluminescence, high quantum yields, chemical and photo stability, and biocompatibility with low toxicity, making them suitable for a wide range of applications, including sensing [4], bioimaging [5], light emitting diodes [6], and chemical logic gates.

Several methods to synthesize CDs have been developed, such as arc-discharge [3], laser ablation/irradiation [7-9], electrochemical synthesis [10, 11], chemical exfoliation [12], thermal pyrolysis [13], hydrothermal process [14], microwave heating [15, 16], anchor/support-based synthesis [17], and MOF template-based process [18]. All these methods can be divided into two categories, either “top down” or “bottom up” methods based on the starting carbon source and fabrication process [19]. Among them, the hydrothermal method is considered as one of the most effective approaches because it is a cost-effective and easily controllable one-step process.

Fe^{3+} is one of the essential trace elements in organisms because of its important roles in many biological processes. In addition, it is important in many industrial areas and the environment. A deficiency or excess from the normal standard of Fe^{3+} ions can cause a range of serious diseases, such as iron deficient erythrocytes, anemia, and iron deficiency of early childhood [20]. In this regard, the development of a simple, rapid, selective, and sensitive method for detecting Fe^{3+} has attracted attention. Recent studies reported that Fe^{3+} ion sensors based on CDs exhibit strong fluorescence, high selectivity and sensitivity, good water dispersity, and high quantum yield [21-24]. On the other hand, there are limited reports

on the application of fluorescent Fe^{3+} sensors in real applications, such as monitoring acid rain.

Ascorbic acid (AA) is a key trace organic substance that can improve the resistance of the humans. AA detection in human blood is very important because a deficiency of AA in the human body can result in scurvy and an excess can also have poor outcomes, such as nausea, diarrhea and heartburn [25]. Therefore, many attempts have been made to detect AA [26, 27]. Fluorescence sensing is considered the most effective among them because of its simplicity, high sensitivity, and low detection limit.

In the present study, nitrogen and boron-enriched CDs (NBCDs) were designed and fabricated for the synchronous analysis of Fe^{3+} and AA through an “on-off-on” signal process (Figure 2.1). The NBCDs was obtained using a low-temperature-hydrothermal method with AA and 4-aminobenzeneboronic acid hydrochloride (4-APBA) as the novel precursors. Under excitation of 350 nm, NBCDs showed strong emission at 454 nm, which could be quenched in the present of Fe^{3+} ions due to the inner filter effect [28]. Importantly, the quenching efficiency was unaffected by the pH in acid environments, which enabled the NBCDs fabricated in this study to monitor the different strengths of acid rain. In addition, the NBCDs-Fe complex was used for AA detection through the recovered photoluminescence (PL). The analysis of Fe^{3+} and AA could be completed rapidly (< 5 min). The NBCDs-based sensors also exhibited excellent selectivity towards interfering chemicals.

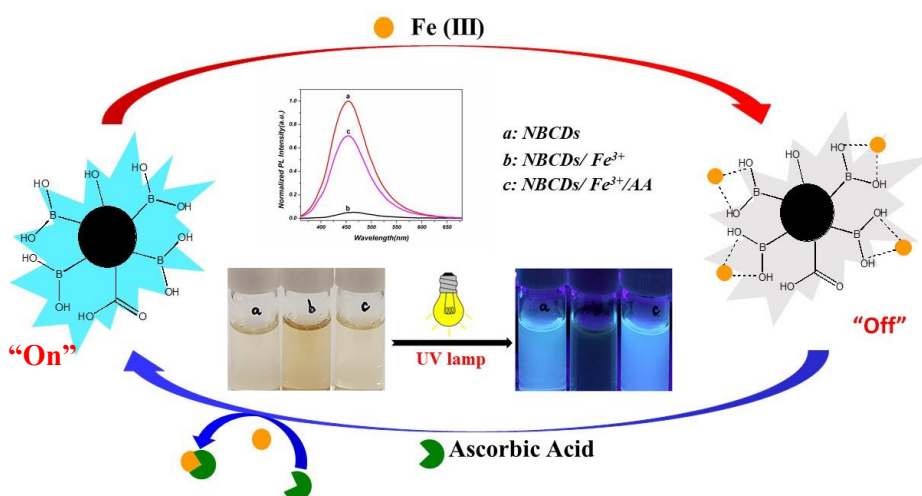


Figure 2.1. Scheme of NBCDs for Fe^{3+} and AA detection.

2.2. Experimental details

2.2.1. Materials

All chemicals in this study were of analytical grade reagents and used as received. Copper(II) sulfate pentahydrate ($\text{CuSO}_4 \cdot 5\text{H}_2\text{O}$), cobalt(II) nitrate hexahydrate ($\text{Co}(\text{NO}_3)_2 \cdot 6\text{H}_2\text{O}$), lead(II) nitrate ($\text{Pb}(\text{NO}_3)_2$), potassium chloride (KCl), calcium chloride (CaCl_2), zinc sulfate heptahydrate ($\text{ZnSO}_4 \cdot 7\text{H}_2\text{O}$), nickel(II) chloride hexahydrate ($\text{NiCl}_2 \cdot 6\text{H}_2\text{O}$), magnesium chloride (MgCl_2), sodium chloride (NaCl), mercury(II) chloride (HgCl_2), iron(II) sulfate heptahydrate ($\text{FeSO}_4 \cdot 7\text{H}_2\text{O}$), iron(III) chloride hexahydrate ($\text{FeCl}_3 \cdot 6\text{H}_2\text{O}$), manganese(II) acetate tetrahydrate ($\text{Mn}(\text{CH}_3\text{COO})_2 \cdot 4\text{H}_2\text{O}$), silver nitrate (AgNO_3), D-(+)-glucose, D-(+)-galactose, D-(-)-fructose, sucrose, lactose, maltose, L-cysteine, glycine, uric acid, citric acid, dopamine, 4-aminobenzenebornic acid hydrochloride (4-APBA) and ascorbic acid (AA) were purchased from Sigma-Aldrich Co.(USA). The deionized water with a resistivity of 18.2 M Ω was used in all experiments.

2.2.2. Characterization

The morphology was visualized by high-resolution transmission electron microscopy (HR-TEM, JEOL JEM-2100, USA) with a working voltage of 200 kV. The oxidation state and elemental composition of the sample were examined by X-ray photoelectron spectroscopy (XPS, K-Alpha, Thermo Fisher Scientific ESCALAB 250Xi, USA) using Al $K\alpha$ X-ray radiation. Fourier transform infrared (FT-IR, NICOLET iS5, Thermo Fisher Scientific, USA) spectroscopy was performed using the KBr disk method in a range of 500–4000 cm^{-1} . The UV–vis spectra were characterized using an ultraviolet-visible spectrophotometer (UV–vis., SPECORD 210 PLUS-223F1107, Germany) in a quartz cell with a 10 mm optical path length. The fluorescence spectra were taken using a Cary Eclipse Fluorescence Spectrophotometer (Agilent Technologies, G9800AA, USA). The concentration of Fe^{3+} ions was measured by ICP spectroscopy (Agilent Technologies, 5510 ICP-OES, USA).

2.2.3. Synthesis of NBCDs

The NBCDs were synthesized using a low-cost, low temperature, and stable hydrothermal process. Typically, 2 ml of a 0.01 M ascorbic acid solution and 1 ml of a 0.01 M 4-aminobenzeneboronic acid hydrochloride solution were added to 3 mL of deionized water and stirred for 5 min. The mixture was then transferred to a 50 mL Teflon-lined autoclave and maintained at 160 °C for 6 h in an oven for further reaction. As shown in Figure 2.2, the optimal reaction conditions, including the reactant ratio, reaction temperature, reaction time, and solvent were examined in detail. The NBCDs solution was collected after cooling to room temperature and centrifugation at 10000 rpm for 20 min. The solution was purified further using a dialysis tube for 12 h to remove the residual chemicals.

2.2.4. Detection of metal ions and biochemical molecules

The detection of Fe^{3+} was carried out in a citric acid-trisodium citrate solution (pH=3). Typically, 0.2 mL of the NBCD ($0.6 \mu\text{g mL}^{-1}$) colloid was diluted with 2 mL of a citric acid-trisodium citrate solution. To determine the Fe^{3+} concentration, Fe^{3+} solutions with a range of 1 μM to 5 mM were added to 2 mL of the NBCDs solution. The fluorescent intensity was measured after 2 min.

The selectivity towards Fe^{3+} was determined by measuring the fluorescence after adding solutions containing other metal ions, such as Mn^{2+} , Ag^+ , K^+ , Na^+ , Zn^{2+} , Mg^{2+} , Ca^{2+} , Cu^{2+} , Fe^{2+} , Ni^{2+} , Co^{2+} , Pb^{2+} , and Hg^{2+} ions. To determine the concentration of biochemical molecules, such as D-(+)-glucose, D-(+)-galactose, D-(-)-fructose, sucrose, lactose, maltose, L-cysteine, glycine, uric acid, citric acid, dopamine, and ascorbic acid (AA), they were added to a Fe^{3+} ion saturated NBCDs solution. The fluorescence emission intensity was collected at 454 nm after 350 nm excitation. All measures were conducted at room temperature.

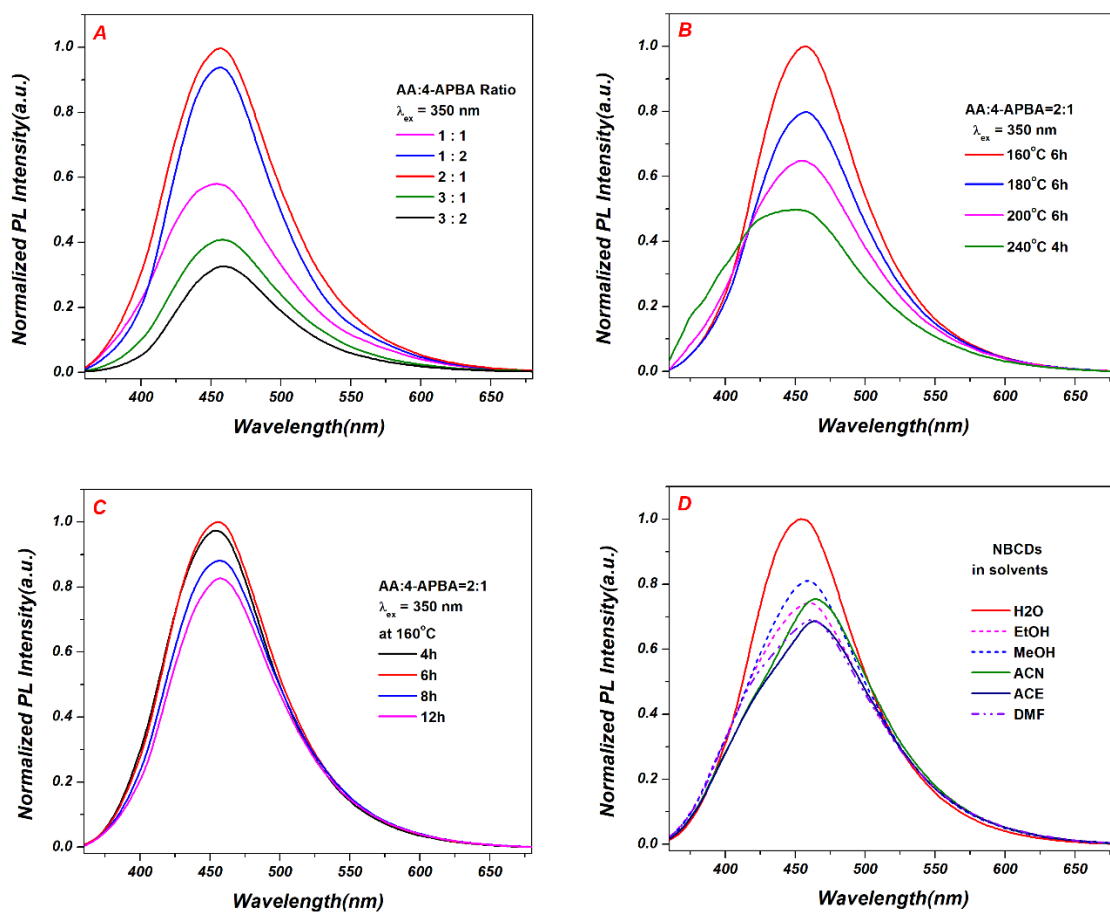


Figure 2.2. The optimization of reaction conditions for the fabrication of NBCDs.

2.3. Results and discussion

2.3.1. Instrumental analysis of NBCDs

2.3.1.1. TEM analysis

The morphology and structure of the NBCDs were analyzed by TEM. All samples were prepared by drop-casting an aqueous colloid on a carbon-coated copper grid. Figure 2.3A presents a typical TEM image of the NBCDs, showing a mean size of approximately 3.3 nm. Figure 2.3B presents the corresponding particle size distribution histogram. High-resolution TEM revealed the NBCDs to have a lattice spacing of 0.21 nm (Figure 2.3C), which is consistent with the (102) diffraction plane of sp^2 graphitic carbon [29, 30].

2.3.1.2. FTIR and XPS analysis

FTIR spectroscopy was conducted to analyze the surface functional groups of the NBCDs, as shown in Figure 2.4A. The O–H and N–H stretching vibrations at approximately 3550 cm^{-1} indicated the presence of hydroxyl and amino groups, which contribute to the hydrophilicity of the NBCDs [31, 32]. The weak bands at 2380 cm^{-1} and 1261 cm^{-1} were assigned to the C–N stretching vibrations [33]. The strong bands at 1710 cm^{-1} and 1400 cm^{-1} were assigned to the stretching vibrations of C=O [34] and C–O [35]. The bands at $1620\text{--}1498\text{ cm}^{-1}$ were ascribed to the C=C stretching vibrations [36], which indicates the presence of sp^2 networks in NBCDs. The strong bands in the region of $1022\text{--}1161\text{ cm}^{-1}$ and $2850\text{--}2920\text{ cm}^{-1}$ can be assigned to the stretching vibrations of C–H [37]. The weak bands at 872 cm^{-1} and 768 cm^{-1} were assigned to the stretching vibrations of B–O and BO_2 , which represents the successful incorporation of boron atoms to the NBCDs fabricated in this study [38].

XPS was used to characterize the elemental composition of the NBCDs. As shown in Figure 2.4B, the XPS survey spectrum showed that the NBCDs are composed mainly of carbon (55.72%), oxygen (31.11%), nitrogen (4.05%), and boron (2.83%). The two weak peaks observed at 400.7 and 191.8 eV were assigned to N1s and B1s, respectively, which indicates the successful incorporation of N and B atoms from 4-APBA by the NBCDs fabricated in this study. Figure 2.5 shows the high-resolution XPS spectra of C1s, O1s, N1s,

and B1s of the NBCDs.

The C1s peak (Figure 2.5A) was deconvoluted to four sub-peaks centered at 284.2, 285.2, 286.0, and 288.3 eV, which were assigned to C–C/C=C, C–N, C–O, and N–C=O/O–C=O, respectively. The B–O, C=O, and C–O groups were observed at 530.6, 531.9, and 533.2 eV in the high resolution O1s spectrum (Figure 2.5B) of NBCDs [39]. The N1s peak (Figure 2.5C) revealed the presence of C–NH (399.8 eV) and N–C=O (400.9 eV) groups [40]. The two peaks at 191.7 and 192.4 eV in the B1s spectrum (Figure 2.5D) were attributed to B–O and B–C groups, respectively [41].

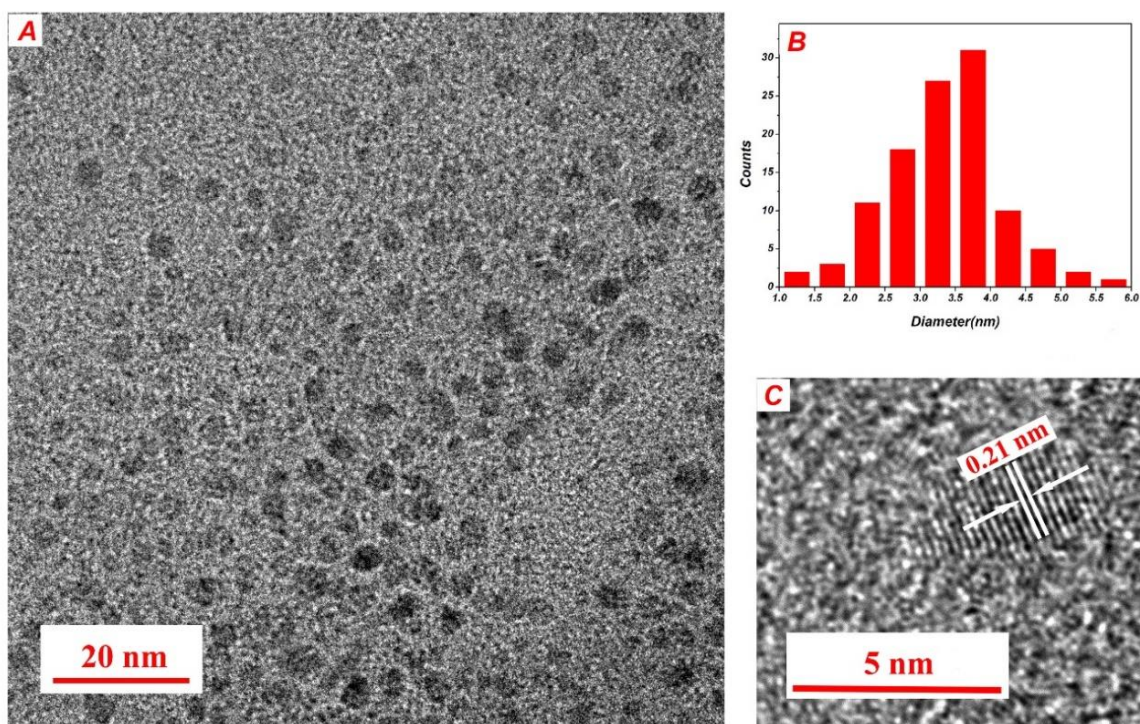


Figure 2.3. (A) TEM image of NBCDs. (B) Particle size distribution histogram of NBCDs. (C) High-resolution TEM image of an individual NBCDs.

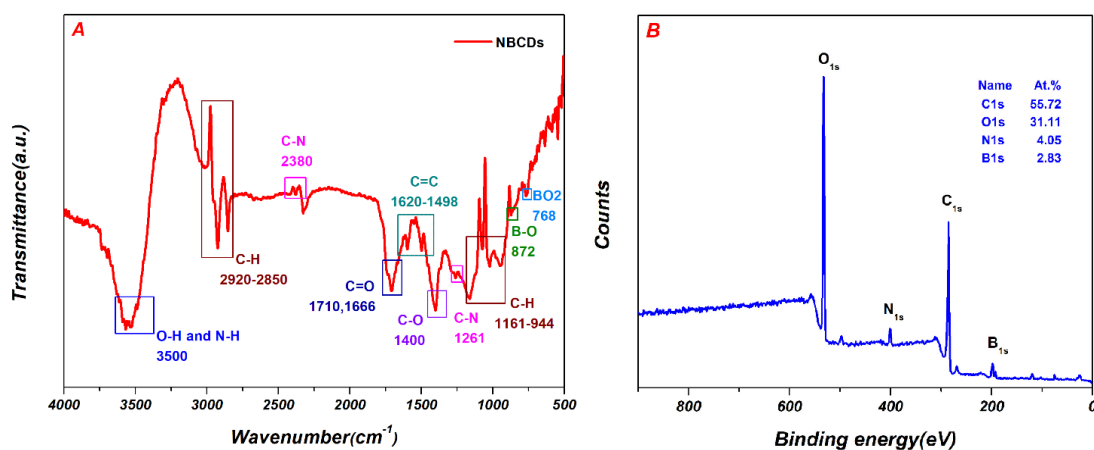


Figure 2.4. (A) FTIR and (B) XPS survey spectra of the NBCDs.

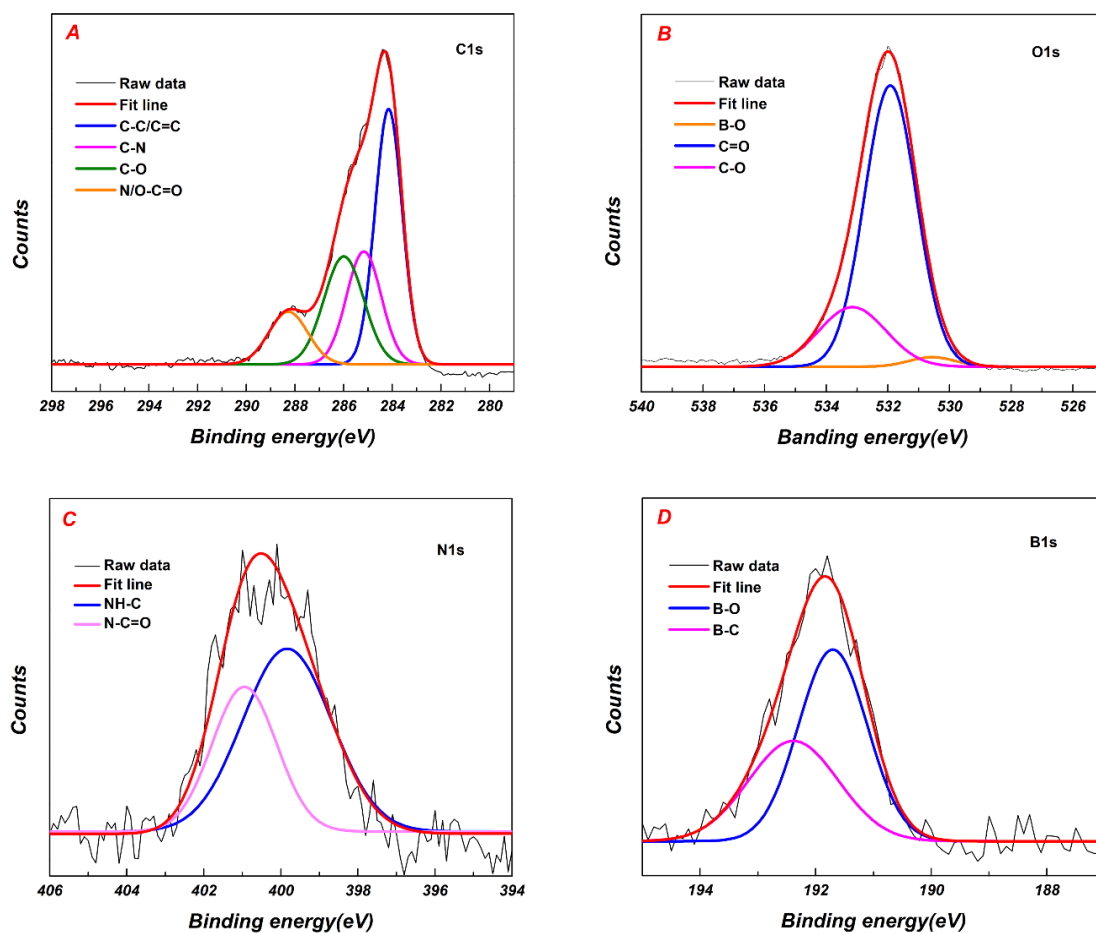


Figure 2.5. High-resolution XPS spectra of (A) C 1s, (B) O 1s, (C) N 1s and (D) B 1s of NBCDs.

2.3.2. Optical properties

2.3.2.1. PL and UV-Visible properties

The PL and UV-vis spectra were analyzed to examine the optical properties of the NBCDs. As shown in Figure 2.6A, the UV-vis absorption spectra of the NBCDs solution revealed two strong absorption peaks at 232 and 280 nm, which were attributed to the $\pi-\pi^*$ transition of the conjugated sp^2 domains from the carbon core. The normalized photoluminescence excitation (PLE) spectra of the NBCDs exhibited a strong excitation peak at 350 nm, which is in accordance with the PL emission at 455 nm. The inset image of Figure 2.6A presents a photograph of the NBCDs solution taken under a sunlight lamp (left) and 365 nm UV lamp (right), which shows that the NBCDs fabricated in this study emit a blue color.

Similar to the common CDs, the NBCDs also exhibited excitation wavelength-dependent PL emission behavior. As shown in Figure 2.6B, as the excitation wavelength was increased from 290 nm to 450 nm, the emission peak shifted to a higher wavelength. The origin of this phenomenon is still in debated but it is believed to be caused by the functional group-induced specific surface traps [42] or giant red-edge effect [43]. The maximum fluorescence intensity could be obtained at 455 nm when the NBCDs were excited at 350 nm. The quantum yield (QY) of the NBCDs was calculated to be 5.13% when quinine sulfate in 0.1M H_2SO_4 was used as a reference (Figure 2.7).

2.3.2.2. Effect of pH on the fluorescence emission of the NBCDs

As shown in Figure 2.8A and B, initially, the fluorescence intensity increased with increasing pH from 1.0 to 3.0. On the other hand, the fluorescence intensity began to decrease rapidly from pH over 3.0. The fluorescence intensity decreased gradually when the pH was increased from 3.0 to 11.0. This might have been caused by protonation-deprotonation of amide groups on the NBCDs surfaces and the aggregation of the NBCDs [33, 44-48]. The Fe^{3+} and AA sensing were performed at pH=3, where the PL intensity was highest.

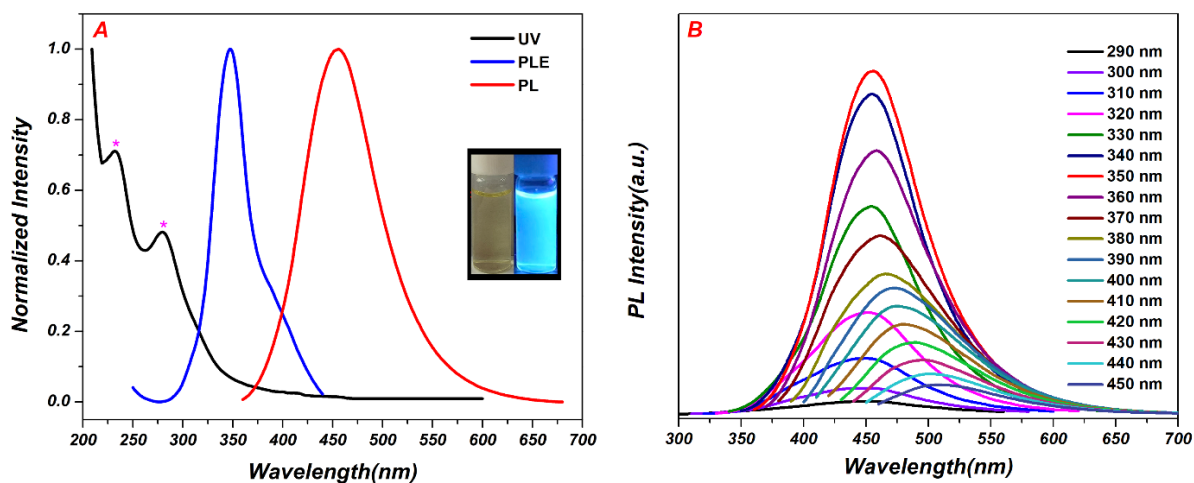


Figure 2.6. (A) Normalized UV–vis absorption PL excitation ($\lambda_{\text{ex}}=455$ nm), and PL emission spectra of the NBCDs solution ($\lambda_{\text{ex}}=350$ nm). The inset in (A): photograph image of the NBCDs solution under the ambient (left) and 365 nm UV lamp (right). (B) PL emission spectra of the NBCDs under the various excitation wavelengths.

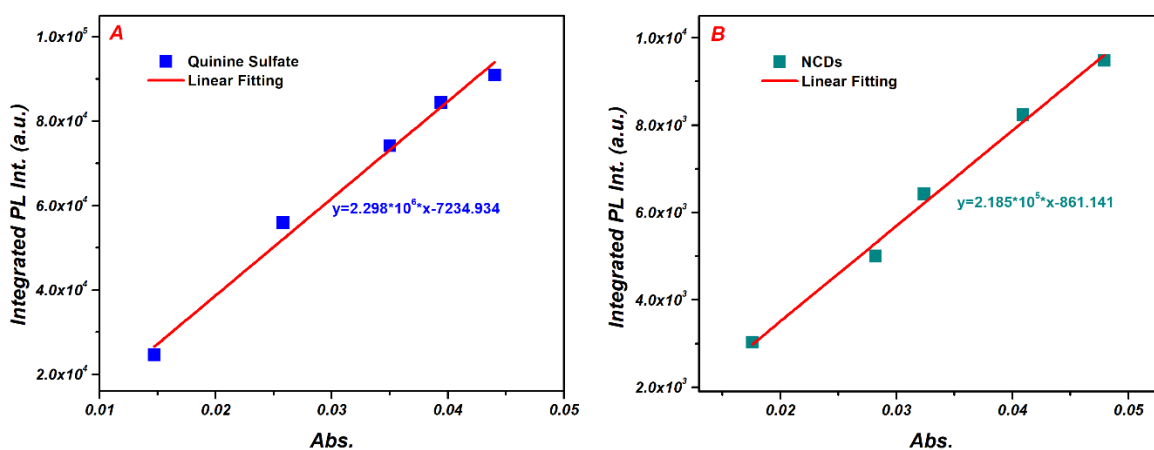


Figure 2.7. Quantum yield of NBCDs compared with quinine sulfate dye as a reference.

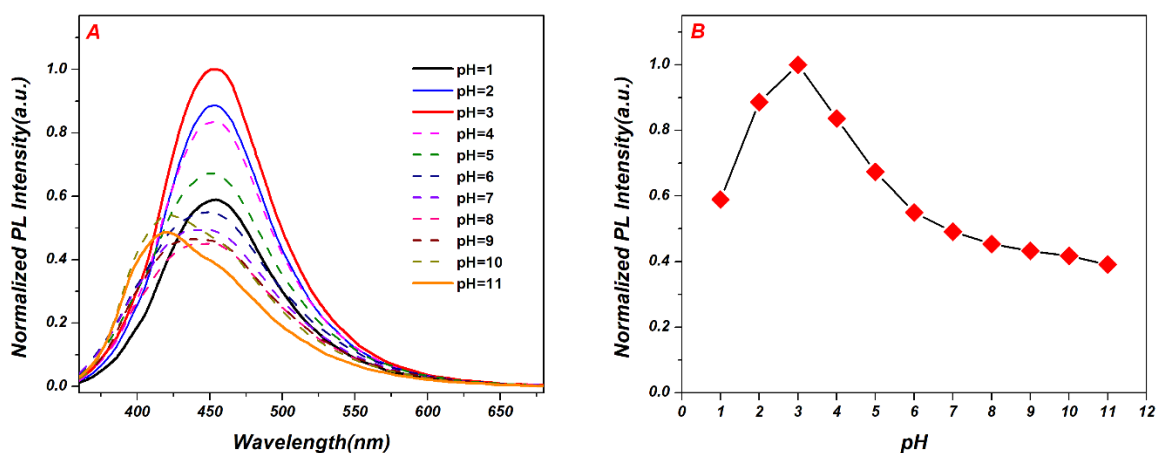


Figure 2.8. (A) PL emissions of the NBCDs at various pH values. (B) PL intensity of the NBCDs at various pH under an excitation wavelength of 350 nm.

2.3.3. Selectivity and Sensitivity towards Fe^{3+}

2.3.3.1. Selectivity

To examine the fluorescence sensing of the NBCDs, the sensing characteristics towards both various metal ions, such as Fe^{3+} , Ag^+ , Mn^{2+} , K^+ , Na^+ , Zn^{2+} , Mg^{2+} , Ca^{2+} , Cu^{2+} , Fe^{2+} , Ni^{2+} , Co^{2+} , Pb^{2+} and Hg^{2+} and some biochemical molecules were studied at different pH solutions. As shown in Figure 2.9, most metal ions exhibited strong PL quenching in pH 7 and pH 11 solutions. This may be due to the high concentration of hydroxyl ions of NBCDs, which can promote the deposition of metal ions on the surface of the NBCDs. In contrast, at pH 3, Fe^{3+} ions showed the strongest PL quenching among all the metal ions examined, as shown in Figure 2.10A and B. Fe^{3+} can quench the fluorescence of NBCDs because they facilitate non-radiative electron/hole recombination annihilation through an effective electron transfer process [49, 50]. In addition, almost no PL quenching was observed, even at pH 3, when the various biomolecules that can cause interference during Fe^{3+} ion detection were added, as shown in Figure 2.11. This shows that the NBCDs exhibit excellent selectivity towards Fe^{3+} ions over other metal ions and biochemical molecules.

2.3.3.2. Sensitivity

The sensing behavior of NBCDs to Fe^{3+} ions was investigated in detail. As shown in Figure 2.10C and D, upon the successive addition of Fe^{3+} ions the PL emission intensity decreased linearly between the regions of 0–0.7 mM and 1–5 mM of Fe^{3+} ions. The following equations were obtained at each range.

$$\log(I_0 / I) = 0.6254 \times [\text{Fe}^{3+}] + 0.0046 \quad (2-1)$$

$$\log(I_0 / I) = 0.3269 \times [\text{Fe}^{3+}] + 0.2750 \quad (2-2)$$

where I_0 and I are the fluorescence intensities of NBCDs at 454 nm before and after the addition of Fe^{3+} ions, respectively. The slopes of 0.6254 and 0.3269 are the quenching constants, which represent the fluorescence quenching efficiency. The relatively high quenching constants suggest that the NBCDs fabricated in this study exhibit high sensitivity for Fe^{3+} ion detection. The limit of detection (LOD) for Fe^{3+} was calculated to be as low as 7.50 μM in the region of 0–0.7 mM, as shown in Figure 2.12A.

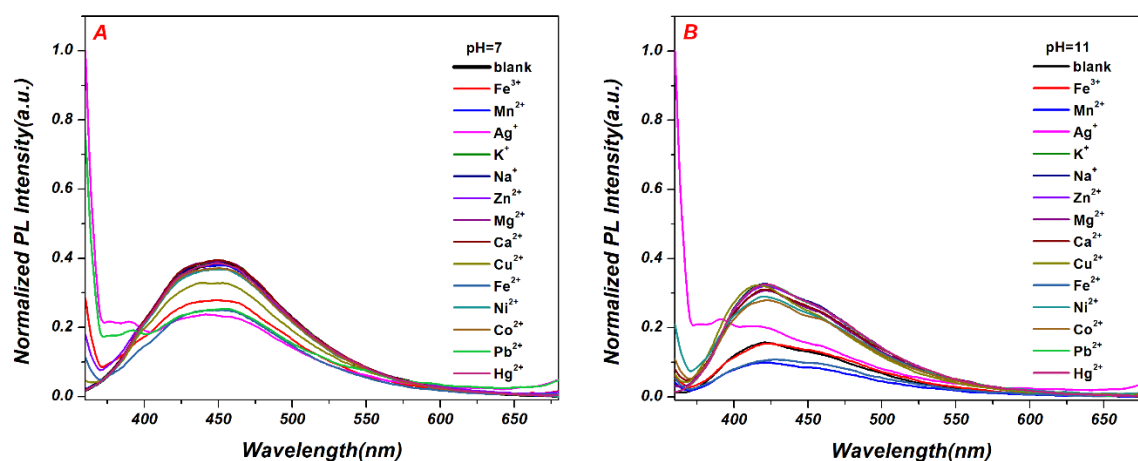


Figure 2.9. The selectivity of the NBCDs in pH 7 (A) and pH 11 (B), and fluorescence response to various metal ions.

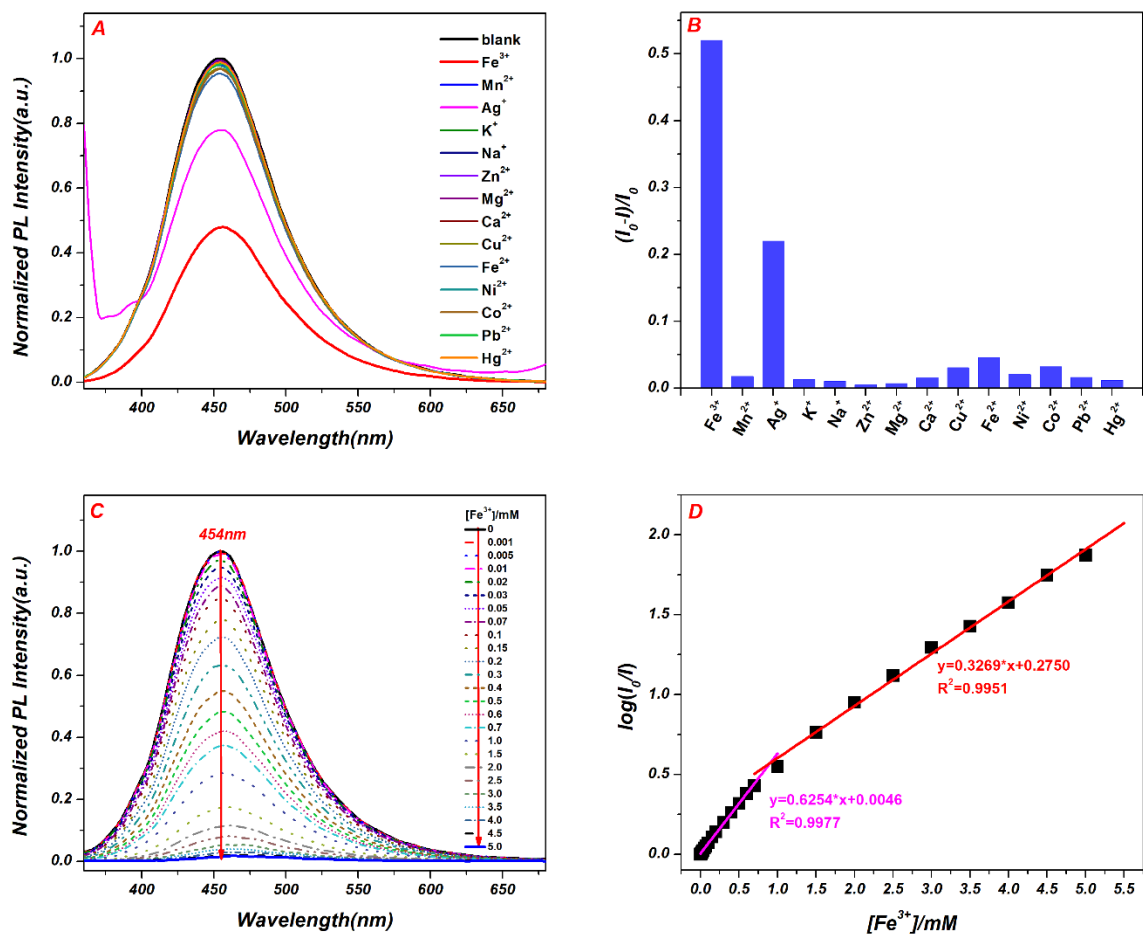


Figure 2.10. (A) Fluorescence response to various metal ions at pH 3. (B) Selectivity of NBCDs towards various metal ions. The concentration of metal ions was 500 μ M. (C) PL emission spectra of the NBCDs with various concentrations of Fe³⁺ ions at pH 3. (D) Linear log (I/I_0) plot of NBCDs quenching by Fe³⁺ ions in aqueous solution.

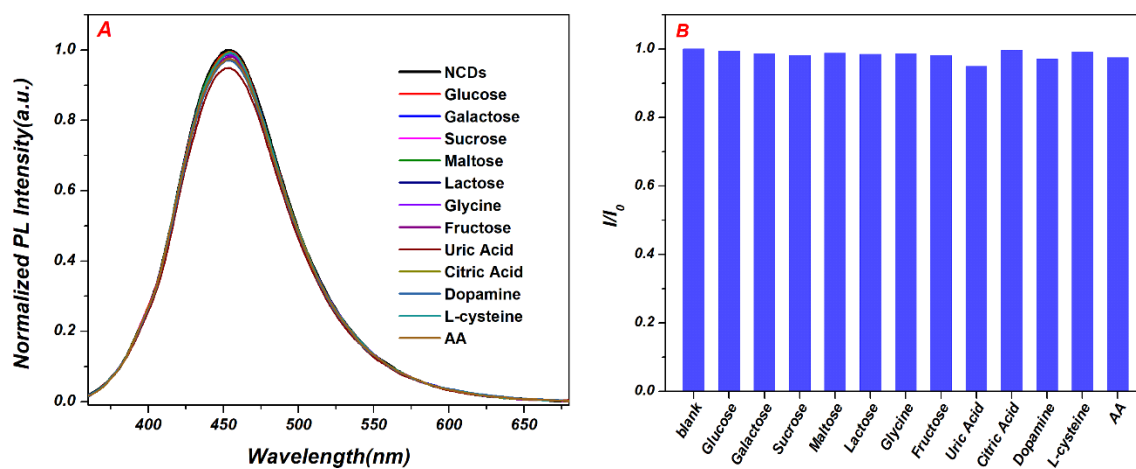


Figure 2.11. The selectivity of the NBCDs in pH 3 solution, and fluorescence response to various biomolecules.

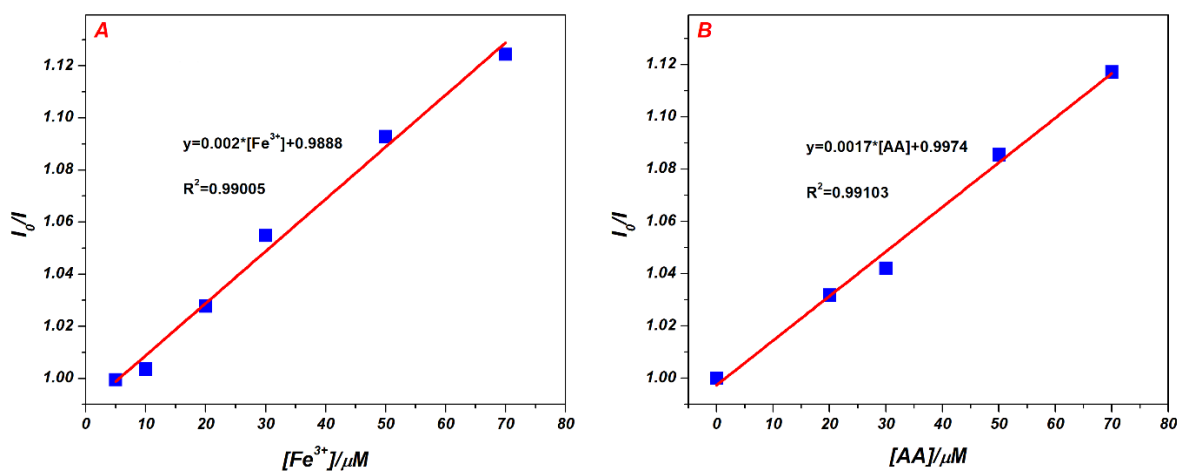


Figure 2.12. (A) Detection limit of NBCDs as the fluorescent probe for Fe^{3+} , $3\sigma/k = 7.50 \mu M$; (B) Detection limit of NBCDs-Fe for AA, $3\sigma/k = 7.72 \mu M$.

2.3.4. One pot selective sensing of AA with Fe³⁺ saturated NBCDs

Interestingly, the NBCDs fabricated in this study could detect Fe³⁺ ions and AA in one pot. As shown in Figure 2.13, after quenching the NBCDs by the addition of 3.0 mM of Fe³⁺ ions, among all biochemical materials tested, only AA could recover the PL. This suggests that Fe³⁺ ion saturated NBCDs can detect AA selectively. The removal of Fe³⁺ ions on the NBCDs by the redox reaction generated between AA and Fe³⁺ ions [51, 52] can explain the recovered PL intensity.

Time-dependent fluorescence measurements were performed to obtain the kinetic parameters during AA sensing with Fe³⁺ saturated NBCDs. When 3.5 mM of AA was added, the PL intensity at 454 nm increased gradually with time, as shown in Figure 2.14A. The recovery was rapid in the initial 5 min and was almost complete within 30 min (Figure 2.14B). As shown in Figure 2.15, the pseudo-first-order rate constant (k_0) was $0.21 \pm 0.014 \text{ min}^{-1}$, suggesting the rapid and selective recognition of Fe³⁺ saturated NBCDs towards AA. In addition, the recovered fluorescence signal remained constant after 24 h, which reveals the irreversible reaction between Fe³⁺ ions and AA on the NBCDs.

The sensitivity of Fe³⁺ saturated NBCDs towards AA was observed by PL emission spectroscopy. As shown in Figure 2.14C, with the gradual addition of AA, the emission intensities increased even at low AA concentration. The linear range was 0–1.5 mM (Figure 2.14D) and the LOD was 7.72 μM (Figure 2.12B).

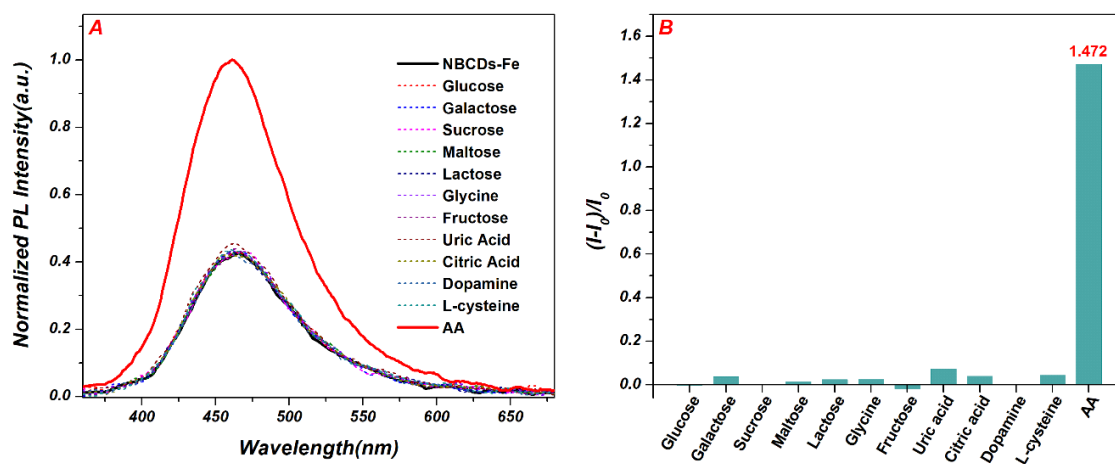


Figure 2.13. (A) PL intensity change and (B) PL recovery ratio of Fe^{3+} saturated NBCDs by various biochemical molecules. The concentration of NBCDs and biomolecules were $0.06 \mu\text{g mL}^{-1}$ and $500 \mu\text{M}$, respectively.

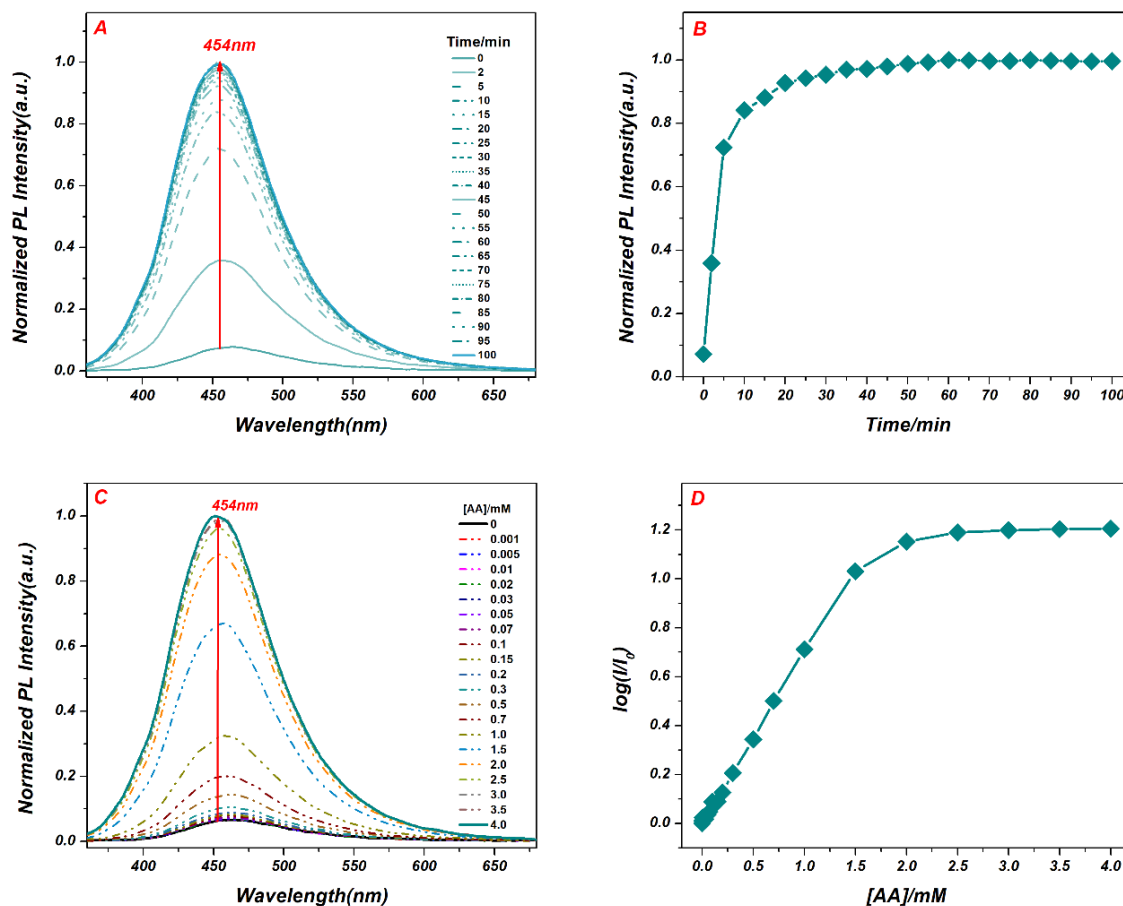


Figure 2.14. (A) Time course of the transition of the Fe³⁺ saturated NBCDs for the addition of 3.5 mM AA. (B) PL intensity changes at 454 nm with time in the presence of 3.5 mM AA. (C) PL emission spectra of Fe³⁺ saturated NBCDs at various AA concentrations. (D) The log(I/I₀) plot of Fe³⁺ saturated NBCDs changing by various concentrations of AA in an aqueous solution.

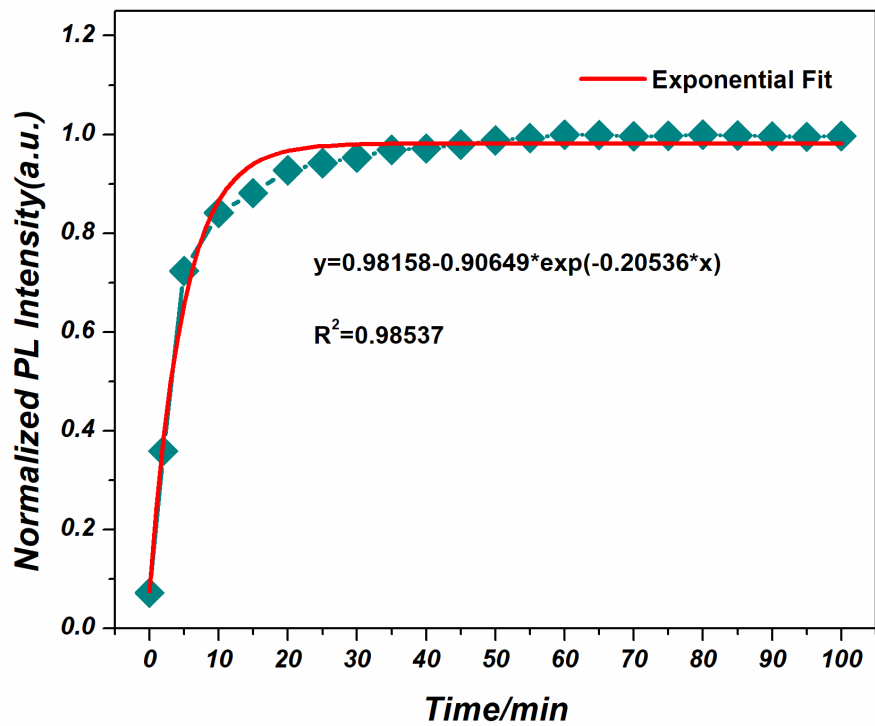


Figure 2.15. Reaction kinetic curve of the Fe^{3+} saturated NBCDs solution with AA.

2.3.5. The mechanism of NBCDs for sensing the Fe³⁺ ion and AA

The fluorescent NBCDs can detect the Fe³⁺ ion and AA sequentially by the “On-Off-On” Mechanism (Figure 2.16). Firstly, the PL emission intensity at 454 nm can be strongly quenched by the Fe³⁺ (“off”) because of the highly efficient chelation or coordination interactions between cationic Fe³⁺ and NBCDs which have abundant negatively charged oxygen-containing functional groups [53]. Secondly, PL intensity can be recovered (“on”) by the addition of AA because AA can reduce Fe³⁺ to Fe²⁺ which shows very weak interaction with NBCDs (Figure 2.14B) in aqueous solution [51, 53, 54].

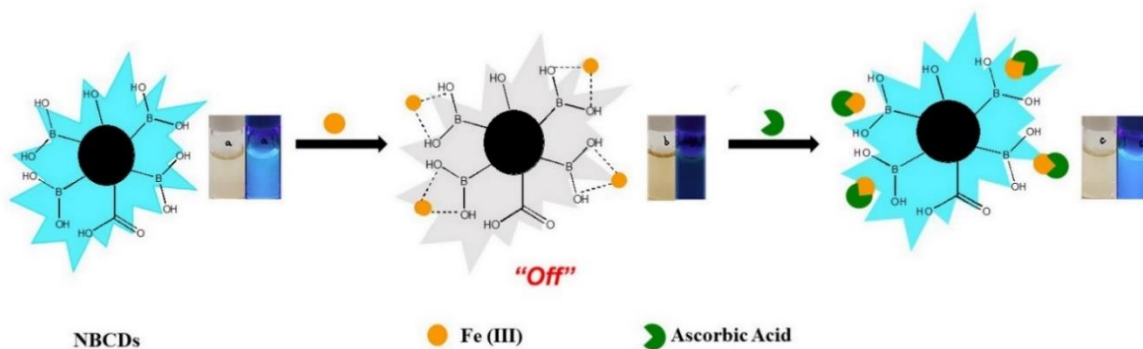


Figure 2.16. The schematic illustration of the Fe³⁺ ion and AA sensing mechanism. (The photograph images (left) under daylight and (right) UV light at each condition.)

2.3.6. Acid rain monitoring

Acid rain with a pH of approximately 5.2 or below can promote the corrosion of metal surfaces and is responsible for the deterioration of buildings and monuments. Considering the outstanding stability and sensitivity of NBCDs fabricated in this study in strong acid environments, an attempt was made to evaluate the strength of acid rain by measuring the Fe^{3+} ion-dependent PL quenching. Iron sheets and an H_2SO_4 aqueous were used to mimic the steels exposed to the various acid rain conditions (pH range of 2–7). Pick six identical pieces of iron sheets, then put them in the prepared H_2SO_4 aqueous solutions, and take 2 mL of resulting solution after reacting for 2 h, 4 h, 6 h, 10 h, 16 h, 24 h and 48 h. The detailed experimental procedures are described in Figure 2.17, and the results are presented in Figures 18–21.

As shown in Figure 2.18, the PL intensity remained constant under various pH conditions with time changed in the acid environment, which suggests that the NBCDs fabricated in this study were highly resistant to high acidic environments. On the other hand, the PL intensity decreased with increasing concentration of Fe^{3+} ions in the solution increased due to the dissolution of Fe by the acid (Figure 2.19). Interestingly, the PL intensity was quenched linearly with slopes that differed according to the pH conditions with different iron ion concentration, which can be used to evaluate the strength of acid rain visually.

As shown in Figure 2.21, the Fe^{3+} concentration in real samples, where iron sheets are dissolved by the acid solution, can be obtained precisely with the NBCDs fabricated in this study.

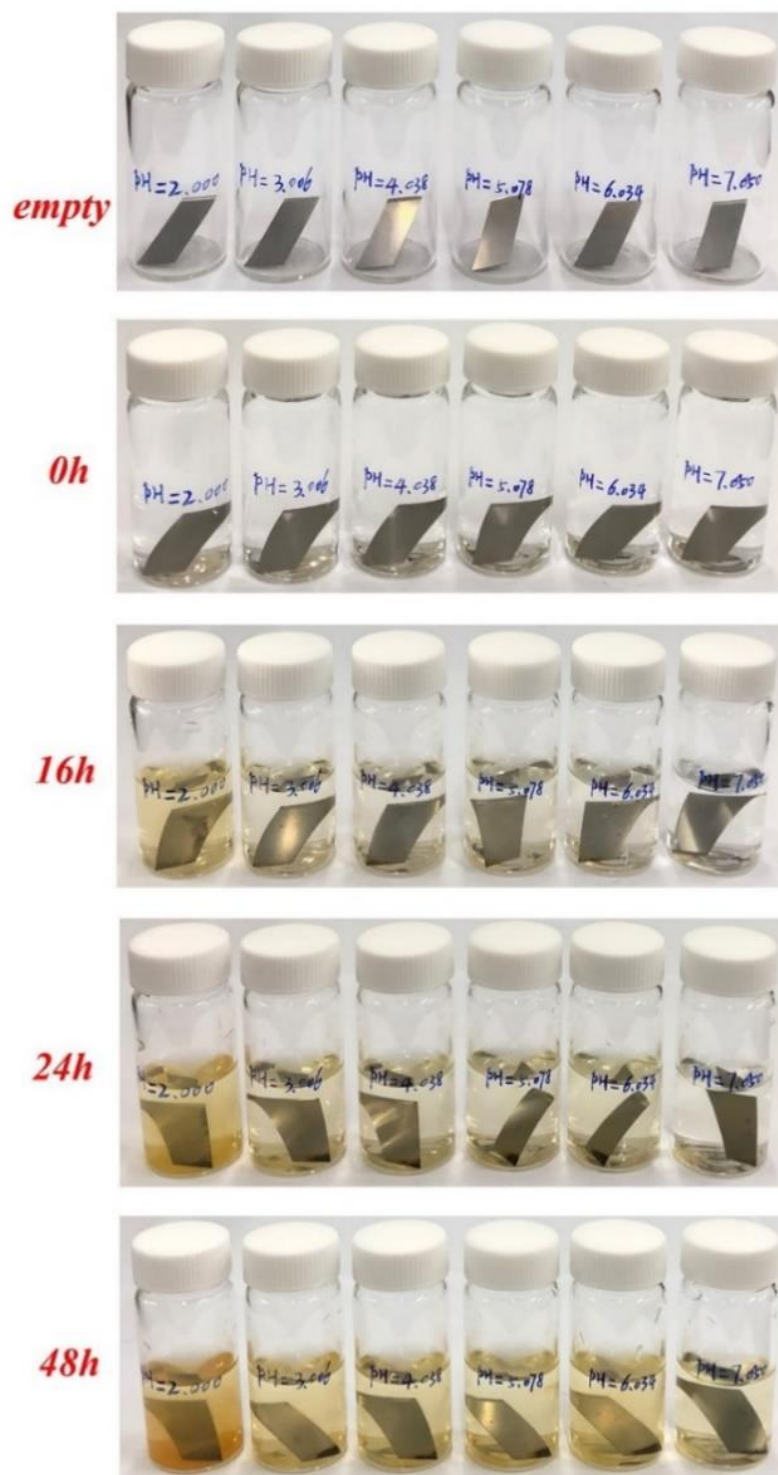


Figure 2.17. The pictures of iron sheets reacted under various pH (2-7) conditions with reaction times increasing from 0 to 48 hours.

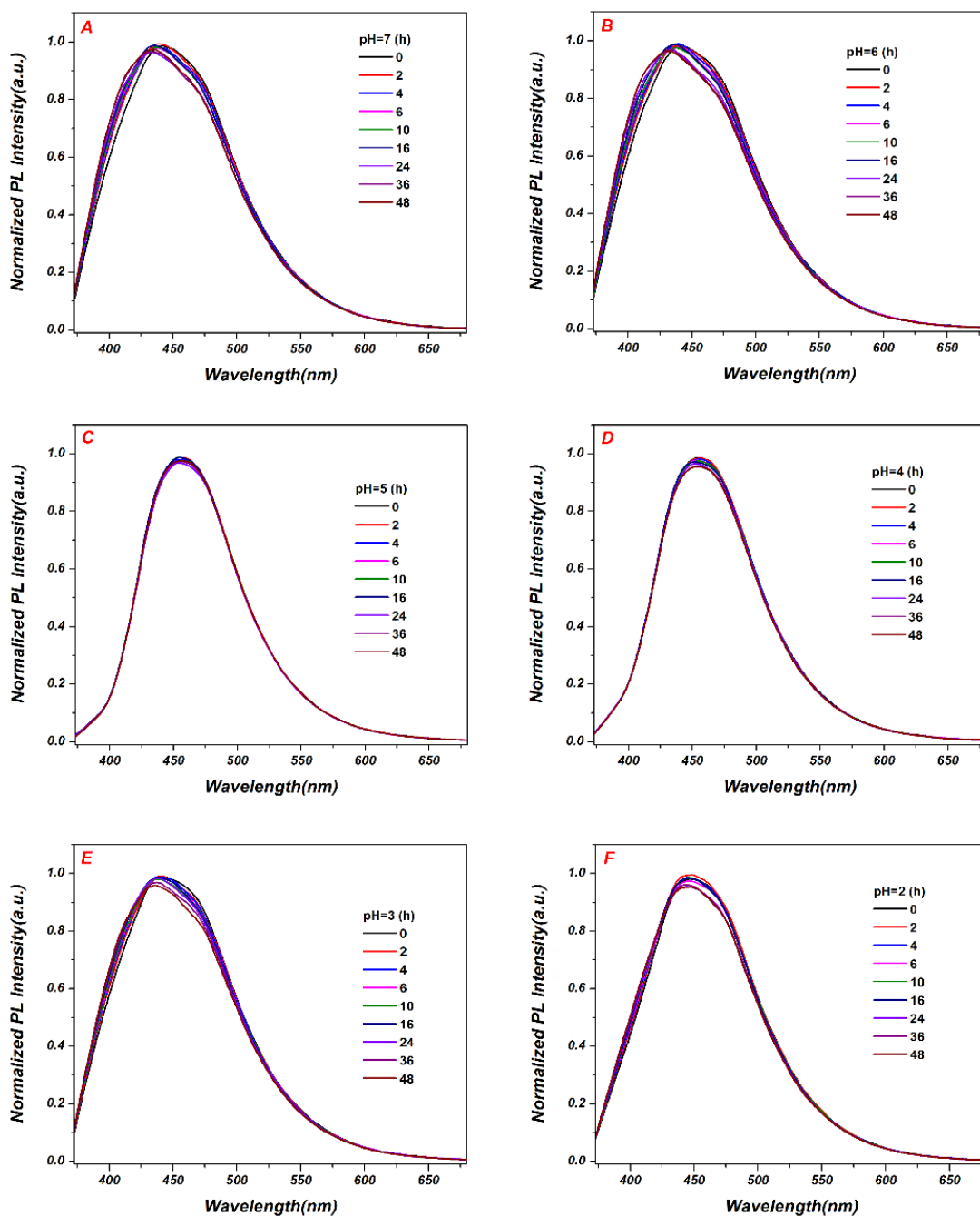


Figure 2.18. The PL emission spectra of the NBCDs under various pH (2-7) solutions with reaction times increasing from 0 to 48 hours, including (A) pH = 7, (B) pH = 6, (C) pH = 5, (D) pH = 4, (E) pH = 3, (F) pH = 2.

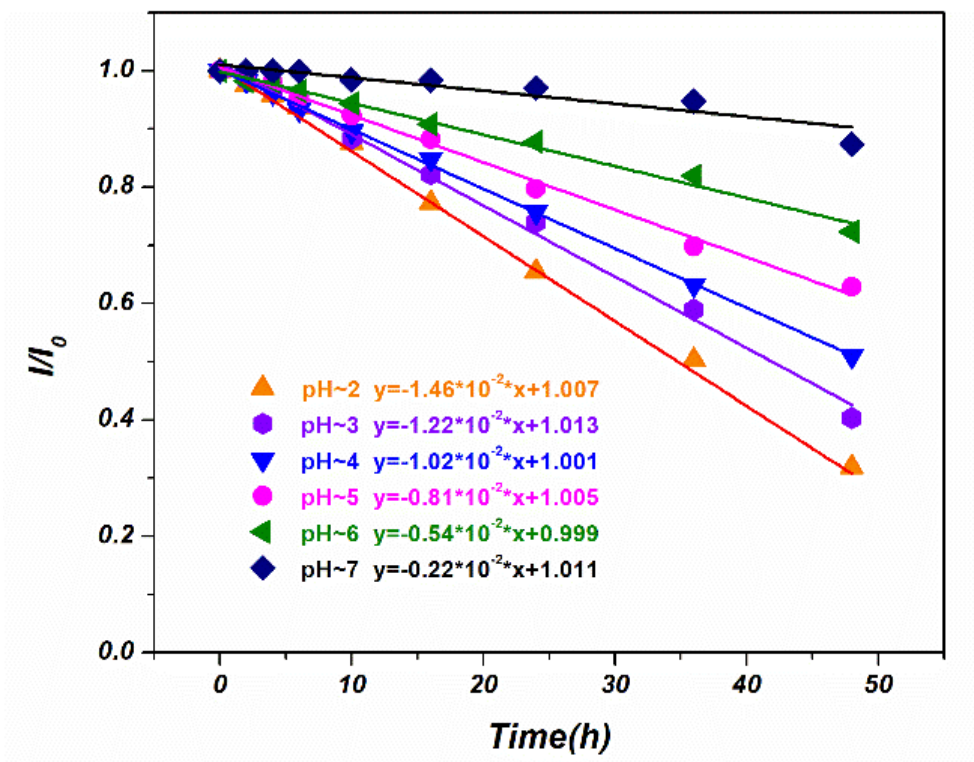


Figure 2.19. PL quenching (I/I_0) of NBCDs at various pH and reaction times.

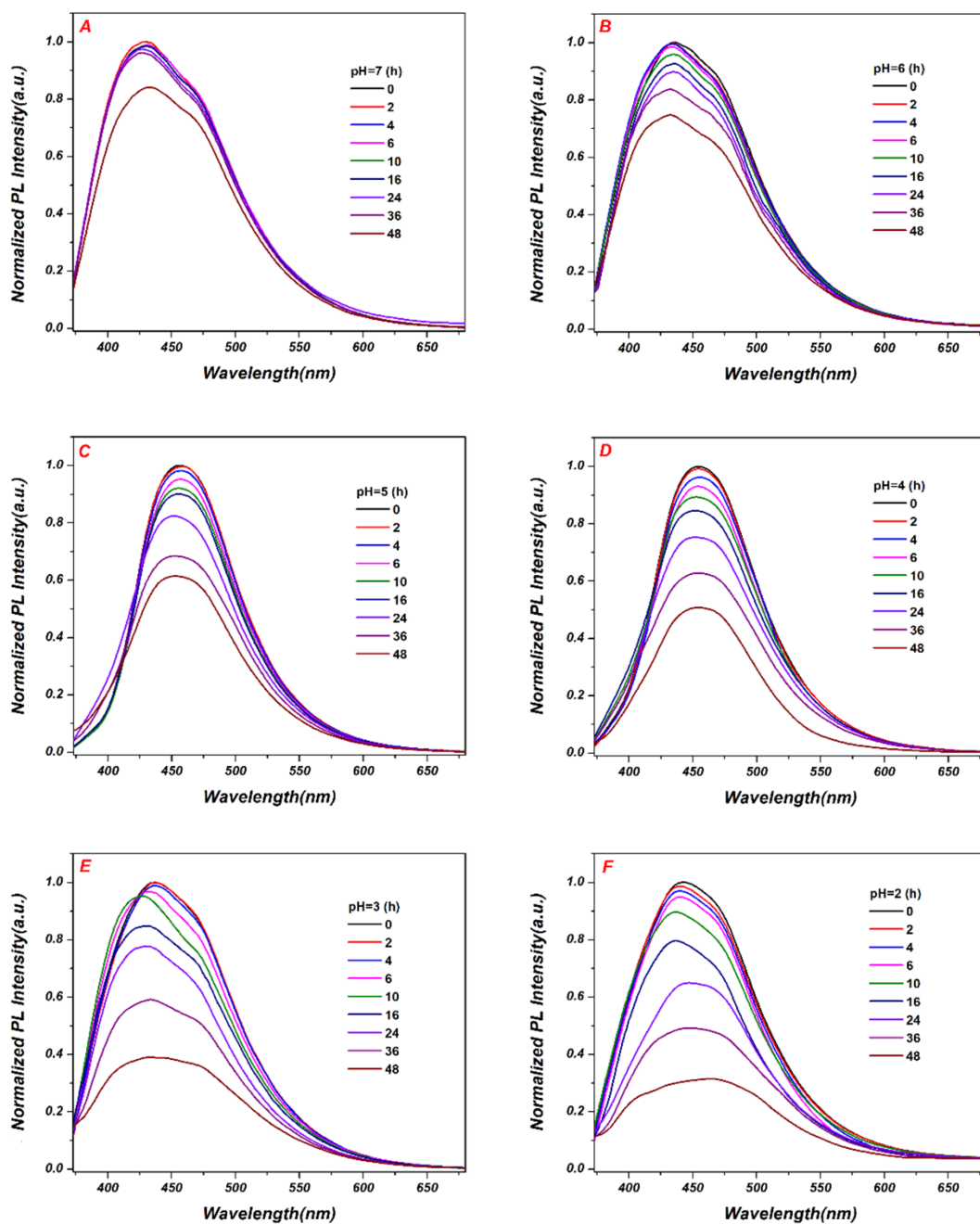


Figure 2.20. PL emission spectra of the NBCDs under various pH (2-7) solutions with different Fe³⁺ ion concentration, including (A) pH = 7, (B) pH = 6, (C) pH = 5, (D) pH = 4, (E) pH = 3, and (F) pH = 2.

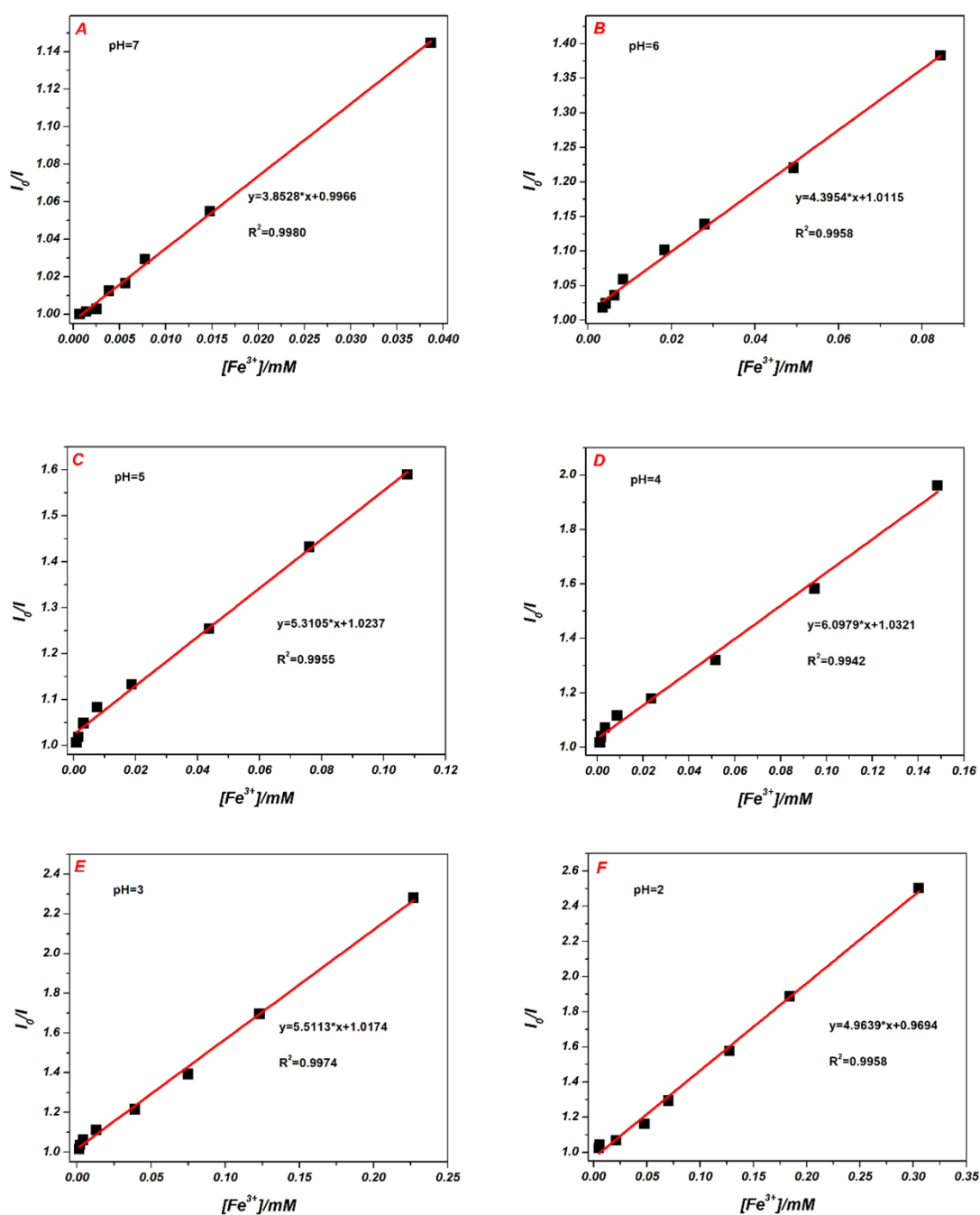


Figure 2.21. Linear regression of PL intensity of the NBCDs under various pH (2-7) solutions with different Fe^{3+} ion concentration, including (A) pH = 7, (B) pH = 6, (C) pH = 5, (D) pH = 4, (E) pH = 3, and (F) pH = 2.

2.4. Conclusion

NBCDs were synthesized by a hydrothermal method with the novel precursors of AA and 4-APBA. The NBCDs obtained exhibited good water solubility, strong fluorescence, and excellent stability without further modification. An “On–Off–On” fluorescence sensor was constructed for the simultaneous detection of Fe^{3+} and AA in one pot with a rapid response and excellent selectivity towards various interfering chemicals. When NBCDs were used in real applications, they could effectively evaluate the strength of acid rain and the Fe^{3+} ion concentration dissolved from an iron sheet by the acid solution.

Reference

- [1] J. Zhang, S. Yu. *Materials Today*, 2016, 19, 382-393.
- [2] Y. Park, J. Yoo, B. Lim, W. Kwon, S. W. Rhee. *Journal of Materials Chemistry A*, 2016, 4, 11582-11603.
- [3] X. Xu, R. Ray, Y. Gu, H. J. Ploehn, L. Gearheart, K. Raker, W. A. Scrivens. *Journal of the American Chemical Society*, 2004, 126, 12736-12737.
- [4] T. S. Atabaev. *Nanomaterials*, 2018, 8, 342.
- [5] J. Zhang, Y. Yuan, G. Liang, S. Yu. *Advanced Science*, 2015, 2, 1500002.
- [6] F. Wang, Y. Chen, C. Liu, D. Ma. *Chemical Communications*, 2011, 47, 3502-3504.
- [7] S. Hu, K. Niu, J. Sun, J. Yang, N. Zhao, X. Du. *Journal of Materials Chemistry*, 2009, 19, 484-488.
- [8] G. Qiao, D. Lu, Y. Tang, J. Gao, Q. Wang. *Dyes and Pigments*, 2019, 163, 102-110.
- [9] D. Lu, Y. Tang, J. Gao, Q. Wang. *Journal of Materials Chemistry C*, 2018, 6, 13013-13022
- [10] J. Zhou, C. Booker, R. Li, X. Zhou, T. Sham, X. Sun, Z. Ding. *Journal of the American Chemical Society*, 2007, 129, 744-745.
- [11] Y. Li, Y. Hu, Y. Zhao, G. Shi, L. Deng, Y. Hou, L. Qu. *Advanced Materials*, 2011, 23, 776-780.

- [12] J. Peng, W. Gao, B. K. Gupta, Z. Liu, R. R. Aburto, L. Ge, L. Song, L. B. Alemany, X. Zhan, G. Gao, S. A. Vithayathil, B. A. Kaiparettu, A. A. Marti, T. Hayashi, J. Zhu, P. M. Ajayan. *Nano Letters*, 2012, 12, 844-849.
- [13] H. G. Baldovi, S. Valencia, M. Alvaro, A. M. Asiri, H. Garcia. *Nanoscale*, 2015, 7, 1744-1752.
- [14] K. Holá, M. Sudolská, S. Kalytchuk, D. Nachtigallová, A. L. Rogach, M. Otyepka, R. Zbořil. *ACS Nano*, 2017, 11, 12402-12410.
- [15] S. Sun, L. Zhang, K. Jiang, A. Wu, H. Lin. *Chemistry of Materials*, 2016, 28, 8659-8668.
- [16] Z. Zhou, Q. Wang, J. Wang, C. C. Zhang. *Carbon*, 2015, 93, 671-680.
- [17] B. Wang, Y. Mu, H. Yin, Z. Yang, Y. Shi, J. Li. *Nanoscale* 2018, 10, 10650-10656
- [18] Z. Gu, D. Li, C. Zheng, Y. Kang, C. Wöll, J. Zhang. *Angewandte Chemie International Edition*, 2017, 56, 6853-6858.
- [19] L. Xiao, H. Sun. *Nanoscale Horizons*, 2018, 3, 565-597.
- [20] B. C. *Clinical Chemistry*, 2003, 49, 1573-1578.
- [21] K. Qu, J. Wang, J. Ren, X. Qu. *Chemistry - A European Journal*, 2013, 19, 7243-7249.
- [22] J. Zhang, J. Wang, J. Fu, X. Fu, W. Gan, H. Hao. *Journal of Nanoparticle Research*, 2018, 20, 41.
- [23] X. Gong, W. Lu, M. C. Paau, Q. Hu, X. Wu, S. Shuang, C. Donga, M. M. F. Choi. *Analytica Chimica Acta*, 2015, 861, 74-84.
- [24] Y. Li, Y. Liu, X. Shang, D. Chao, L. Zhou, H. Zhang. *Chemical Physics Letters*, 2018, 705, 1-6.
- [25] A. L, Y. ME. *Vitamins and Hormones*, 2011, 86, 287-305.
- [26] Y. Song, C. Gong, D. Su, Y. Shen, Y. Song, L. Wang. *Analytical Methods*, 2016, 8, 2290-2296.
- [27] W. Kong, D. Wu, G. Li, X. Chen, P. Gong, Z. Sun, G. Chen, L. Xia, J. You, Y. Wu. *Talanta*, 2017, 165, 677-684.

- [28] M. Zheng, Z. Xie, D. Qu, D. Li, P. Du, X. Jing, Z. Sun. *ACS Applied Materials & Interfaces*, 2013, 5, 13242-13247.
- [29] S. N. Baker, G. A. Baker. *Angewandte Chemie International Edition*, 2010, 49, 6726-6744.
- [30] H. Nie, M. Li, Q. Li, S. Liang, Y. Tan, L. Sheng, W. Shi, S. X.-A. Zhang. *Chemistry of Materials*, 2014, 26, 3104-3112.
- [31] J. Jiang, Y. He, S. Li, H. Cui. *Chemical Communications*, 2012, 48, 9634-9636.
- [32] X. Cui, Y. Wang, J. Liu, Q. Yang, B. Zhang, Y. Gao, Y. Wang, G. Lu. *Sensors and Actuators B: Chemical*, 2017, 242, 1272-1280.
- [33] D. K. Dang, S. Chandrasekaran, Y.-L. T. Ngo, J. S. Chung, E. J. Kim, S. H. Hur. *Sensors and Actuators B: Chemical*, 2018, 255, 3284-3291.
- [34] Z. Wu, M. Gao, T. Wang, X. Wan, L. Zheng, C. Huang. *Nanoscale*, 2014, 6, 3868-3874
- [35] Q. Wang, I. Kaminska, J. Niedziolka-Jonsson, M. Opallo, M. Li, R. Boukherroub, S. Szunerits. *Biosensors and Bioelectronics*, 2013, 50, 331-337.
- [36] S. Basiruddin, S. K. Swain. *Materials Science and Engineering: C*, 2016, 58, 103-109.
- [37] Y. Chen, Y. Wu, B. Weng, B. Wang, C. Li. *Sensors and Actuators B: Chemical*, 2016, 233, 689-696.
- [38] K. S. Vasu, S. S., S. Sampath, A. K. Sood. *Sensors and Actuators B: Chemical*, 2015, 221, 1209-1214.
- [39] P. M. Sudeep, S. Vinod, S. Ozden, R. Sruthi, A. Kukovecz, Z. Konya, R. Vajtai, M. R. Anantharaman, P. M. Ajayan, T. N. Narayanan. *RSC Advances*, 2015, 5, 93964-93968.
- [40] B. J. Matsoso, K. Ranganathan, B. K. Mutuma, T. Lerotholi, G. Jones, N. J. Coville. *New Journal of Chemistry*, 2017, 41, 9497-9504
- [41] J. Yun, L. Chen, X. Zhang, J. Feng, L. Liu. *Polymers*, 2016, 8, 35.
- [42] H. Dong, A. Kuzmanoski, D. M. Gößl, R. Popescu, D. Gerthsen, C. Feldmann. *Chemical Communications*, 2014, 50, 7503-7506.
- [43] Z. Sun, X. Li, Y. Wu, C. Wei, H. Zeng. *New Journal of Chemistry*, 2018, 42, 4603-4611.

- [44] D. Pan, J. Zhang, Z. Li, C. Wu, X. Yan, M. Wu. *Chemical Communications*, 2010, 46, 3681-3683
- [45] M. J. Krysmann, A. Kelarakis, P. Dallas, E. P. Giannelis. *Journal of the American Chemical Society*, 2012, 134, 747-750.
- [46] Y. Guo, Z. Wang, H. Shao, X. Jiang. *Carbon*, 2013, 52, 583-589.
- [47] Z. Yang, M. Xu, Y. Liu, F. He, F. Gao, Y. Su, H. Wei, Y. Zhang. *Nanoscale*, 2014, 6, 1890-1895.
- [48] X. Sun, J. He, Y. Meng, L. Zhang, S. Zhang, X. Ma, S. Dey, J. Zhao, Y. Lei. *Journal of Materials Chemistry A*, 2016, 4, 4161-4171.
- [49] L. Zhou, Y. Lin, Z. Huang, J. Ren, X. Qu. *Chemical Communications*, 2012, 148, 1147-1149.
- [50] L. Zhao, X. Xin, P. Ding, A. Song, Z. Xie, J. Shen, G. Xu. *Analytica Chimica Acta*, 2016, 926, 99-106.
- [51] X. Guo, G. Yue, J. Huang, C. Liu, Q. Zeng, L. Wang. *ACS Applied Materials & Interfaces*, 2018, 10, 26118-26127.
- [52] Y. Yan, C. Zhang, W. Gu, C. Ding, X. Li, Y. Xian. *Journal of Physical Chemistry C*, 2016, 120, 12170-12177.
- [53] X. Gao, X. Zhou, Y. Ma, T. Qian, C. Wang, F. Chu. *Applied Surface Science*, 2019, 469, 911-916.
- [54] L. Shi, Z. Hou, C. Zhang, G. Zhang, Y. Zhang, C. Dong, S. Shuang. *Analytical Methods*, 2019, 11, 669-676.

CHAPTER 3. Glutathione Modified N-doped Carbon Dots for Sensitive and Selective Dopamine Detection

3.1. Introduction

Dopamine, 3,4-dihydroxyphenethylamine, (DA) is well-known as being a very important catecholamine neurotransmitters, which performs critical roles in the functioning of the renal, cardiovascular, and central nervous systems [1, 2]. DA is produced by the decarboxylation of 3,4-dihydroxy phenylalanine [3]. The deficiency of DA mainly causes neurological disorders, which can lead to neurological diseases such as dementia, Parkinson's disease, schizophrenia, epilepsy, and attention deficit hyperactivity disorder [4-6]. Such physiological and pathophysiological effects make the roles that DA plays in neurosystems highly significant [7].

In light of the significance of DA, different methods have been developed for DA determination, such as high-performance liquid chromatography [8, 9], electrochemical methods [10-13], capillary electrophoresis [14-16], chemiluminescence [17, 18], colorimetric methods [19, 20], and fluorescence methods [21-23]. Recently, the fluorescent approach has attracted more attention, because of its high sensitivity, good reliability, operational simplicity, real-time detection, low cost, and rapid nature [24-27].

Carbon dots (CDs) are one class of luminescent nanoparticle materials that are mainly comprised of carbon [28]. In recent years, the methods for synthesizing CDs have developed rapidly, such as arc-discharge, laser ablation/irradiation, electrochemical synthesis, chemical exfoliation, microwave, ultrasonic preparation, and hydrothermal processes [29]. In relation to the synthetic methods, the hydrothermal method is a simple, cost-effective, and easily controllable one-step process [30, 31]. CDs have some advantages that include easy synthesis, good stability, low toxicity, good biocompatibility, high water solubility, and unique optical properties [32, 33]. Owing to the advantages, CDs are successfully used and show potential in biosensing, bioimaging, photocatalysts, optoelectronic devices, and analytical applications [34-39]. The sensing processes of the designed optical chemosensor

are carried out through different methods, such as inner filter effect, photo-induced electron transfer, fluorescence resonance energy transfer, intra-molecular charge transfer, and metal-ligand charge transfer [40]. In addition, the CDs might be an oxidizing or reducing reagent and have intermolecular interaction with the analyte molecules, owing to the excellent electron acceptance or electron donation properties [41].

Reduced L-glutathione (GSH) is a tri-peptide and has significant roles in signals processing [42]. The GSH compounds have many functional groups, including carboxyl, thiols, peptide bond, and amino groups, which can be appropriately utilized for sensing purposes. These functionalities can be used for the surface passivation of CDs, to provide better surface activity of CDs. GSH can be attached to the CD surface through chemical reactions, and the resultant passivated CDs would result in better dispersion in water [43, 44]. The surface modification of CDs by GSH improves the optical properties, and enhances their applicability towards biological imaging and applications [45, 46].

In this work, shown in Figure 3.1, a sensitive DA nanosensor, GSH-NCDs was designed by combining GSH and NCDs. Citric acid and urea were used as the carbon and nitrogen atom sources for NCDs synthesis, and NCDs were synthesized through the hydrothermal methods. GSH served as a sulfur atom, and with abundant functional groups, including carboxyl, thiols, and amino groups. The obtained GSH-NCDs exhibited high water solubility and intense blue fluorescence in aqueous solution. The fluorescence was quenched with the addition of DA, and the limit of detection was calculated to be 1.01 nM, which is one of the lowest values ever reported (Table 3.1). The fluorescence quenching was due to the interaction between the DA and GSH-NCDs through GSH-DA electrostatic interaction. In addition, the GSH-NCDs exhibited excellent selectivity towards other analyzing biomolecules, such as citric acid (CA), ascorbic acid (AA), uric acid (UA), fructose (Fru), glucose (Glu), L-cysteine (Cys), and sucrose (Suc), DL-Homocysteine (Hcy), L-tyrosine (Tyr), Urea, creatine monohydrate (45reate), and creatinine (Cre). The application of the nanosensor was also confirmed by using the standard DA in real urine samples with satisfactory recovery values.

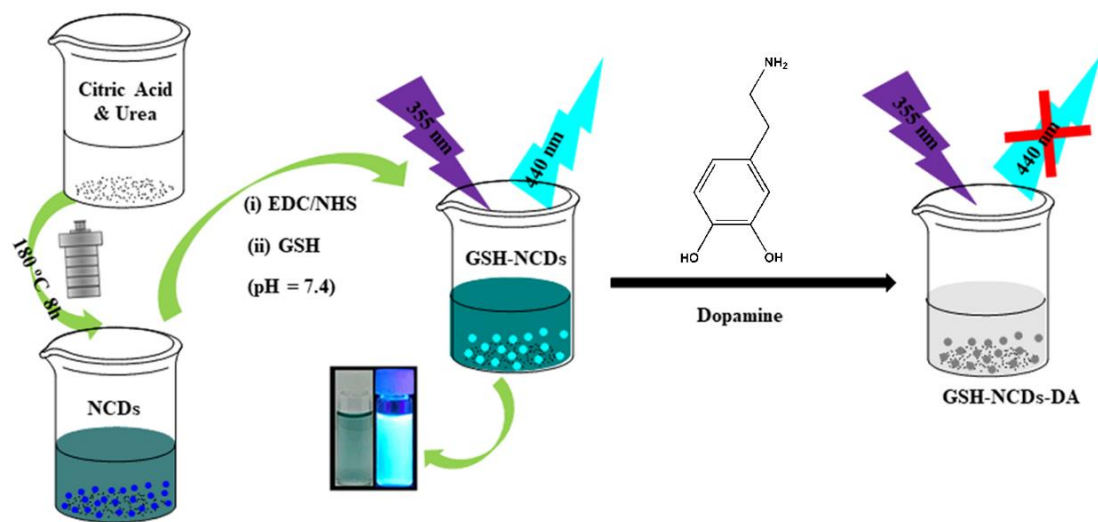


Figure 3.1. Schematics of the GSH-NCDs fabrication process and DA detection by the as-synthesized GSH-NCDs.

Table 3.1. The comparison of different fluorometric sensors for DA determination.

Materials	Limit of detection (nM)	Linear range (μ M)	Ref.
rGO–Co ₃ O ₄	277	0-30	[2]
TCCP/CCG/GCE	10	0.01-70	[5]
CB-GCE	60	0.1-20	[10]
PTCA/RGO/Au NPs/GCE	70	1-100	[11]
Au/GCNE	10	0.02-5.6	[16]
Ag ₂ Se QDs	100	0.5-19	[17]
DSP-AuNPs	2	0.005-0.6	[19]
GQDs	90	0.25-50	[21]
Fe-CQDs	5	0.01-50	[22]
N, P-Doped CQDs	21	10-500	[23]
AgNPs	0.75	0.005-0.4	[24]
pDA NPs	5.5	0.01-5	[25]
ZnO-Associated CDs	1.06	0.18-15	[26]
N-doped GQDs	3.3	0.01-3	[27]
GSH-NCDs	1.01	0.02-10	Present work

3.2. Experimental Section

3.2.1. Materials

Citric acid (CA), urea, 1-Ethyl-3-(3-dimethylaminopropyl)carboxylate hydrochloride (EDC), N-Hydroxysuccinimide (NHS), L-Glutathione reduced (GSH), dopamine (DA), ascorbic acid (AA), uric acid (UA), fructose (Fru), glucose (Glu), sucrose (Suc), L-cysteine (Cys), DL-Homocysteine (Hcy), L-tyrosine (Tyr), Urea, creatine monohydrate (Creat), and creatinine (Cre), potassium phosphate monobasic, and sodium phosphate monobasic monohydrate were purchased from Sigma-Aldrich Co. (USA). The urine samples were collected from healthy volunteers. All chemical reagents were used as received without further purification. Deionized (DI) water was used in all experiments.

3.2.2. Characterization

The fluorescence of the samples was recorded using a Cary Eclipse fluorescence spectrophotometer (Agilent Technologies, USA) using a 1.0 cm quartz cuvette. The absorption study of the samples was performed with the help of a UV-Vis spectrometer (UV-Vis, SPECORD 210 PLUS, Analytik Jena, Germany). The analysis of functional groups was done using the Fourier Transform Infrared (FTIR, Nicolet iS5, Thermo Fisher Scientific, USA) spectroscopy. X-ray photoelectron spectroscopy (XPS, Thermo ESCALAB 250 Xi, Thermo Fisher Scientific, USA) using Al K α X-ray radiation (1486.6 eV) was used to determine the oxidation states of the constituent elements. X-ray diffraction (XRD, Rigaku D/MAZX 2500V/PC model, Japan) was carried out using Cu K α radiation (40 kV, 30 mA, $\lambda = 1.5415 \text{ \AA}$) at a scan rate of 2° min^{-1} over the 2θ range of $10\text{-}100^\circ$. The size and morphology of the as-synthesized particles were monitored by high-resolution transmission electron microscopy (HR-TEM, JEM-2100 F, JEOL, Japan, operating voltage 200 kV).

3.2.3. Synthesis of the NCDs

Typically, the hydrothermal method was used for the synthesis of the NCDs. Citric

acid (0.42 g, 2 mmol) and urea (0.36 g, 6 mmol) were added to deionised water (12 mL) and stirred for 5 min, to form a homogeneous and transparent solution. The mixed solution was then transferred to a 50 mL Teflon-lined autoclave, and then maintained at 180 °C for 8 h in an oven for further reaction. The NCDs solution was centrifuged with 10000 rpm 10 min, and dialyzed for 24 h after cooling to room temperature (RT), and was then freeze-dried for further reaction.

3.2.4. Synthesis of the GSH-NCDs and Quantum Yield (QY) Measurement

To synthesize the GSH-associated NCDs, phosphate buffer solution (pH = 7.4) (8 mL) and EDC (0.192 g, 1 mmol) and NHS (0.115 g, 1 mmol) was added to NCDs (10 mg/mL, 2 mL), and the mixed solution was sonicated for 15 min in dark with the addition of the ice. The 5 mL 0.154 g GSH solution was added to the mixed solutions, and then stirred for 10 h in the dark at RT. The solution was centrifuged and dialyzed to remove the residual starting materials, and then freeze-dried for 48 h to obtain the final product, GSH-NCDs. The QY was measured with the quinine sulfate as the reference sample.

3.3. Results and discussion

3.3.1. Physical characterization of the GSH-NCDs

Figure 3.2A exhibits the transmission electron microscopy (TEM) image of the synthesized GSH-NCDs. Figure 3.2B presents that the GSH-NCDs particles had an average diameter of 3.53 nm. Further close observations with a high-resolution TEM (HRTEM) image shows the lattice space of 0.23 nm (Figure 3.2C), which corresponds to the (100) plane of graphite carbon [22]. The XRD pattern in Figure 3.2D presents a large broad peak at approximately $2\theta = 23^\circ$, which can be assigned to disordered carbon atoms [47].

Fourier transform infrared spectroscopy (FTIR) was employed to study the surface functional groups of the GSH-NCDs nanoparticles. Figure 3.2E shows the FTIR spectra of

the GSH-NCDs, which exhibited the characteristic peaks. The stretching vibrations of O–H/N–H, –CH₂, S–H, C=C/C=O, CO–NH, C–N, and C–O were shown at 3497, 2951, 2367, 1650, 1401, 1234, and 1073 cm⁻¹, respectively [48]. Comparison with the FTIR spectra of GSH, those of the NCDs and GSH-NCDs exhibited two new peaks of S–H and CO–NH at 2367 and 1234 cm⁻¹, respectively, from the GSH-NCDs, indicating the successful incorporation of GSH structure in the NCDs [44].

X-ray photoelectron spectroscopy (XPS) was employed to explore the elemental composition and functional groups of the GSH-NCDs nanoparticles. Figure 3.3A shows the XPS survey spectra, which revealed that the GSH-NCDs were composed mainly of carbon (C), nitrogen (N), oxygen (O), and sulfur (S) elements. The high-resolution XPS spectrum of C1s was deconvoluted into four peaks at 283.9, 284.9, 285.9, and 288.3 eV, which were assigned to C=C, C–C, C–O/C–N, and C=O bonds, respectively [41]. The N1s spectra revealed two peaks at 399.5 and 401.3 eV, which were attributed to C–N and N–H bonds, respectively [44]. The O1s spectrum was revealed two peaks at 531.2 and 533.1 eV, which were corresponded to C=O and C–O bonds, respectively [49]. The S 2p spectrum showed the S 2p_{3/2} and S 2p_{1/2} peaks with binding energies at 161.4 and 163.8 eV, respectively, which could be assigned to the thiols of GSH [50]. The characterization analysis results of the GSH-NCDs indicated the presence of –COOH, –NH₂, –SH, and –CO–NH functional groups at its surface.

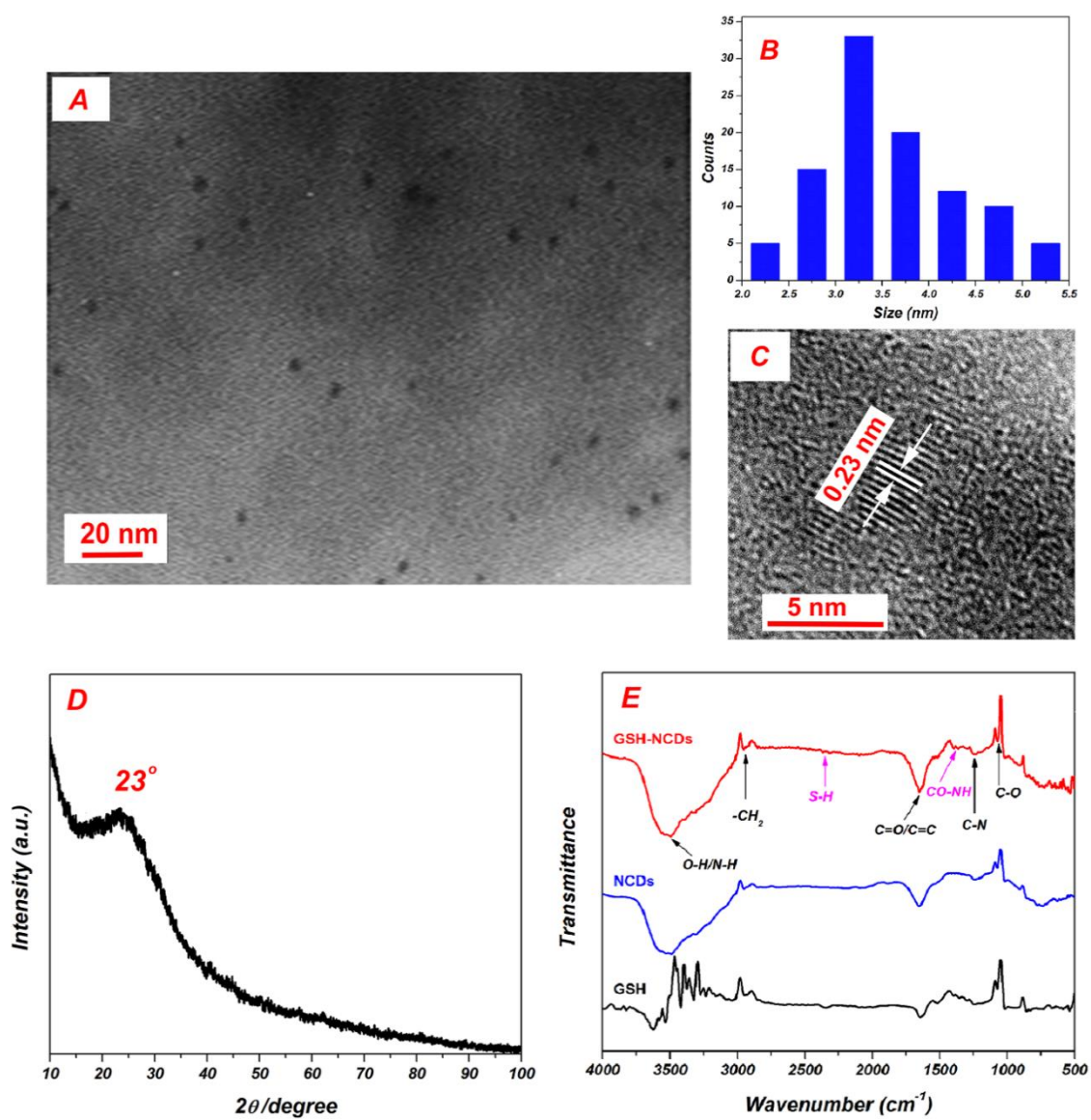


Figure 3.2. (A) TEM image of the GSH-NCDs. (B) The particle size distribution histogram of the GSH-NCDs. (C) HRTEM image of the GSH-NCDs with lattice fringe. (D) XRD pattern of the GSH-NCDs, and (E) FTIR spectra of the GSH, NCDs, and GSH-NCDs.

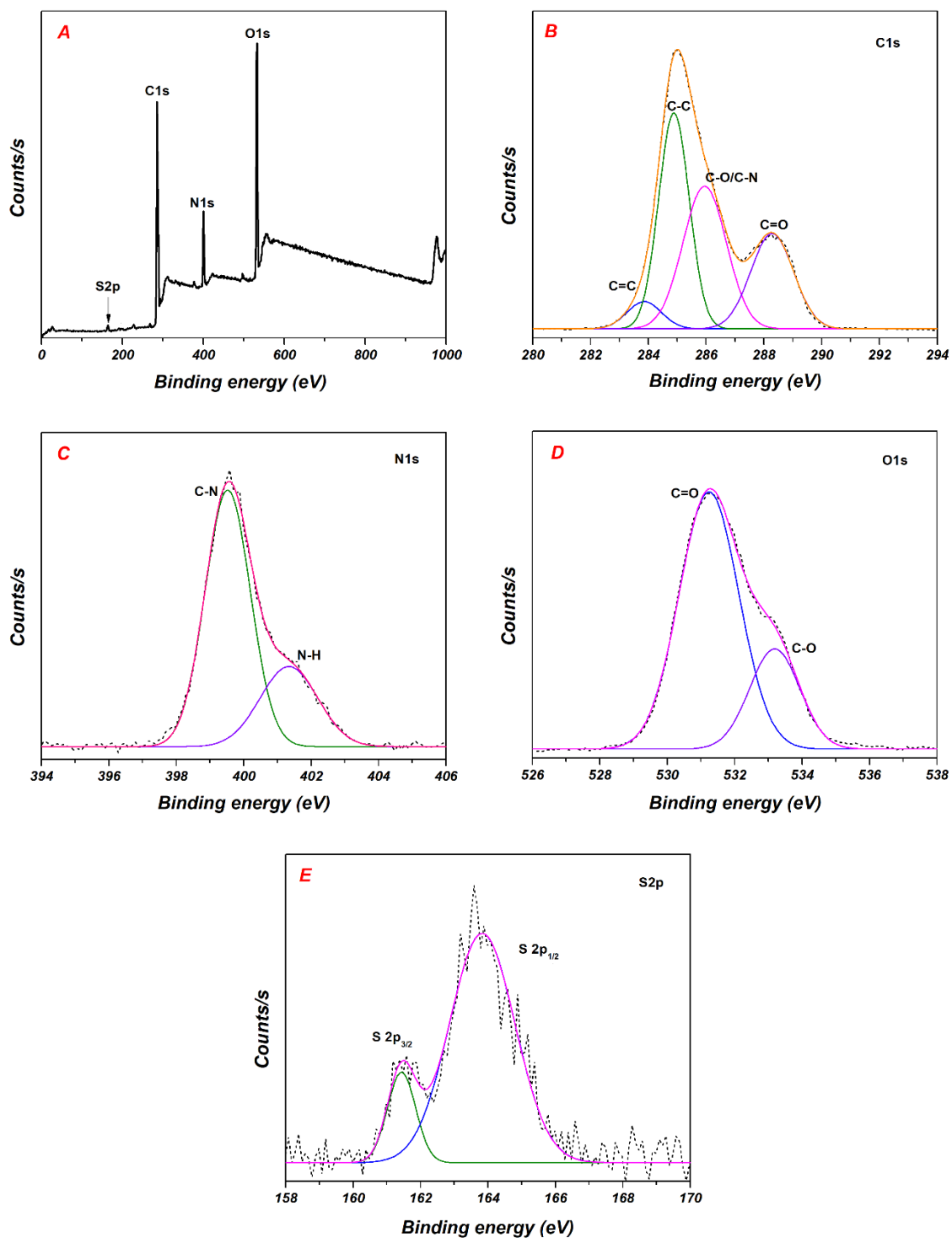


Figure 3.3. (A) XPS survey spectra of the GSH-NCDs. The high-resolution XPS spectra of (B) C 1s, (C) N 1s, (D) O 1s, and (E) S 2p of the GSH-NCDs.

3.3.2. Optical Characterization of the GSH-NCDs

As shown in Figure 3.4A, the UV-vis absorption spectra exhibited two distinct peaks at 264 and 334 nm, which were attributed to the π - π^* transition of the aromatic C=C bond and n - π^* transition of the C=O bond, respectively [44]. The GSH-NCDs aqueous solution exhibited a green hue under daylight lamp illumination, and emitted a blue fluorescence under UV illumination ($\lambda = 365$ nm), as shown in Figure 3.1. While excited at 355 nm, the GSH-NCDs revealed strong blue fluorescence, with a maximum PL emission wavelength at 440 nm. The fluorescence excitation spectra of the GSH-NCDs, with exciting at 440 nm, showed a peak at approximately 355 nm. When the excitation wavelength was changed from 300 to 430 nm, the PL emission spectra revealed the excitation wavelength-independent phenomenon, the PL emission peak was nearly no shift with excitation wavelength increasing, as shown in Figure 3.4B [51]. The quantum yield (QY) of the GSH-NCDs was obtained to be 11.25 % when quinine sulfate (QS) in aqueous H₂SO₄ (0.1 M) was used as the reference (Figure 3.5). The stability of the GSH-NCDs was also checked for over 2 months, and the PL intensities showed no significant change (Figure 3.6), which indicates the good stability of the GSH-NCDs. Furthermore, in order to check the stability of the GSH-NCDs under high ionic concentration conditions, the PL emission spectra of the GSH-NCDs were carried out in different concentrations of NaCl solutions. The result revealed that no obvious changes of the fluorescent property of the GSH-NCDs (Figure 3.7), suggesting the substantial stability of the GSH-NCDs under high ionic concentration condition.

The effects of pH on the PL emission intensities and UV-vis absorption of the GSH-NCDs were examined. Figure 3.8 shows that the GSH-NCDs exhibited lower PL intensities at lower pH solutions, and the intensities were enhanced with the pH range of 2–6; but with further increase in pH of the medium, there was no change in the fluorescence intensity of the GSH-NCDs. The UV-vis absorption peak was observed to be increased with increasing the pH, which further supported the changes in the PL emission intensities. This phenomenon might be attributed to the aggregation of the GSH-NCDs, which was caused by the protonation of carboxyl and amide groups at low solution pH [52]. The result revealed that the GSH-NCDs were stable at mild acidic and alkaline conditions, and sensitive towards the strong acidic solutions.

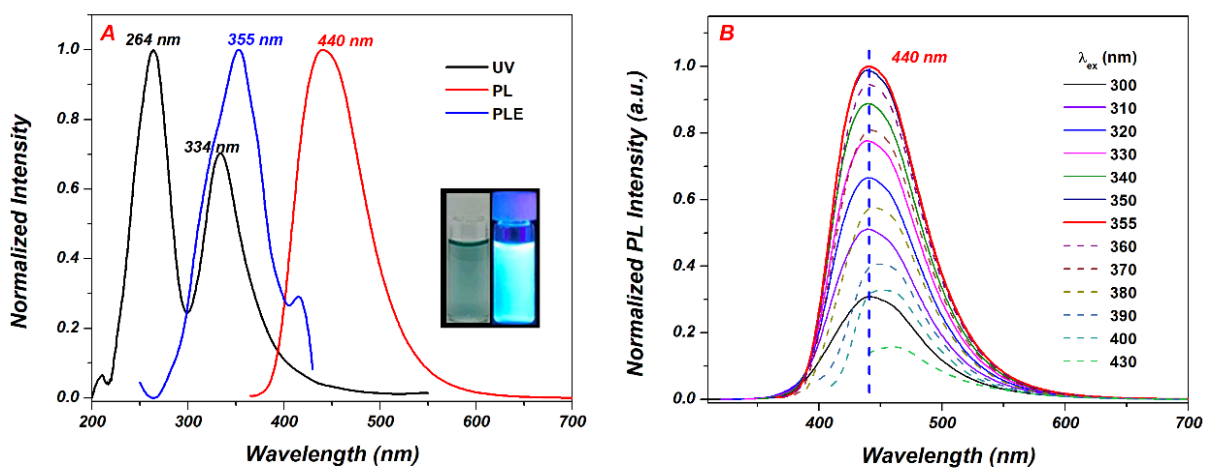


Figure 3.4. (A) The UV-vis absorption (UV), emission (PL), and excitation (PLE) spectra of the GSH-NCDs in the aqueous solution (Inset: the photographs of the GSH-NCDs under daylight lamp (left) and UV light ($\lambda=365$ nm) (right) illumination.). (B) Emission spectra of the GSH-NCDs at different excitation wavelength.

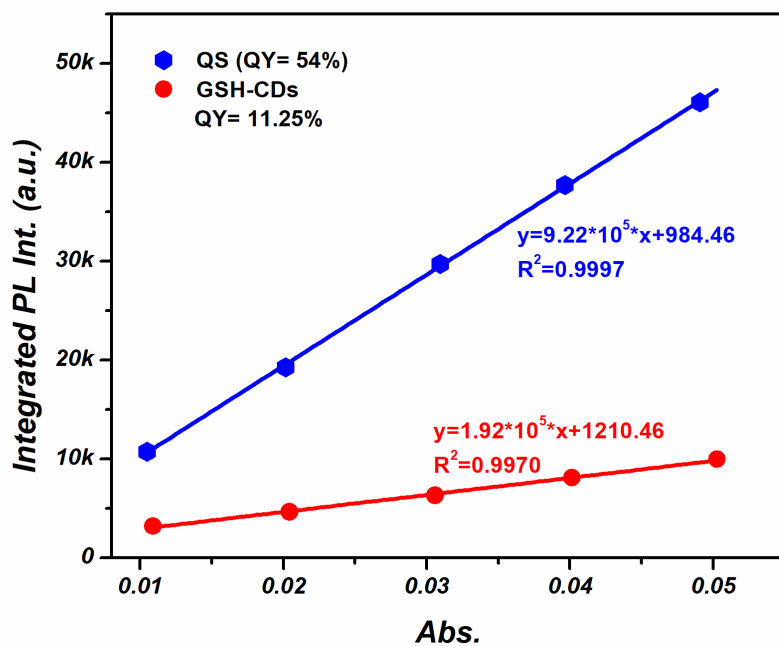


Figure 3.5. QY of GSH-NCDs use the QS as the reference.

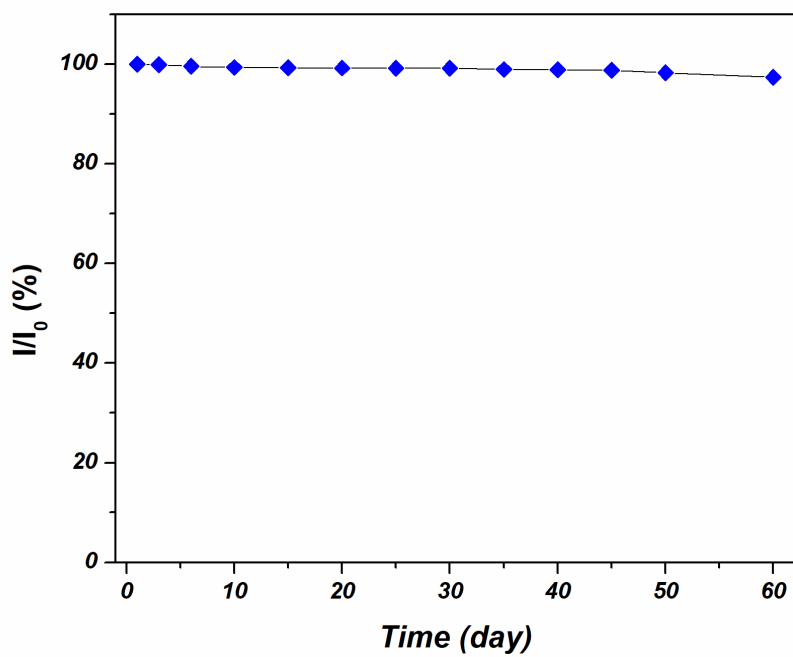


Figure 3.6. Stability of GSH-NCDs with the relative PL intensity.

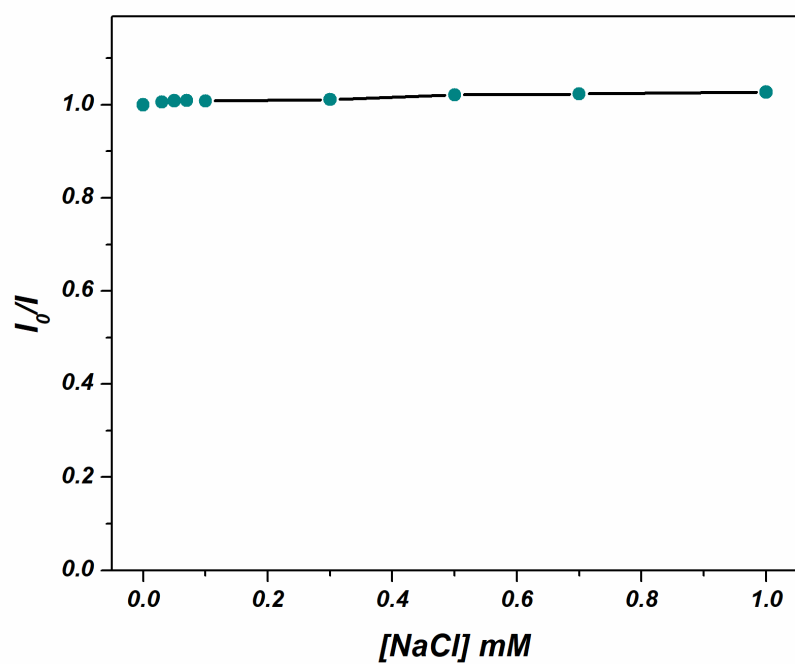


Figure 3.7. Effect of different concentrations of NaCl solutions on the emission of GSH-NCDs.

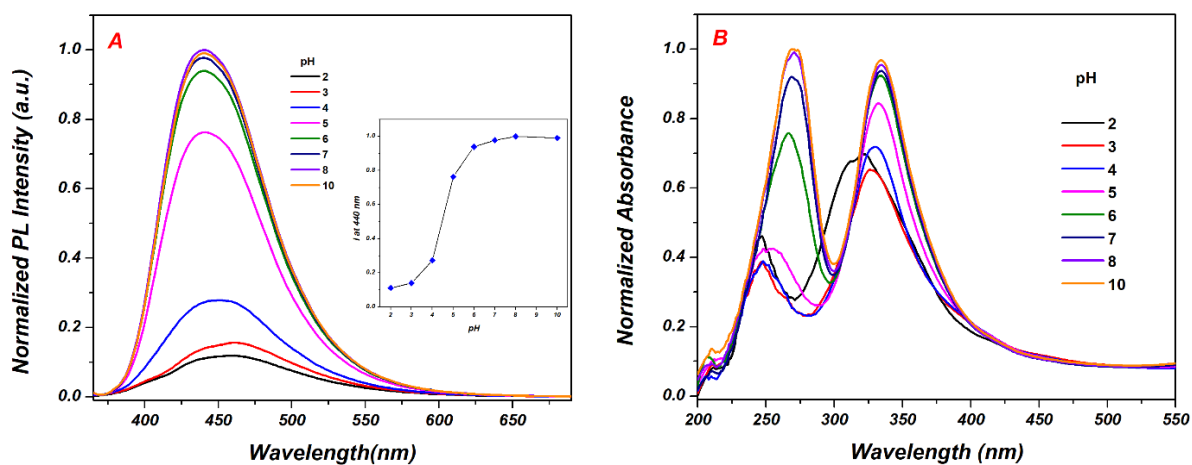


Figure 3.8. (A) PL emission and (B) absorption spectra of GSH-NCDs at different pH solutions.

3.3.3. Effect of biomolecules on the fluorescence of the GSH-NCDs

The individual effect of co-existing biomolecules [ascorbic acid (AA), dopamine (DA), citric acid (CA), uric acid (UA), fructose (Fru), glucose (Glu), L-cysteine (Cys), sucrose (Suc), DL-Homocysteine (Hcy), L-tyrosine (Tyr), Urea, creatine monohydrate (Creat), and creatinine (Cre)] on the fluorescence of the GSH-NCDs was examined in phosphate buffer solution (pH = 7.4) at RT. Figure 3.9A shows that DA selectively causes quenching of GSH-NCDs fluorescence. The UV-vis absorption spectra of the GSH-NCDs in the presence of different biomolecules were also recorded (Figure 3.9B). The absorption peaks of the GSH-NCDs at 264 and 334 nm were found to be slightly shifted in the presence of AA and DA. The shift can be illustrated by the individual absorbance of AA and DA in the aqueous solutions [26, 53]. The selective DA induced fluorescence quenching of the GSH-NCDs was used for selective dopamine sensing.

The fluorescence quenching of the GSH-NCDs was devoted to the quantitative determination of DA, which was carried out in pH 7.4 phosphate buffer solution. Figure 3.10 shows the spectrum, which reveals that with the gradual addition to the DA concentration, the emission intensities of the GSH-NCDs were quenched. The relative PL emission intensity (I_0/I) at the wavelength of 440 nm was measured as a correlation function of the DA concentration ([DA]), and the concentration range of [DA] was 0-1.0 mM. The fluorescence quenching [54] of the GSH-NCDs was depicted by using the Stern-Volmer plot, as follows:

$$I_0/I = 1 + K_{SV}[Q] \quad (3-1)$$

where, K_{SV} is the Stern-Volmer constant, and Q is the quencher in equation. In the plot, a linear relationship was obtained from the relative PL emission intensity (I_0/I) and the DA concentration ([DA]). The good linear detection ranges from 20 nM to 10 μ M ($R^2 = 0.992$)

was observed with a very low limit of detection (LOD) of 1.01 nM (S/N = 3:1). This indicates the sensitive detection of DA by the GSH-NCDs. Compared to other previous studies (Table 3.1), our presented work showed an impressive limit detection.

The effects of DA on the fluorescence of the GSH-NCDs was checked in various pH conditions. Figure 3.11 shows that with increasing pH, the PL intensity of the GSH-NCDs decreased gradually in the presence of DA. Since the aggregation of GSH-NCDs are affected by protonation of its functional groups at different pH, its fluorescence and absorption spectra get modified at different pH. In Figure 3.11, it is observed that only at pH = 6, AA and CA caused quenching in GSH-NCDs fluorescence. Although the extent of quenching is not significant compared to DA, the quenching can be explained through facile interaction between GSH-NCDs and the molecules. Again, with the increase in medium pH, the extent of DA-induced quenching increased due to change in redox condition of DA that improved the IFE. All DA sensing experiments were conducted at pH 7.4 phosphate buffered saline solution, to mimic the typical biological system.

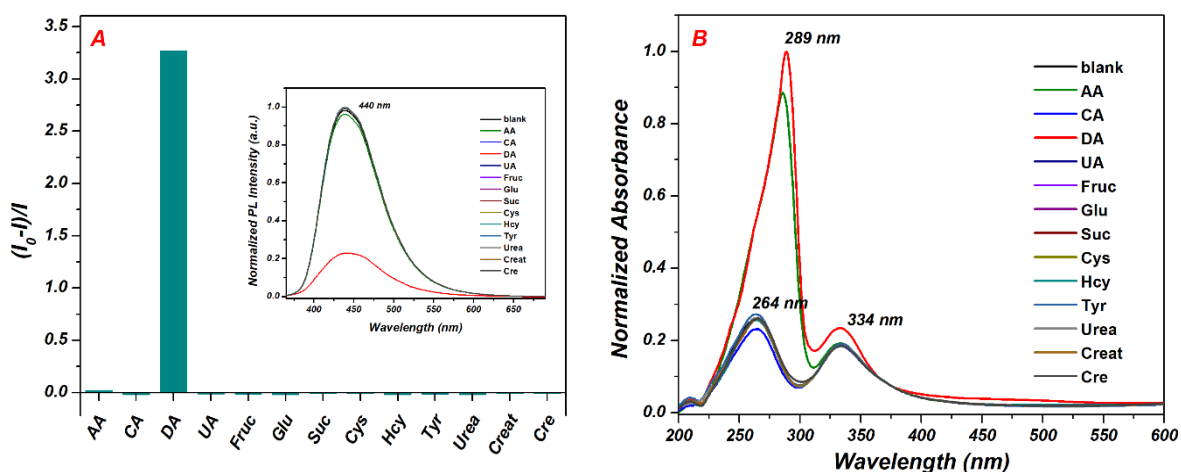


Figure 3.9. (A) The relative PL emission intensities, and (B) absorbance spectra of the GSH-NCDs in different biomolecules. (Inset: the PL emission intensities spectra of the GSH-NCDs in different biomolecules.) $\lambda_{\text{ex}} = 355 \text{ nm}$, $[\text{GSH-NCDs}] = 0.1 \text{ mg/mL}$, $[\text{biomolecules}] = 1 \times 10^{-3} \text{ M}$, where I_0 and I show the PL emission intensity of the GSH-NCDs in the absence and presence of biomolecules, respectively.

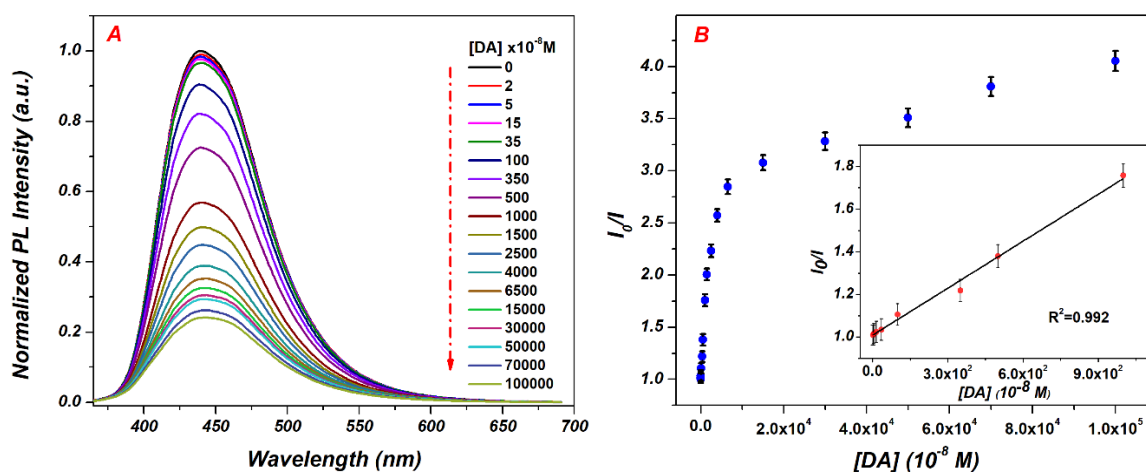


Figure 3.10. (A) The variation of the PL emission intensities of the GSH-NCDs with the gradually addition of DA. (B) The relative PL emission intensities (I_0/I) of the GSH-NCDs vs $[\text{DA}]$. Inset (B): the linear relationship of the relative PL emission intensity on $[\text{DA}]$. I_0 is the PL emission intensity of the GSH-NCDs, and I denote the PL emission intensities of the GSH-NCDs in the presence of DA with different concentrations.

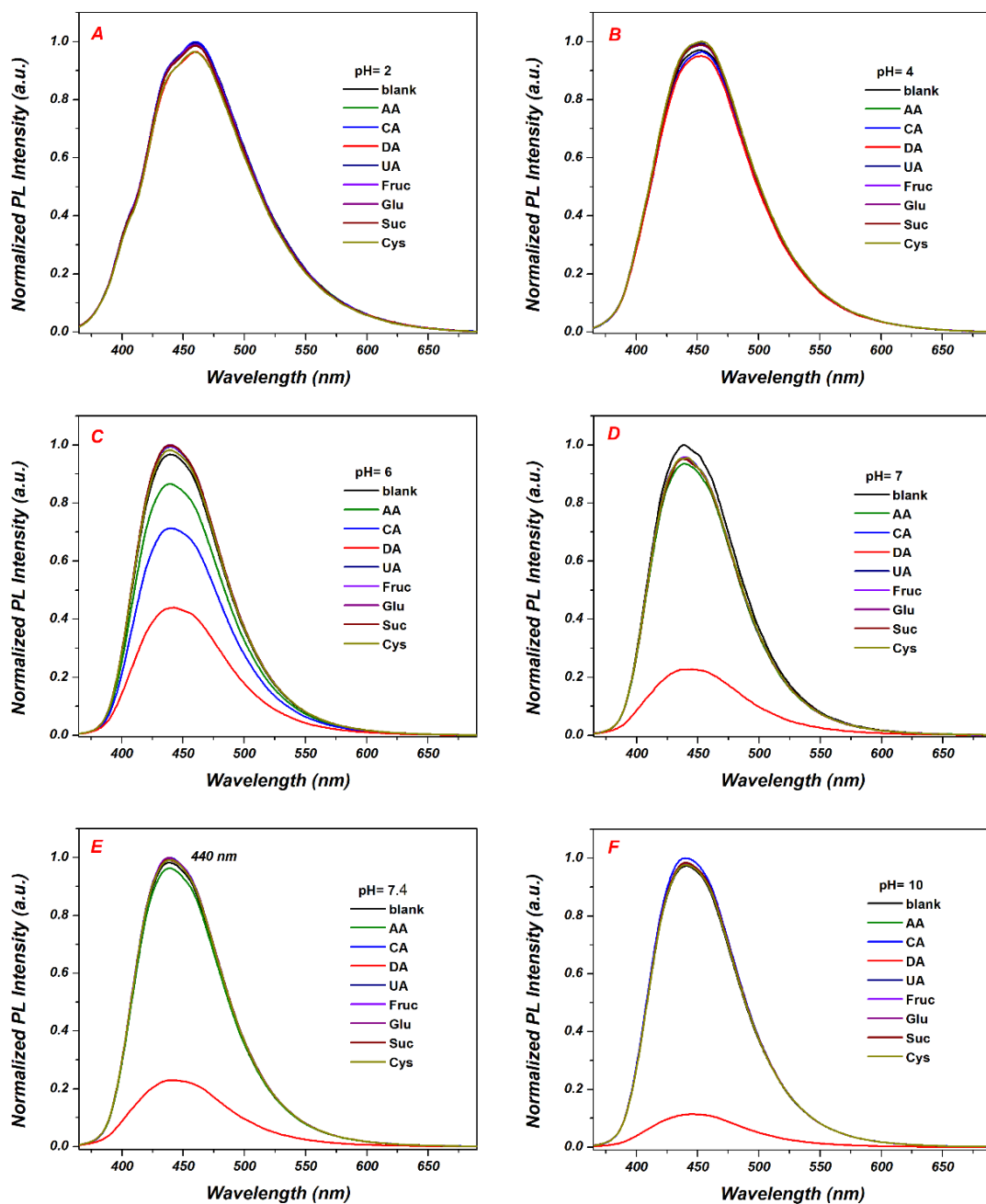


Figure 3.11. PL spectra of GSH-NCDs in the presence of biomolecules at different pH solutions. (A) pH = 2, (B) pH = 4, (C) pH = 6, (D) pH = 7, (E) pH = 7.4 and (F) pH = 10.

3.3.4. The study on interference for DA sensing

The interference study was performed for DA detection in the presence of equimolar biomolecules and ions [AA, CA, UA, Fru, Glu, Suc, Cys, Hcy, Tyr, Urea, Creat, Cre, K(I), and Na(I)] in phosphate buffer solution (pH = 7.4) at RT. As observed from Figure 3.12 the compounds did not cause any significant change in the spectral profile of GSH-NCDs-DA system. Interestingly, AA and UA also did not show any interference despite of possessing similar electrochemical properties as DA. This overcomes the interference related limitation of electrochemical detection process for DA and provides a selective as well as sensitive platform for DA detection in aqueous medium.

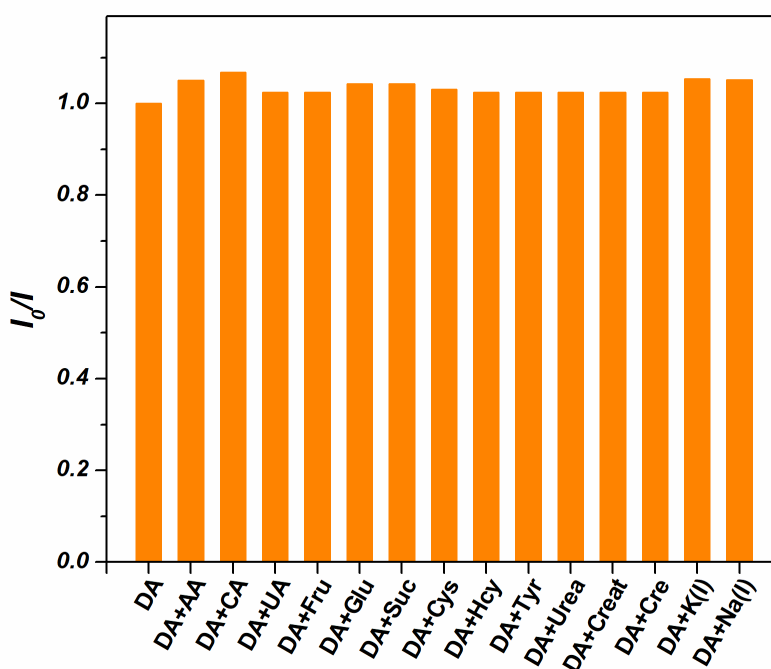


Figure 3.12. The relative PL emission intensities of the GSH-NCDs-DA system with addition of other molecules. [GSH-NCDs] = 0.1 mg/mL, [DA and other molecules] = 1.0×10^{-3} M.

3.3.5. Fluorescence quenching mechanism of the GSH-NCDs

The interaction between GSH-NCDs and DA can be understood through evaluation of the zeta potential. The zeta potential values of the GSH-NCDs in absence and presence of DA were calculated to be -18.3 and -7.35 mV, respectively (Figure 3.13). The obvious change of the zeta potential values shows that the strong electrostatic interaction between GSH-NCDs and DA [55]. For further confirmation, the FTIR spectrum of GSH-NCDs and GSH-NCDs-DA were compared. As observed in Figure 3.14, the position and intensities of $-OH$ and $-NH_2$ peaks of GSH-NCDs-DA were changed. This indicated an interaction within GSH-NCDs and DA molecules [56].

The significant fluorescence quenching of GSH-NCDs by DA was mainly attributed to the interaction between functional groups of the GSH, present at the surface of GSH-NCDs, and DA through hydrogen bonding leading to the energy transfer within GSH-NCDs-DA system [57]. For further understanding of the quenching mechanism, the fluorescence lifetimes of GSH-NCDs were measured in absence and presence of DA. Figure 3.15 shows that the fluorescence decay profile did not change significantly. The average lifetime values were calculated to be 7.76 ns for GSH-NCDs and 7.60 ns for GSH-NCDs-DA. The lifetime values indicated static type quenching of GSH-NCDs in presence of DA. The overlap between absorbance spectrum of acceptor, DA and excitation spectrum of donor, GSH-NCDs (Figure 3.16A) and the insignificant change in lifetime value of GSH-NCDs in presence of DA indicated possibility of photoinduced electron transfer (PET) assisted inner filter effect (IFE) within the system [58]. Also, the unmodified absorption spectra of GSH-NCDs in presence of DA (Figure 3.16B) ruled out the possibility of formation of ground state complexation. Hence, it can be concluded that the quenching phenomenon possibly follows IFE/PET process (Figure 3.17).

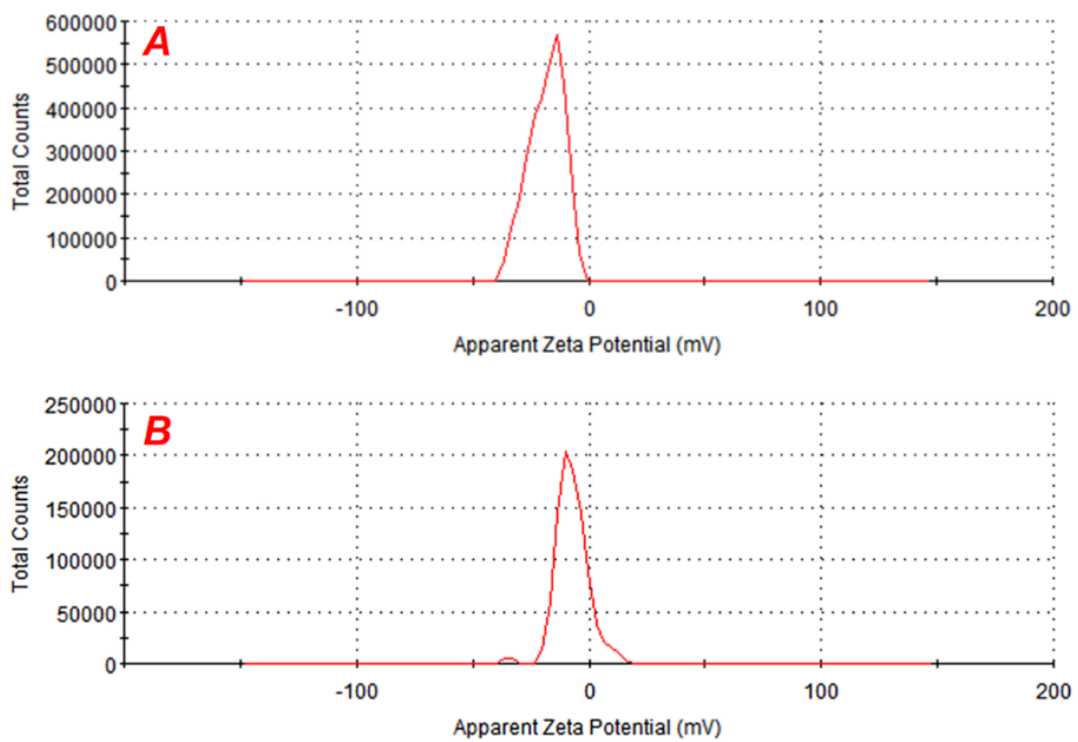


Figure 3.13. The zeta potential values for (A) GSH-CDs and (B) GSH-CDs -DA (in the presence of DA).

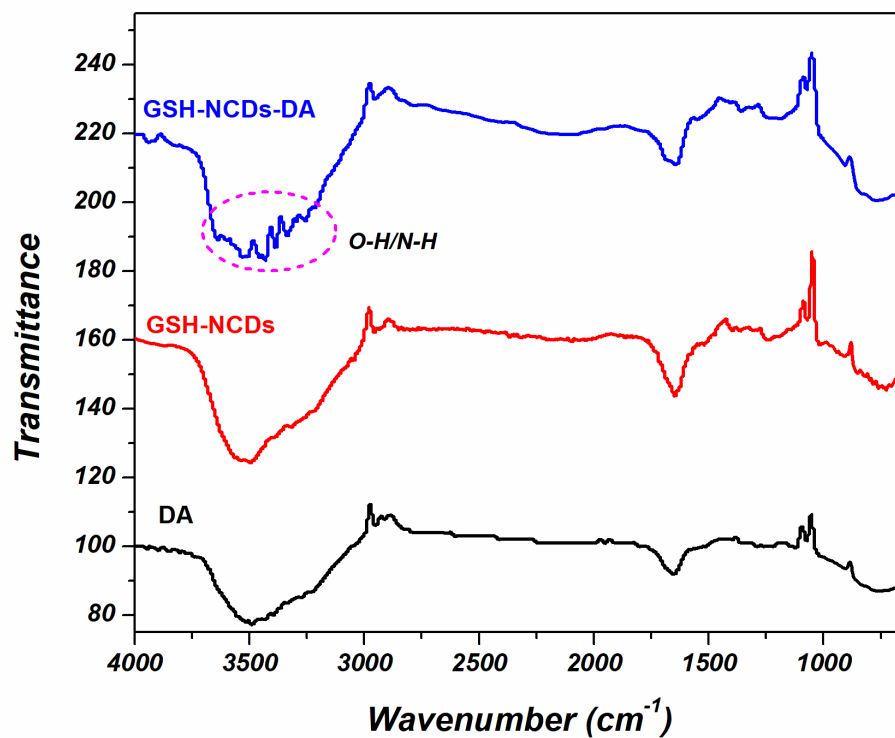


Figure 3.14. The FTIR spectra of DA, GSH-NCDs and GSH-NCDs-DA.

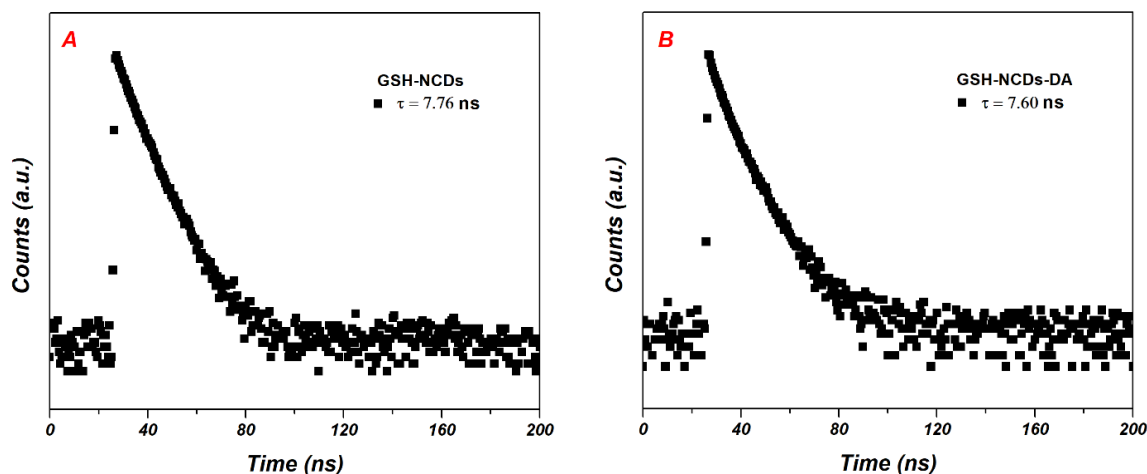


Figure 3.15. Time-resolved fluorescence decay curves of GSH-NCDs (A) and GSH-NCDs-DA (B) excited at 375 nm with the emission peak at 440 nm. [GSH-NCDs] = 0.1 mg/mL, [DA] = 1×10^{-3} M.

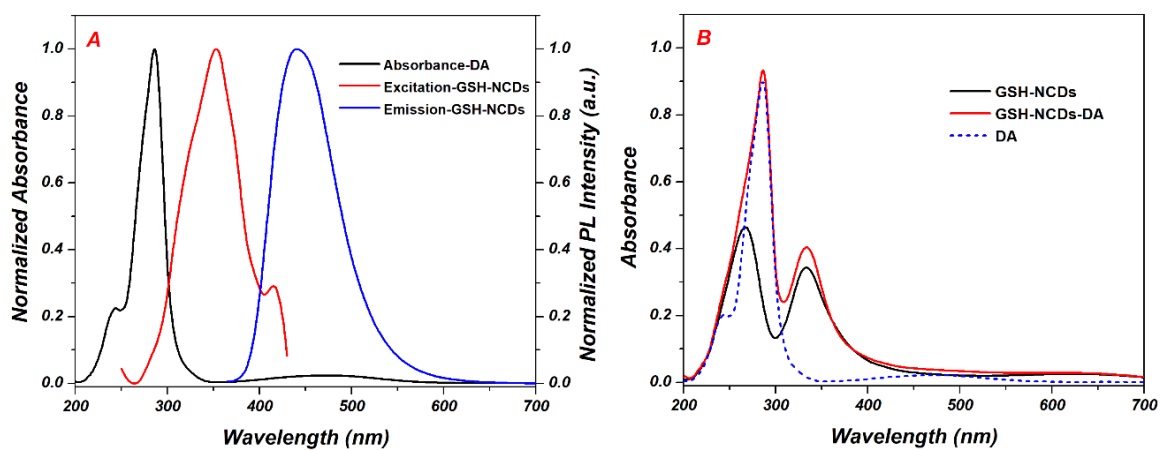


Figure 3.16. (A) Normalized UV–vis spectrum of DA overlap with normalized emission and excitation spectra of GSH-NCDs in the aqueous solution. (B) UV–visible spectra of GSH-NCDs in the absence and presence of 1 mM DA.

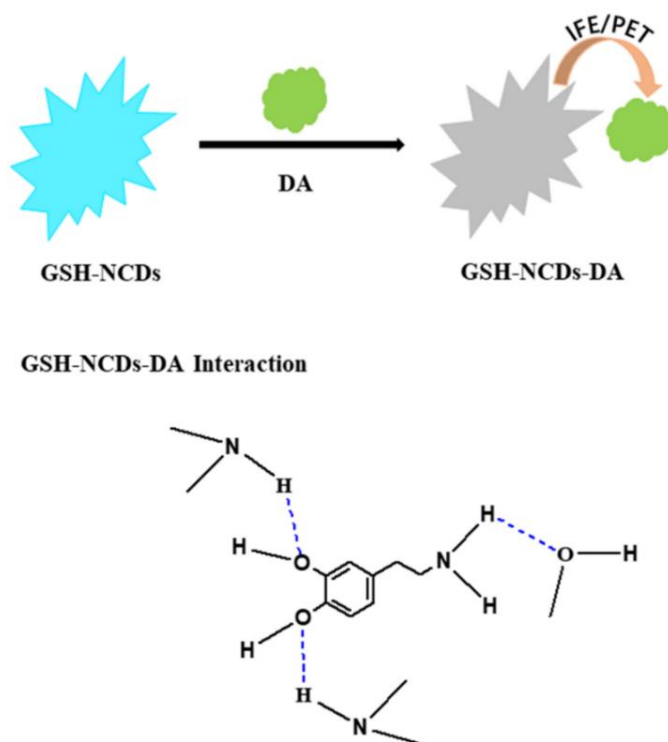


Figure 3.17. Schematic of the interaction between DA and the GSH-NCDs.

3.3.6. Analysis of DA in real samples

To evaluate the feasibility of GSH-NCDs in detecting the DA concentration in real samples, the measures are performed using human urine, in which the DA concentration were known. The human urine sample diluted 100-fold was spiked with 25 μM , 100 μM , and 200 μM of DA. Table 3.2 shows that good recovery results of DA in real urine samples were observed. Hence, the proposed GSH-NCDs fluorescent sensing system may well have practicability and reliability for DA determination in biological samples.

Table 3.2. Detection of DA in real urine samples.

Samples	Added (μM)	Found (μM)	Recovery (%)	RSD (%)
I	25	24.91	99.6	1.30
		25.43	101.7	
		25.50	102.0	
II	100	100.29	100.3	1.46
		101.45	101.5	
		103.19	103.2	
III	200	199.52	99.8	1.14
		200.60	100.3	
		203.89	101.9	

3.4. Conclusion

The designed GSH-modified N-doped carbon dots showed good selectivity and sensitivity for DA detection. The GSH-modified NCDs showed selective quenching in the presence of DA. The quenching can be attributed to the GSH-DA electrostatic interaction on the GSH-NCDs surface. The linear ranges of detection from 20 nM to 10 μ M with a very low detection limit of 1.01 nM, with excellent selectivity and stability. The synthesized GSH-NCDs were also very effective for real sample analysis using human urine.

References

- [1] Y. Yang, W. Li. *Biosensors and Bioelectronics*, 2014, 56, 300-306.
- [2] A. Numan, M. M. Shahid, F. S. Omar, K. Ramesh, S. Ramesh. *Sensors and Actuators B: Chemical*, 2017, 238, 1043-1051.
- [3] M. Baranyi, E. Milusheva, E. S. Vizi, B. Sperlágh. *Journal of Chromatography A*, 2006, 1120, 13-20.
- [4] C. W. Christine, M. J. Aminoff. *The American Journal of Medicine*, 2004, 117, 412-419.
- [5] L. Wu, L. Feng, J. Ren, X. Qu. *Biosensors and Bioelectronics*, 2012, 34, 57-62.
- [6] M. L. Huffman, B. J. Venton. *Analyst*, 2009, 134, 18-24.
- [7] J. Chen, X. Yan, K. Meng, S. Wang. *Analytical Chemistry*, 2011, 83, 8787-8793.
- [8] K. T. Ngo, E. L. Varner, A. C. Michael, S. G. Weber. *ACS Chemical Neuroscience*, 2017, 8, 329-338.
- [9] K. Syslová, L. Rambousek, M. Kuzma, V. Najmanová, V. Bubeníková-Valešová, R. Šlamberová, P. Kačer. *Journal of Chromatography A*, 2011, 1218, 3382-3391.
- [10] L. Jiang, G. W. Nelson, J. Abda, J. S. Foord. *ACS Appl Mater Interfaces*, 2016, 8, 28338-28348.
- [11] C. Zhang, J. Ren, J. Zhou, M. Cui, N. Li, B. Han, Q. Chen. *Analyst*, 2018, 143, 3075-3084.
- [12] H. Zou, B. Li, H. Luo, N. Li. *Sensors and Actuators B: Chemical*, 2015, 207, 535-541.

- [13] X. Qing, Y. Wang, Y. Zhang, X. Ding, W. Zhong, D. Wang, W. Wang, Q. Liu, K. Liu, M. Li, Z. Lu. *ACS Appl Mater Interfaces*, 2019, 11, 13105-13113.
- [14] S. Wang, M. Sun, Y. Zhang, H. Du, L. He. *Journal of Chromatography A*, 2010, 1217, 5246-5252.
- [15] E. Sánchez-López, C. Montealegre, A. L. Crego, M. L. Marina. *TrAC Trends in Analytical Chemistry*, 2015, 67, 82-99.
- [16] Y. Liu, Q. Yao, X. Zhang, M. Li, A. Zhu, G. Shi. *Biosensors and Bioelectronics*, 2015, 63, 262-268.
- [17] R. Cui, Y. Gu, L. Bao, J. Zhao, B. Qi, Z. Zhang, Z. Xie, D. Pang. *Anal Chem*, 2012, 84, 8932-8935.
- [18] A. Joshi, W. Schuhmann, T. C. Nagaiah. *Sensors and Actuators B: Chemical*, 2016, 230, 544-555.
- [19] L. Liu, S. Li, L. Liu, D. Deng, N. Xia. *Analyst*, 2012, 137, 3794-3799.
- [20] J. Zhu, X. Peng, W. Nie, Y. Wang, J. Gao, W. Wen, J. N. Selvaraj, X. Zhang, S. Wang. *Biosensors and Bioelectronics*, 2019, 141, 111450.
- [21] J. Zhao, L. Zhao, C. Lan, S. Zhao. *Sensors and Actuators B: Chemical*, 2016, 223, 246-251.
- [22] S. Zhuo, Y. Guan, H. Li, J. Fang, P. Zhang, J. Du, C. Zhu. *Analyst*, 2019, 144, 656-662.
- [23] S. K. Tammina, D. Yang, S. Koppala, C. Cheng, Y. Yang. *Journal of Photochemistry and Photobiology B: Biology*, 2019, 194, 61-70.
- [24] S. Yang, X. Sun, Z. Wang, X. Wang, G. Guo, Q. Pu. *Sensors and Actuators B: Chemical*, 2017, 253, 752-758.
- [25] Y. Pang, Y. Shi, Y. Pan, Y. Yang, Y. Long, H. Zheng. *Sensors and Actuators B: Chemical*, 2018, 263, 177-182.
- [26] J. Jana, J. S. Chung, S. H. Hur. *ACS Omega*, 2019, 4, 17031-17038.
- [27] Y. Ma, A. Y. Chen, X. F. Xie, X. Y. Wang, D. Wang, P. Wang, H. J. Li, J. H. Yang, Y. Li. *Talanta*, 2019, 196, 563-571.

- [28] Y. Dong, R. Wang, H. Li, J. Shao, Y. Chi, X. Lin, G. Chen. *Carbon*, 2012, 50, 2810-2815.
- [29] L. Xiao, H. Sun. *Nanoscale Horiz*, 2018, 3, 565-597.
- [30] Y. Yang, J. Cui, M. Zheng, C. Hu, S. Tan, Y. Xiao, Q. Yang, Y. Liu. *Chem Commun*, 2012, 48, 380-382.
- [31] L. Wang, J. S. Chung, S. H. Hur. *Dyes and Pigments*, 2019, 171, 107752.
- [32] S. Das, N. Debnath, Y. Cui, J. Unrine, S. R. Palli. *ACS Appl Mater Interfaces*, 2015, 7, 19530-19535.
- [33] S. Wang, Z. Chen, I. Cole, Q. Li. *Carbon*, 2015, 82, 304-313.
- [34] W. Wei, C. Xu, J. Ren, B. Xu, X. Qu. *Chem Commun*, 2012, 48, 1284-1286.
- [35] S. Y. Lim, W. Shen, Z. Gao. *Chem Soc Rev*, 2015, 44, 362-381.
- [36] Q. Huang, X. Lin, C. Lin, Y. Zhang, S. Hu, C. Wei. *RSC Adv*, 2015, 5, 54102-54108.
- [37] T. S. Atabaev. *Nanomaterials*, 2018, 8, 342.
- [38] M. Park, H. Yoon, J. Lee, J. Kim, J. Lee, S. E. Lee, S. Yoo, S. Jeon. *Advanced Materials*, 2018, 30, 1802951.
- [39] H. Yoon, K. Lee, H. Kim, M. Park, T. G. Novak, G. Hyun, M. S. Jeong, S. Jeon. *Advanced Sustainable Systems*, 2019, 3, 1900084.
- [40] L. Kong, H. L. Wong, A. Y. Y. Tam, W. H. Lam, L. Wu, V. W. W. Yam. *ACS Appl Mater Interfaces*, 2014, 6, 1550-1562.
- [41] X. Zeng, L. Zhang, J. Yang, Y. Guo, Y. Huang, H. Yuan, Y. Xie. *New J Chem*, 2017, 41, 15216-15228.
- [42] O. Zitka, S. Skalickova, J. Gumulec, M. Masarik, V. Adam, J. Hubalek, L. Trnkova, J. Kruseova, T. Eckschlager, R. Kizek. *Oncol Lett*, 2012, 4, 1247-1253.
- [43] C. Wang, Y. Huang, H. Lin, Z. Xu, J. Wu, M. G. Humphrey, C. Zhang. *RSC Adv*, 2015, 5, 61586-61592.
- [44] C. Wang, K. Jiang, Z. Xu, H. Lin, C. Zhang. *Inorg Chem Front*, 2016, 3, 514-522.

- [45] L. Kong, X. Chu, X. Ling, G. Ma, Y. Yao, Y. Meng, W. Liu. *Microchimica Acta*, 2016, 183, 2185-2195.
- [46] L. Kong, K. Lu, X. Ling, P. Zhu, W. Liu, H. Guan, C. Wang. *Chemistry Select*, 2016, 1, 4092-4100.
- [47] H. Fu, Z. Ji, X. Chen, A. Cheng, S. Liu, P. Gong, G. Li, G. Chen, Z. Sun, X. Zhao, F. Cheng, J. You. *Analytical and Bioanalytical Chemistry*, 2017, 409, 2373-2382.
- [48] C. Wang, Z. Xu, H. Cheng, H. Lin, M. G. Humphrey, C. Zhang. *Carbon*, 2015, 82, 87-95.
- [49] S. H. Ribut, C. A. C. Abdullah, M. Mustafa, M. Z. M. Yusoff, S. N. A. Azman. *Materials Research Express*, 2014, 6, 025018.
- [50] X. Cui, J. Wang, B. Liu, S. Ling, R. Long, Y. Xiong. *J Am Chem Soc*, 2018, 140, 16514-16520.
- [51] X. Zhu, X. Xiao, X. Zuo, Y. Liang, J. Nan. *Particle & Particle Systems Characterization*, 2014, 31, 801-809.
- [52] D. Zhong, H. Miao, K. Yang, X. Yang. *Materials Letters*, 2016, 166, 89-92.
- [53] J. Lin, C. Yu, Y. Yang, W. Tseng. *Phys Chem Chem Phys*, 2015, 17, 15124-15130.
- [54] R. J. Campbell, E. W. Schlag, B. W. Ristow. *J Am Chem Soc*, 1967, 89, 5098-5102.
- [55] X. Zhou, P. Ma, A. Wang, C. Yu, T. Qian, S. Wu, J. Shen. *Biosensors and Bioelectronics*, 2015, 64, 404-410.
- [56] R. Rajamanikandan, M. Ilanchelian. *New J Chem*, 2017, 41, 15244-15250.
- [57] L. Chang, X. He, L. Chen, Y. Zhang. *Nanoscale*, 2017, 9, 3881-3888.
- [58] A. S. Tanwar, L. R. Adil, M. A. Afroz, P. K. Iyer. *ACS sensors*, 2018, 3, 1451-1461.

CHAPTER 4. Multicolor emitting N-doped carbon dots derived from ascorbic acid and phenylenediamine precursors

4.1. Introduction

Recently fluorescent carbon dots (CDs) have drawn considerable attention owing to their high quantum yields, low toxicity, excellent biocompatibility, and facile preparation procedures [1-4]. CDs can be widely used in sensing, display, and bioimaging applications. Most of CDs emit in blue or green region that limits their application in living tissue imaging since this process needs deep penetration of light and removal of autofluorescence as well as background light scattering related limitations. Henceforth, synthesis of CDs that emit at larger wavelength has become important. In this regard, green chemical synthesis of multi-color emissive CDs is important that would exclude the associated synthetic hazards and critical separation steps [5].

Adjusting the surface of CDs by doping of hetero atoms, such as nitrogen (N), boron (B), and sulfur (S) atoms, can be used to modify the fluorescence properties of CDs. For this purpose, organic/inorganic molecules with hetero-atom functionalities might be used as co-precursor along with the carbon source or as precursor [6-8]. Phenylenediamine isomers [o-phenylenediamine (o-PDA), m-phenylenediamine (m-PDA), and p-phenylenediamine (p-PDA)], with amine (-NH₂) functionalities, have proved to be efficient heteroatom source for synthesis of N-doped CDs [3, 9, 10].

In this work, the green, blue, and orange color emitting N-doped CDs were successfully synthesized from hydrothermal treatment of ascorbic acid (AA) and individual m-PDA, o-PDA, and p-PDA, respectively (**Am-, Ao-, and Ap-CDs, respectively**). The effects of the reaction conditions and solvents, and pH of solution on the fluorescence properties of each type of CDs were systematically investigated. In particular, green color emitting CDs synthesized from ascorbic acid and m-PDA exhibited very high quantum yield (QY) in the ethanol solvent.

4.2. Experimental section

4.2.1. Materials

Ascorbic acid (AA), m-phenylenediamine (m-PDA), o-phenylenediamine (o-PDA), p-phenylenediamine (p-PDA), rhodamine 101, quinine sulfate (QS) and rhodamine B were purchased from Sigma-Aldrich Co. (USA). All chemicals were analytical grade reagents and used as purchased without further purification. The deionized water with a resistivity of 18.2 M Ω was used in all experiments.

4.2.2. Characterizations

The fluorescence of the samples was recorded using a Cary Eclipse fluorescence spectrophotometer (Agilent Technologies, USA) using a 1.0 cm quartz cuvette. The absorption study of the samples was performed with the help of a UV-Vis spectrometer (UV-Vis, SPECORD 210 PLUS, Analytik Jena, Germany). The analysis of functional groups was done using the Fourier Transform Infrared (FTIR, Nicolet iS5, Thermo Fisher Scientific, USA) spectroscopy. X-ray photoelectron spectroscopy (XPS, Thermo ESCALAB 250 Xi, Thermo Fisher Scientific, USA) using Al K α X-ray radiation (1486.6 eV) was used to determine the oxidation states of the constituent elements. X-ray diffraction (XRD, Rigaku D/MAZX 2500V/PC model, Japan) was carried out using Cu K α radiation (40 kV, 30 mA, $\lambda = 1.5415 \text{ \AA}$) at a scan rate of 2° min^{-1} over the 2θ range of $10\text{-}100^\circ$. The size and morphology of the as-synthesized particles were monitored by high-resolution transmission electron microscopy (HR-TEM, JEM-2100 F, JEOL, Japan, operating voltage 200 kV). Zeta potential measurements was carried out using Malvern Nano ZS instrument (Worcestershire, UK).

4.2.3. Synthesis of Am-, Ao-, and Ap-CDs

To prepare Am-CDs, ascorbic acid (0.1 M, 0.8 mL) and m-phenylenediamine (0.1 M, 0.8 mL) (ratio of AA: m-PDA = 1: 1) were added into 10.4 mL deionized water, and stirred for 5 min. Then, the mixture was transferred into a 50 mL Teflon-lined autoclave, and heated and maintained at 160°C for 6 h in an oven for further reaction. After cooling down to room

temperature (RT), the Am-CDs were collected after removing the suspended particles via centrifugation at 10,000 rpm for 20 min, and further purified by dialysis tube for 6 h to remove the residual chemicals. The as-obtained Am-CDs solution was stored at 4 °C for further characterization.

To prepare Ao-CDs and Ap-CDs, all experimental procedures were the same as those of Am-CDs, except for the precursor ratio. For Ao-CDs, ascorbic acid (0.1 M, 1.2 mL) and o-phenylenediamine (0.1 M, 0.8 mL) (ratio of AA: o-PDA = 3: 2) were used; and for Ap-CDs, ascorbic acid (0.1 M, 0.8 mL) and p-phenylenediamine (0.1 M, 0.4 mL) (ratio of AA: p-PDA = 2: 1) were used, respectively.

Figure 4.1 shows that the reaction temperature and the precursor ratio were optimized to obtain the highest fluorescence for each CDs.

Figure 4.2 shows that the emission intensity and wavelength of the as-synthesized CDs are totally different from those of the precursor materials. The overall comparison has been summarized in Table 4.1. It is interesting to note that green emitting Am-CDs can be obtained from cyan and blue emitting AA and m-PDA, while blue color emitting Ao-CDs can be obtained from cyan and yellow emitting AA and o-PDA, which indicates the new conjugated structure formed from the reaction between AA and PDAs.

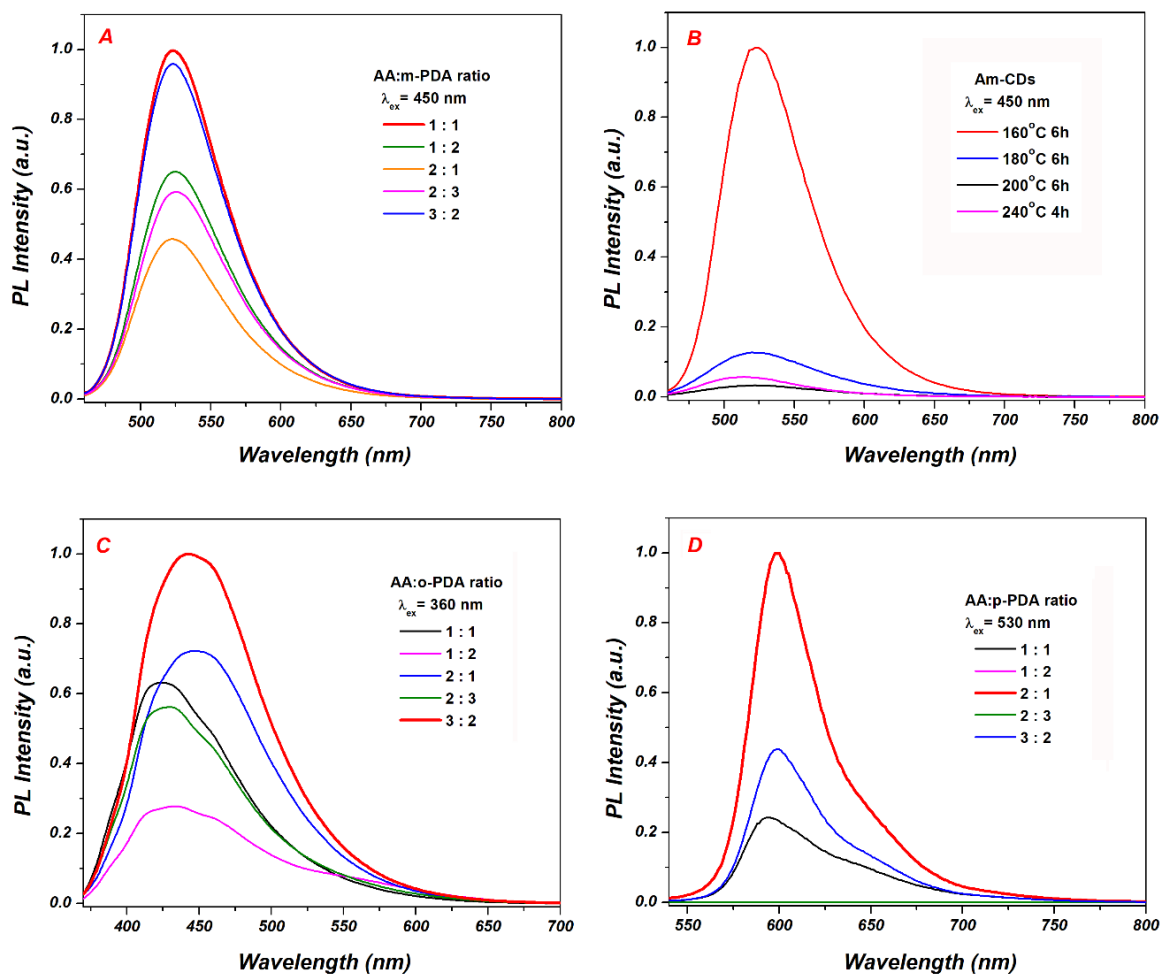


Figure 4.1. (A, B) Fluorescence spectra of Am-CDs at different ratio, and different reaction temperature and time from AA and m-PDA. (C) Fluorescence spectra of Ao-CDs at different ratio from AA and o-PDA. (D) Fluorescence spectra of Ap-CDs at different ratio from AA and p-PDA.

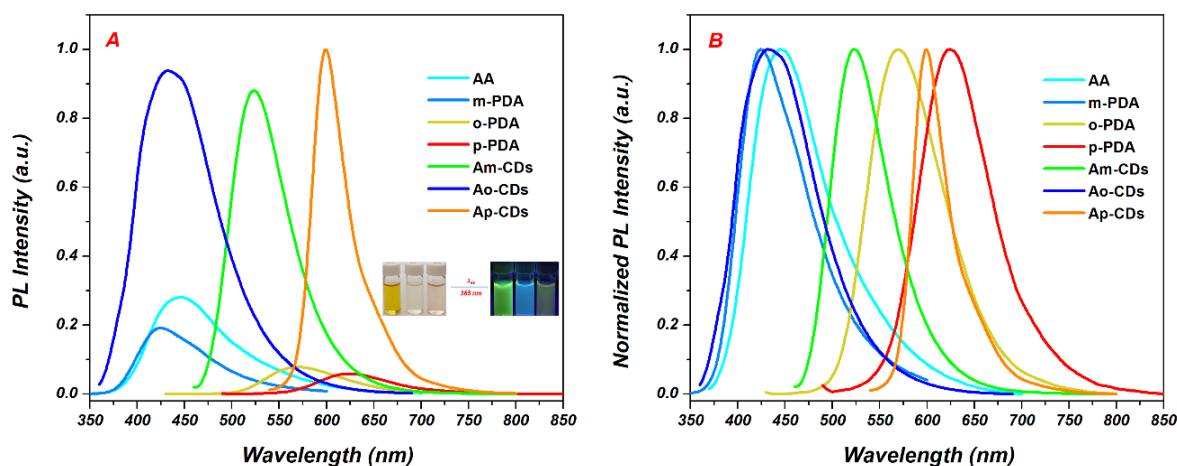


Figure 4.2. (A) Fluorescence spectra, and (B) normalized fluorescence spectra of Ax-CDs and various precursor materials. Inset: Photographs of Am-CDs, Ao-CDs, and Ap-CDs dispersed in water under natural light (left), and under UV irradiation ($\lambda_{\text{ex}} = 365 \text{ nm}$) (right).

Table 4.1. The excitation wavelength, emission peak wavelength and fluorescence color of different CDs.

CDs raw materials	$\lambda_{\text{ex}}/\text{nm}$	Emission peak/nm	Fluorescence color
AA	360	446	Blue
m-PDA	310	425	Blue
o-PDA	420	569	Yellow-green
p-PDA	480	624	Red
AA + m-PDA	450	524	Green
AA + o-PDA	360	432	Blue
AA + p-PDA	530	599	Orange

4.2.4. Quantum yield measurement

The quantum yields (QYs) of the Am-, Ao-, and Ap-CDs were obtained by a well-known relative slope method at RT using various dyes that match their emissions with those of each CDs [9]. For Am-CDs (excitation wavelength of 450 nm), Rhodamine 101 in ethanol (QY= 100 %) was selected as the reference; for Ao-CDs (excitation wavelength of 360 nm), quinine sulfate (QS) in 0.1 M sulfuric acid solution (QY= 54 %); and for Ap-CDs (excitation wavelength of 514 nm), rhodamine B in water (QY= 31 %).

To calculate the QYs, the integrated PL intensities of the sample and reference were plotted against absorbance at several concentrations, and the gradients were obtained and compared.

The QYs of the three CDs were obtained from the following equation:

$$\Phi_s = \Phi_r * \frac{K_s}{K_r} * \frac{\eta_s}{\eta_r} \quad (4-1)$$

where, Φ is the relative quantum yield, K is the slope of the fitted line, and η is the refractive index of the solvent. The subscript “r” refers to the reference, and “s” to the sample. The values of refractive index for water and ethanol are 1.33 and 1.36, respectively.

4.3. Results and discussions

4.3.1. Characterization of the as-synthesized CDs

The morphology and size of the Ax-CDs (x = m, o, and p) were analyzed from TEM images. Figures 4.3–4.5 show that the mean diameters of Am-CDs, Ao-CDs, and Ap-CDs were 3.39 nm, 3.65 nm, and 4.45 nm, respectively. The interplanar spacings of Ax-CDs were 0.23 nm, 0.21 nm, and 0.35 nm analyzed from HR-TEM images, respectively, which correspond to the (100) and (002) planes of graphite carbon [11].

The crystal structures of the Ax-CDs were investigated by XRD. Figure 4.6A shows that the three CDs have a broad single diffraction peak around $2\theta = 21\text{--}23^\circ$, which originates from graphitic carbon structure [3, 12].

The chemical bonds and surface functional groups of Ax-CDs were analyzed by FT-

IR spectra. Figure 4.6B shows the peaks at ~ 3460 and $\sim 3313\text{--}3353\text{ cm}^{-1}$ that can be attributed to the stretching vibrations of O–H and N–H, respectively. The presence of hydrophilic groups can improve the solubility of CDs in polar solvent by the formation of hydrogen bonding [13, 14]. The peaks at ~ 1070 , ~ 2877 and $\sim 2964\text{ cm}^{-1}$ can be assigned to the stretching vibrations of C–H [8]. The strong peak observed at $\sim 1633\text{ cm}^{-1}$ can be ascribed to the stretching vibration of C=O bond in the amide group, which confirms the amidation reaction between the carboxylic acids of AA and amines of PDAs [15]. The peaks that appear at $\sim 1520\text{ cm}^{-1}$ can originate from the bending vibration of C=C [16]. In addition, the peaks observed at $\sim 1361\text{ cm}^{-1}$ can be ascribed to the stretching vibration of C–N, which confirms the presence of nitrogen atom in the as-synthesized CDs [10]. The near identity of the FT-IR spectra of all three CDs indicates the presence of similar chemical bonds and functional groups on the CDs, regardless of the position of amine group in PDA isomers species.

XPS was used to analyze the elemental composition and functional groups of the Ax-CDs. Figure 4.7A shows the XPS survey spectrum of Am-CDs, which indicates the existence of C, O, and N atoms in the synthesized Am-CDs. Figures 4.8 and 4.9 show that the three CDs have similar elemental compositions, as summarized in Table 4.2. The XPS analyses also indicate similar oxidation state and functionalities in the three CDs. Figures 4.6–4.8 show the high-resolution C1s XPS spectra for Ax-CDs, which reveal that carbon can be deconvoluted into several peaks centered at ~ 284.0 , ~ 285.2 , ~ 286.9 , and $\sim 290.1\text{ eV}$, which correspond to C=C, C–C, C–O, and N–C=O groups, respectively. The high-resolution O1s spectra can be deconvoluted into peaks shown at ~ 531.8 and $\sim 532.8\text{ eV}$ that can be attributed to C=O and C–O groups, respectively [17]. The N1s spectra reveal the presence of N–H, C–N–C, and graphitic N groups shown at ~ 399.0 , ~ 400.0 , and $\sim 401.4\text{ eV}$, respectively [18].

Table 4.2. The elemental compositions of Ax-CDs.

Sample	C (%)	O (%)	N (%)
Am-CDs	70.23	18.50	11.27
Ao-CDs	69.30	21.85	8.85
Ap-CDs	70.63	20.28	9.09

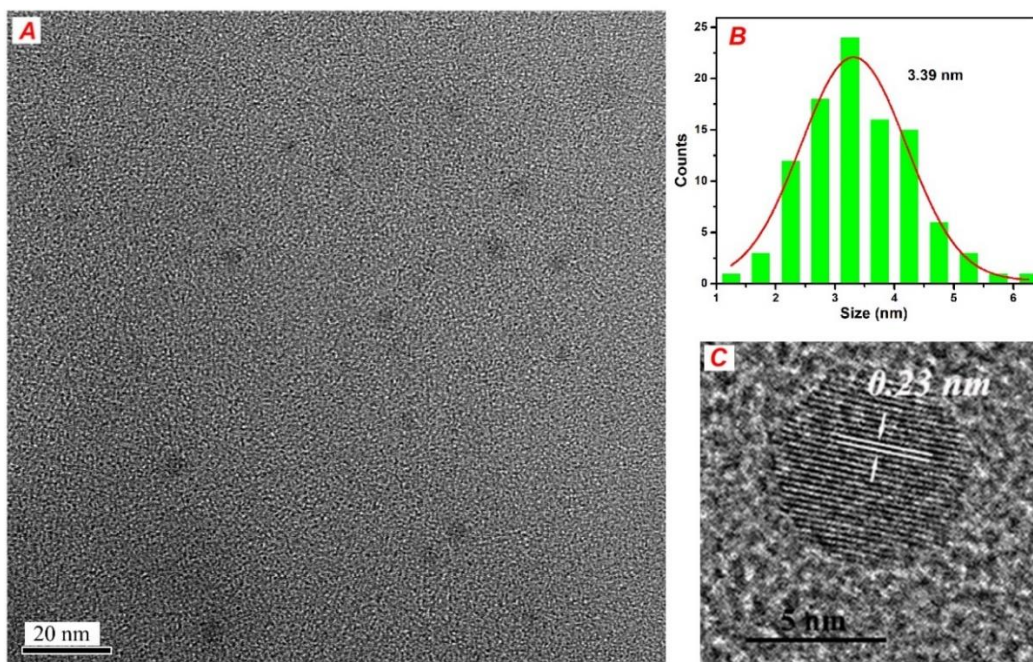


Figure 4.3. (A) TEM images of Am-CDs, (B) the particle size distribution histograms, and (C) HR-TEM images.

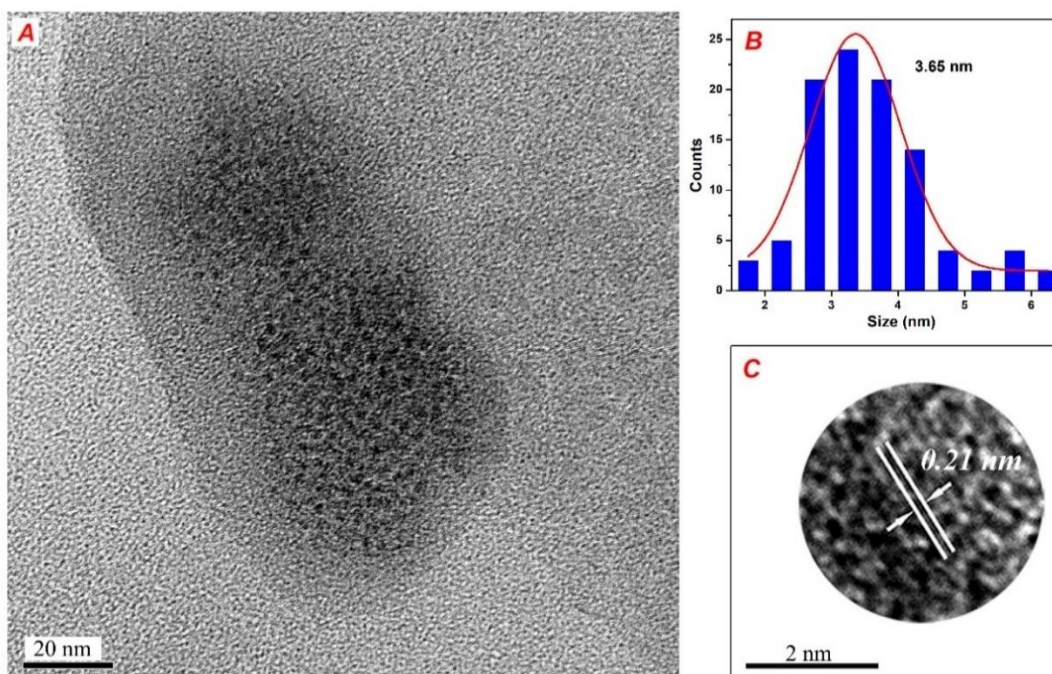


Figure 4.4. (A) TEM images of Ao-CDs, (B) the particle size distribution histograms, and (C) HR-TEM images.

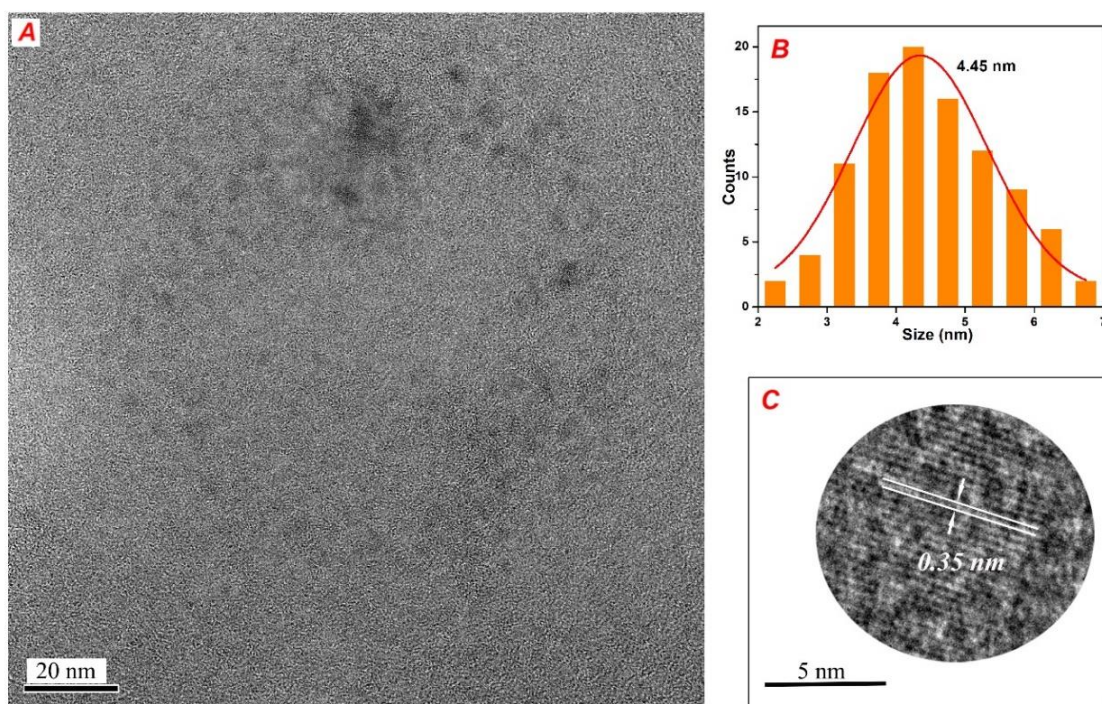


Figure 4.5. (A) TEM images of Ap-CDs, (B) the particle size distribution histograms, and (C) HR-TEM images.

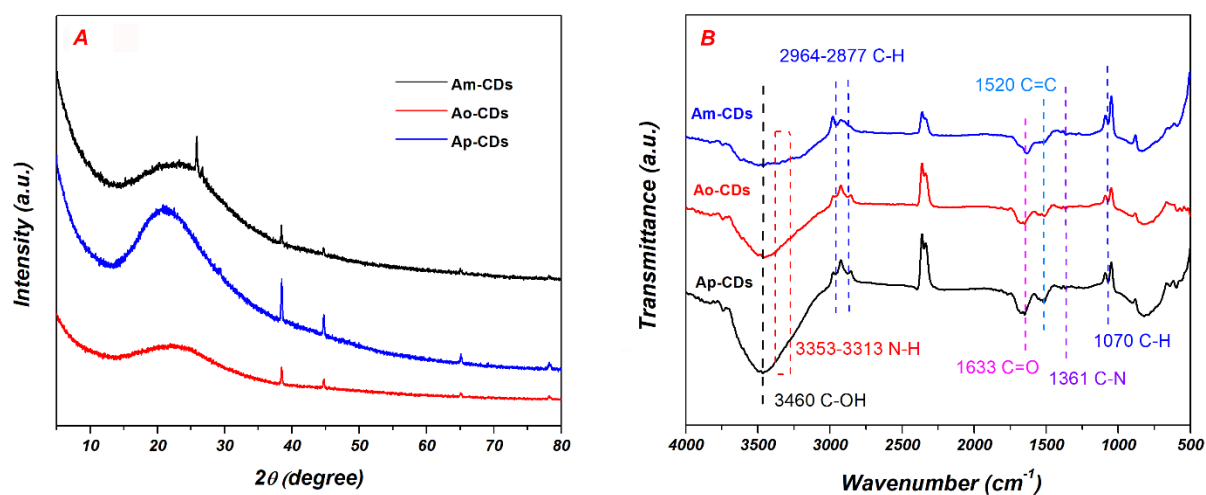


Figure 4.6. (A) XRD patterns, and (B) FTIR spectra of Ax-CDs.

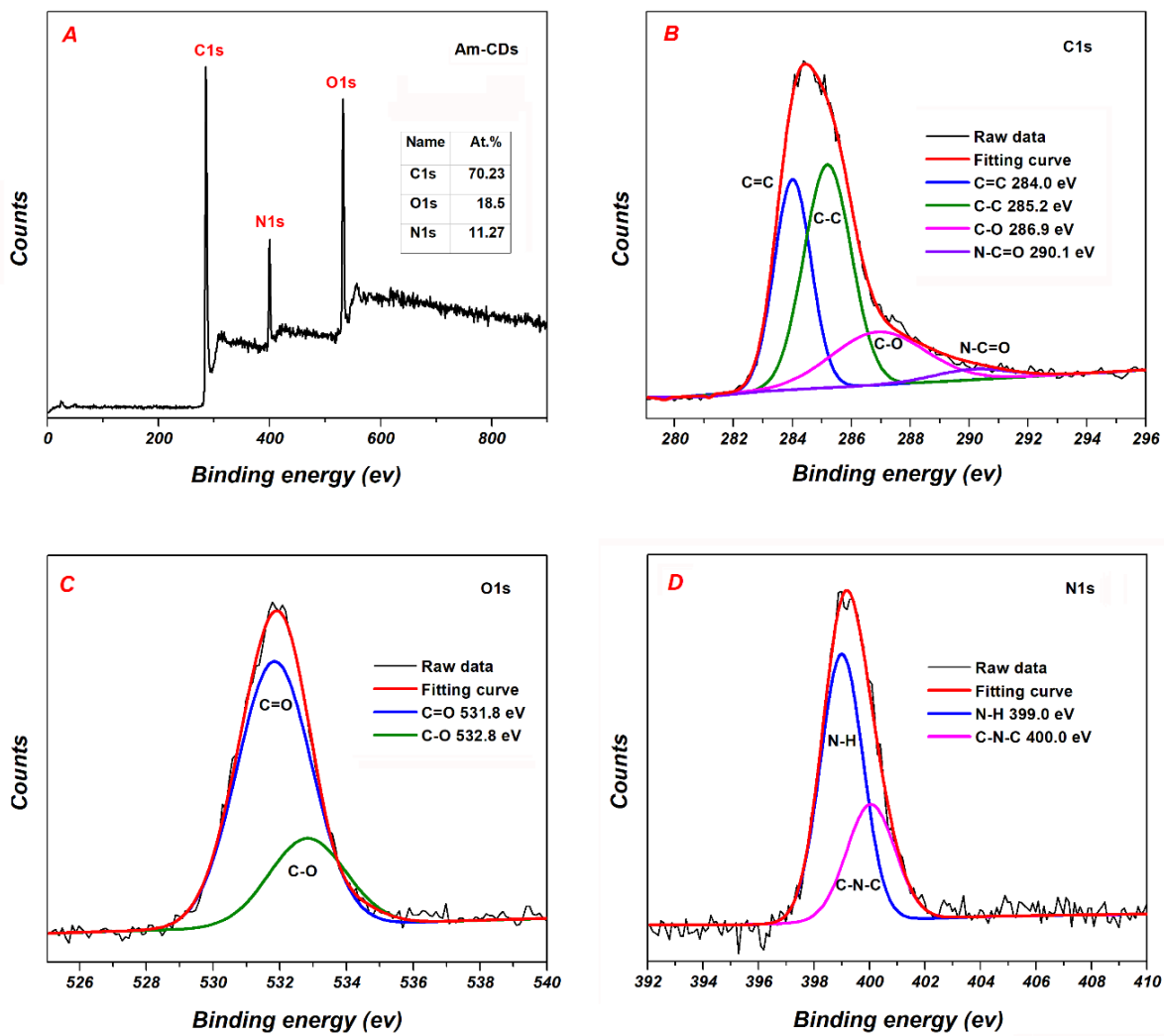


Figure 4.7. (A) XPS survey spectrum of Am-CDs. The high resolution (B) C1s, (C) O1s, and (D) N1s XPS spectra of Am-CDs.

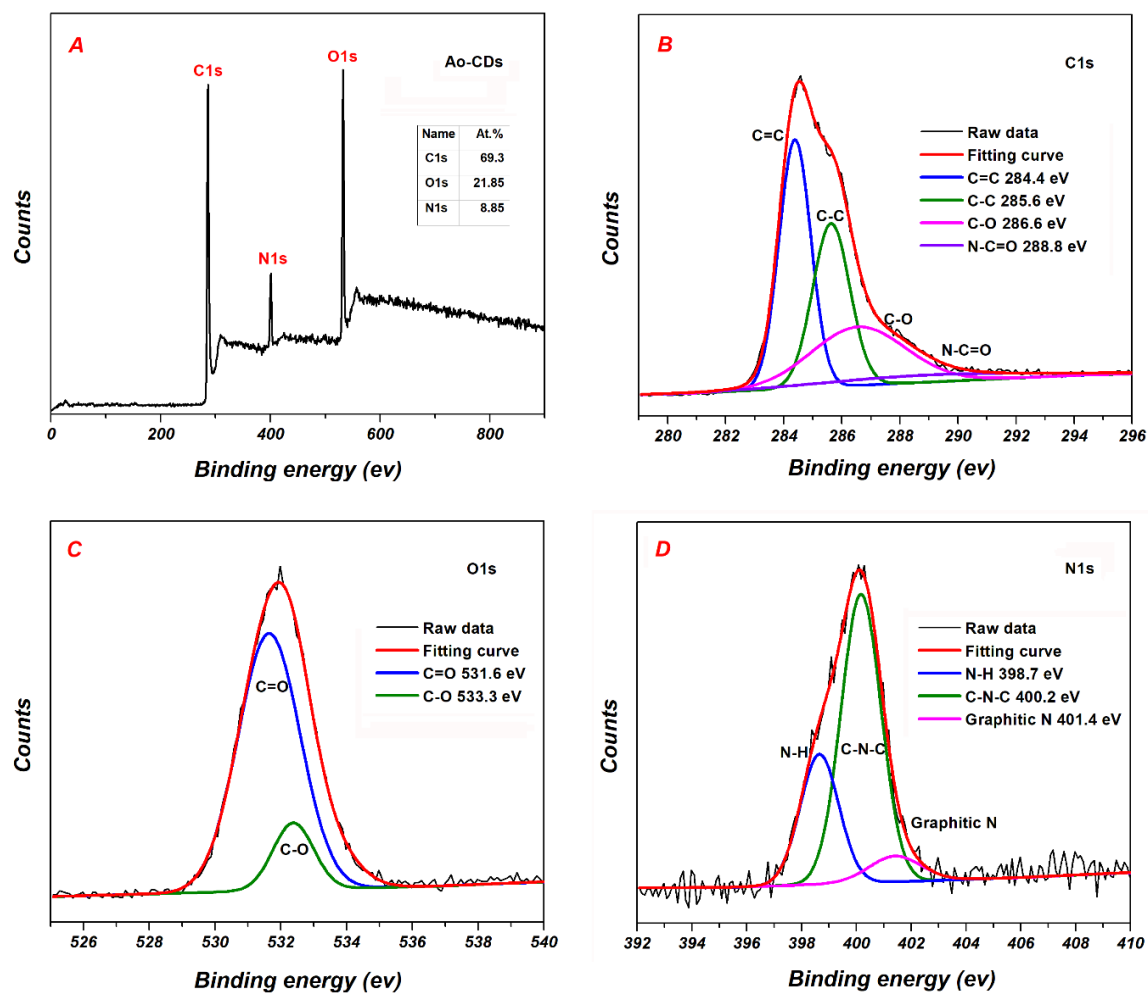


Figure 4.8. (A) XPS survey spectrum of Ao-CDs. The high resolution (B) C1s, (C) O1s, and (D) N1s XPS spectra of Ao-CDs.

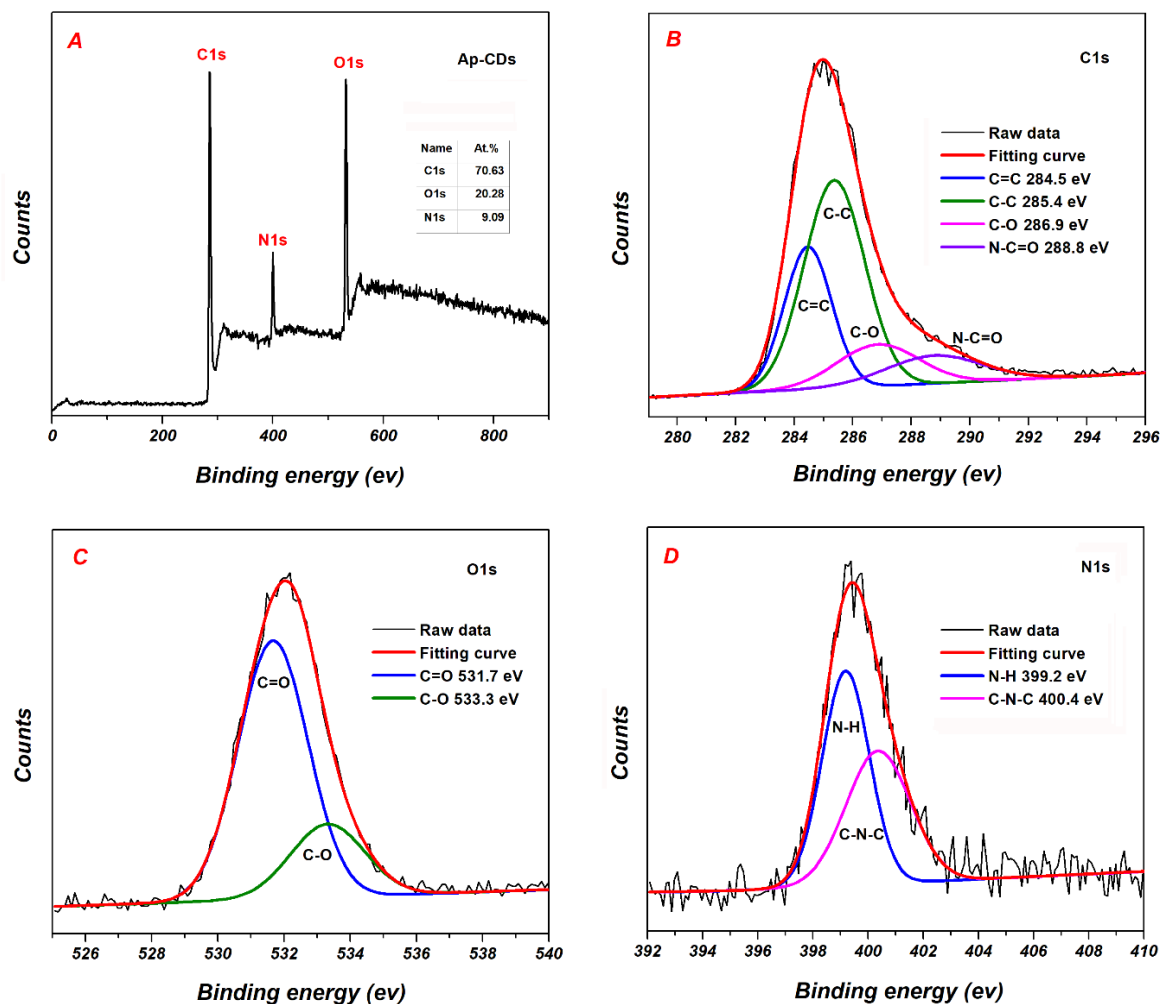


Figure 4.9. (A) XPS survey spectrum of Ap-CDs. The high resolution (B) C1s, (C) O1s, and (D) N1s XPS spectra of Ap-CDs.

4.3.2. Optical properties of the Ax-CDs

The optical properties of the Ax-CDs were explored by the UV-vis absorption and PL spectra. Figure 4.10 shows the UV-vis absorption, photoluminescence excitation (PLE), and PL spectra of the Ax-CDs. Two absorption peaks centered at 289 and 400 nm are observed in the UV-vis absorption of Am-CDs (Figure 4.10A), which correspond to the $\pi-\pi^*$ transitions of the C=C structure, and the $n-\pi^*$ transitions of C=O groups [15]. Ao-CDs and Ap-CDs showed two peaks in the UV-vis spectra, however the peak positions and intensities were different (Figures 4.10(C, E)). This difference might be attributed to the different extent of electronic transitions. Moreover, the additional broad absorption peak shown at ~ 510 nm can be attributed to the surface absorption of the Ap-CDs, and succedent excitation of the PL emission [19]. Accordingly, the PLE and PL spectra are different for all three Ax-CDs. The Am-CDs show emission in the green region at 521 nm when excited at 450 nm. The Ao-CDs and Ap-CDs show excitation peaks at 360 and 580 nm and emit at blue region at 432 nm and orange region at 596 nm, respectively.

Figures 4.10(B, D, F) show that Am- and Ao-CDs show excitation dependent emission while Ap-CDs show excitation independent emission. The excitation wavelength-dependent PL emission behavior might originate from the nonuniform CDs size, and presence of various surface defects, and various surface functional groups in the CDs [20, 21]. The excitation wavelength-independent PL emission behavior of Ap-CDs indicates uniform emission states, which also result in narrow emission width. The different excitation wavelength related PL properties among the Ax-CDs imply the different energy states, and their morphology [22, 23].

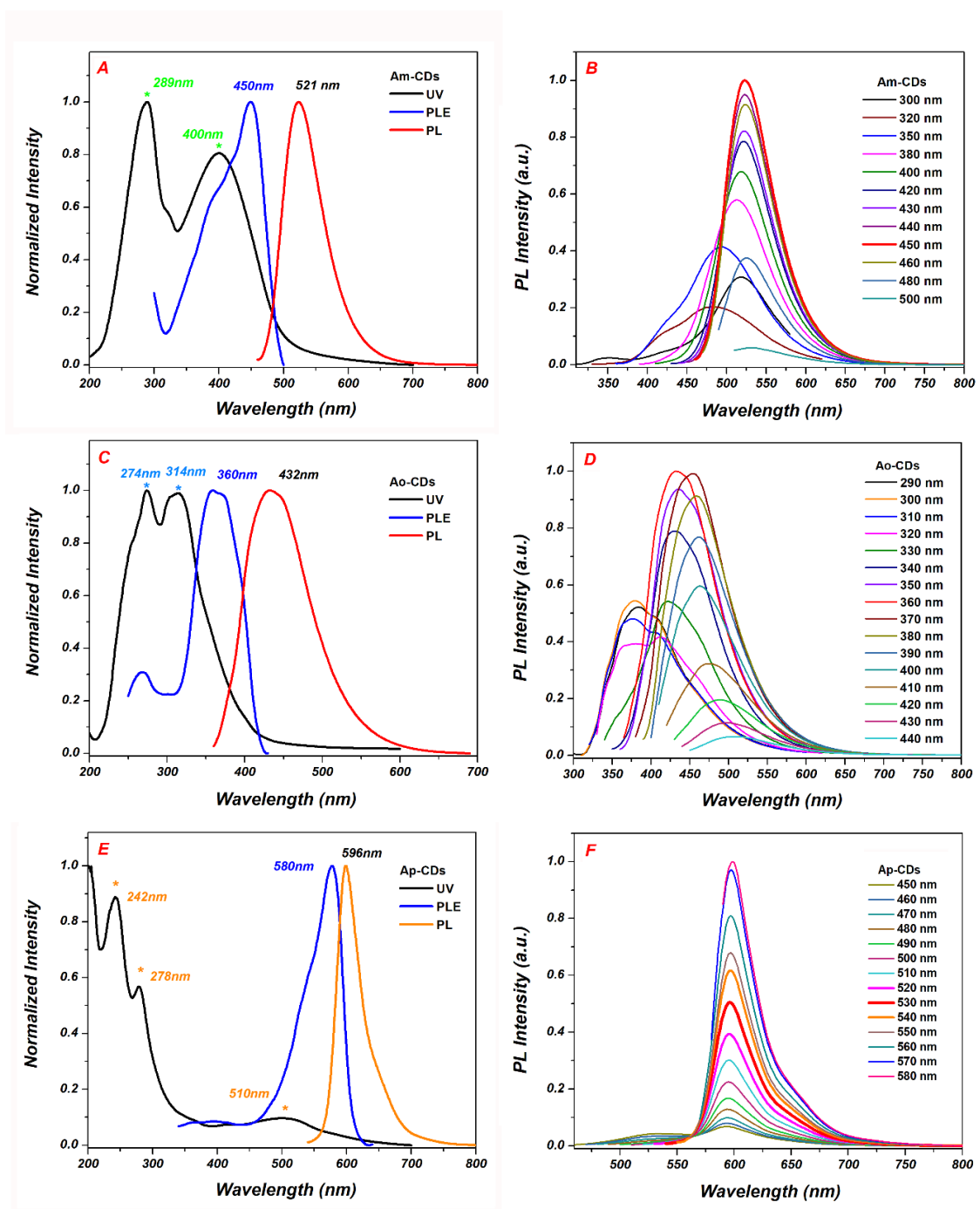


Figure 4.10. The normalized UV–vis absorption spectra, PL excitation, and PL emission spectra of the (A) Am-CDs, (C) Ao-CDs, and (E) Ap-CDs. The normalized PL emission spectra of the (B) Am-CDs, (D) Ao-CDs, and (F) Ap-CDs at different excitation wavelengths.

4.3.3. Solvent effects and QY on the PL emission properties

The effects of solvent, including deionized water (H₂O), Methanol (MeOH), Ethanol (EtOH), Isopropyl alcohol (IPA), Acetone (ACE), Acetonitrile (ACN), N, N-Dimethylformamide (DMF), and Dimethyl sulfoxide (DMSO) on the PL emission properties of the Ax-CDs were investigated. Figure 4.11 shows that the PL emission wavelength changes at different solvents. This shows the typical solvatochromic properties of CDs caused by the interaction between surface functional groups of CDs and solvents [21, 24].

Figure 4.12 shows that the Am-CDs possessed the highest QY among the three CDs. In addition, the Ax-CDs in ethanol solvent exhibit higher QY than those in water, which can be explained by (1) higher extent of agglomeration of CDs in high polar solvent, (2) increased rate of non-radiative decay during the interaction between highly polar solvent and CDs, and (3) water-induced morphological change [25].

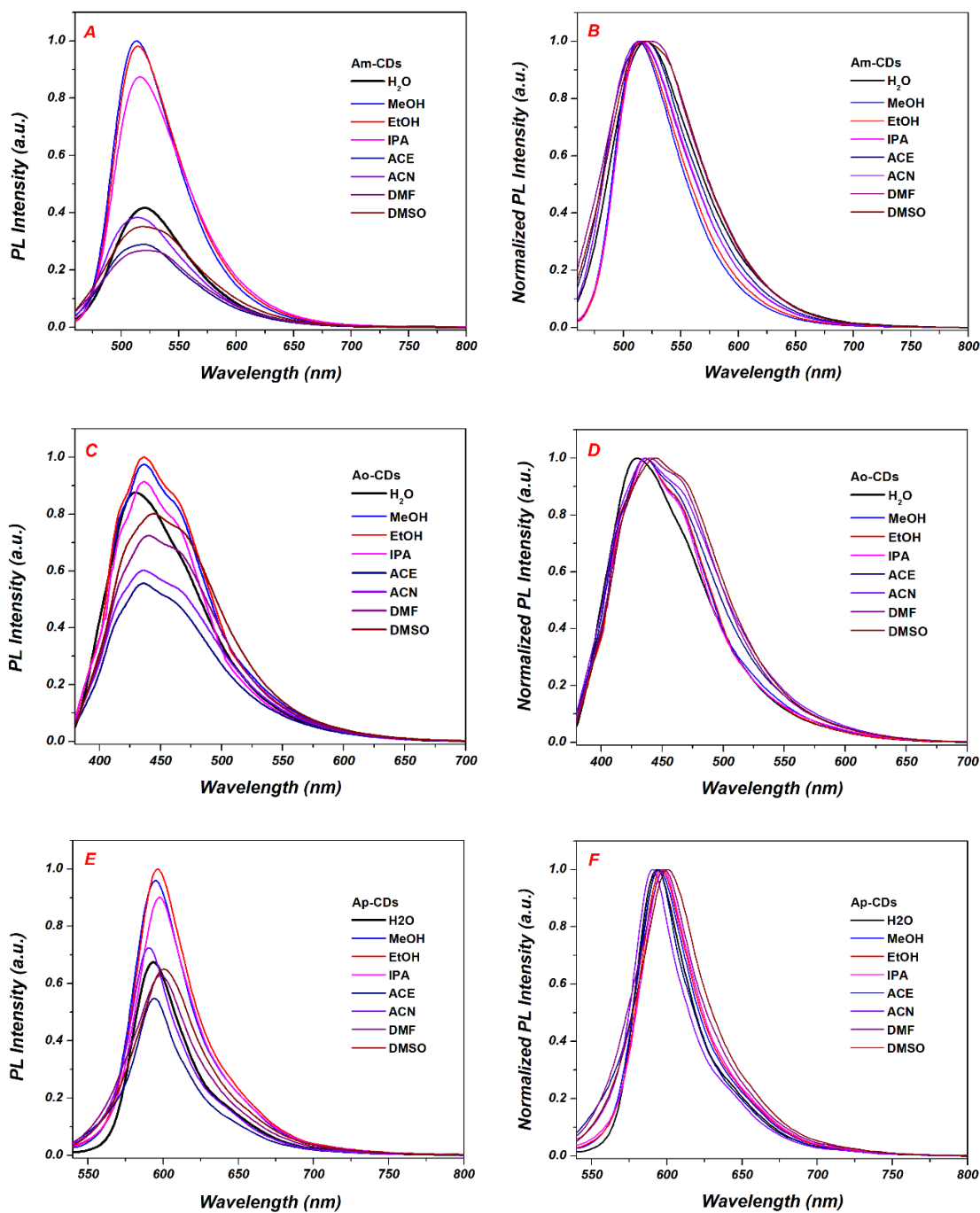


Figure 4.11. The effect of different solvents on PL emission properties of (A, B) Am-CDs, (C, D) Ao-CDs and (E, F) Ap-CDs.

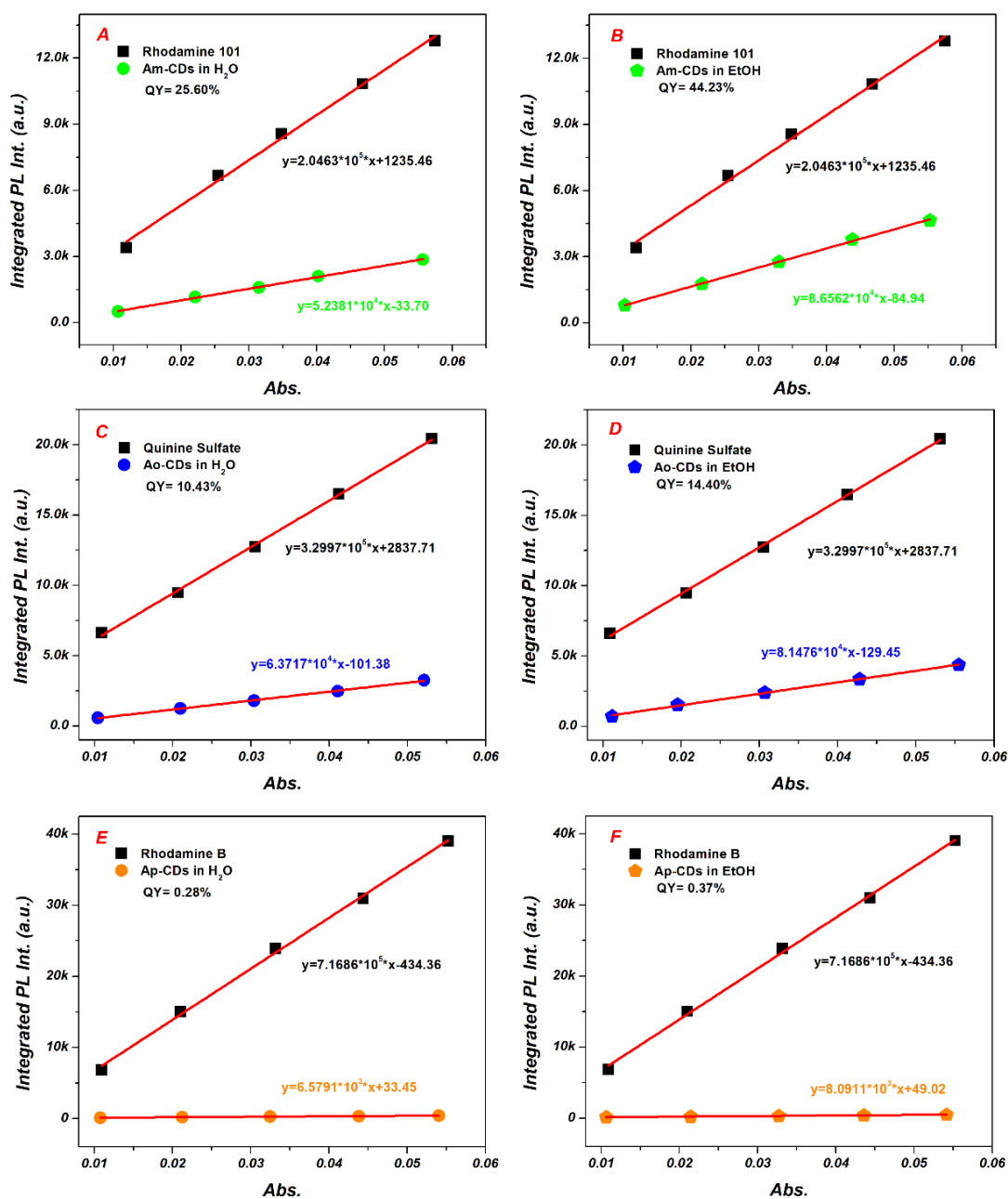


Figure 4.12. (1) Plots of integrated PL intensity of Am-CDs and rhodamine 101 as a function of optical absorbance at 450 nm in (A) water and (B) ethanol, respectively. (2) Plots of integrated PL intensity of Ao-CDs and quinine sulfate as a function of optical absorbance at 360 nm in (C) water and (D) ethanol, respectively. (3) Plots of integrated PL intensity of Ap-CDs and rhodamine B as a function of optical absorbance at 514 nm in (E) water and (F) ethanol, respectively.

4.3.4. pH effects on the fluorescence emission of Ax-CDs

The PL emission intensities of the as-prepared Am-, Ao-, and Ap-CDs were monitored at various pH conditions. Figure 4.13 shows that Am- and Ao-CDs exhibit similar PL emission behavior as the pH of solution changes. The decrease of PL emission as the pH increases can be attributed to the deprotonation of the surface functional groups of the Am- and Ao-CDs, resulting in the agglomeration of CDs [26-29].

On the other hand, for Ap-CDs, the PL intensity increases as the pH of solution increases. This phenomenon can be attributed to the different surface charge of Ap-CDs from the other CDs.

To investigate the different pH-dependent behaviors between Ax-CDs, the zeta potential was monitored at various pH values. As shown in Figure 4.14, the zeta potentials of the Am- and Ao-CDs gradually decreased with increasing pH, whereas the zeta potential of Ap-CDs increased with increasing pH. This might result in lesser agglomeration and enhanced the PL intensity of Ap-CDs [30, 31].

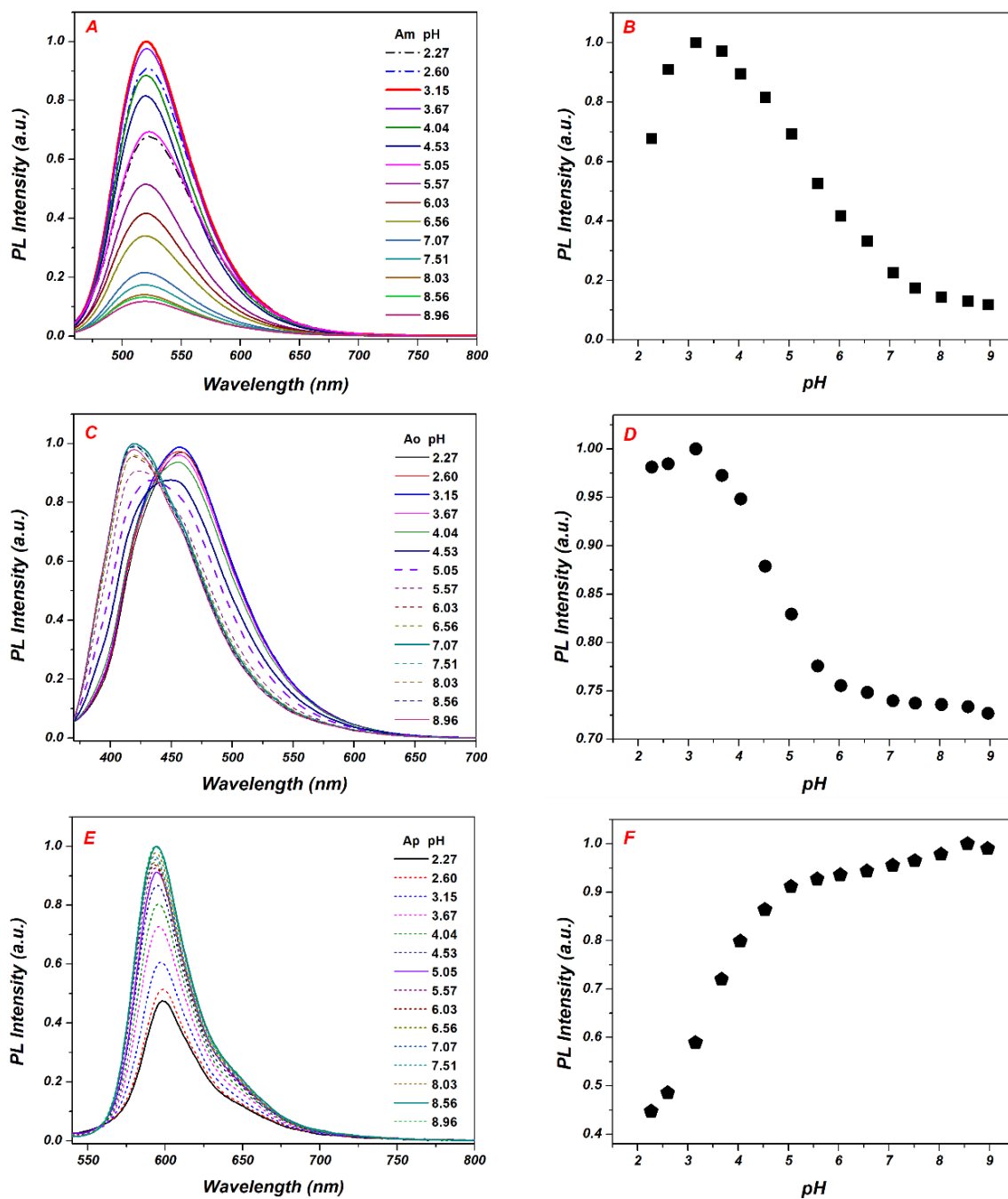


Figure 4.13. PL emission and intensity change of (A, B) Am-CDs, (C, D) Ao-CDs, and (E, F) Ap-CDs under various pH conditions.

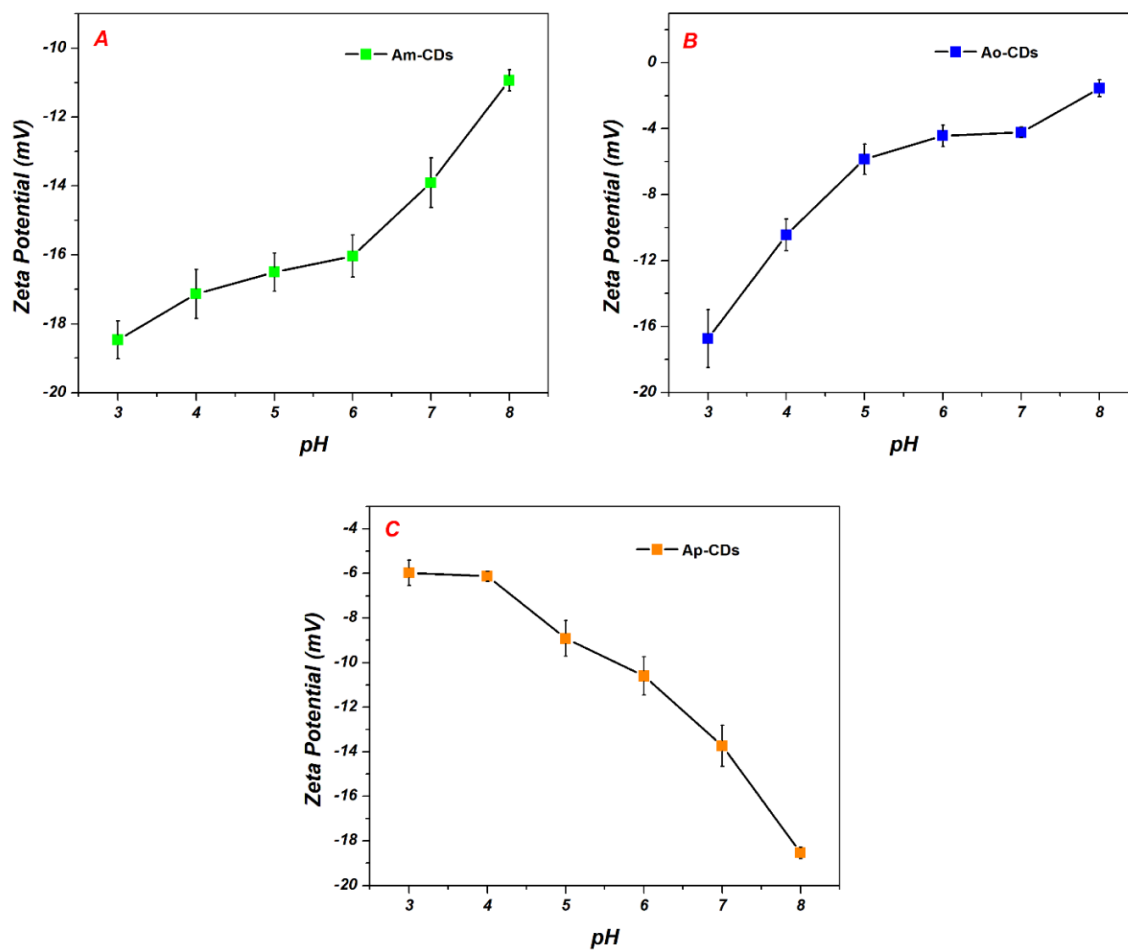


Figure 4.14. Zeta potential of (A) Am-CDs, (B) Ao-CDs, and (C) Ap-CDs under various pH values, respectively.

4.4. Conclusion

In this work, the green, blue, and orange color emitting N-doped CDs have been successfully synthesized from the reaction between ascorbic acid (AA) and m-PDA, o-PDA, and p-PDA, respectively. For this purpose, a simple low temperature hydrothermal synthesis method has been employed. The photophysical and optical properties of the three CDs have been investigated thoroughly at different solvents and pH. The as-synthesized Ax-CDs exhibited higher QYs in ethanol than that in water. The lesser agglomeration, reduced rate of non-radiative decay, and lesser morphological change of CDs might be the reason behind such behavior. In addition, the surface charge of synthesized Ax-CDs resulted in different pH-dependent PL emission properties. These unique properties of the as-synthesized CDs will enable their applications in different fields of imaging and sensing.

Reference

- [1] J. Zhang, S. Yu. *Materialstoday*, 2016, 19, 382-393.
- [2] T. S. Atabaev. *Nanomaterials*, 2018, 8, 342.
- [3] D. Lu, Y. Tang, J. Gao, Q. Wang. *J Mater Chem C*, 2018, 6, 13013-13022.
- [4] T. Pal, S. Mohiyuddin, G. Packirisamy. *ACS Omega*, 2018, 3, 831-843.
- [5] C. Wang, K. Jiang, Q. Wu, J. Wu, C. Zhang. *Chemistry-A European Journal*, 2016, 22, 14475-14479.
- [6] J. Zhang, Y. Yuan, G. Liang, S. Yu. *Advanced Science*, 2015, 2, 1500002.
- [7] Z.-b. Qu, X. Zhou, L. Gu, R. Lan, D. Sun, D. Yu, G. Shi. *Chem Commun*, 2013, 49, 9830-9832.
- [8] Y. Chen, Y. Wu, B. Weng, B. Wang, C. Li. *Sensors and Actuators B: Chemical*, 2016, 223, 689-696.
- [9] K. Jiang, S. Sun, L. Zhang, Y. Lu, A. Wu, C. Cai, H. Lin. *Angew Chem Int Ed*, 2015, 54, 5360-5363.
- [10] L. Song, Y. Cui, C. Zhang, Z. Hu, X. Liu. *RSC Adv*, 2016, 6, 17704-17712.

- [11] H. Nie, M. Li, Q. Li, S. Liang, Y. Tan, L. Sheng, W. Shi, S. X.-A. Zhang. *Chem Mater*, 2014, 26, 3104-3112.
- [12] G. Qiao, D. Lu, Y. Tang, J. Gao, Q. Wang. *Dyes and Pigments*, 2019, 163, 102-110.
- [13] V. Ramanan, S. H. Subray, P. Ramamurthy. *New J Chem*, 2018, 42, 8933-8942.
- [14] S. Zhu, Q. Meng, L. Wang, J. Zhang, Y. Song, H. Jin, K. Zhang, H. Sun, H. Wang, B. Yang. *Angew Chem Int Ed*, 2013, 52, 3953-3957.
- [15] J. Zhu, X. Bai, J. Bai, G. Pan, Y. Zhu, Y. Zhai, H. Shao, X. Chen, B. Dong, H. Zhang, H. Song. *Nanotechnology*, 2018, 29, 085705.
- [16] S. Basiruddin, S. K. Swain. *Materials Science and Engineering: C*, 2016, 58, 103-109.
- [17] L. Li, C. Lu, S. Li, S. Liu, L. Wang, W. Cai, W. Xu, X. Yan, Y. Liu, R. Zhang. *J Mater Chem B*, 2017, 5, 1935-1942.
- [18] D. K. Dang, S. Chandrasekaran, Y.-L. T. Ngo, J. S. Chung, E. J. Kim, S. H. Hur. *Sensors and Actuators B: Chemical*, 2018, 255, 3284-3291.
- [19] Y. Jiao, X. Gong, H. Han, Y. Gao, W. Lu, Y. Liu, M. Xian, S. Shuang, C. Dong. *Analytica Chimica Acta*, 2018, 1042, 125-132.
- [20] S. Khan, A. Gupta, N. C. Verma, C. K. Nandi. *Nano Lett*, 2015, 15, 8300-8305.
- [21] W. U. Khan, D. Wang, Y. Wang. *Inorg Chem*, 2018, 57, 15229-15239.
- [22] L. Pan, S. Sun, L. Zhang, K. Jiang, H. Lin. *Nanoscale*, 2016, 8, 17350-17356.
- [23] J. Chen, J. Wei, P. Zhang, X. Niu, W. Zhao, Z.-Y. Zhu, H. Ding, H.-M. Xiong. *ACS Appl Mater Interfaces*, 2017, 9, 18429-18433.
- [24] H. Wang, C. Sun, X. Chen, Y. Zhang, V. L. Colvin, Q. Rice, J. Seo, S. Feng, S. Wang, W. W. Yu. *Nanoscale*, 2017, 9, 1909-1915.
- [25] H. J. Lee, J. Jana, Y.-L. T. Ngo, L. L. Wang, J. S. Chung, S. H. Hur. *Materials Research Bulletin*, 2019, 119, 110564.
- [26] L. Wang, J. S. Chung, S. H. Hur. *Dyes and Pigments*, 2019, 171, 107752.
- [27] D. Pan, J. Zhang, Z. Li, C. Wu, X. Yan, M. Wu. *Chem Commun*, 2010, 46, 3681-3683.

- [28] X. Sun, J. He, Y. Meng, L. Zhang, S. Zhang, X. Ma, S. Dey, J. Zhao, Y. Lei. *J Mater Chem A*, 2016, 4, 4161-4171.
- [29] C. Wang, Z. Xua, H. Cheng, H. Lin, M. G. Humphrey, C. Zhang. *Carbon*, 2015, 82, 87-95.
- [30] Y. Sun, X. Wang, C. Wang, D. Tong, Q. Wu, K. Jiang, Y. Jiang, C. Wang, M. Yang. *Microchimica Acta*, 2018, 185, 83.
- [31] Y. Guo, Z. Wang, H. Shao, X. Jiang. *Carbon*, 2013, 52, 583-589.

CHAPTER 5. High quantum yield aminophenylboronic acid-functionalized N-doped carbon dots for highly selective hypochlorite ion detection

5.1. Introduction

The hypochlorite ion (ClO^-) is a reactive oxygen species (ROS) with effective antibacterial and pro- and anti-inflammatory properties that plays an important role in biological and environmental systems [1-3]. The strong oxidation ability of ClO^- makes it an effective disinfectant to treat drinking water, swimming pool water, and wastewater [4, 5]. Moreover, ClO^- is used widely as a disinfectant and bleach in industry [6, 7]. Endogenous ClO^- is produced primarily by a myeloperoxidase enzyme-catalyzed reaction between hydrogen peroxide and chloride ions and is treated as an antimicrobial agent in the immune system [8, 9]. On the other hand, an excess of ClO^- may cause severe damage to the body, including lung injury, atherosclerosis, neuron degeneration, cardiovascular diseases, and even cancer [10-12]. Therefore, the development of a novel analytical tool for the detection of ClO^- is critical.

Several approaches for ClO^- detection include liquid chromatography [13], chemiluminescence [14], colorimetry [15], potentiometric titration [16], and electrochemical analysis [17]. On the other hand, these methods require complicated steps in sample preparation, sophisticated and expensive analyzing equipment, and specialized users. In this regard, fluorometric detection techniques have emerged as an alternative way to monitor the ClO^- level owing to its high accuracy and high signal-to-noise ratio [18]. Among the various fluorometric probes available, carbon dots (CDs) have become very popular because of their unique properties, including physico-chemical properties, easy synthesis, non-toxicity, biocompatibility, water-solubility, high quantum yield, tunable emission, good stability, and photostability [19-21]. The unique physico-chemical properties of CDs have extended their applications to sensing, photocatalysts, electrochemistry, bioimaging, and environmental applications [22]. The facile electron-accepting / donating properties of CDs enable the

versatile design of CD-based sensors. The fluorescence-based sensing processes of CDs take place through a range of mechanisms, including photoinduced electron transfer (PET), Forster resonance energy transfer (FRET), intramolecular charge transfer (ICT), and inner filter effect (IFE) [23] depending on the properties of the analytes and the interactions between the CDs and analytes.

In this study, high quantum yield 3-aminophenylboronic acid-functionalized nitrogen-doped carbon dots (GAAP-CDs) were fabricated as a highly selective ClO^- nanosensor through the hydrothermal treatment of glutaric acid (GA) and 3-aminophenylboronic acid monohydrate (3-APBA), as shown in Figure 5.1. Physical and chemical characterization showed that the GAAP-CDs contain a nitrogen atom as a heteroatom at the carbon core and amino and boronic acid functional groups at the surface, which contributed to the high quantum yield and excellent selectivity of as-prepared CDs towards ClO^- ions. The presence of the hetero atoms would modify the electronic state of the GAAP-CDs and would create more surface defects. Presence of defects would modify the radiative recombination and that would result in increment of quantum yield of GAAP-CDs [24]. The GAAP-CDs exhibited strong absorption and intense blue fluorescence (quantum yield (QY) = 58.28 %) in aqueous solutions, which decreased significantly in the presence of ClO^- ions. The severe quenching might occur through specific intermolecular interactions between the boronic acid group and ClO^- ions. The experimental results showed that ClO^- induced a C–B to C–OH transformation, resulting in fluorescence quenching. The quenching mechanism followed the ground state quenching model. ClO^- was detected by UV–vis absorbance and fluorescence spectroscopy with a detection limit of 0.77 μM (linear range of 0–100 μM), and 0.50 μM (linear range of 0.1–100 μM), respectively. The resulting GAAP-CDs were also very effective for real sample analysis, such as tap water and drinking water.



Figure 5.1. Schematic diagram of GAAP-CDs fabrication and ClO^- detection. (GA: Glutaric acid, and 3-APBA: 3-Aminophenylboronic acid.)

5.2. Experimental Section

5.2.1. Materials

3-Aminophenylboronic acid monohydrate (3-APBA), glutaric acid (GA), sodium hypochlorite (NaClO), hydrogen peroxide (H_2O_2), quinine sulfate (QS), D-(+)-glucose (Glu), D-(-)-fructose (Fruc), L-cystine (L-cys), sodium fluoride (NaF), sodium chloride (NaCl), sodium bromide (NaBr), sodium iodide (NaI), sodium nitrite (NaNO_2), sodium nitrate (NaNO_3), sodium acetate (NaOAc), sodium azide (NaN_3), potassium thiocyanate (KSCN), sodium sulfite anhydrous (Na_2SO_3), sodium sulfide pentahydrate ($\text{Na}_2\text{S}\cdot 5\text{H}_2\text{O}$), potassium chloride (KCl), potassium dihydrogen phosphate (KH_2PO_4) and di-sodium hydrogen phosphate (Na_2HPO_4) were purchased from Sigma-Aldrich Co. (USA). All chemical reagents were used as received without further purification. Deionized (DI) water was used for the preparation of the samples in all experiments.

5.2.2. Instruments

An ultrasonic treatment was performed using a UPC-10 (Jeio-Tech Co., Ltd., South Korea). The analysis of functional groups was done using the Fourier Transform Infrared (FTIR, Nicolet iS5, Thermo Fisher Scientific, USA) spectroscopy. X-ray diffraction (XRD, D/MAZX 2500V/PC model, Rigaku, Japan) was carried out using $\text{Cu K}\alpha$ radiation (40 kV,

30 mA, $\lambda = 1.5415 \text{ \AA}$) at a scan rate of 2° min^{-1} over the 2θ range of $10\text{-}80^\circ$. X-ray photoelectron spectroscopy (XPS, Thermo ESCALAB 250 Xi, Thermo Fished Scientific, USA) was performed using Al K α X-ray radiation (1486.6 eV) to determine the oxidation states of the constituent elements. High-resolution transmission electron microscopy (HR-TEM, JEM-2100 F, JEOL, Japan) images were taken at an operating voltage of 200 kV.

Ultraviolet visible (UV-vis, SPECORD 210 PLUS, Analytik Jena, Germany) absorption spectroscopy was performed. The photoluminescence spectra (PL) were recorded using a Cary Eclipse fluorescence spectrophotometer (Agilent Technologies, USA) with a 1.0 cm quartz cell.

5.2.3. Synthesis of GAAP-CDs

To prepare GAAP-CDs, glutaric acid (GA, 0.2 M 1 mL) and 3-Aminophenylboronic acid monohydrate (3-APBA, 0.2 M 1 mL) were added to 10 mL deionized water and sonicated for 5 min to produce a well-dispersed homogenous solution. Then, the mixture was transferred to a 50 mL Teflon-lined autoclave, and it heated and maintained at 180°C for 6h in an oven for further reaction. After cooling down to room temperature (RT), GAAP-CDs was collected after removing the suspended particles via centrifugate at 10000 rpm for 10 min and further purified by using dialysis tube for 12 h to remove the residual chemicals. The obtained yellowish GAAP-CDs solution was stored at RT for further characterization.

As shown in the Figure 5.2, the reaction temperature and the precursor ratio were optimized to obtain the highest fluorescence for GAAP-CDs. The GAAP-CDs were obtained at 180°C for 6 h with a 1 : 1 molar ratio of GA and 3-APBA.

5.2.4. ClO⁻ sensing

To determine the ClO⁻ level, various amounts of GAAP-CDs containing solutions were added to 2 mL of phosphate buffer solution (PBS, pH = 7.0), as shown in Figure 5.3. After shaking constantly, the photoluminescence intensity of each sample containing 0.19 mg/mL GAAP-CDs was measured at 375 nm under an excitation wavelength of 310 nm. A time dependent quenching study showed that the significant result was obtained after 2 h.

The selectivity of ClO^- detection in the presence of interfering species was examined using a similar methodology. The interference study was performed by mixing ClO^- ions and other interfering species at a 1:1 ratio. The water samples (real samples) were collected from our department and were centrifuged and treated with UV to remove any unwanted component.

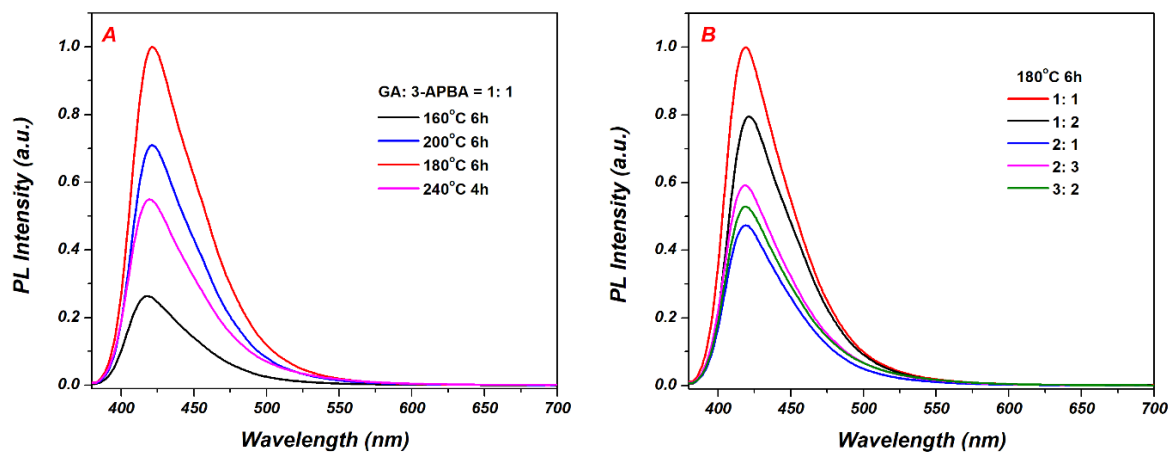


Figure 5.2. The reaction temperature (A) and the precursor ratio (B) were optimized to obtain the highest fluorescence for the GAAP-CDs.

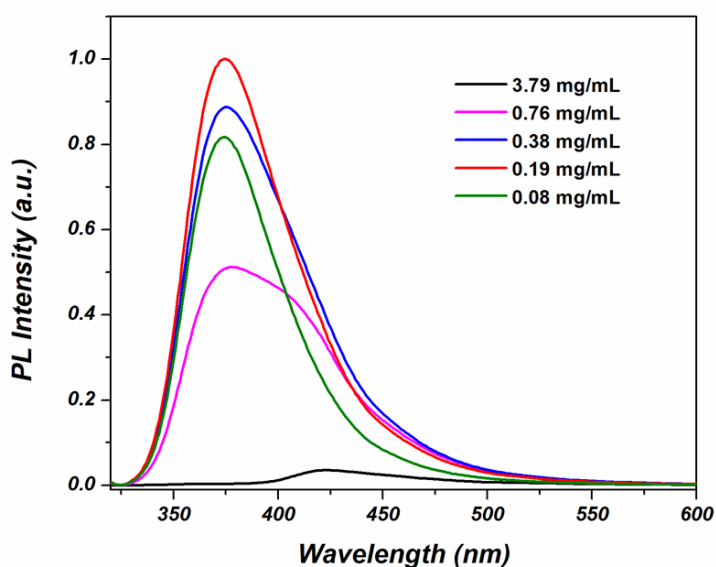


Figure 5.3. The optimize concentration of GAAP-CDs. PL emission spectra of GAAP-CDs with different concentration under excitation wavelength at 310 nm, buffer pH = 7.

5.3. Results and discussion

5.3.1. Characterization of GAAP-CDs

Transmission electron microscopy (TEM) showed that the mean diameter of the as-synthesized GAAP-CDs was 4.19 nm with a uniform distribution (Figure 5.4A). The selected area electron diffraction (SAED) pattern revealed amorphous GAAP-CDs (Figure 5.4B). Powder X-ray diffraction (XRD) (Figure 5.4C) showed a distinct broad single peak at $22^\circ 2\theta$, corresponding to amorphous carbon [25].

Fourier transform infrared spectroscopy (FTIR) was used to examine the functional groups of GAAP-CDs. Figure 5.4D shows the characteristic peaks of GAAP-CDs in the FTIR spectra. The peaks at approximately 3400, 2973, 1714, 1560, 1374, 1344, 1256, 1154, 1047, 879, 799, and 710 cm^{-1} can be attributed to the stretching vibrations of O–H/N–H, $-\text{CH}_2$, C=O, C=C, N–C=O, C–O, C–N, B–C, C–H, B–O–H, B–O, and B–O₂, respectively [26–28]. The stretching vibration of the N–C=O group at approximately 1374 cm^{-1} revealed amide functionality on the surface of the GAAP-CDs.

X-ray photoelectron spectroscopy (XPS) was used to examine the elemental composition and oxidation state of each element in the as-synthesized GAAP-CDs. The wide range survey spectra of GAAP-CDs revealed C, N, O, and B (Figure 5.5A). The high-resolution C1s XPS spectra of GAAP-CDs (Figure 5.5B) showed three peaks at ~ 282.72 , ~ 284.29 , and $\sim 286.69\text{ eV}$, which were assigned to C–C/C=C (sp^2 graphitic carbon), C–O/C–N (sp^3 -bond carbon with oxygen), and N–C=O/O–C=O (sp^2 -hybridized carbon atoms with nitrogen and oxygen), respectively [29]. The N1s XPS spectra (Figure 5.5C) exhibited two peaks at ~ 397.87 and $\sim 399.89\text{ eV}$ attributed to N–C and N–H bonds, respectively [30]. The O1s XPS spectrum (Figure 5.5D) could be resolved into three peaks. The three peaks centered at ~ 530.13 , ~ 531.59 , and $\sim 532.54\text{ eV}$ originated from N–C=O, C–O, and B–O bonds, respectively [31]. The B 1s XPS spectrum of GAAP-CDs could also be deconvoluted into two peaks at ~ 188.85 and $\sim 190.59\text{ eV}$ corresponding to B–C and B–O bonds, respectively (Figure 5.5E) [32]. The characterization results indicated that GA and 3-APBA had reacted to form the GAAP-CDs.

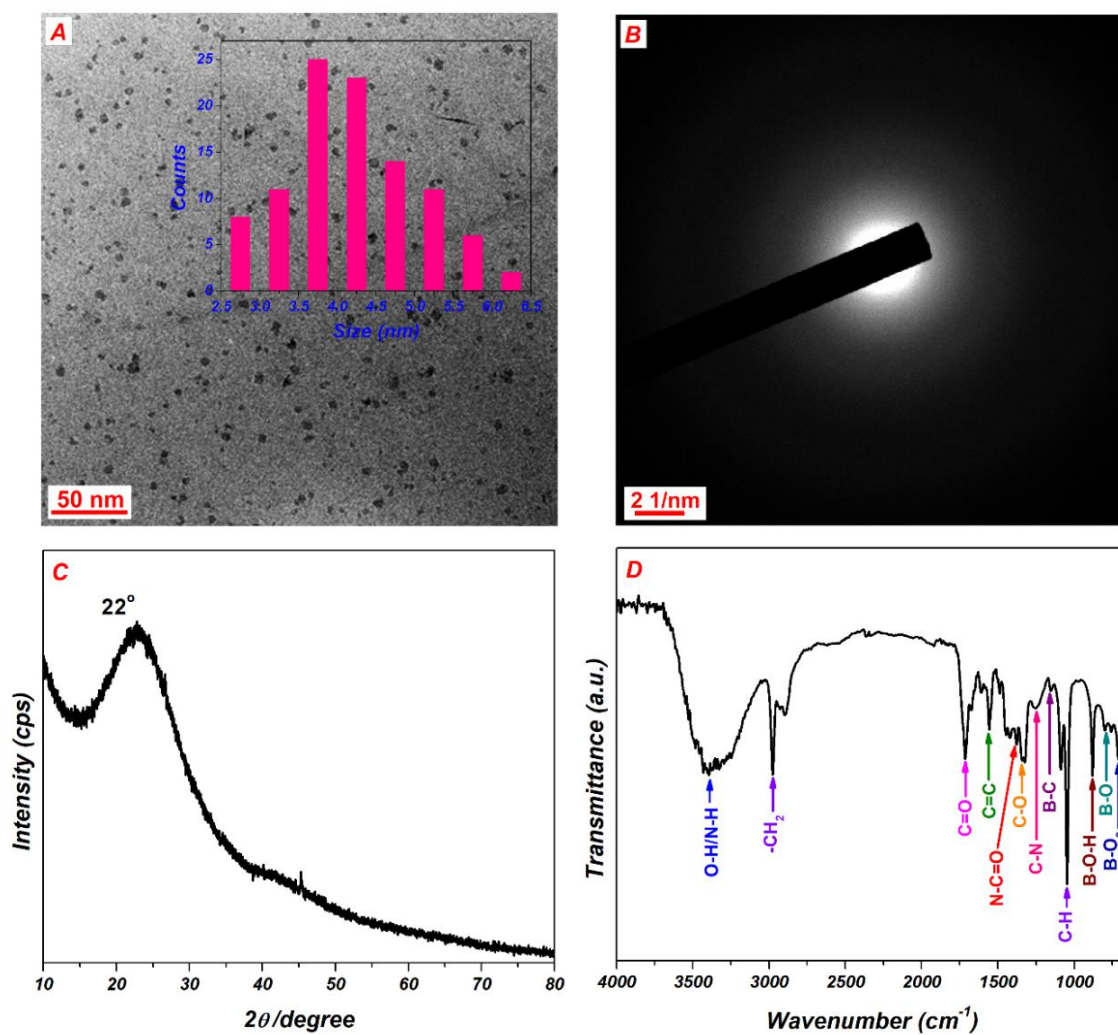


Figure 5.4. (A) TEM image (Inset: particle size distribution), (B) SAED image, (C) XRD pattern, and (D) FTIR spectrum of GAAP-CDs.

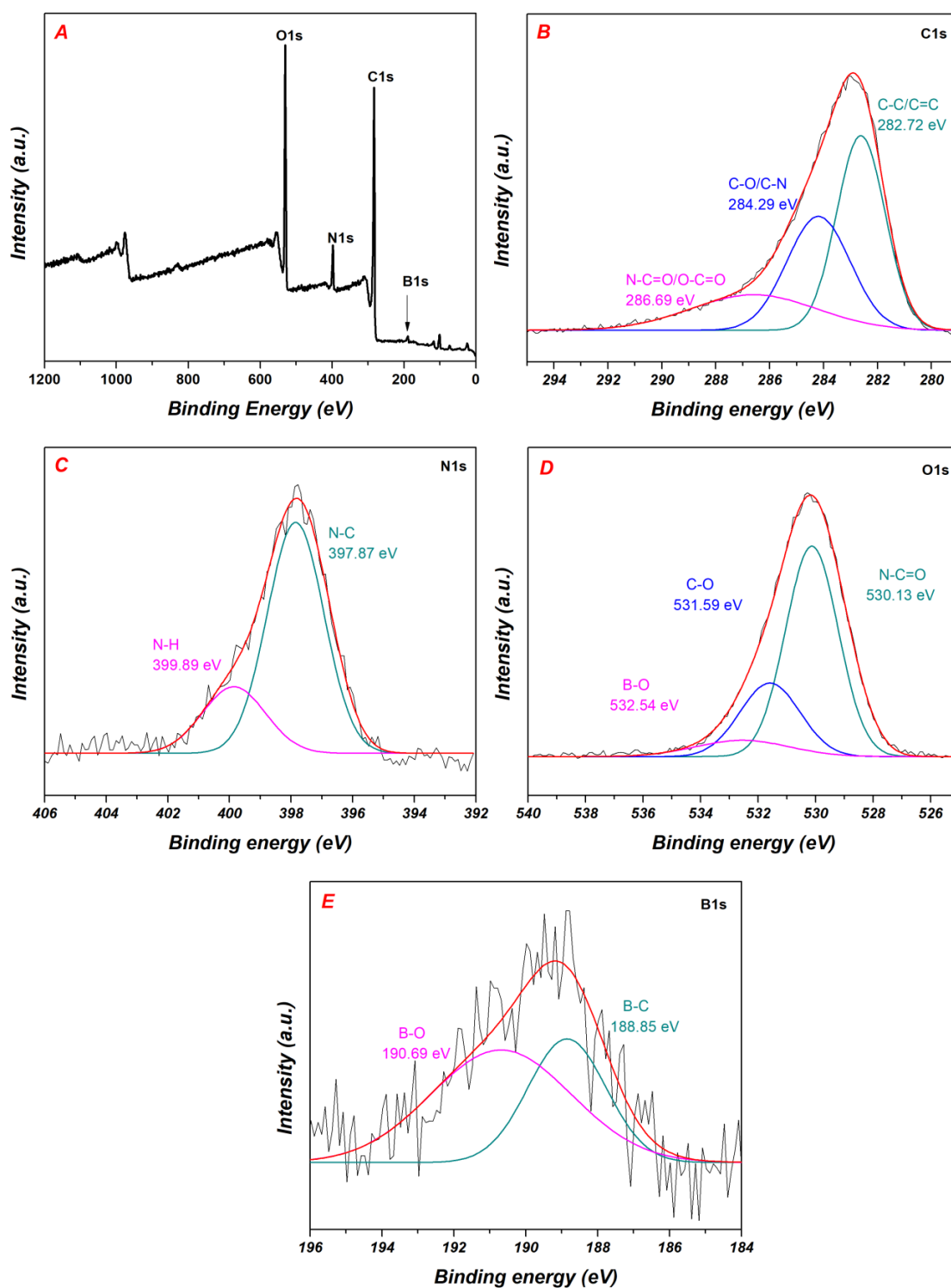


Figure 5.5. (A) XPS survey spectra of GAAP-CDs. The high-resolution XPS spectra of (B) C 1s, (C) N 1s, (D) O 1s, and (E) B 1s for GAAP-CDs.

5.3.2. Optical properties of GAAP-CDs

The UV–vis absorption and PL spectroscopy were conducted to examine the optical properties of as-synthesized GAAP-CDs. As shown in Figure 5.6A, the UV–vis absorption spectra of GAAP-CDs showed a weak shoulder peak at 252 nm, a strong peak at 297 nm, and a broad peak at 370 nm, which were attributed to the π – π^* and n – π^* electronic transition, respectively [33]. The photoluminescence excitation (PLE) spectra at a 375 nm excitation wavelength showed two peaks at approximately 250 and 300 nm, suggesting that more than one center caused the trapping of excitation energy at the surface of the GAAP-CDs [34]. The inset photograph in Figure 5.6A showed that the GAAP-CDs in aqueous solution were slightly yellow under visible light and emitted bright blue fluorescence under UV light at 365 nm. A suitable excitation wavelength was chosen using a trial and error method. As shown in Figure 5.6B, when the excitation wavelength was varied from 300 to 400 nm, the emission spectra exhibited excitation wavelength-dependent fluorescence behavior, which was attributed to the various surface functional groups of GAAP-CDs [35]. The maximum emission peak was observed at 375 nm when the GAAP-CDs were excited at 310 nm.

The fluorescence properties of the as-synthesized GAAP-CDs were examined further by analyzing the fluorescence quantum yield (QY) using quinine sulfate (QS) aqueous (0.1 M H₂SO₄) as a reference. As shown in Figure 5.7 and summarized in Table 5.1, the QY of the obtained GAAP-CDs was as high as 58.28%, which was higher than that reported for systems using carbon nanoparticles for the ClO[−] detection.

The variation in the I/I_0 value of this quenching system was negligible even after three months of incubation at RT, indicating excellent stability of the as-synthesized GAAP-CDs in the aqueous solution (Figure 5.8). In addition, the stability of GAAP-CDs in NaCl solutions at different concentrations was examined. The PL emission intensities showed no noticeable change in the NaCl solution over the wide concentration range from 0 – 1 mM (Figure 5.9), also revealing the substantial stability of the as-synthesized GAAP-CDs, even at high ionic concentrations.

The influence of the pH of GAAP-CDs on the UV–vis absorption and PL emission intensity was investigated to determine the optimal conditions for sensing applications. As shown in Figure 5.10, the intensity of PL emission at 375 nm of GAAP-CDs varied with

solution pH over the pH range of 3–8. This can be attributed to the agglomeration of GAAP-CDs through the protonation of surface functional groups, such as carboxylic acid and amide groups [36]. The responses to the ClO^- of both UV–vis absorption and PL emission were highest at approximately $\text{pH} = 7$. Moreover, ClO^- mediated fluorescence quenching of GAAP-CDs with respect to time was examined, and the maximum quenching was achieved after 2 h (Figure 5.11). Hence, all ClO^- sensing experiments were conducted in a neutral PBS solution ($\text{pH} = 7$). This shows that the GAAP-CDs fabricated in this study could be used effectively to monitor the ClO^- level in biological samples.

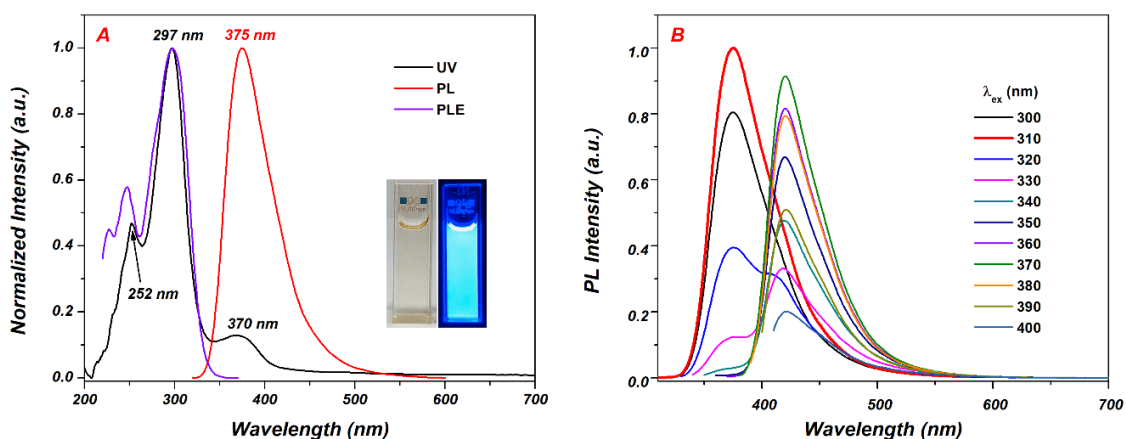


Figure 5.6. (A) The UV–vis absorption (UV), PL emission (PL), and PL excitation (PLE) spectra of GAAP-CDs in the aqueous solution. The inset shows the photographs of GAAP-CDs under visible light (left) and UV light (right). (B) PL emission spectra of GAAP-CDs at various excitation wavelengths.

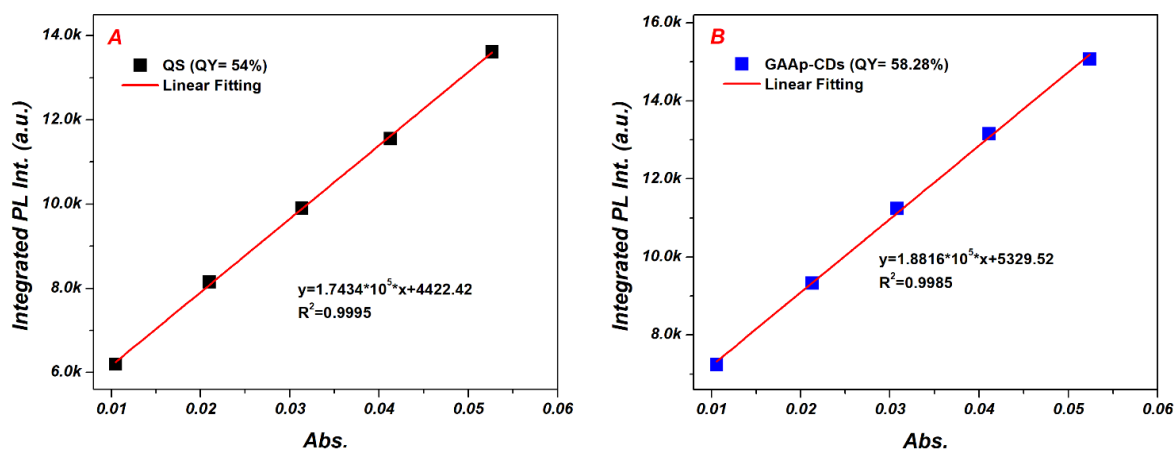


Figure 5.7. Plots integrated PL intensity of quinine sulfate (QS, the reference) and GAAP-CDs as a function of optical absorbance at 360 nm and relevant data.

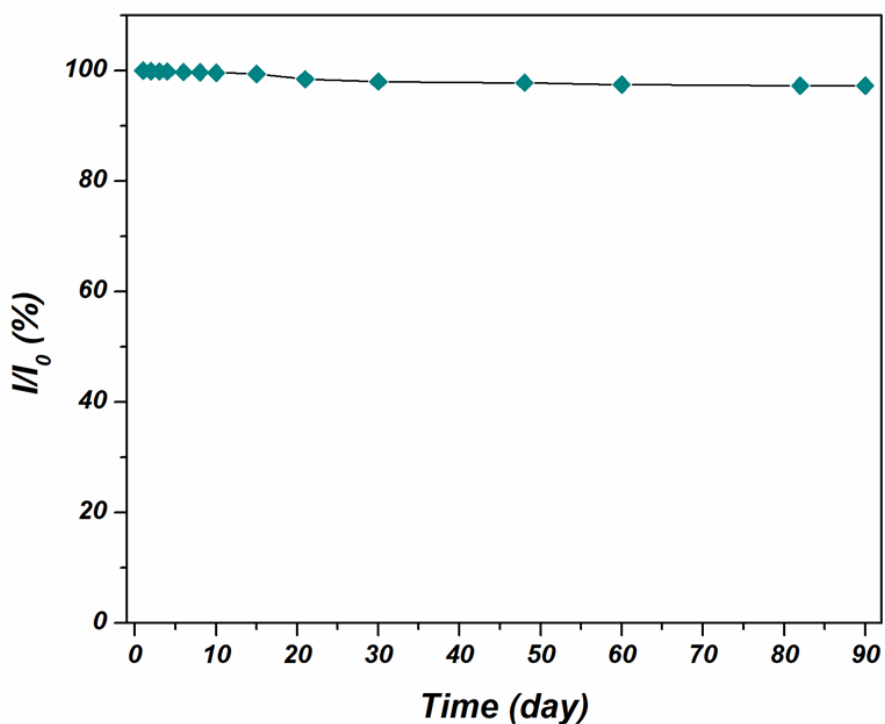


Figure 5.8. Long-term stability of as-synthesized GAAP-CDs.

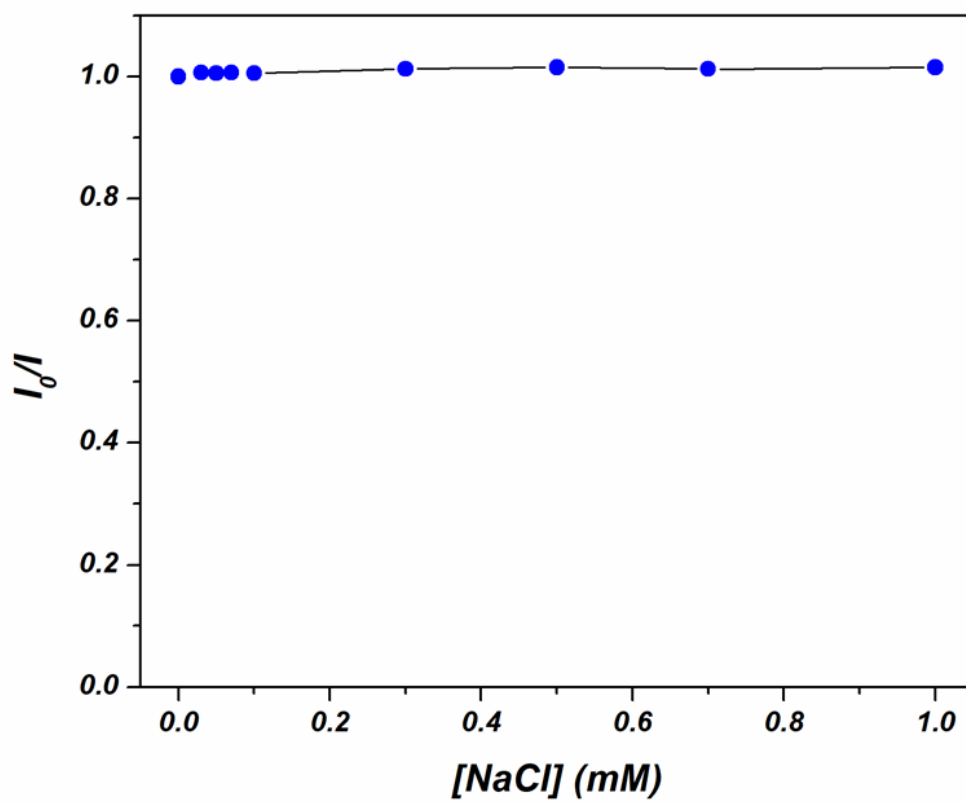


Figure 5.9. Effect of different concentrations of NaCl solutions on the emission of GAAP-CDs.

Table 5.1. The comparison of different sensors for ClO⁻ detection.

Materials	Method of detection	Limit of detection (μM)	Linear range (μM)	QY	Ref.
MTPE-M	fluorescence	0.47	0.5–110	–	[7]
4-aminoantipyrine and phenol	chromatography	10 $\mu\text{g/ml}$	47–200 $\mu\text{g/ml}$	–	[13]
Graphene quantum dots	chemiluminescence	0.3	0.5–1000	–	[14]
	fluorescence	0.41	0–10	21%	[15]
Phenothiazine probe	colorimetry	0.95	0–20		
Commercial bleach samples	potentiometric titration	0.00027 g g^{-1}	0.002–0.027 g g^{-1}	–	[16]
Boron-doped diamond	electrochemical analysis	–	0.02–1.41 M	–	[17]
APBA-ARS CDs	fluorescence	4.47	0–200	1.8%	[38]
	fluorescence	0.50	0.1–100	58.28%	Present
GAAP-CDs	absorbance	0.77	0–100		work

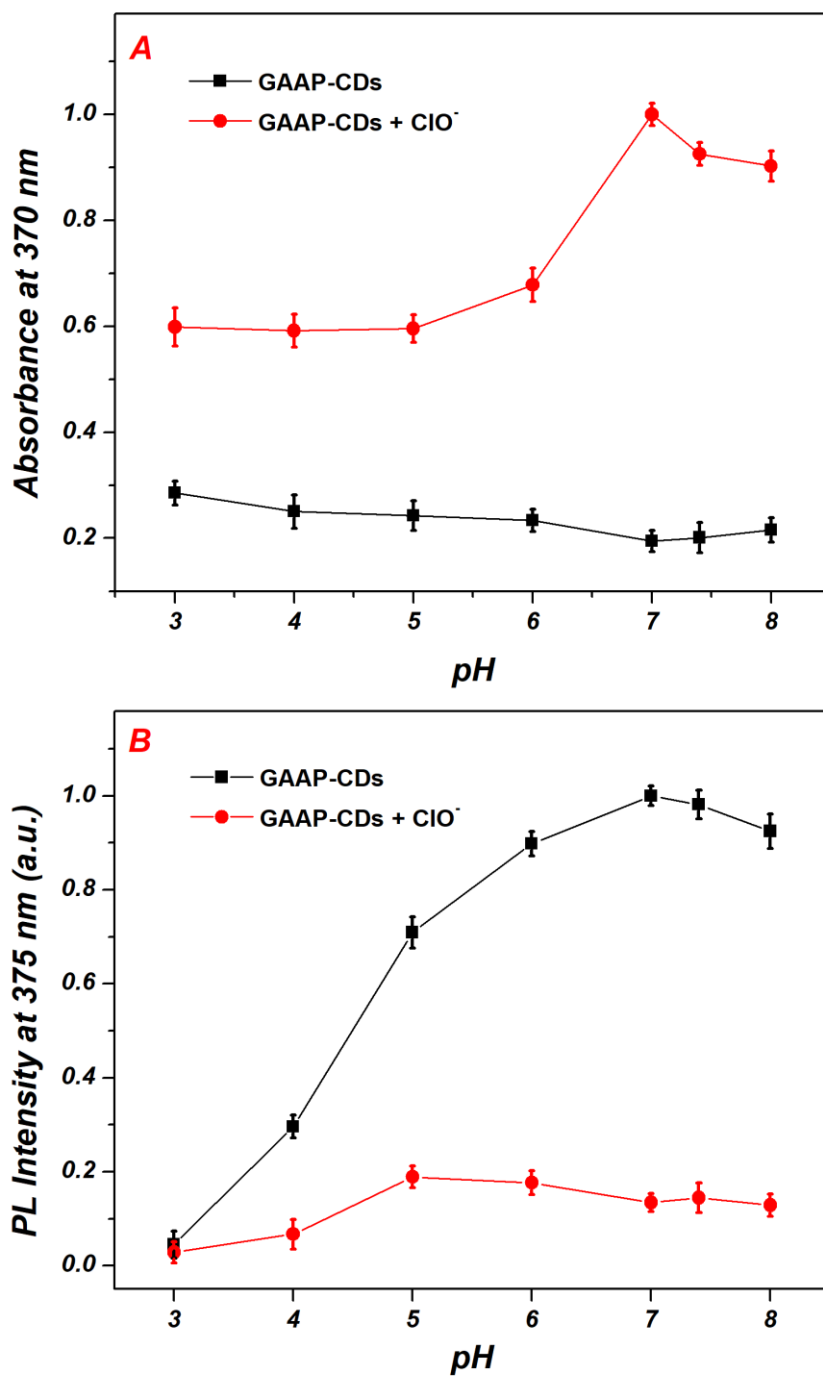


Figure 5.10. The influence of pH on (A) UV–vis absorbance at 370 nm, and (B) PL emission intensity at 375 nm of GAAP-CDs in the absence and presence of 1 mM ClO⁻ in various pH solutions, respectively. Measurement conditions: [GAAP-CDs] = 0.19 mg/mL, [ClO⁻ & interfering analytes] = 200 μM, pH = 7, and λ_{ex} = 310 nm.

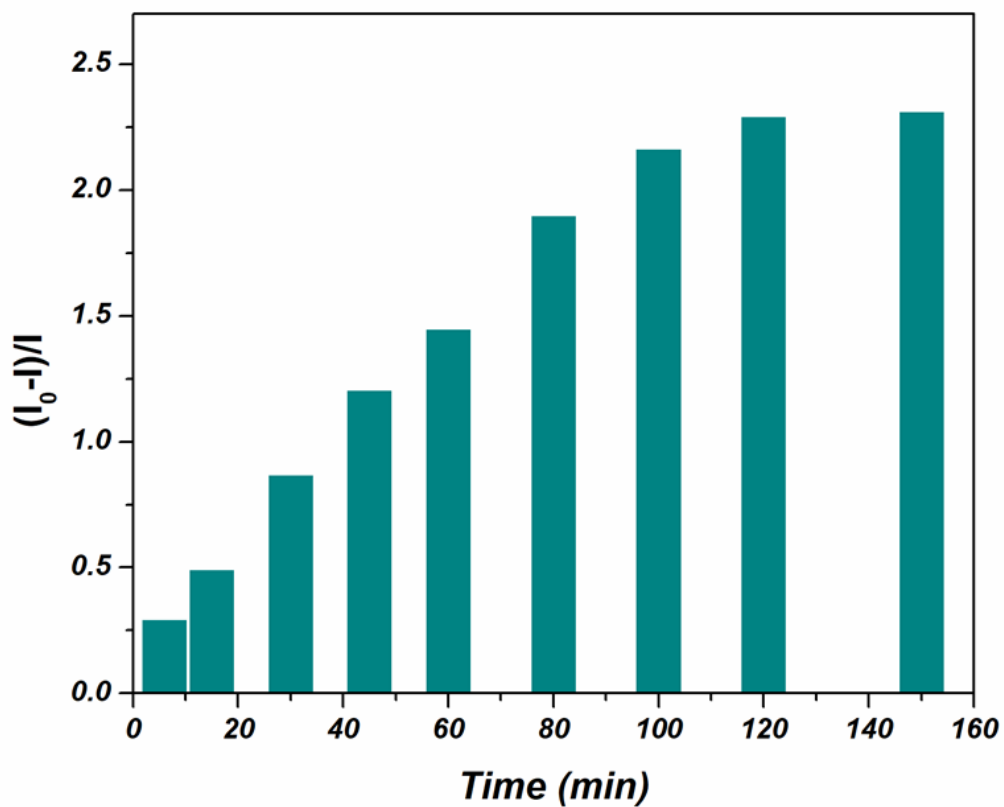


Figure 5.11. The bar diagram showing ClO⁻ mediated quenching of the fluorescence of GAAP-CDs with respect to time, [ClO⁻] = 1.0 mM, [GAAP-CDs] = 0.19 mg/mL, λ_{ex} = 310 nm.

5.3.3. ClO⁻ sensing with as-synthesized GAAP-CDs

The ClO⁻ sensing characteristics of the as-synthesized GAAP-CDs were examined by UV-vis absorption and PL emission spectra in a PBS solution (pH = 7). As shown in Figure 5.12A, the UV-vis absorption peaks at 252 nm and 370 nm increased considerably with the gradual evolution of a new peak at 490 nm as the concentration of ClO⁻ was increased. The two linear detection ranges were observed from 0 to 100 μM ($R_1^2 = 0.993$) and 100 to 1000 μM ($R_2^2 = 0.996$), respectively (Figure 5.12B). The limit of detection (LOD) of 0.77 μM ($3\sigma/K$) was obtained from the lower part of the relative absorbance vs. concentration relation. The color of the GAAP-CDs solution in the presence of various concentrations of ClO⁻ changed gradually from light yellow to dark brown (Figure 5.12C), which was attributed to the transformation of C-B bonds to C-O bonds induced by ClO⁻ ions [37]. A comparative study with respect to the previous colorimetric ClO⁻ anion assay (Table 5.1) suggested that GAAP-CDs could be used as a sensitive colorimetric sensor for ClO⁻ detection with a wider detection range.

In addition to the colorimetric detection process, a fluorometric process was also used for ClO⁻ detection because it caused the selective fluorescence quenching of GAAP-CDs. Figure 5.13A showed that with gradual addition to ClO⁻ ions, the PL emission intensities of the GAAP-CDs were quenched accordingly. The relative PL emission intensity $[(I_0-I)/I_0]$ at a wavelength of 375 nm was measured as a function of the ClO⁻ concentration ($[ClO^-]$) (Figure 5.13B) over the concentration range of 0–1000 μM. The fluorescence quenching mechanism of GAAP-CDs might be understood using a Stern-Volmer plot [24], as follows:

$$I_0 / I = 1 + K_q \tau_0 [Q] = 1 + K_{sv} [Q] \quad (5-1)$$

where K_{sv} is the Stern-Volmer constant, and $[Q]$ is the concentration of the quencher in the equation. K_q denotes the quenching rate constant, τ_0 is the average lifetime (10^{-8} s) [24]. The linearity of the plot depends on the quenching mechanism [38]. The relative PL intensity vs. concentration of analyte plot does not show overall linearity. Rather, points can be fitted into three linear regions individually as shown in Figure 5.13. The linear region at the lower part of the relative intensity vs. concentration relation shows a micromolar detection limit for ClO⁻ through fluorometric process. The LOD was observed to be 0.5 μM ($3\sigma/K$) over a

region of 0.1 μM to 100 μM with $R_1^2 = 0.995$. The GAAP-CDs in this study showed relative linear detection from both absorbance and fluorescence processes, and higher quantum yield than those reported elsewhere (Table 5.1).

The selectivity of the as-synthesized GAAP-CDs towards ClO^- ions was evaluated. The UV–vis absorption and fluorescence responses of the GAAP-CDs were examined in the presence of various interfering analytes, including H_2O_2 , D-(+)-glucose (Glu), D-(–)-fructose (Fruc), L-cystine (Cys), F^- , Cl^- , Br^- , I^- , F^- , NO_2^- , NO_3^- , H_2PO_4^- , OAc^- , N_3^- , SCN^- , SO_3^{2-} , S^{2-} , K^+ , and Na^+ in a PBS solution ($\text{pH} = 7$). The concentrations of ClO^- and all the interfering analytes were set to 200 μM . As shown in Figure 5.14, the GAAP-CDs fabricated in this study showed excellent selectivity towards ClO^- for both UV-Vis absorption and fluorescence-based experimental conditions. The high selectivity of as-synthesized GAAP-CDs was confirmed by performing an interference test in the presence of co-existing analytes, as shown in Figure 5.15. The experimental results indicated that the UV–vis absorption and PL emission responses of the GAAP-CDs towards ClO^- were relatively unaffected by other competing analytes [39]. The excellent anti-interference and high selectivity of GAAP-CDs towards ClO^- can be attributed to the boronic acid-induced specific reaction between GAAP-CDs and ClO^- .

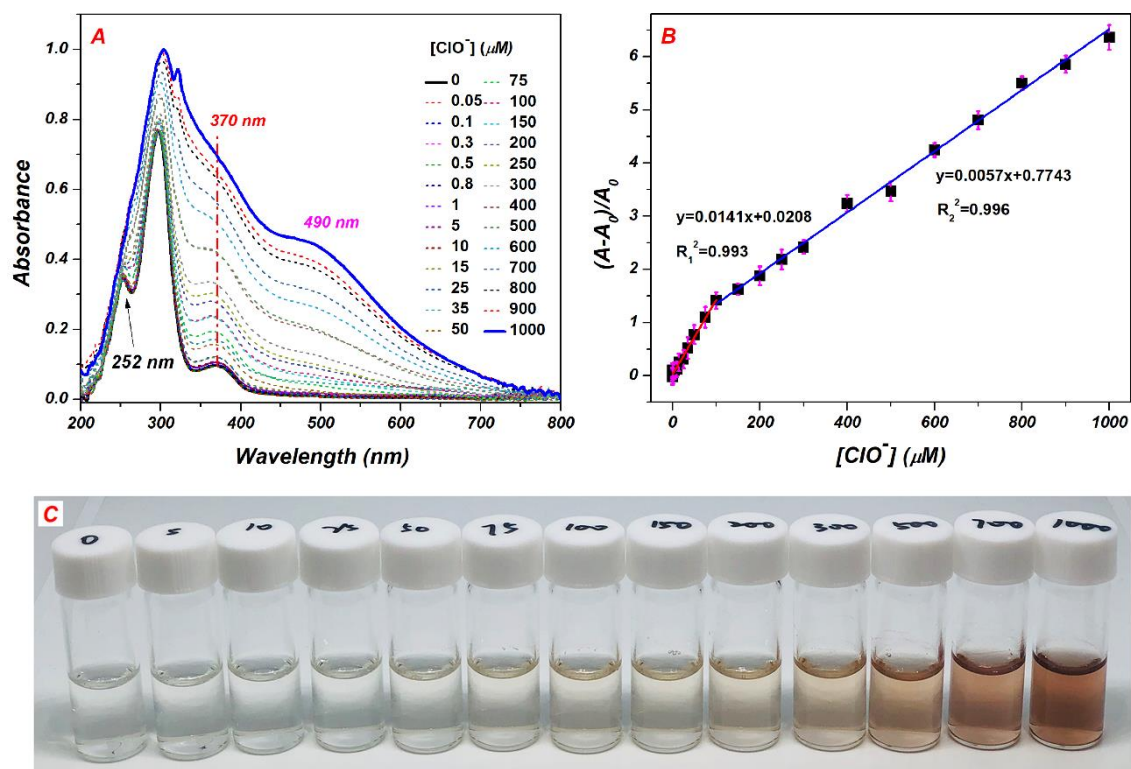


Figure 5.12. (A) The UV-vis absorbance of GAAP-CDs in the presence of various concentration of ClO^- . (B) The relative absorbance $[(A-A_0)/A_0]$ of GAAP-CDs at 370 nm vs $[\text{ClO}^-]$. (C) The photographs of GAAP-CDs in various concentration of ClO^- under visible light. Measurement conditions: $[\text{GAAP-CDs}] = 0.19 \text{ mg/mL}$, $\text{pH} = 7$, and $\lambda_{\text{ex}} = 310 \text{ nm}$.

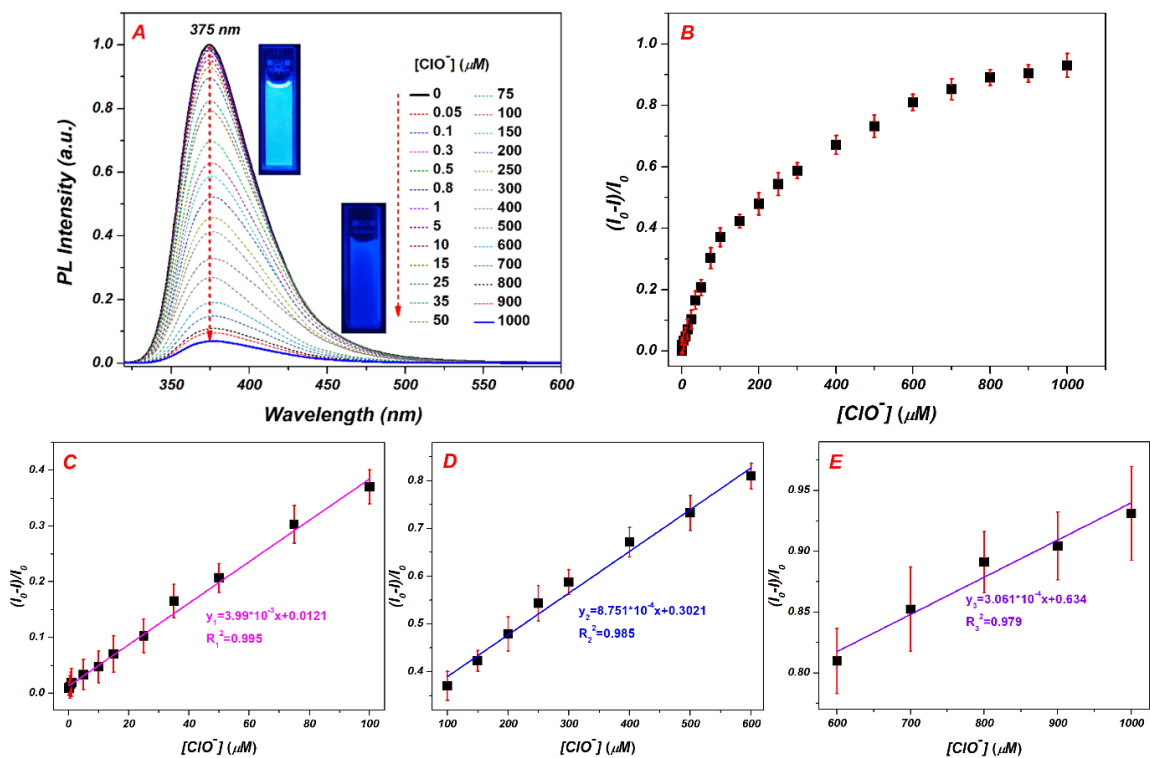


Figure 5.13. (A) Variation of the PL emission intensities of GAAP-CDs with the gradual addition of ClO^- . Inset: photographs of GAAP-CDs in the absence and presence of 1 mM ClO^- under 365 nm UV light (right). (B) Relative PL emission intensities $[(I_0-I)/I_0]$ of GAAP-CDs vs $[\text{ClO}^-]$. The linear relationships of the relative PL emission intensity vs. $[\text{ClO}^-]$ over (C) 0.1–100 μM , (D) 100–600 μM , and (E) 600–1000 μM , respectively. Measurement conditions: $[\text{GAAP-CDs}] = 0.19 \text{ mg/mL}$, $\text{pH} = 7$, and $\lambda_{\text{ex}} = 310 \text{ nm}$.

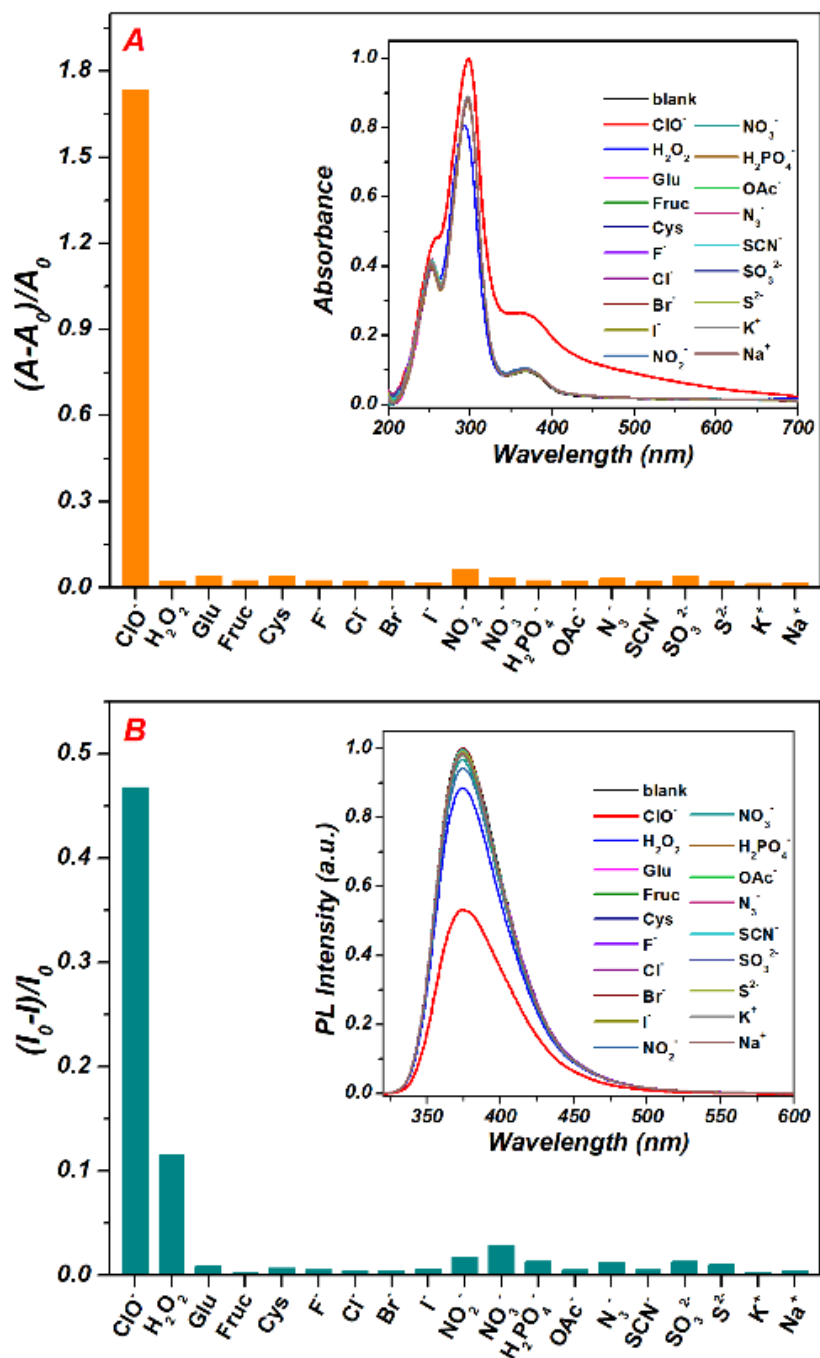


Figure 5.14. (A) Relative UV-vis absorbance and (B) relative PL emission intensity spectra of GAAP-CDs in the presence of various analytes, respectively. [Inset: (A) The absorbance and (B) PL emission intensity spectra of GAAP-CDs in the presence of various analytes, respectively.] Measurement conditions: [GAAP-CDs] = 0.19 mg/mL, [ClO^- & interfering analytes] = 200 μM , pH = 7, and λ_{ex} = 310 nm.

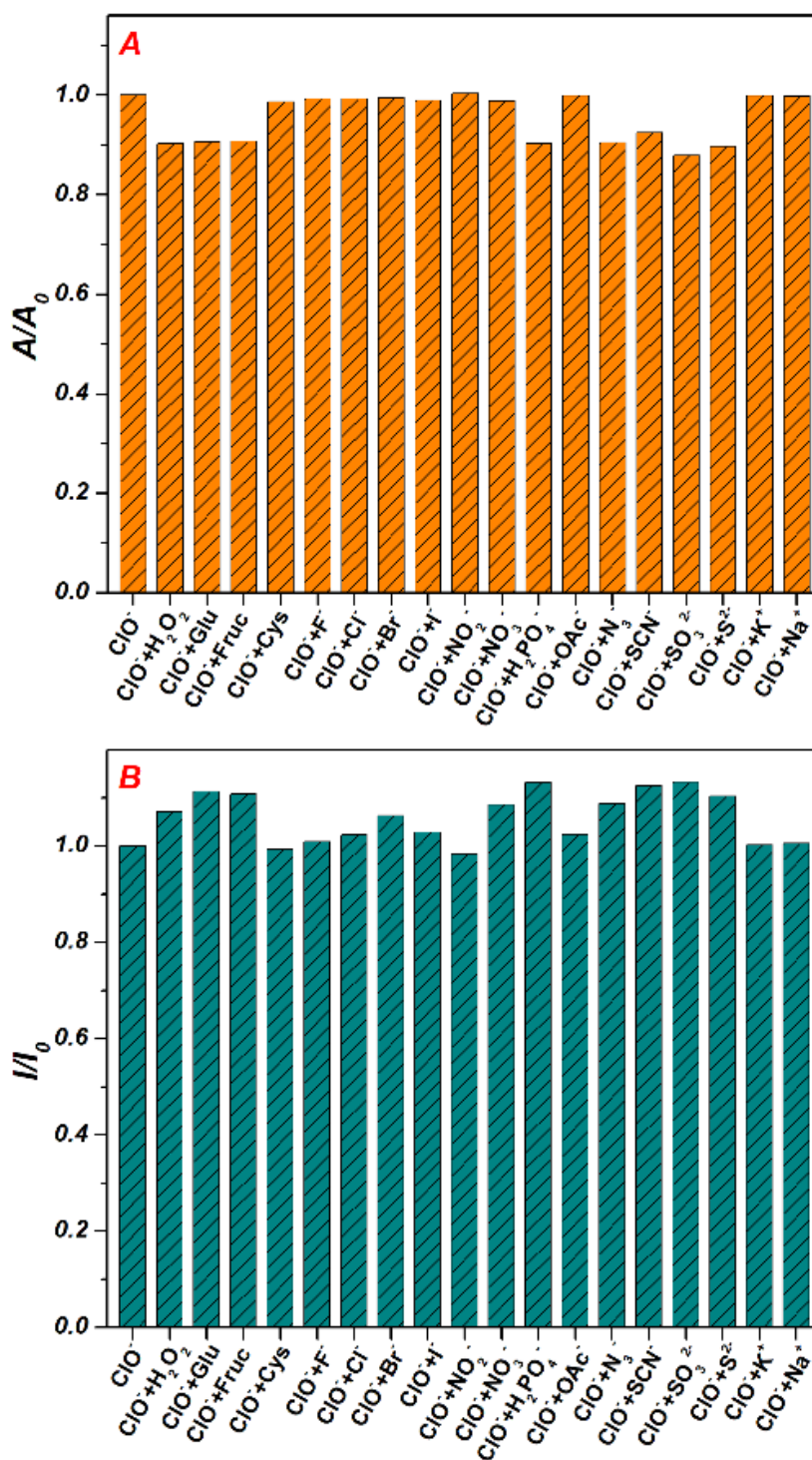


Figure 5.15. (A) The relative UV-vis absorbance and (B) relative PL emission spectra of the GAAP-CDs-ClO⁻ system in the presence of various analytes, respectively. [GAAP-CDs] = 0.19 mg/mL, [ClO⁻ & interfering analytes] = 200 μM, pH = 7, and λ_{ex} = 310 nm.

5.3.4. Fluorescence quenching mechanism

When ClO^- ions were added into the GAAP-CDs-containing aqueous solution, ClO^- promoted the transformation of C–B bonds to the C–OH groups [40, 41], leading to prominent color and spectral changes (Figure 5.16A). The possible intermolecular interaction between GAAP-CDs and ClO^- was characterized carefully by FTIR spectroscopy. As observed in Figure 5.16B, in the presence of ClO^- , the peaks for C–B disappeared, and the change of position and intensities of –OH and –NH₂ peaks were observed. These phenomena highlighted the chemical interactions between GAAP-CDs and ClO^- in aqueous solution. For further confirmation, the zeta potential of GAAP-CDs and GAAP-CDs- ClO^- were compared in PBS solution (pH = 7) (Figure 5.17). The zeta potential values of GAAP-CDs and GAAP-CDs- ClO^- were calculated to be -31.1 mV and -43.3 mV, respectively. The obvious change of the zeta potential values shows that the strong interaction between GAAP-CDs and ClO^- ions. Moreover, the change in the UV–vis spectra in the presence of ClO^- could be attributed to the change in surface functionalities in GAAP-CDs [37, 42, 43].

The quenching mechanism was examined further by measuring the fluorescence lifetimes of GAAP-CDs in the absence and presence of ClO^- . The average lifetime values calculated using equation (1) (CHAPTER 1) were 3.79 ns for GAAP-CDs and 3.22 ns for GAAP-CDs- ClO^- (at highest concentration 1 mM of ClO^-) (Figure 5.16C). Even at this much high concentration of analyte such small change in lifetime was observed, that surely indicated that the change in lifetime with analyte concentration is insignificant. The almost unaltered lifetimes under experimental conditions indicated ground state quenching [44]. Moreover, the quenching experiments were performed at RT, the results were shown in Figure 5.13. Fitting of the quenching data to the Stern-Volmer equation yielded K_q of $3.99 \times 10^{12} \text{ L}\cdot\text{mol}^{-1}\cdot\text{s}^{-1}$ for GAAP-CDs- ClO^- system, which was far greater than the maximum diffusion rate constant ($2.0 \times 10^{10} \text{ L}\cdot\text{mol}^{-1}\cdot\text{s}^{-1}$) in aqueous, suggesting that the fluorescence quenching effects were initiated by static quenching instead of dynamic collision [45]. Furthermore, there was not continuous linearity instead, three linear ranges were observed at different concentrations. Hence, the dynamic quenching was not considered. The spectral overlap of the absorbance spectrum of ClO^- and excitation spectrum of GAAP-CDs (Figure

5.18) and the insignificant changes in the lifetime and quenching experiments of GAAP-CDs in the presence of ClO^- indicates the possibility of an inner filter effect (IFE) within the system [46, 47].

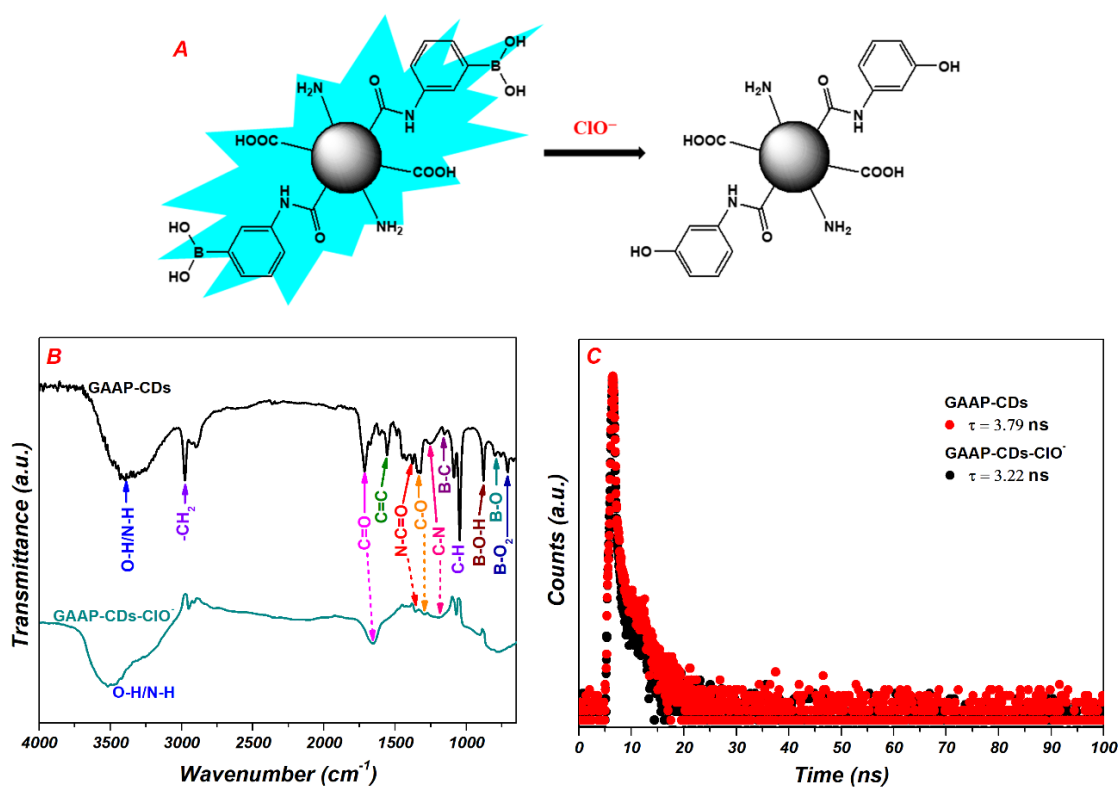


Figure 5.16. (A) Proposed reaction mechanism within GAAP-CDs- ClO^- system. (B) FTIR spectra of GAAP-CDs in the absence and presence of ClO^- , respectively. (C) Time-resolved fluorescence decay curves of GAAP-CDs and GAAP-CDs- ClO^- , respectively, and $[\text{GAAP-CDs}] = 0.19$ mg/mL, $[\text{ClO}^-] = 1$ mM, $\text{pH} = 7$, and $\lambda_{\text{ex}} = 375$ nm.

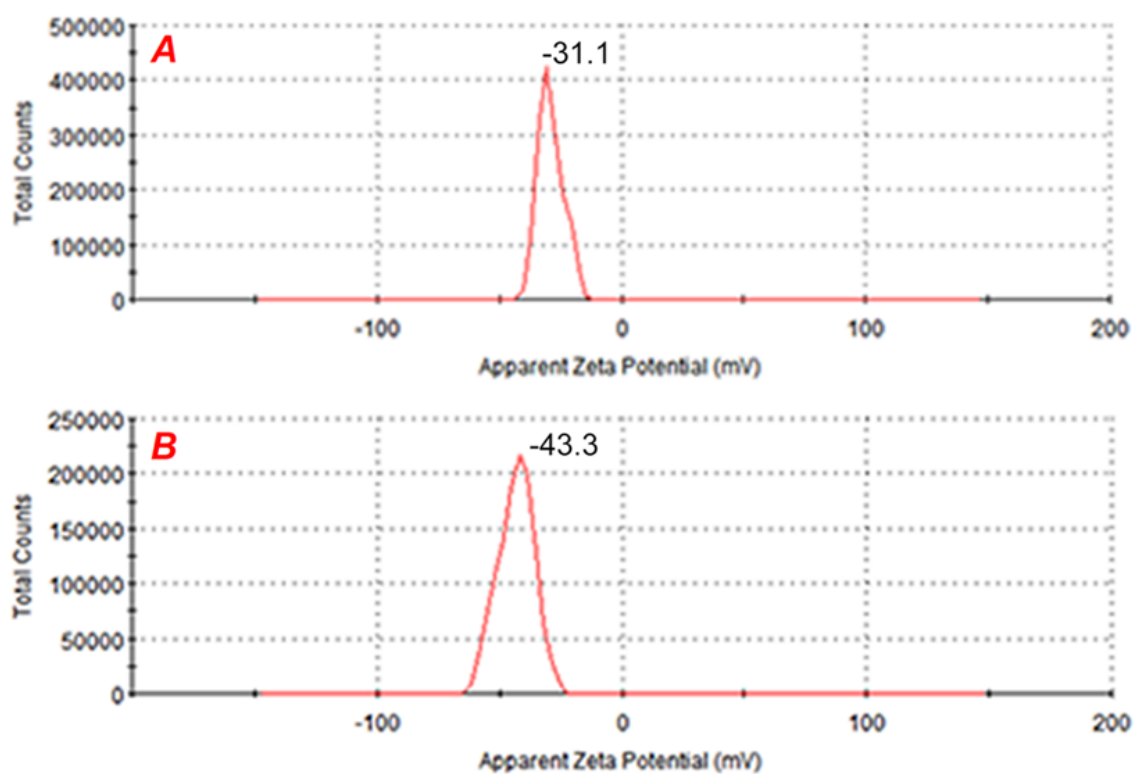


Figure 5.17. The zeta potential values for (A) GAAP-CDs and (B) GAAP-CDs-ClO⁻ (in the presence of ClO⁻), respectively. [GAAP-CDs] = 0.19 mg/mL, [ClO⁻] = 1 mM, pH = 7.

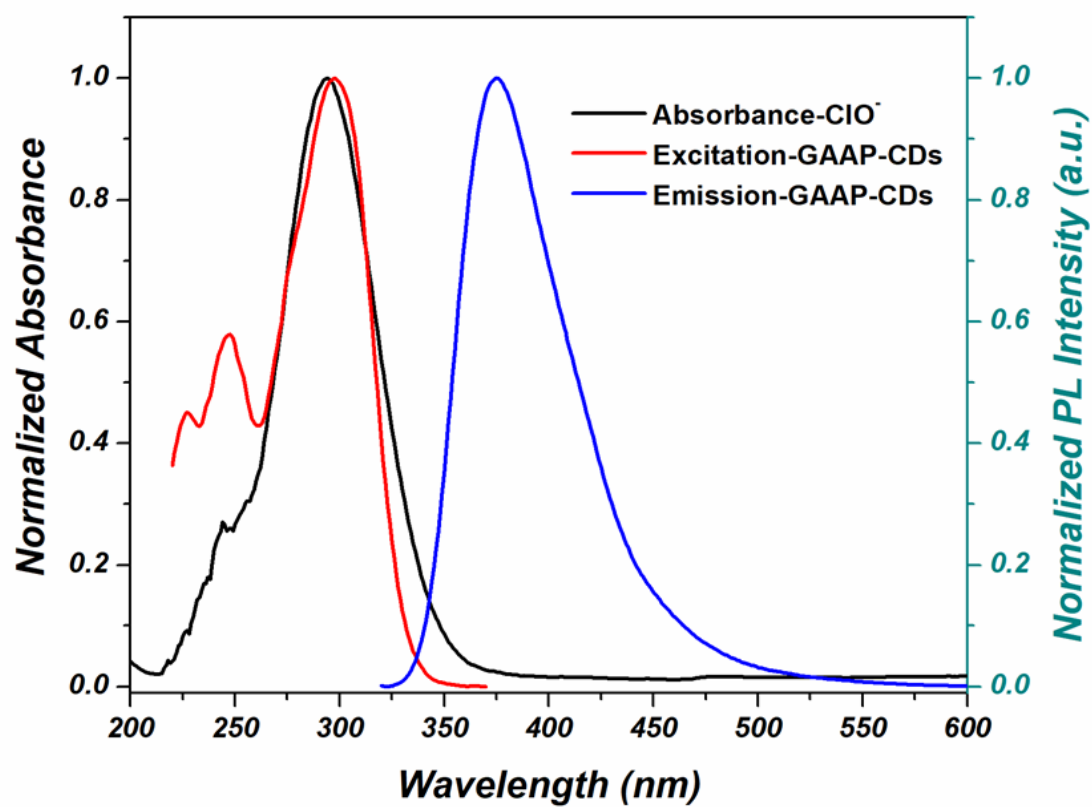


Figure 5.18. Normalized UV-vis spectrum of ClO^- overlap with normalized emission and excitation spectra of GAAP-CDs in the aqueous solution.

5.3.5. Analysis of ClO⁻ in real samples

The feasibility of the as-synthesized GAAP-CDs for detecting ClO⁻ in real samples was tested using tap water and drink water collected from the authors' department. To mimic real environmental measurements, the water samples were spiked with various concentrations of ClO⁻. The as-synthesized GAAP-CDs were then added to those samples, and the fluorescence of each sample was measured accordingly. As summarized in **Table 5.2**, excellent recovery results in ClO⁻ sensing were obtained, suggesting promising application of GAAP-CDs for ClO⁻ detection.

Table 5.2. Detection of ClO⁻ in tap water and drink water samples (n=3).

	Samples	Spiked (μM)	Found (μM)	Recovery (%)	RSD (%)
Tap water	I	–	1.32	–	0.02
	II	25	25.10	100.4	1.84
	III	50	49.58	99.2	1.32
	IV	100	100.77	100.8	0.60
Drink water	I	–	0.91	–	0.22
	II	25	24.85	99.4	1.43
	III	50	50.35	100.7	1.80
	IV	100	99.84	99.8	0.71

5.4. Conclusion

High quantum yield GAAP-CDs were synthesized with GA and 3-APPA using a simple hydrothermal process. The as-synthesized GAAP-CDs showed excellent sensitivity and selectivity towards highly toxic ClO^- ions with wide linear ranges in both the UV-vis- and photoluminescence-based sensing experiments. The incorporated nitrogen atoms enhanced the quantum yield, and boronic acid induced excellent selectivity towards ClO^- ions. Instrumental analyses revealed a specific reaction between the boronic acid of GAAP-CDs and ClO^- , resulting in high selectivity and quenching via static quenching instead of a dynamic quenching mechanism. Furthermore, the as-synthesized GAAP-CDs showed precise ClO^- level monitoring, even for the real samples, such as tap water and drinking water.

Reference

- [1] H. N. Siti, Y. Kamisah, J. Kamsiah. *Vascular Pharmacology*, 2015, 71, 40-56.
- [2] R. K. Gupta, A. K. Patel, N. Shah, A. K. Choudhary, U. K. Jha, U. C. Yadav, P. K. Gupta, U. Pakuwal. *Asian Pacific Journal of Cancer Prevention*, 2014, 15, 4405-4409.
- [3] X. Chen, F. Wang, J. Y. Hyun, T. Wei, J. Qiang, X. Ren, I. Shin, J. Yoon. *Chem Soc Rev*, 2016, 45, 2976-3016.
- [4] S. Goswami, A. Manna, S. Paul, C. K. Quah, H.-K. Fun. *Chem Commun*, 2013, 49, 11656-11658.
- [5] K. Xiong, F. Huo, C. Yin, Y. Chu, Y. Yang, J. Chao, A. Zheng. *Sensors and Actuators B: Chemical*, 2016, 224, 307-314.
- [6] H. Chen, T. Sun, X. Qiao, Q. Tang, S. Zhao, Z. Zhou. *Spectrochimica Acta Part A: Molecular and Biomolecular Spectroscopy*, 2018, 204, 196-202.
- [7] X. Lou, Y. Zhang, J. Qin, Z. Li. *Sensors and Actuators B: Chemical*, 2012, 161, 229-234.
- [8] Y. Zhou, K. Song, R. G. Painter, M. Aiken, J. Reiser, B. A. Stanton, W. M. Nauseef, G. Wang. *Journal of innate immunity*, 2013, 5, 219-230.

- [9] Y. Huang, P. Zhang, M. Gao, F. Zeng, A. Qin, S. Wu, B. Z. Tang. *Chem Commun*, 2016, 52, 7288-7291, 2016, 52, 7288-7291.
- [10] L. Lu, J. Zhang, X. Yang. *Sensors and Actuators B: Chemical*, 2013, 184, 189-195.
- [11] D. Li, J. Sun, Z. Gan, H. Chen, D. Guo. *Analytica Chimica Acta*, 2018, 1018, 104-110.
- [12] C. Gorrini, I. S. Harris, T. W. Mak. *Nature Reviews Drug Discovery*, 2013, 12, 931-947.
- [13] T. Watanabe, T. Idehara, Y. Yoshimura, H. Nakazawa. *Journal of Chromatography A*, 1998, 796, 397-400.
- [14] T. Hallaj, M. Amjadi, J. L. Manzoori, R. Shokri. *Microchimica Acta*, 2015, 182, 789-796.
- [15] L. Wang, Y. Hu, Y. Qu, J. Xu, J. Cao. *Dyes and Pigments*, 2016, 128, 54-59.
- [16] F. B. Gonzaga, L. R. Cordeiro. *Accreditation and Quality Assurance*, 2014, 19, 283-287.
- [17] R. E. P. Meyler, M. A. Edwards, J. V. Macpherson. *Electrochemistry Communications*, 2018, 86, 21-25.
- [18] J. R. Lakowicz. Springer, Boston, MA, 2006.
- [19] L. Wang, J. S. Chung, S. H. Hur. *Dyes and Pigments*, 2019, 171, 107752.
- [20] S. Zhu, Q. Meng, L. Wang, J. Zhang, Y. Song, H. Jin, K. Zhang, H. Sun, H. Wang, B. Yang. *Angewandte Chemie*, 2013, 125, 4045-4049.
- [21] S. Wang, Z. Chen, I. Cole, Q. Li. *Carbon*, 2015, 82, 304-313.
- [22] S. Y. Lim, W. Shen, Z. Gao. *Chemical Society Reviews*, 2015, 44, 362-381.
- [23] J. Wu, W. Liu, J. Ge, H. Zhang, P. Wang. *Chemical Society Reviews*, 2011, 40, 3483-3495.
- [24] H. Wu, J. Jiang, X. Gu, C. Tong. *Microchimica Acta*, 2017, 184, 2291-2298.
- [25] G. Tong, J. Wang, R. Wang, X. Guo, L. He, F. Qiu, G. Wang, B. Zhu, X. Zhu, T. Liu. *Journal of Materials Chemistry B*, 2015, 3, 700-706.
- [26] X. Gong, W. Lu, M. C. Paa, Q. Hu, X. Wu, S. Shuang, C. Dong, M. M. F. Choi. *Analytica Chimica Acta*, 2015, 861, 74-84.

- [27] K. S. Vasu, S. S., S. Sampath, A. K. Sood. *Sensors and Actuators B: Chemical*, 2015, 221, 1209-1214.
- [28] A. Bigdeli, F. Ghasemi, S. Abbasi-Moayed, M. Shahrajabian, N. Fahimi-Kashani, S. Jafarinejad, M. A. Nejad, M. R. Hormozi-Nezhad. *Analytica Chimica Acta*, 2019, 1079, 30-58.
- [29] Y. Han, D. Tang, Y. Yang, C. Li, W. Kong, H. Huang, Y. Li, Z. Kang. *Nanoscale*, 2015, 7, 5955-5962.
- [30] Z. Li, H. Yu, T. Bian, Y. Zhao, C. Zhou, L. Shang, Y. Liu, L. Wu, C. Tung, T. Zhang. *Journal of Materials Chemistry C*, 2015, 3, 1922-1928.
- [31] P. Shen, Y. Xia. *Analytical chemistry*, 2014, 86, 5323-5329.
- [32] X. Liu, X. Hu, Z. Xie, P. Chen, X. Sun, J. Yan, S. Zhou. *Analytical Methods*, 2016, 8, 3236-3241.
- [33] Z. Yang, M. Xu, Y. Liu, F. He, F. Gao, Y. Su, H. Wei, Y. Zhang. *Nanoscale*, 2014, 6, 1890-1895.
- [34] Z. Yang, X. Li, J. Wang. *Carbon*, 2011, 49, 5207-5212.
- [35] W. U. Khan, D. Wang, Y. Wang. *Inorganic chemistry*, 57(24), 2018, 57, 15229-15239.
- [36] D. Zhong, H. Miao, K. Yang, X. Yang. *Materials Letters*, 2016, 166, 89-92.
- [37] Q. Wang, C. Liu, J. Chang, Y. Lu, S. He, L. Zhao, X. Zeng. *Dyes and Pigments*, 2013, 99, 733-739.
- [38] R. J. Campbell, E. W. Schlag, B. W. Ristow. *Journal of the American Chemical Society*, 1967, 89, 5098-5102.
- [39] E. F.C.Simões, L. P. d. Silva, J. C. G. E. Silva, J. M. M. Leitão. *Talanta*, 2020, 208, 120447.
- [40] A. Sikora, J. Zielonka, M. Lopez, J. Joseph, B. Kalyanaraman. *Free Radical Biology and Medicine*, 2009, 47, 1401-1407.
- [41] J. Zielonka, A. Sikora, M. Hardy, J. Joseph, B. P. Dranka, B. Kalyanaraman. *Chemical research in toxicology*, 2012, 25, 1793-1799.

- [42] P. Zhang, Y. Wang, L. Chen, Y. Yin. *Microchimica Acta*, 2017, 184, 3781-3787.
- [43] Z. Wang, X. Jin, Y. Gao, F. Kong, W. Wang, W. Wang. *Microchimica Acta*, 2019, 186, 1-9.
- [44] G. Li, ChanglunTong. *Analytica Chimica Acta*, 2020, 1133, 11-19.
- [45] H. Wu, C. Tong. *Journal of agricultural and food chemistry*, 2019, 67, 2794-2800.
- [46] Z. Mohammadpour, A. Safavi, A. Omidvar, A. Mohajeri, N. Mobaraki, M. Shamsipur. *Journal of Fluorine Chemistry*, 2016, 190, 12-22.
- [47] A. Abbasia, M. Shakir. *New Journal of Chemistry*, 2018, 42, 293-300.

CHAPTER 6. A selective and sensitive sensor for fluorescent determination of nitrite based on high quantum yield nitrogen and boron doped carbon nanodots

6.1. Introduction

Nitrite ions (NO_2^-) are treated to be an important nitrogen-containing composition played a significant role in the nitrogen cycle of the nature. Nitrites are usually used as fertilizer for plants [1]. Nitrites are extensively as food additive, for improving the presentation and flavors and storing [2]. Moreover, nitrite is considered to be an inorganic contaminants in drinking water, and an excessive intake can lead to healthy problems, such as blue baby syndrome, hypertension and esophageal cancer [3-5]. The World Health Organization (WHO) has stipulated the maximum amount of nitrite ions in drinking water should not exceed 3 mg/L or 65 μM [6]. Therefore, the nitrite determination in monitoring the drinking water quality and living environment has become extremely significant. Various analytical techniques have been employed and utilized for nitrite ions detection, including electrochemistry [7], spectrophotometry [8], ion chromatography [9], chemiluminescence [10], surface-enhanced Raman scattering spectroscopy [11], and fluorescence sensing methods [12, 13]. Due to the expensive and complicated instruments, toxic raw materials and solvents, and complicated synthetic pathways of some methods, the development of a nontoxicity, simple operation, low-cost synthesis, high selectivity, and excellent sensitivity nitrite detecting method has become important.

Recently, carbon dots synthesized by different processes have been extensively explored [14, 15]. Compared with the conventional detecting methods, carbon dots have some unique properties, such as low-cost, non-toxic, easy synthesis, chemically resistant, water-soluble, photostability, wide absorption range, tunable emission and high quantum yield [16-19]. Owing to their unique physic-chemical properties, carbon dots have been successfully employed for electrochemistry, photocatalysts, bioimaging, biosensing, intelligent drug delivery, and environmental applications [20-24]. The target determination

is usually observed through the fluorescence quenching or enhancement of carbon dots in the presence of analytes. The sensing mechanisms mainly involve photoinduced electron transfer (PET), inner filter effect (IFE), Forster resonance energy transfer (FRET), static quenching, and dynamic quenching [25, 26].

In this work, low-cost and abundant nitrogen and boron-doped high quantum yield carbon dots (CPAP-CDs) with a mean particle diameter of 3.07 nm were successfully synthesized through the facile hydrothermal process at 240 °C for 4h. The obtained CPAP-CDs showed wide absorption and strong fluorescence in solutions, the quantum yield can be achieved to 64.07%. The presence of the heteroatoms to the core and surface functional groups have modified the optoelectronic property, surface and local chemical reactivity of the obtained carbon dots [27]. As a nanosensor, the CPAP-CDs exhibited enormous potential for selective and sensitive sensing of nitrite in water. In the present experiment, the bright fluorescence of CPAP-CDs was quenched in the presence of nitrite. The detection limit as low as 6.6 nM. It was assumed that there would be a diazotization between nitrites and the amino groups on the surface of CPAP-CDs results in aggregation of CPAP-CDs that quenching the inherent fluorescence. The effects of synthesis conditions, pH and the interference effect of other anions for carbon dots were studied in detail. The obtained carbon dots have been used for real water samples analysis, such as tap, drinking and sea water.

6.2. Experimental details

6.2.1. Materials

3-Aminophenylboronic acid monohydrate (3-APBA), 3-Carboxyphenylboronic acid (3-CPBA), quinine sulfate (QS), sodium nitrite (NaNO_2), sodium nitrate (NaNO_3), sodium tetraborate decahydrate ($\text{Na}_2\text{B}_4\text{O}_7 \cdot 10\text{H}_2\text{O}$), sodium carbonate anhydrous (Na_2CO_3), sodium sulfide pentahydrate ($\text{Na}_2\text{S} \cdot 5\text{H}_2\text{O}$), di-sodium hydrogen phosphate (Na_2HPO_4), sodium azide (NaN_3), potassium thiocyanate (KSCN), sodium iodide (NaI), sodium bromide (NaBr), sodium chloride (NaCl), sodium fluoride (NaF), potassium dihydrogen phosphate (KH_2PO_4), sodium acetate (NaAc) and acetic acid (HAc) were purchased from Sigma-Aldrich Co. (USA). All chemicals were analytical grade reagents and used as purchased without further purification. The deionized (DI) water with a resistivity

of 18.2 M Ω was used for the preparation of the samples in all experiments.

6.2.2. Characterization

An ultrasonic treatment was performed using a UPC-10 (Jeio-Tech Co., Ltd., South Korea). The analysis of functional groups was done using the Fourier Transform Infrared (FTIR, Nicolet iS5, Thermo Fisher Scientific, USA) spectroscopy. X-ray diffraction (XRD, D/MAZX 2500V/PC model, Rigaku, Japan) was carried out using Cu K α radiation (40 kV, 30 mA, $\lambda = 1.5415 \text{ \AA}$) at a scan rate of 2° min^{-1} over the 2θ range of $10\text{-}80^\circ$. X-ray photoelectron spectroscopy (XPS, Thermo ESCALAB 250 Xi, Thermo Fisher Scientific, USA) was performed using Al K α X-ray radiation (1486.6 eV) to determine the oxidation states of the constituent elements. High-resolution transmission electron microscopy (HR-TEM, JEM-2100 F, JEOL, Japan) images were taken at an operating voltage of 200 kV.

Ultraviolet visible (UV-vis, SPECORD 210 PLUS, Analytik Jena, Germany) absorption spectroscopy was performed. The photoluminescence spectra (PL) were recorded using a Cary Eclipse fluorescence spectrophotometer (Agilent Technologies, USA) with a 1.0 cm quartz cell.

6.2.3. Synthesis of CPAP-CDs

To prepare CPAP-CDs, 3-Carboxyphenylboronic acid (3-CPBA, 0.2 M 1 mL) and 3-Aminophenylboronic acid monohydrate (3-APBA, 0.2 M 1 mL) were added to 10 mL deionized water and sonicated for 5 min to produce a well-dispersed homogenous solution. Then, the mixture was transferred to a 50 mL Teflon-lined autoclave, and it heated and maintained at 240°C for 4h in an oven for further reaction. After cooling down to the room temperature, CPAP-CDs was collected after removing the suspended particles via centrifugate at 10000 rpm for 10 min and further purified by using dialysis tube (3500 Da) for 4 h to remove the residual chemicals. The obtained yellowish CPAP-CDs solution was stored at RT for further characterization.

Figure 6.1 exhibited the precursor ratio and reaction temperature were optimized to obtain the highest fluorescence for CPAP-CDs.

6.2.4. NO₂⁻ sensing

To determine the NO₂⁻ level, various amounts of NO₂⁻ were added into 2 mL of HOAc–NaOAc solutions (pH = 3.0) containing 0.22 mg/mL CPAP-CDs. After shaking constantly around 2 h at room temperature, the photoluminescence intensity of each sample was measured at 421 nm under an excitation wavelength of 370 nm. All photoluminescence experiments were measured with 2.5 nm excitation slit and 5 nm emission slit. The selectivity of NO₂⁻ detection towards interfering species was examined in a similar manner, as described above except that the interfering species were added to the solution with the ratio 1 : 1.

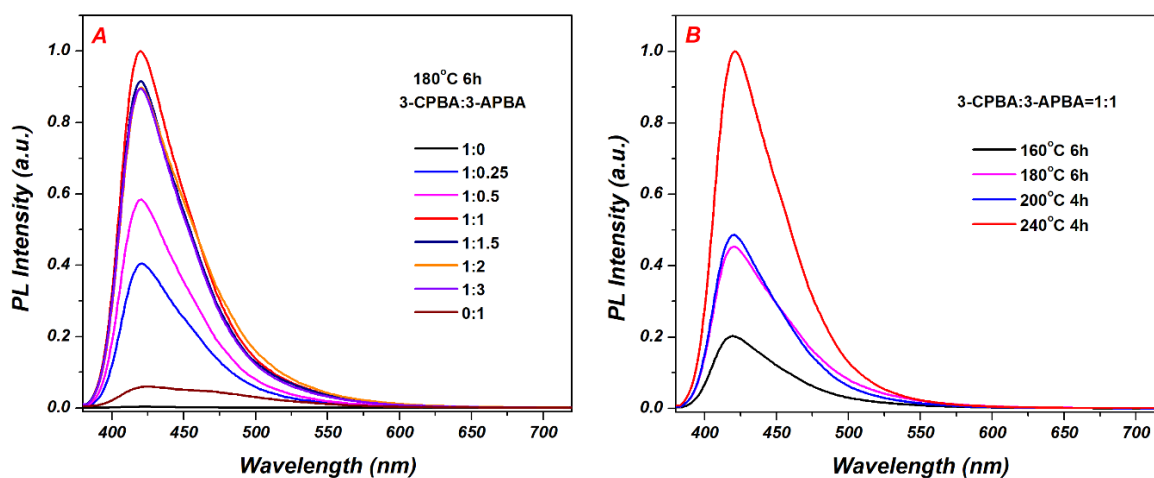


Figure 6.22. (A) The precursor ratio and (B) reaction temperature were optimized to obtain the highest fluorescence for CPAP-CDs.

6.3. Results and discussion

6.3.1. Characterization of CPAP-CDs

Figure 6. 2A showed the transmission electron microscopy (TEM) image of the as-obtained CPAP-CDs. The particles were distributed with a mean particle diameter of 3.07 nm (Figure 6. 2B). The selected area electron diffraction (SAED) pattern exhibited the amorphous nature of CPAP-CDs (image inset in Figure 6. 2A). The X-ray Powder Diffraction (XRD) pattern in Figure 6. 2C presented a distinct broad single diffraction peak approximately at $2\theta = 21^\circ$, which corresponds to the amorphous carbon [28]. Fourier transform infrared spectroscopy (FTIR) and X-ray photoelectron spectroscopy (XPS) were employed to investigate the elemental composition and functional groups of the obtained particles. As observed by FTIR spectrum in Figure 6. 2D, the characteristic peaks at around 3455 cm^{-1} , $3346\text{--}3228\text{ cm}^{-1}$, 1655 cm^{-1} , 1553 cm^{-1} , 1399 cm^{-1} , 1358 cm^{-1} , 1294 cm^{-1} , 1161 cm^{-1} , and 1070 cm^{-1} , which were corresponded to the stretching vibration of O–H, stretching vibration of $-\text{NH}_2$, stretching vibration of C=O, stretching vibration of C=C, stretching vibration of B–O, stretching vibration of C–N, stretching vibration of C–O, stretching vibration of B–O–H, and stretching vibration of C–H, respectively [16, 29]. As shown in Figure 6. 3, the XPS spectra revealed that CPAP-CDs were comprised by carbon, oxygen, boron, and nitrogen elements. The high-resolution C1s XPS spectra of CPAP-CDs could be fitted to four peaks centered at ~ 282.18 , ~ 282.68 , ~ 284.17 , and ~ 286.80 eV, which were assigned to C–B, C–C/C=C, C–O, and N–C=O, respectively [30]. The O1s XPS spectrum could be resolved into three peaks with centered at ~ 529.52 , ~ 530.43 , and ~ 531.72 eV, originated from C=O, C–O, and B–O bonds, respectively [31]. The B 1s XPS spectrum of CPAP-CDs could also be deconvoluted into two peaks at ~ 189.69 and ~ 191.24 eV corresponding to B–C and B–O bonds, respectively [32]. Fitting of the N1s XPS spectra exhibited two main peaks at ~ 397.54 and ~ 399.20 eV, which were attributed to N–C and N–H bonds, respectively [33]. The above characterization analysis indicated that the as-obtained CPAP-CDs might have functional groups, such as $-\text{NH}_2$, $-\text{COOH}$ and N–C=O, which might be associated with the carbonized entity.

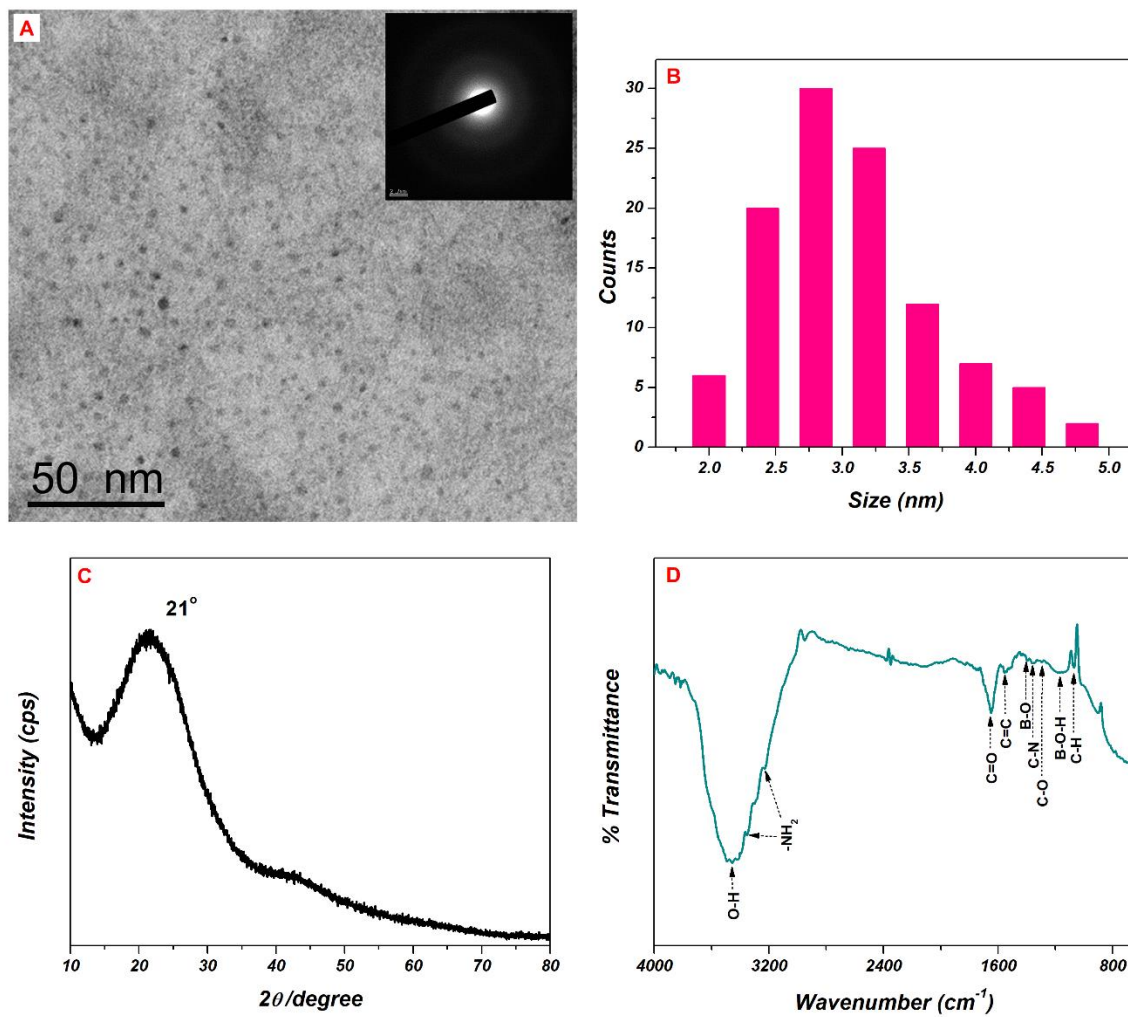


Figure 6.23. (A) TEM image (Inset: SAED image), (B) particle size distribution, (C) XRD pattern, and (D) FTIR spectrum of CPAP-CDs.

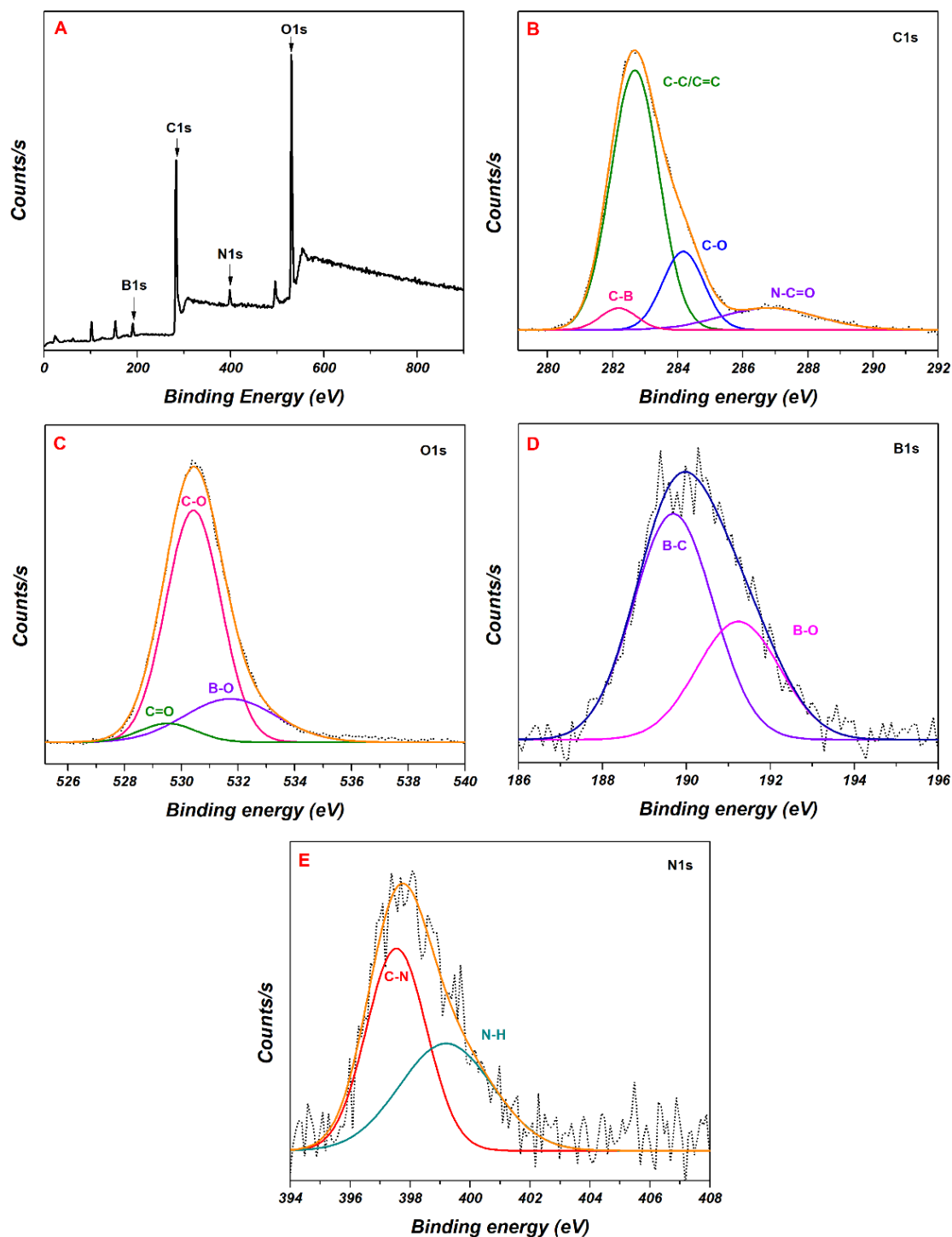


Figure 6.24. (A) XPS survey spectra of CPAP-CDs. The high-resolution XPS spectra of (B) C1s, (C) O1s, (D) B1s, and (E) N1s for CPAP-CDs. XPS analysis was done using the vacuum dried solid under 60 °C.

6.3.2. Optical properties of CPAP-CDs

The UV–vis absorption and PL emission spectroscopy were conducted to examine the optical properties of the as-obtained CPAP-CDs. As shown in Figure 6. 4A, the UV–vis absorption spectra of CPAP-CDs revealed two distinct peaks at 283 and 373 nm, which were attributed to the π – π^* electronic transition of the aromatic C=C bond and n– π^* electronic transition of C=O bond, respectively [34, 35]. The CPAP-CDs aqueous solution emitted strong blue fluorescence under UV light at a wavelength of 365 nm. While excited at 370 nm, CPAP-CDs showed strong fluorescence with the maximum emission of 421 nm. The inset photograph showed that the CPAP-CDs in aqueous solution were slightly yellow under visible light and emitted bright blue fluorescence under UV light. The fluorescence excitation spectra of the CPAP-CDs with a maximum emission at 421 nm, showed a peak approximately at 370 nm. When the excitation wavelength was varied from 290 to 400 nm in 10 nm increments (Figure 6. 4B), the PL emission spectra exhibited the excitation wavelength-dependent fluorescence behavior, which was attributed to the different sizes or the various surface functional groups of CPAP-CDs [16, 36]. The fluorescence quantum yield (QY) was examined to be 64.07% using quinine sulfate (QS) aqueous (0.1 M H₂SO₄) as a reference (Figure 6. 5). The lifetime was calculated to be 9.05 ns from the fluorescence decay profile (Figure 6. 6). The stability of CPAP-CDs was examined with respect to the emission intensity over 120 days (Figure 6. 7). The results exhibited the long-term stability and usability of CPAP-CDs. Besides, the stability of CPAP-CDs in NaCl solutions with different concentrations was examined (Figure 6. 8). The results showed no noticeable fluorescence change, also revealing the substantial stability of the as-synthesized CPAP-CDs, even at high ionic concentrations. Furthermore, CPAP-CDs was found to be responsive to pH. While increasing the pH value, the PL emission was quite significantly decreased (Figure 6. 9). Previously it was reported that the hydrophilicity and dispersion of carbon dot particles increase at low pH [21, 37].

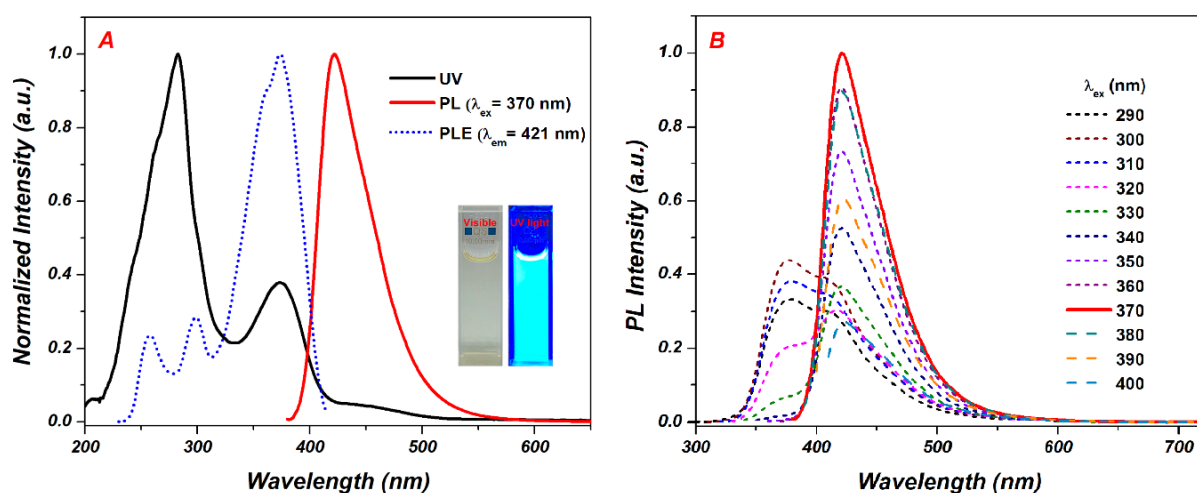


Figure 6.25. (A) Spectra of CPAP-CDs, blank line: UV–vis absorbance, peaks at 283 and 373 nm; red line: PL emission spectra at excitation wavelength of 370 nm; blue dot line: PL excitation spectra at the emission wavelength of 421 nm. The inset shows the photographs of CPAP-CDs under visible light (left) and UV light (right). (B) PL emission spectra of CPAP-CDs with different excitation wavelengths.

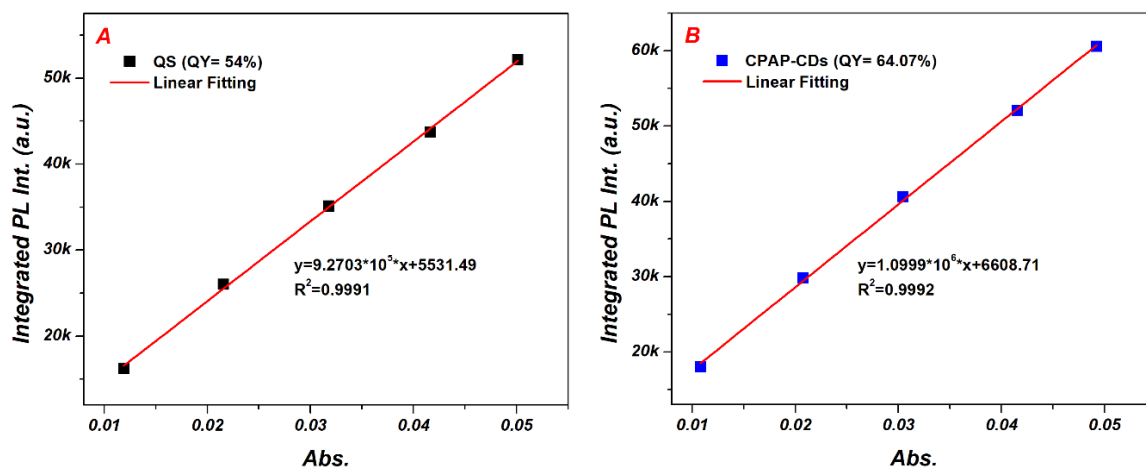


Figure 6.26. Plots integrated PL intensity of quinine sulfate (QS, the reference) and CPAP-CDs as a function of optical absorbance at 360 nm and relevant data.

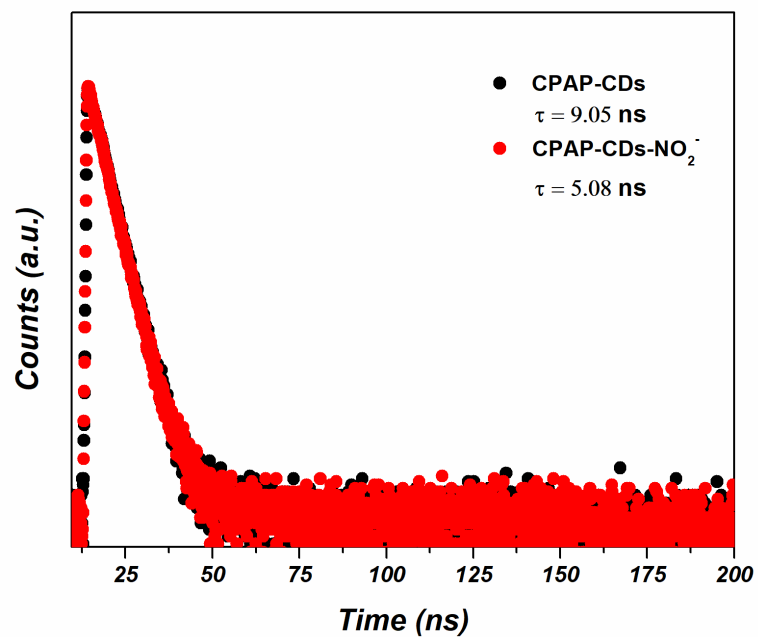


Figure 6.27. Time-resolved fluorescence decay curves of CPAP-CDs and CPAP-CDs- NO_2^- , respectively, and $[\text{CPAP-CDs}] = 0.22 \text{ mg/mL}$, $[\text{NO}_2^-] = 1 \text{ mM}$, $\text{pH} = 3$, and $\lambda_{\text{ex}} = 375 \text{ nm}$.

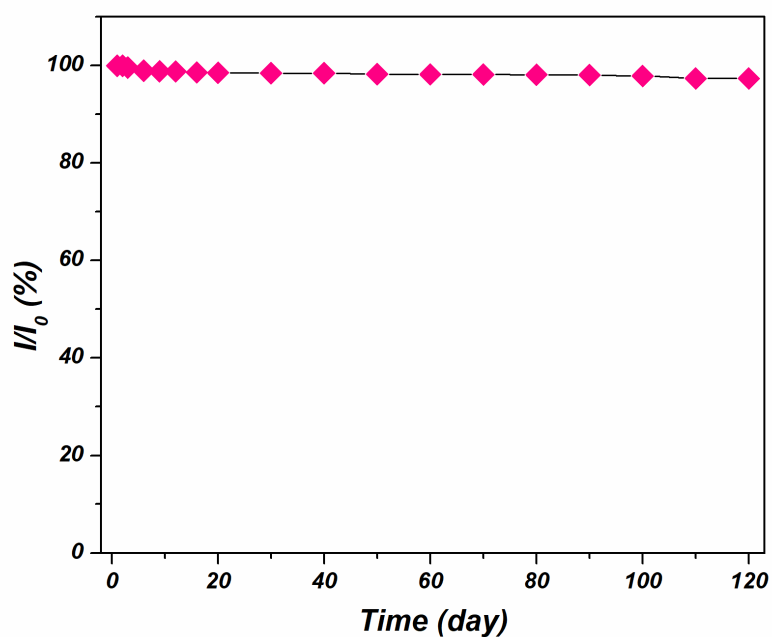


Figure 6.28. Stability of CPAP-CDs with the relative PL intensity.

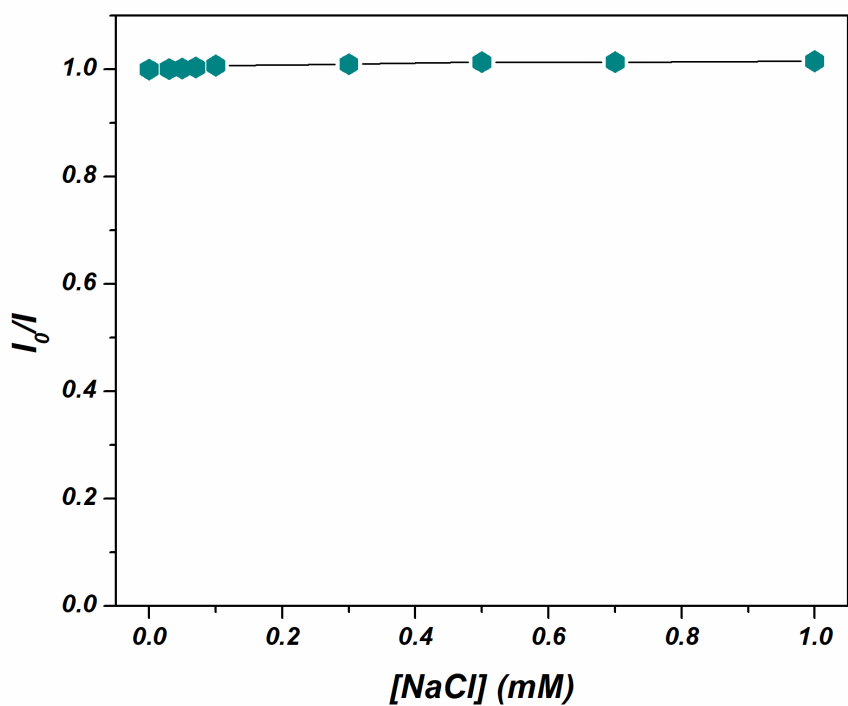


Figure 6.29. Effect of different concentrations of NaCl solutions on the emission of CPAP-CDs.

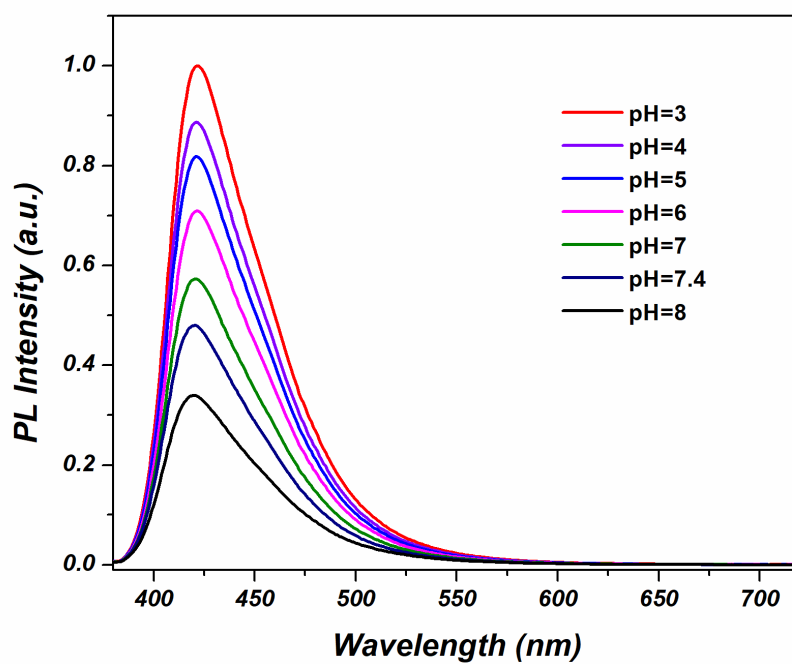


Figure 6.30. PL emission spectral of CPAP-CDs in various pH solutions. [CPAP-CDs] = 0.22 mg/mL and $\lambda_{\text{ex}} = 370$ nm.

6.3.3. Nitrites sensing of CPAP-CDs

The effects of fluorescence response and UV–vis absorption of the as-synthesized CPAP-CDs toward various anions [NO_2^- , NO_3^- , $\text{B}_4\text{O}_7^{2-}$, CO_3^{2-} , S^{2-} , HPO_4^{2-} , N_3^- , SCN^- , I^- , Br^- , Cl^- , F^-] were investigated individually. Figure 6. 10 showed the PL emission and UV–vis absorption spectra of CPAP-CDs in the presence of different anions, almost no other anions except for NO_2^- caused significant changes (photograph inset Figure 6. 10B). Maximum quenching was obtained after 2 h (Figure 6. 11). The PL emission spectra showed that in the presence of NO_2^- , the position of CPAP-CDs emission peak was not significantly altered. On the other hand, the UV–vis absorbance spectra showed in the presence of NO_2^- , the appearance of a new peak at 444 nm, and the red shift of the CPAP-CDs peaks along with the increase of the absorbance intensity. The color of the CPAP-CDs solution in the presence of NO_2^- changed from light yellow to dark yellow (photograph inset Figure 6. 10D).

The pH of the medium solution was a significant detection condition for sensing applications. As shown in Figure 6. 12, the PL emission intensities of CPAP-CDs in the absence and presence of NO_2^- were measured at various pH solutions from 3 to 8. The NO_2^- induced quenching could be interfered by pH, the PL intensity of CPAP-CDs was more sensitive to nitrite with the decrease of pH. This phenomenon occurred possibly because in stronger acidic medium, the diazotization between nitrites and primary arylamines is more easily happened and the NO_2^- -induced quenching of CPAP-CDs became more prominent [38]. All NO_2^- sensing experimental conditions were conducted in a medium pH = 3.

The fluorescence quenching of CPAP-CDs by NO_2^- was examined by the quantitative detection of NO_2^- . Figure 6. 13 showed that the fluorescence quenching was dependent on the concentration of NO_2^- . The PL emission intensities of CPAP-CDs decreased with the gradually increasing of NO_2^- concentration. The relative PL emission intensity (I_0/I) at a wavelength of 421 nm was measured as a function of the NO_2^- concentration ($[\text{NO}_2^-]$) over the concentration range from 0–1000 μM . The fluorescence quenching of CPAP-CDs in the

presence of NO_2^- was describes using a Stern-Volmer plot, as follows:

$$I_0/I = 1 + K_{SV}[Q] \quad (6-1)$$

where, K_{SV} is the Stern-Volmer constant, and $[Q]$ is the concentration of NO_2^- in equation. I_0 and I denote the PL intensity of CPAP-CDs in the absence and presence of NO_2^- , respectively. In the plot, a linear relationship was obtained from the relative PL emission intensity (I_0/I) and the NO_2^- concentration ($[\text{NO}_2^-]$) at the linear range from 2–1000 μM ($R^2 = 0.978$). At the low concentration range of 0–0.5 μM , the linear relationship was observed ($R^2 = 0.988$). The limit of detection ($\text{LOD} = 3\sigma/k$) was calculated to be 6.6 nM. This result makes the CPAP-CDs a very sensitive probe for NO_2^- detection.

Figure 6. 14 showed that at the concentration ratio 1:1 of NO_2^- and other anions, there was no significant change in the PL emission intensity of the co-existing CPAP-CDs- NO_2^- system. Compared to other previous studies (Table 6.1), the results of our work presented a significantly important detection limit of NO_2^- with an impressive quantum yield.

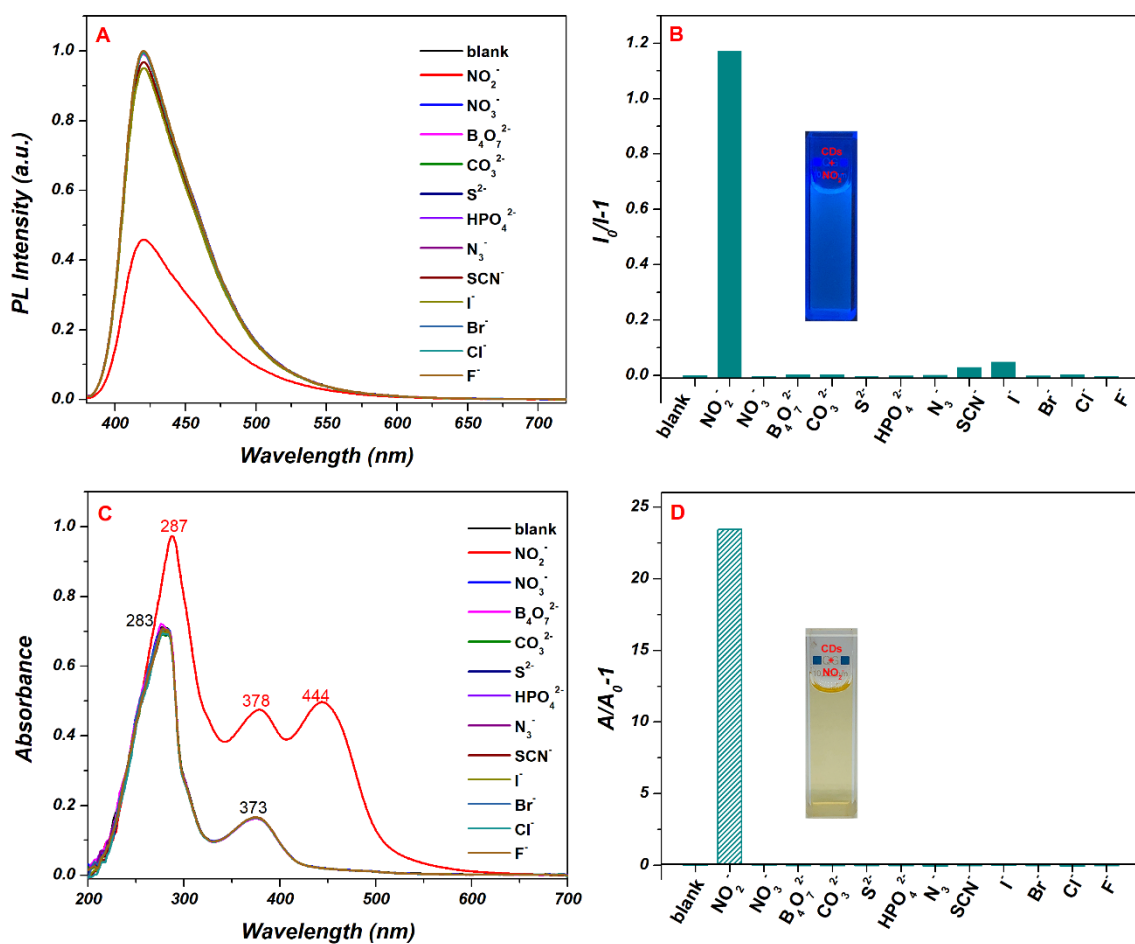


Figure 6.31. (A) The PL emission, (B) relative PL emission (at 421 nm), (C) absorbance, and (D) relative UV–vis absorbance spectra (at 444 nm) of CPAP-CDs in the presence of various analytes, respectively. The inset: the photographs of CPAP-CDs in the presence of NO_2^- under UV light (B) and visible light (D). [CPAP-CDs] = 0.22 mg/mL, pH = 3, and $\lambda_{\text{ex}} = 370$ nm.

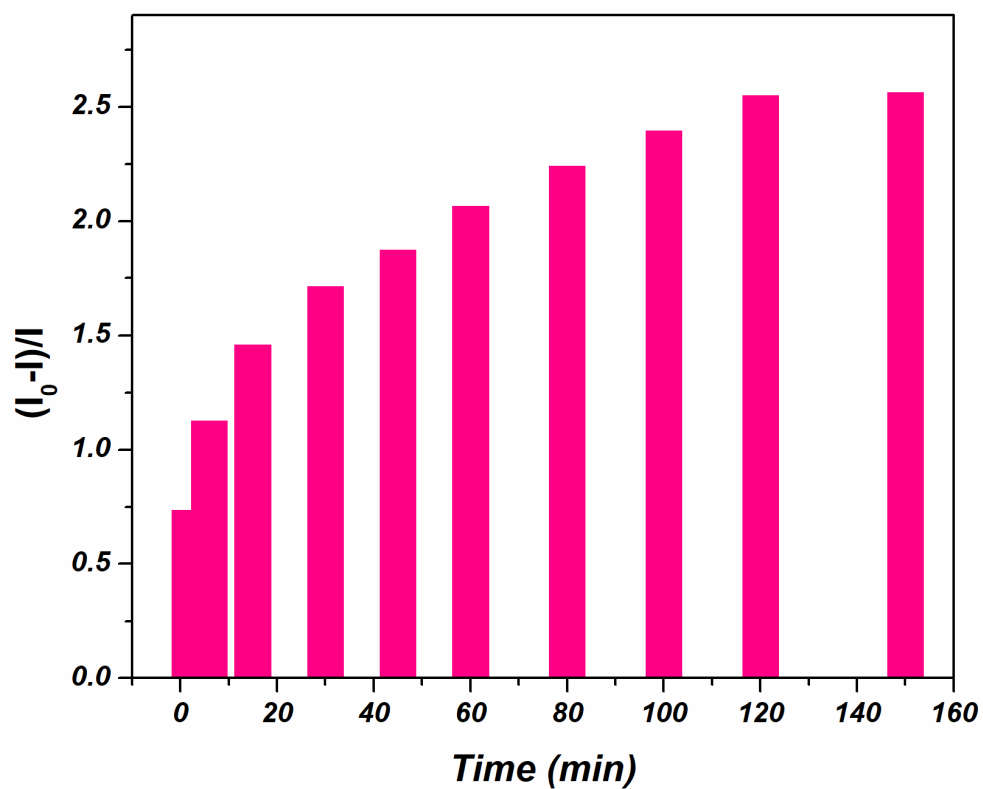


Figure 6.32. The bar diagram showing NO_2^- mediated quenching of the fluorescence of CPAP-CDs with respect to time, $[\text{NO}_2^-] = 1.0 \text{ mM}$, $[\text{CPAP-CDs}] = 0.22 \text{ mg/mL}$, $\lambda_{\text{ex}} = 370 \text{ nm}$.

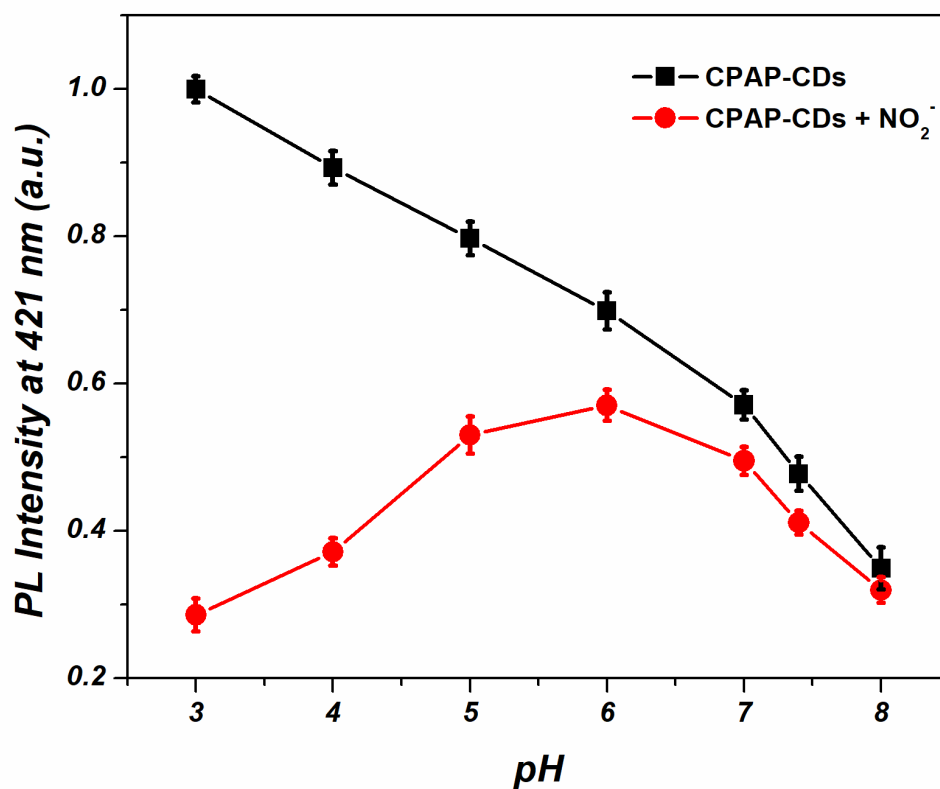


Figure 6.33. The influence of pH on PL emission intensity at 421 nm of CPAP-CDs in the absence and presence of 1 mM NO₂⁻ in various pH solutions, respectively. [CPAP-CDs] = 0.22 mg/mL and $\lambda_{\text{ex}} = 370$ nm.

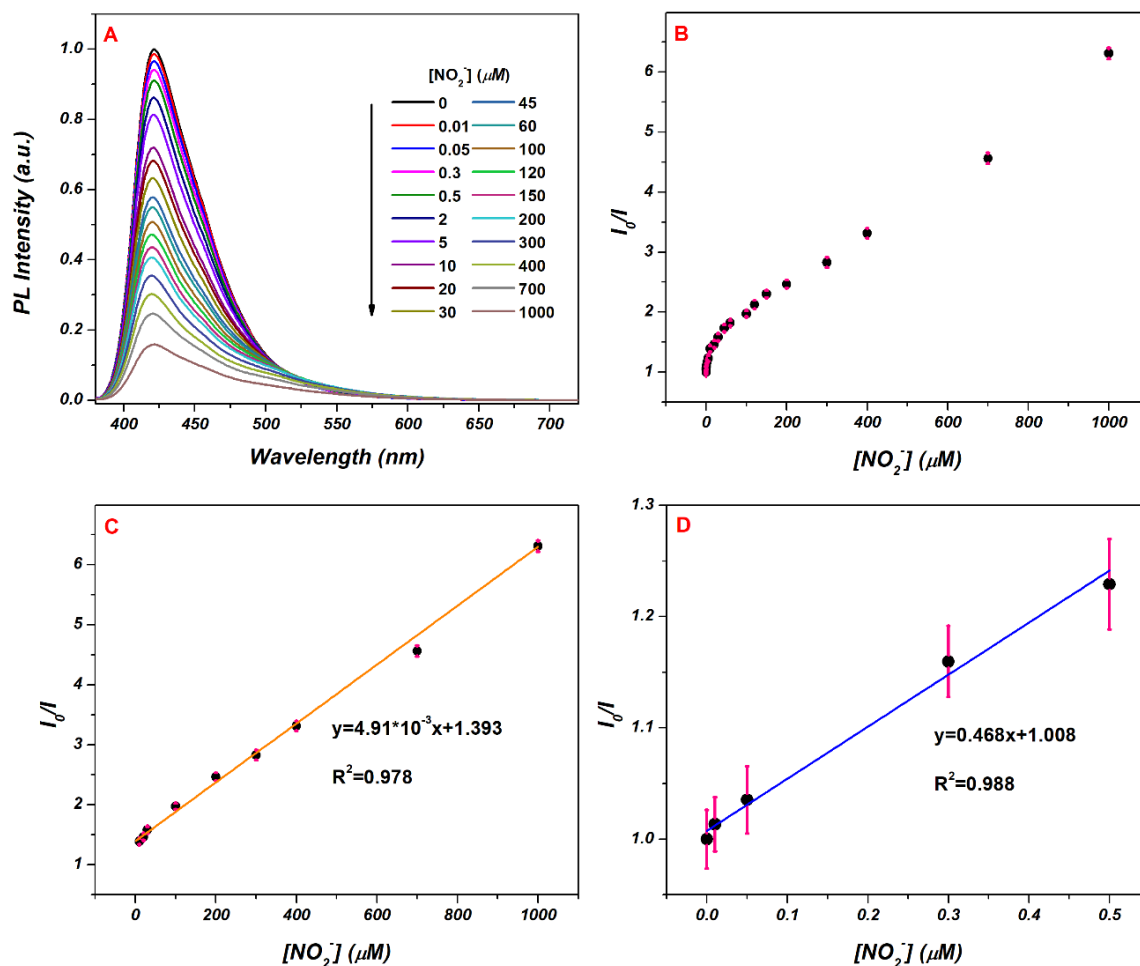


Figure 6.34. (A) Variation of the PL emission intensities of CPAP-CDs with different concentrations of NO_2^- . (B) Relative PL emission intensities of CPAP-CDs vs $[\text{NO}_2^-]$. (C) The linear dynamic range of the relative PL emission intensity vs. $[\text{NO}_2^-]$ from 2–1000 μM . (D) The linear relationships at the low concentration range from 0–0.5 μM . [CPAP-CDs] = 0.22 mg/mL, pH = 3, and $\lambda_{\text{ex}} = 370 \text{ nm}$.

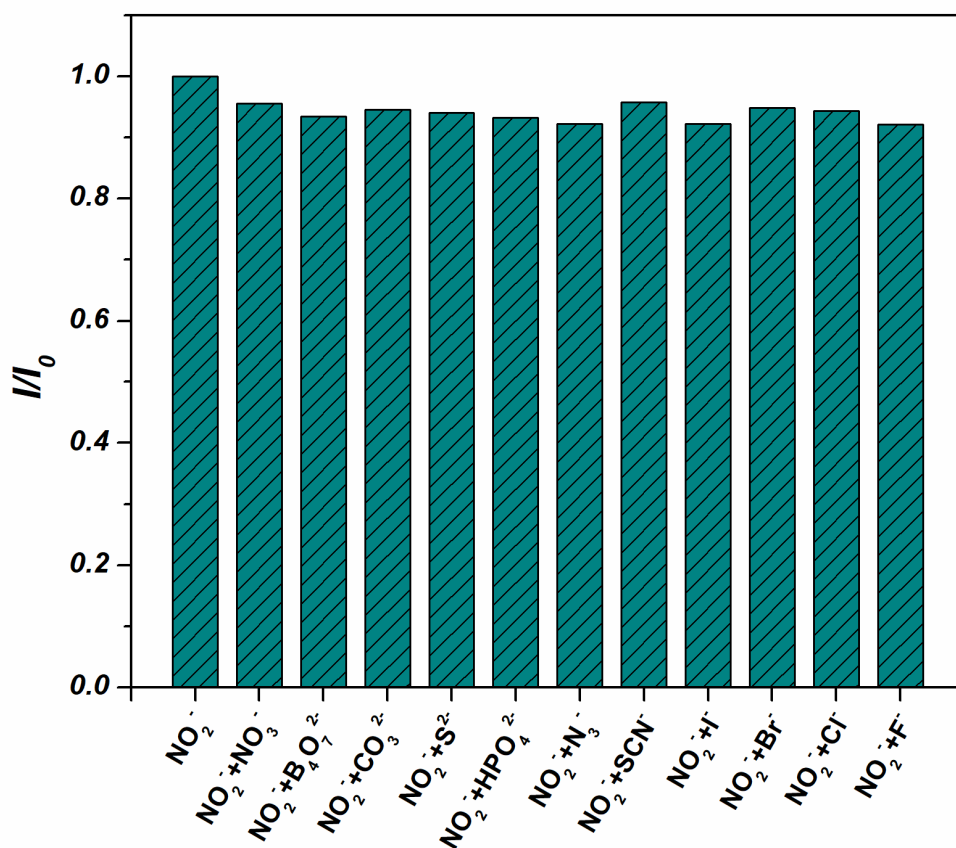


Figure 6.35. The relative PL emission spectra of the CPAP-CDs- NO_2^- system in the presence of various anions. [CPAP-CDs] = 0.22 mg/mL, [NO_2^- /other anions] = 500 μM , pH = 3, and λ_{ex} = 370 nm.

Table 6.3. The comparison of different sensors for NO₂⁻ detection.

Materials	Detection method	LOD	Linear range (μM)	QY	Ref.
C-dots-NR system	colorimetry	196 nM	0.145–4.34 μM	–	[2]
MoS ₂ QDs-AuNCs nanocomposite	Fluorescence (Visualization)	0.67 nM 27.32 nM	0.5–20 mg/L (1.0–20 mg/L)	–	[5]
carbon fiber paper (CFP)	Electrochemistry	0.07 μM	0.1–3838.5 μM	–	[7]
poly(3,4-ethylenedioxythiophene)hollow micro-flowers	Electrochemistry	0.59 μM	50–7500 μM	–	[8]
phosphatidylcholines (PCs)	chromatography	4.21 μg/L	0.5–15 μg mL ⁻¹	–	[9]
N,P-doped polymer carbon dots	fluorescence	0.55 μM	2–100 μM	3.8%	[12]
N,B-doped Carbon Dots	Fluorescence	6.06 nM	0–0.5 μM 2–1000 μM	64.07%	Present work

6.3.4. Fluorescence quenching mechanism

NO_2^- can quench the fluorescence of CPAP-CDs prepared in this experiment, which may be related to the amino groups on the surface of CPAP-CDs. The average fluorescence lifetime value of the CPAP-CDs was changed from 9.05 ns to be 5.08 ns in the presence of NO_2^- (Figure 6. 6), , proved that a dynamic quenching might occur [39]. As well, the zeta potential values of CPAP-CDs and CPAP-CDs- NO_2^- were calculated to be -11.3 mV and 10.4 mV, respectively (Figure 6. 15). The significant altered of fluorescence lifetime and the zeta potential values under experimental conditions indicated the strong interactions between CPAP-CDs and nitrites.

The possible quenching mechanism of CPAP-CDs towards nitrite is proposed to proceed via a diazotization mechanism. This has been confirmed by extensive reports that primary arylamines can be diazotized by nitrites to form diazonium salts in strongly acidic media [38]. The corresponding fluorescence quenching mechanism may be ascribed to the formation of an azo compound. The absorption peak of CPAP-CDs after participating in the coupling reaction with NO_2^- exhibited a 71 nm red shift (from 373 to 444 nm) (Figure 6. 10C), which was attributed to the formation of an azo group (N=N) via a diazo coupling reaction [40, 41]. Meanwhile, the color change of CPAP-CDs solutions may also arise from the formation of an azo compound. Further, the FTIR spectra of CPAP-CDs after the diazo coupling reaction with NO_2^- was also examined (Figure 6. 16). It indicated that the aromatic amine peaks at $3346\text{-}3228\text{ cm}^{-1}$ were nearly vanished, while a new peak at 1698 cm^{-1} appeared, which was attributed to the formation of a diazo group [42], and the peak strength of the functional group changes significantly. Besides, in the high-resolution XPS spectra of N1s of CPAP-CDs- NO_2^- system (Figure 6. 17), the presence of a =N- peak (397.33 eV) [43, 44] indicated that the successful diazotization between CPAP-CDs and NO_2^- . Moreover, the hydrodynamic diameter of CPAP-CDs changed from 37.84 nm to 1446 nm after adding 1 mM NO_2^- (Figure 6. 18). Based on this result, the DLS data showed that CPAP-CDs aggregated in presence of NO_2^- . In additional, NO_2^- -caused fluorescence quenching was found to be unrecoverable in the presence of various cations (Figure 6. 19), indicating a strong interaction between NO_2^- and the CPAP-CDs. Therefore, we hypothesized that the

detection mechanism is predominantly attributed to the strong reaction of NO_2^- and $-\text{NH}_2$ on the surface of CPAP-CDs, resulting in aggregation of CPAP-CDs, which leading to an aggregation-induced emission quenching ultimately (Figure 6. 20).

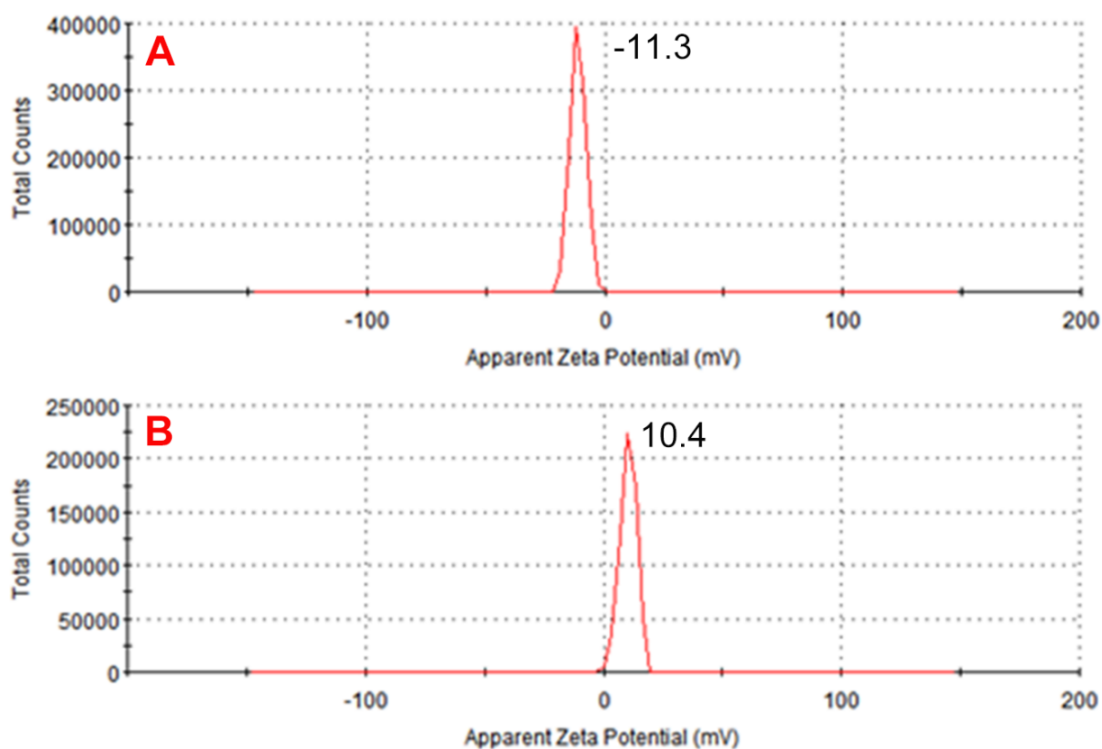


Figure 6.36. The zeta potential values for (A) CPAP-CDs and (B) CPAP-CDs- NO_2^- system, respectively. $[\text{CPAP-CDs}] = 0.22 \text{ mg/mL}$, $[\text{NO}_2^-] = 1 \text{ mM}$, and $\text{pH} = 3$.

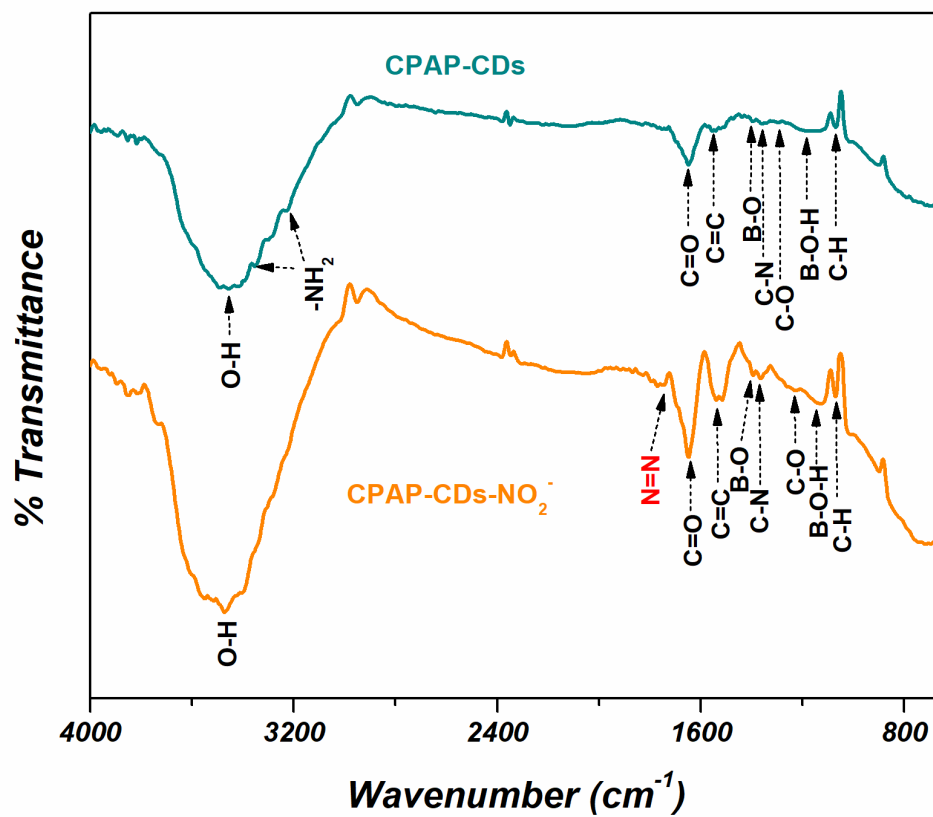


Figure 6.37. FTIR spectra of CPAP-CDs in the absence and presence of NO₂⁻.

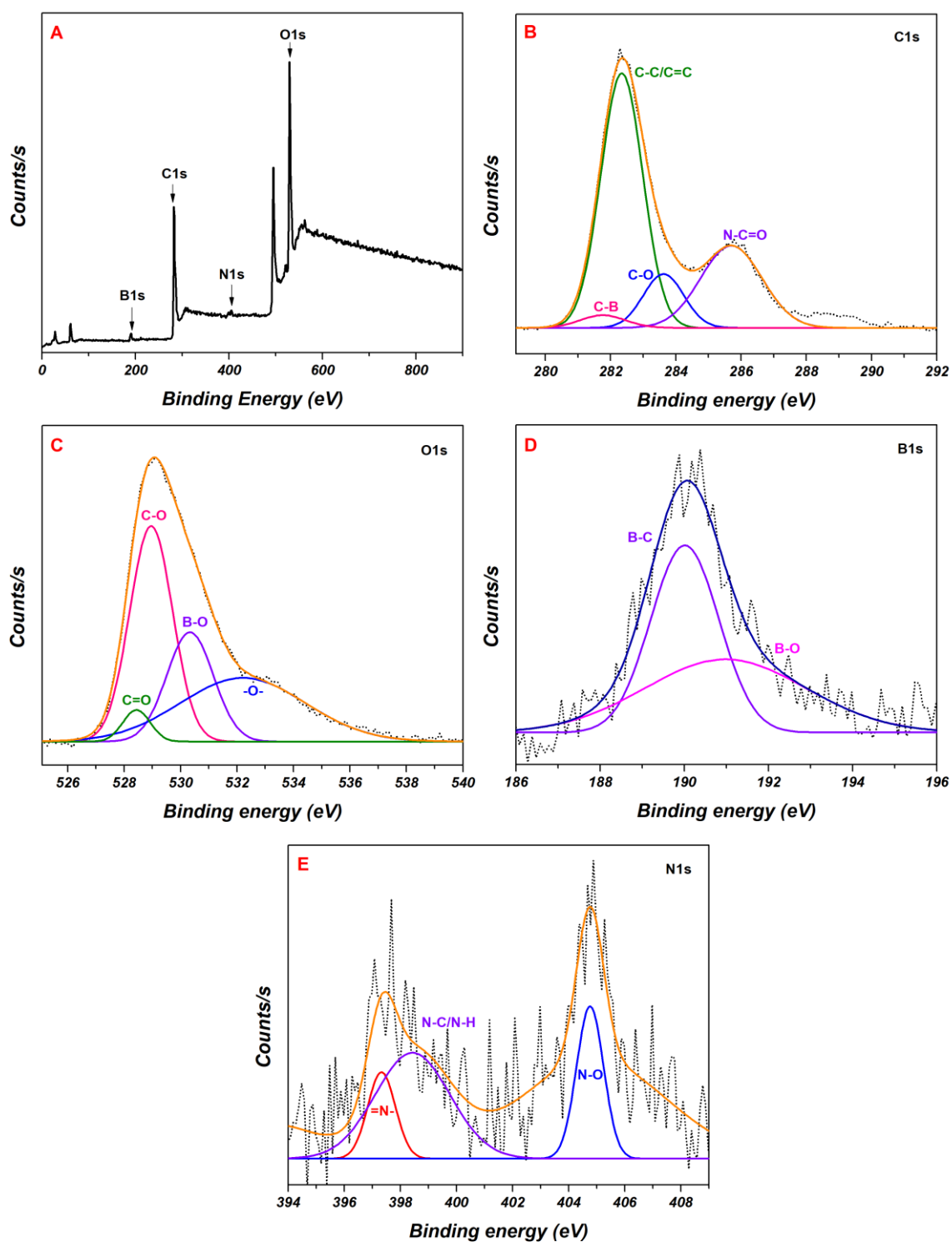


Figure 6.38. (A) XPS survey spectra of CPAP-CDs-NO₂⁻. The high-resolution XPS spectra of (B) C1s, (C) O1s, (D) B1s, and (E) N1s for CPAP-CDs. XPS analysis was done using the vacuum dried solid under 60 °C.

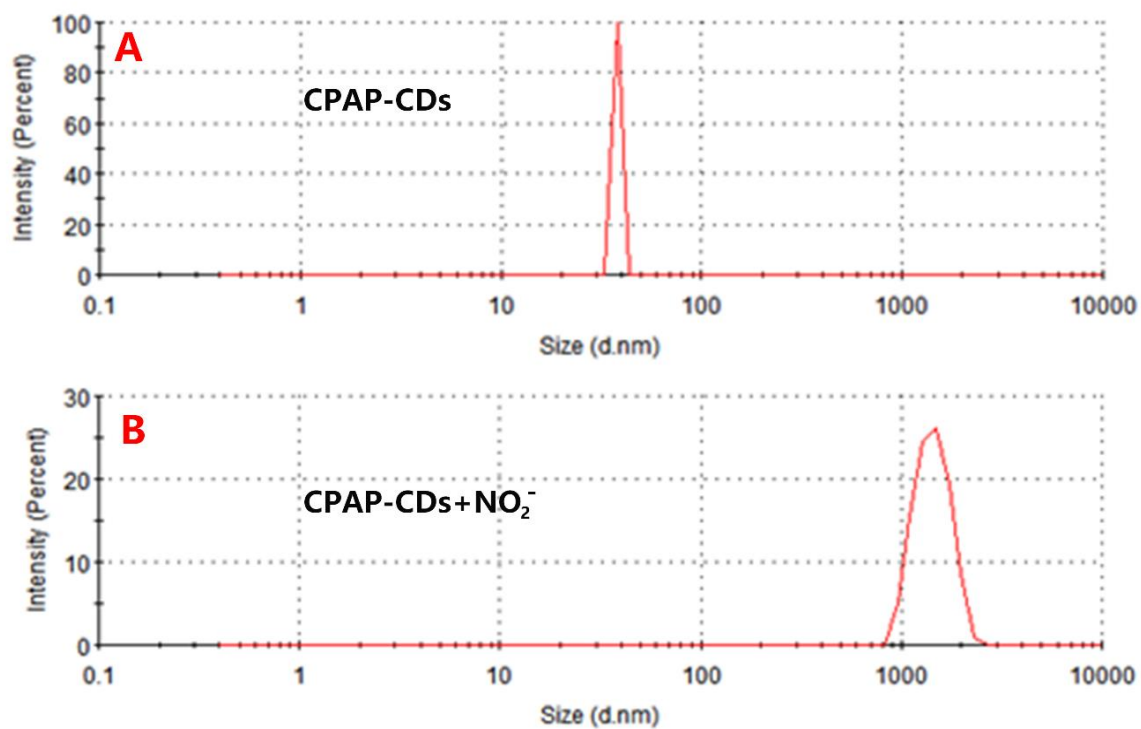


Figure 6.39. The hydrodynamic diameter values for (A) CPAP-CDs and (B) PAP-CDs-NO₂⁻ system, respectively. [CPAP-CDs] = 0.22 mg/mL, [NO₂⁻] = 1 mM, and pH = 3.

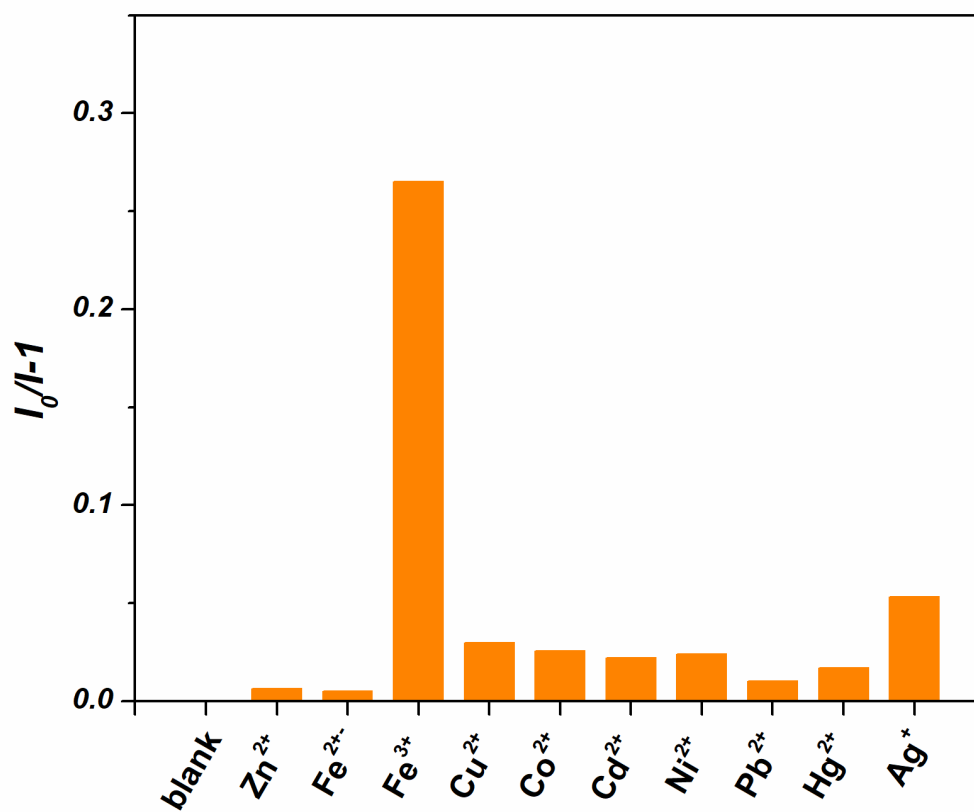


Figure 6.40. (A) The spectra showing the effect of various cations on the relative PL emission of CPAP-CDs-NO₂⁻ system.

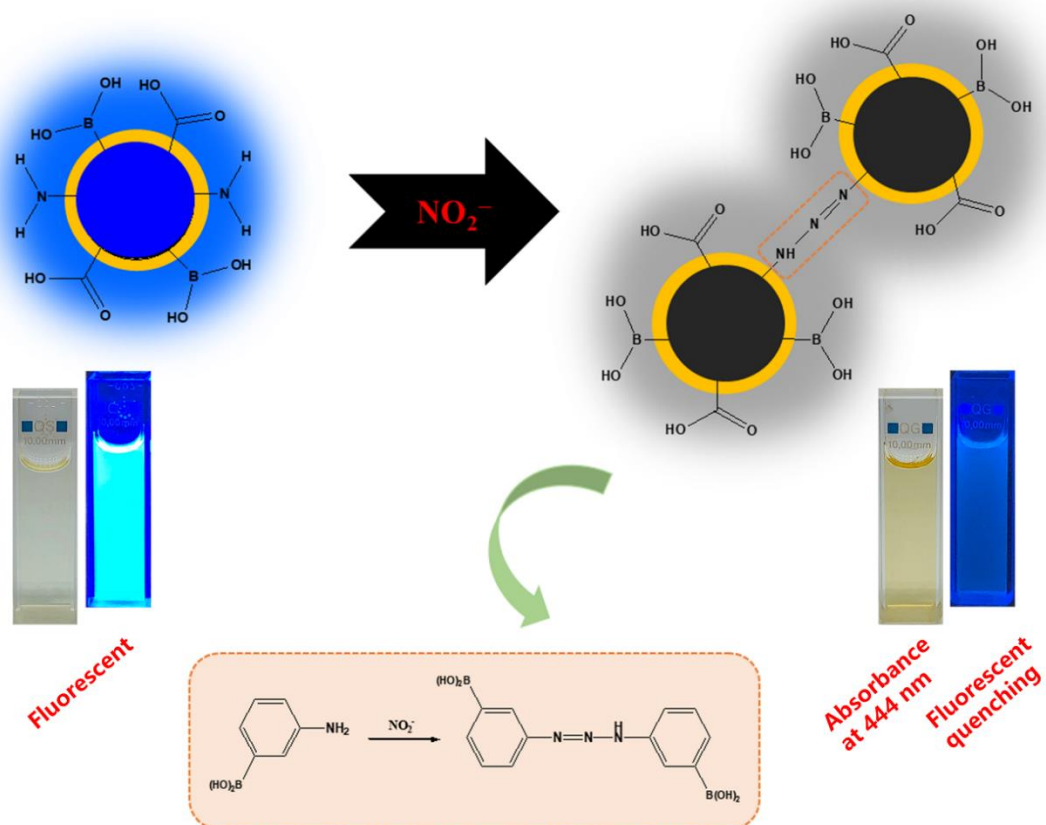


Figure 6.41. Schematic illustration of a suggested fluorescence quenching mechanism of CPAP-CDs in the presence of NO_2^- in solutions (pH=3) (not to scale).

6.3.5. Analysis of NO₂⁻ in real samples

To determine the applicability of the as-designed CPAP-CDs for detecting the concentration of NO₂⁻ was performed in real water samples, including the tap water, drinking water and sea water. The water samples were collected from the local area, and were centrifuged and treated with UV to remove any unwanted components. To mimic real environmental conditions, the water samples were spiked with different concentrations of NO₂⁻ and the PL intensity of each sample were measured accordingly under experimental conditions. As shown in Table 6.2, the obtained recovery results upon the spiked concentration of NO₂⁻ in the real water samples indicating that the potential applicability of CPAP-CDs for the selective and sensitive detection of NO₂⁻ in real water samples.

Table 6.4. Detection of the concentration of NO₂⁻ in water obtained from different sources using the proposed method (n=3).

	Samples	Spiked (μM)	Found (μM)	Recovery (%)	RSD (%)
Tap water	I	25	22.8	91.1	3.20
	II	50	52.5	105.0	2.12
	III	100	102.2	102.2	0.73
	IV	200	198.4	99.2	0.24
Drinking water	I	25	22.6	90.3	2.48
	II	50	50.1	100.1	2.63
	III	100	105.3	105.3	0.81
	IV	200	197.7	98.8	0.96
Sea water	I	25	22.8	91.2	3.03
	II	50	50.4	100.9	2.85
	III	100	104.3	104.3	1.29
	IV	200	198.6	99.3	0.96

6.4. Conclusion

A nitrogen and boron-doped high quantum yield carbon dot was designed for the selective and sensitive detection of nitrite. The sensing performance of the synthesized CPAP-CDs was evaluated through a fluorescence “turn off” phenomenon. The aggregation-induced emission quenching was attributed to the diazo coupling reaction between the $-NH_2$ group of the as-obtained carbon dot particles and nitrites in aqueous solutions. The proposed sensor achieved a nanomolar detection limit in the pH medium solutions. The applicability of the sensor was checked using different water samples with reasonable RSD values. The medium pH-dependent behavior of the CPAP-CDs provided a platform for NO_2^- detection to a satisfactory level. The proposal has the potential in extending to the sensitive and selective detection of nitrite in different fields of water environments.

References

- [1] J. O. Hall. *Veterinary Toxicology*, 2018, 941-946.
- [2] X. Hu, J. Shi, Y. Shi, X. Zou, H. E. Tahir, M. Holmes, W. Zhang, X. Huang, Z. Li, Y. Xu. *Meat science*, 2019, 147, 127-134.
- [3] D. M. Manassaram, L. C. Backer, D. M. Moll. *Environmental Health Perspectives*, 2006, 114, 320-327.
- [4] V. Sharma, S. Manu. *International Research Journal of Pharmacy*, 2012, 3, 60-65.
- [5] W. Li, Y. Shi, X. Hu, Z. Li, X. Huang, M. Holmes, Y. Gong, J. Shi, X. Zou. *Food Control*, 2019, 106, 106704.
- [6] WHO. Geneva, Switzerland: World Health Organization, 2008.
- [7] W. Zhu, Y. Zhang, J. Gong, Y. Ma, J. Sun, T. Li, J. Wang. *ACS Sensors*, 2019, 4, 2980-2987.
- [8] Y.-H. Cheng, C.-W. Kung, L.-Y. Chou, R. Vittal, K.-C. Ho. *Sensors and Actuators B: Chemical*, 2014, 192, 762-768.
- [9] M. Tatarczak-Michalewska, J. Flieger, J. Kawka, W. Płaziński, W. Flieger, E. Blicharska, D. Majerek. *Molecules*, 2019, 24, 1754.

- [10] X. Yin, Q. Chen, H. Song, M. Yang, H. Wang. *Electrochemistry communications*, 2013, 34, 81-85.
- [11] H. Yang, Y. Xiang, X. Guo, Y. Wu, Y. Wen, H. Yang. *Sensors and Actuators B: Chemical*, 2018, 271, 118-121.
- [12] Y. J. Jiang, M. Lin, T. Yang, R. S. Li, C. Z. Huang, J. Wang, Y. F. Li. *Journal of Materials Chemistry B*, 2019, 7, 2074-2080.
- [13] X. Luo, Y. Qu, Y. Zhang, Y. Wu, W. Yuan, L. Wang. *Chemical Engineering Journal*, 2021, 415, 129095.
- [14] B. Gayen, S. Palchoudhury, J. Chowdhury. *Journal of Nanomaterials*, 2019, 2019, 3451307.
- [15] M. Li, T. Chen, J. J. Gooding, J. Liu. *ACS Sensors*, 2019, 4, 1732-1748.
- [16] L. Wang, W. M. Choi, J. S. Chung, S. H. Hur. *Nanoscale Research Letters*, 2020, 15, 1-10.
- [17] L. Wang, J. Jana, J. S. Chung, S. H. Hur. *Spectrochimica Acta Part A: Molecular and Biomolecular Spectroscopy*, 2021, 260, 119895.
- [18] S. Wang, Z. Chen, I. Cole, Q. Li. *Carbon*, 2015, 82, 304-313.
- [19] T.-Y. Wang, C.-Y. Chen, C.-M. Wang, Y. Z. Tan, W.-S. Liao. *ACS Sensors*, 2017, 2, 354-363.
- [20] L. Wang, J. Jana, J. S. Chung, S. H. Hur. *Dyes and Pigments*, 2021, 186, 109028.
- [21] L. Wang, J. S. Chung, S. H. Hur. *Dyes and Pigments*, 2019, 171, 107752.
- [22] H. Li, R. Liu, S. Lian, Y. Liu, H. Huang, Z. Kang. *Nanoscale*, 2013, 5, 3289-3297.
- [23] Q. Zeng, D. Shao, X. He, Z. Ren, W. Ji, C. Shan, S. Qu, J. Li, L. Chen, Q. Li. *Journal of Materials Chemistry B*, 2016, 4, 5119-5126.
- [24] S. Y. Lim, W. Shen, Z. Gao. *Chemical Society Reviews*, 2015, 44, 362-381.
- [25] J. Wu, W. Liu, J. Ge, H. Zhang, P. Wang. *Chemical Society Reviews*, 2011, 40, 3483-3495.
- [26] A. S. Tanwar, L. R. Adil, M. A. Afroz, P. K. Iyer. *ACS Sensors*, 2018, 3, 1451-1461.
- [27] H. Wu, J. Jiang, X. Gu, C. Tong. *Microchimica Acta*, 2017, 187, 2291-2298.

- [28] G. Tong, J. Wang, R. Wang, X. Guo, L. He, F. Qiu, G. Wang, B. Zhu, X. Zhu, T. Liu. *Journal of Materials Chemistry B*, 2015, 3, 700-706.
- [29] X. Liu, J. Pang, F. Xu, X. Zhang. *Scientific Reports*, 2016, 6, 1-8.
- [30] Y. Han, D. Tang, Y. Yang, C. Li, W. Kong, H. Huang, Y. L. Kang. *Nanoscale*, 2015, 7, 5955-5962.
- [31] P. Shen, Y. Xia. *Analytical Chemistry*, 2014, 86, 5323-5329.
- [32] X. Liu, X. Hu, Z. Xie, P. Chen, X. Sun, J. Yana, S. Zhou. *Analytical Methods*, 2016, 8, 3236-3241.
- [33] Z. Li, H. Yu, T. Bian, Y. Zhao, C. Zhou, L. Shang, Y. Liu, L.-Z. Wu, C.-H. Tung, T. Zhang. *Journal of Materials Chemistry C*, 2015, 3, 1922-1928.
- [34] Z. Yang, M. Xu, Y. Liu, F. He, F. Gao, Y. Su, H. Wei, Y. Zhang. *Nanoscale*, 2014, 6, 1890-1895.
- [35] Y. Wang, S. Kalytchuk, Y. Zhang, H. Shi, S. V. Kershaw, A. L. Rogach. *The Journal of Physical Chemistry Letters*, 2014, 5, 1412-1420.
- [36] S. Zhu, Y. Song, X. Zhao, J. Shao, J. Zhang, B. Yang. *Nano Research*, 2015, 8, 355-381.
- [37] Y. Liu, Y. Liu, S.-J. Park, Y. Zhang, T. Kim, S. Chae, M. Park, H.-Y. Kim. *Journal of Materials Chemistry A*, 2015, 3, 17747-17754.
- [38] R. N. BUTLER. *Chemical Reviews*, 1975, 75, 241-257.
- [39] H. Wu, C. Tong. *Journal of agricultural and food chemistry*, 2019, 67, 2794-2800.
- [40] L. Zhang, J. M. Cole, X. Liu. *The Journal of Physical Chemistry C*, 2013, 117, 26316-26323.
- [41] W. Li, S. Huang, H. Wen, Y. Luo, J. Cheng, Z. Jia, P. Han, W. Xue. *Analytical and Bioanalytical Chemistry*, 2020, 412, 993-1002.
- [42] J. Qiu, J. Xiao, B. Tang, B. Ju, S. Zhang. *Dyes and Pigments*, 2019, 160, 524-529.
- [43] M.-Y. Hua, C.-J. Chen, H.-C. Chen, R.-Y. Tsai, W. Cheng, C.-L. Cheng, Y.-C. Liu. *Sensors*, 2011, 11, 5873-5885.
- [44] H. Wang, N. Leukosol, Z. He, G. Fei, C. Si, Y. Ni. *Cellulose*, 2013, 20, 1587-1601.

CHAPTER 7. Summary

In this dissertation, several fluorescent nanoparticles based on several organic molecules (such as ascorbic acid, aminophenylboronic acid, phenylenediamine, and L-glutathione) were designed and synthesized, and several fluorescent sensor analysis systems were prepared.

The chemical-physical properties of heteroatoms doped carbon dots and their applications in environmental and biological systems have been investigated. Basic characterizations were carried out by FT-IR, XRD, and HR-TEM to determine the chemical composition and their morphology in the synthesized materials. The interactions between different components within the as-synthesized materials were identified by XPS analysis. On the other hand, the optical properties of the as-obtained carbon dots were examined by UV-vis absorbance and fluorescence spectroscopy.

Conclusion 1, the first work on carbon dots was N,B-doped carbon dots (NBCDs) for Fe^{3+} and ascorbic acid (AA) sensing. The NBCDs obtained exhibited good water solubility, strong fluorescence, and excellent stability without further modification. Fe^{3+} selectively showed quenching, and the LOD was $7.5 \mu\text{M}$ ($3\sigma/k$). The enhancement is selective for AA, and the LOD was $7.72 \mu\text{M}$. I assumed that the interaction between Fe^{3+} of -OH of NBCDs caused quenching, when AA was added, AA and Fe^{3+} reacted, then the PL of CDs recovered. The NBCDs have applied for the detection of Fe^{3+} in acid rain.

Conclusion 2, L-glutathione (GSH) has been used for synthesizing GSH-modified N-doped carbon dots (GSH-NCDs) by the surface passivation. DA is neurotransmitter, and its balance in human body is important. The designed GSH-NCDs showed good selectivity and sensitivity for DA detection. It showed the selective quenching for DA, and LOD was 1.01 nM in the linear ranges of detection from 20 nM to $10 \mu\text{M}$. The quenching phenomenon possibly followed IFE/PET process. The GSH-NCDs were successfully applied into the urine sample analysis.

Conclusion 3, the multicolor emitting N-doped carbon dots were obtained by hydrothermal treatment. Product functional groups came from the precursors, there was no

variation in functional groups, but the optical properties are different. The PL and QY were changed with solvent polarity. The effects of pH and zeta potential were found different behaviors, which caused by the different core structures. We can see that differently directed functional groups in precursors changed product nature, but the morphology remained almost same, exhibiting the orientation of molecule is important for reacting.

Conclusion 4, the work on CDs was high quantum yield GAAP-CDs for hypochlorite ions (ClO^-) detection. ClO^- ions have the effective antibacterial and pro- and anti-inflammatory properties that plays an important role in biological and environmental systems. The as-synthesized GAAP-CDs showed excellent sensitivity and selectivity towards highly toxic ClO^- ions with wide linear ranges in both the UV-vis- and photoluminescence-based sensing experiments. We assumed that the direct chemical interaction of surface functional groups and ClO^- ions. The quenching phenomenon possibly followed IFE process. The GAAP-CDs were successfully used for the analysis of ClO^- in tap and drinking water.

Conclusion 5, the final work was nitrogen and boron-doped high quantum yield carbon dots for the selective and sensitive detection of nitrite. Nitrites play important roles in food preservatives, biological nitrogen cycle, environment system etc. An excess amount of nitrite can cause health risks, such as methemoglobinemia due to interference in blood oxygen transport, stomach cancer etc. The fluorescence quenching was attributed to the diazo coupling reaction between the as-obtained carbon dot particles and nitrites in aqueous solutions. The medium pH-dependent behavior of the obtained carbon dots provided a platform for nitrites detection to a satisfactory level.

In summary, the physical and optical properties of four different CDs have been studied and applied for sensing. Introduced different heteroatoms can improve the PL properties, high QY, and electronic environment for facile redox reaction; introduced different functional groups for different sensing; chosen CDs for its high sensitivity, easy reactivity, and nontoxicity. With time, the structure and properties of CDs are changed, and more experiments are going on.

LIST OF PUBLICATIONS

1. **Linlin Wang**, Seung Hyun Hur. A selective and sensitive sensor for fluorescent determination of nitrite based on high quantum yield nitrogen and boron doped carbon nanodots. Under Preparation (2021).
2. **Linlin Wang**, Jayasmita Jana, Jin Suk Chung, Seung Hyun Hur. High quantum yield aminophenylboronic acid-functionalized N-doped carbon dots for highly selective hypochlorite ion detection. *Spectrochimica Acta Part A: Molecular and Biomolecular Spectroscopy*, 2021, Available online, 119895.
3. **Linlin Wang**, Jayasmita Jana, Jin Suk Chung, Seung Hyun Hur, Glutathione modified N-doped carbon dots for sensitive and selective dopamine detection. *Dyes and Pigments*, 2021, 186, 109028.
4. **Linlin Wang**, Won Mook Choi, Jin Suk Chung, Seung Hyun Hur, Multicolor emitting N-doped carbon dots derived from ascorbic acid and phenylenediamine precursors. *Nanoscale research letters*, 2020, 15, 1-10.
5. **Linlin Wang**, Jin Suk Chung, Seung Hyun Hur, Nitrogen and boron-incorporated carbon dots for the sequential sensing of ferric ions and ascorbic acid sensitively and selectively. *Dyes and Pigments*, 2019, 171, 107752.
6. Hye Jin Lee, Jayasmita Jana, Yen-Linh Thi Ngo, **Linlin Wang**, Jin Suk Chung, Seung Hyun Hur. The effect of solvent polarity on emission properties of carbon dots and their uses in colorimetric sensors for water and humidity. *Materials Research Bulletin*, 2019, 119, 110564